

Title	Insertion of metal oxides into block copolymer nanopatterns as robust etch masks for nanolithography
Authors	Cummins, Cian
Publication date	2015
Original Citation	Cummins, C. A. 2015. Insertion of metal oxides into block copolymer nanopatterns as robust etch masks for nanolithography. PhD Thesis, University College Cork.
Type of publication	Doctoral thesis
Rights	© 2015, Cian A. Cummins - <a href="http://creativecommons.org/licenses/by-nc-nd/3.0/">http://creativecommons.org/licenses/by-nc-nd/3.0/</a>
Download date	2024-04-26 01:15:42
Item downloaded from	<a href="https://hdl.handle.net/10468/2131">https://hdl.handle.net/10468/2131</a>

# **Insertion of Metal Oxides into Block Copolymer Nanopatterns as Robust Etch Masks for Nanolithography**

**Cian Anthony Cummins, B.Sc. (Hons)**

Department of Chemistry,  
University College Cork,  
Ireland.



# UCC

Coláiste na hOllscoile Corcaigh, Éire  
University College Cork, Ireland

Presented for the PhD. Degree to the National University of Ireland

**Supervisor: Prof. Michael A. Morris**

Co-supervisor: Prof. Justin D. Holmes

Head of Department: Prof. Martyn Pemble

**Declaration**

I, Cian Anthony Cummins, certify that this thesis is my own research work and I have not obtained a degree in University College Cork or elsewhere on the basis of this PhD thesis.

---

**Cian Anthony Cummins**

## **Abstract**

Directed self-assembly (DSA) of block copolymers (BCPs) is a prime candidate to further extend dimensional scaling of silicon integrated circuit features for the nanoelectronic industry. Top-down optical techniques employed for photoresist patterning are predicted to reach an endpoint due to diffraction limits. Additionally, the prohibitive costs for “fabs” and high volume manufacturing tools are issues that have led the search for alternative complementary patterning processes. This thesis reports the fabrication of semiconductor features from nanoscale on-chip etch masks using “high  $\chi$ ” BCP materials. Fabrication of silicon and germanium nanofins via metal-oxide enhanced BCP on-chip etch masks that might be of importance for future Fin-field effect transistor (FinFETs) application are detailed.

Chapter 1 introduces the key reasons and main motivations for the research carried out during this PhD. Nanoelectronic industry challenges are outlined that have led to increased interest in BCP materials for device patterning. The fundamental characteristics of block copolymer self-assembly are explained and favorable BCP systems for on-chip etch masks are discussed. A literature review detailing early methods incorporating inorganic material in self-assembled or “neat” BCP thin films is presented. Furthermore, more recent reports for infiltrating BCP thin films are reviewed including atomic layer deposition, sequential infiltration synthesis, metal-salt inclusion, and aqueous metal reduction. Salient work on applications beyond on-chip etch masks are also mentioned.

Chapter 2 details the selective etching of polylactic acid (PLA) from a poly(styrene)-block-poly(D,L)lactide (PS-*b*-PLA) BCP. PS-*b*-PLA was chosen for study as it is a “high  $\chi$ ” BCP that can potentially access small features sizes at low molecular weights. Also the degradable nature of PLA provides a possibly facile method for creating porous nanoscale on-chip etch masks for nanolithography. “Solvo-microwave” annealing was employed to produce well-ordered nanoscale patterns. A range of wet etch (solution) and dry etch (plasma) procedures for etching PLA were examined in chapter 2 in a view to develop porous on-chip etch masks for silicon patterning at sub-20 nm features.

Chapter 3 focuses on the self-assembly of PS-*b*-PLA using conventional solvent vapor annealing. Grazing incidence small angle X-ray scattering (GISAXS) was employed to probe the thin film interior and to analyze the ordering of microdomains at different stages after solvent vapor annealing. The chapter details PS-*b*-PLA thin films that are suitable for nanolithography. Optimized wet etching of the PLA block is demonstrated in chapter 3 as characterized by electron microscopy and GISAXS. Directed self-assembly is also utilized to align PS-*b*-PLA microdomains for nanolithography where both parallel and perpendicular alignments of features to guiding sidewalls was observed.

Chapter 4 introduces another “high  $\chi$ ” BCP of interest for nanolithography, PS-*b*-poly(4-vinylpyridine). Chapter 4 focuses on the importance of substrate surface functionalization to enhance and orient BCP microdomains. Metal oxide inclusion is also discussed for enhancing etch contrast of nanodot arrays to enable high aspect ratio silicon nanopillars following pattern transfer.

Line space features and DSA are demonstrated in Chapter 5 using PS-*b*-P4VP BCP. Robust metal oxide nanowires are formed and produce high aspect ratio silicon nanofins after pattern transfer. Graphoepitaxial alignment using hydrogen silsesquioxane (HSQ) prepatterns over macroscopic areas is also shown for this system producing near-defect free patterns.

Chapter 6 focuses on an unusual microdomain perturbation observed using graphoepitaxy and PS-*b*-P4VP line patterns that may be related to polymer expansion during solvent vapor annealing. Alternative strategies are put forward to alleviate this issue. Whilst reducing features has been the path followed for increased device performance, high mobility materials are also of much interest.

In chapter 7, long range alignment of PS-*b*-P4VP line space features through electron beam lithographically defined HSQ prepatterns on germanium and germanium-on-insulator substrates is demonstrated for the first time. Pattern transfer of metal oxide nanowires hardmask arrays to the underlying substrates produces sub-10 nm aligned germanium nanofins.

Chapter 8 summarizes the key achievements of each chapter and examines future directions of BCP nanopatterns for nanoelectronic device technology.

## **Acknowledgements**

The work presented in this thesis has been made possible through the efforts of my colleagues, collaborators and friends. I thank each one for their help along the way.

I sincerely appreciate the opportunity, vision, and constant encouragement from my supervisor, Prof. Mick Morris. I thank him for showing faith in me and giving me the opportunity and funding to carry out my PhD research in his laboratory. He was always available for advice and insights on the work and I thank him endlessly for this.

I would also like to thank my co-supervisor, Prof. Justin Holmes, for his help and support throughout the research. I thank senior post-docs both past and present. Ben, Dipu, Parvaneh, Tandra, and Siby (UCC) have provided endless ideas and perspective. Their assistance in the laboratory is invaluable, and will continue to inspire and guide students. I also thank Vladimir Djara and Alan Hydes (Tyndall) for their help in etching. I thank Pascal and Christophe for the GISAXS measurements detailed in chapter 3 and their great analysis and suggestions. I thank and also apologise for annoying Anushka and Roisin for their expertise that contributed to later chapters in this thesis. I sincerely thank all members of the Department of Chemistry for their help and assistance. For all the enjoyable teas and nights out with members past and present of labs 115 and 343, you've made my time in UCC special and a time of my life that I will never forget.

Finally – I thank my parents and my sister. Without my family's support and love, I would not be where and who I am. I cannot thank them enough for everything. Last but not least, I thank Roisin for her brilliant support in the past couple of years and the good times we've had together.

## Published Articles

- 1) **Cummins, C.**; Gangnaik, A.; Kelly, R. A.; Hydes, A. J.; O'Connell, J.; Petkov, N.; Georgiev, Y. M.; Borah, D.; Holmes, J. D.; Morris, M. A. Parallel Arrays of Sub-10 nm Aligned Germanium Nanofins from an In Situ Metal Oxide Hardmask using Directed Self-Assembly of Block Copolymers. *Chemistry of Materials* **2015**, 27 (17), 6091-6096.
- 2) **Cummins, C.**; Gangnaik, A.; Kelly, R. A.; Borah, D.; O'Connell, J.; Petkov, N.; Georgiev, Y. M.; Holmes, J. D.; Morris, M. A., Aligned silicon nanofins via the directed self-assembly of PS-*b*-P4VP block copolymer and metal oxide enhanced pattern transfer. *Nanoscale* **2015**, 7 (15), 6712-6721.
- 3) **Cummins, C.**; Kelly, R. A.; Gangnaik, A.; Georgiev, Y. M.; Petkov, N.; Holmes, J. D.; Morris, M. A., Solvent Vapor Annealing of Block Copolymers in Confined Topographies: Commensurability Considerations for Nanolithography. *Macromolecular Rapid Communications* **2015**, 36 (8), 762-767.
- 4) **Cummins, C.**; Mokarian-Tabari, P.; Holmes, J. D.; Morris, M. A., Selective etching of polylactic acid in poly(styrene)-*block*-poly(d,l)lactide diblock copolymer for nanoscale patterning. *Journal of Applied Polymer Science* **2014**, 131 (18).
- 5) **Cummins, C.**; Borah, D.; Rasappa, S.; Chaudhari, A.; Ghoshal, T.; O'Driscoll, B. M. D.; Carolan, P.; Petkov, N.; Holmes, J. D.; Morris, M. A., Self-assembly of polystyrene-*block*-poly(4-vinylpyridine) block copolymer on molecularly functionalized silicon substrates: fabrication of inorganic nanostructured etchmask for lithographic use. *Journal of Materials Chemistry C* **2013**, 1 (47), 7941-7951.
- 6) Mokarian-Tabari, P.; Vallejo-Giraldo, C.; Fernandez-Yague, M.; **Cummins, C.**; Morris, M. A.; Biggs, M. J. P., Nanoscale neuroelectrode modification via sub-20 nm silicon nanowires through self-assembly of block copolymers. *Journal of Materials Science-Materials in Medicine* **2015**, 26 (2).
- 7) Mokarian-Tabari, P.; **Cummins, C.**; Rasappa, S.; Simao, C.; Sotomayor Torres, C. M.; Holmes, J. D.; Morris, M. A., Study of the Kinetics and Mechanism of Rapid Self-Assembly in Block Copolymer Thin Films during Solvo-Microwave Annealing *Langmuir* **2014**, 30 (35), 10728-10739.

# Table of Contents

<b>Chapter 1. Introduction</b> .....	<b>1</b>
1.1. Abstract .....	2
1.2. Block copolymers .....	2
1.3. Motivation and scope .....	6
1.4. Evaporation and sputtering of metals on block copolymer templates .....	11
1.5. Atomic layer deposition methods and block copolymer templates .....	21
1.6. Sequential infiltration synthesis of block copolymers .....	28
1.7. Spin coating methodologies for metal nanoparticle alignment and metal oxide inclusion with “activated” block copolymer templates .....	36
1.8. Aqueous metal reduction and block copolymer nanopatterns .....	42
1.9. Triblock polymers and inorganic incorporation .....	48
1.10. Summary and Outlook .....	55
1.11. References .....	57
<b>Chapter 2. Selective Etching of Polylactic Acid in Poly(styrene)-block-poly(D,L)lactide Diblock Copolymer for Nanoscale Patterning</b> .....	<b>69</b>
2.1. Abstract .....	70
2.2. Introduction .....	70
2.3. Experimental .....	72
2.4. Results and Discussion .....	77
2.4.1. Self-Assembly and Surface Modification .....	77
2.4.2. PLA Degradation with Sodium Hydroxide Route .....	79
2.4.3. PLA Degradation with Ammonium Hydroxide Route .....	82
2.4.4. PLA Degradation with Enzymatic Route .....	84
2.4.5. Dry Etch Studies and Route for PLA removal .....	86
2.4.6. FTIR studies of etch routes .....	93
2.5. Conclusions .....	94
2.6. References .....	96
2.7. Appendix – Chapter 2 .....	100
<b>Chapter 3. Directed self-assembly of lamellar forming poly(styrene)-<i>block</i>-poly(D,L-lactide) block copolymer thin films via solvo-thermal vapor annealing for on-chip etch mask application</b> .....	<b>104</b>
3.1. Abstract .....	105
3.2. Introduction .....	105
3.3. Experimental .....	108
3.4. Results and Discussion .....	111
3.4.1. Microphase separation of PS- <i>b</i> -PLA BCP .....	111
3.4.2. Directed Self-Assembly of PS- <i>b</i> -PLA via Topographic Substrates .....	115
3.4.3. Contributing factors to fast self-assembly .....	119
3.4.4. PLA block removal forming PS mask template .....	122
3.5. Conclusions .....	125
3.6. References .....	125
3.7. Appendix – Chapter 3 .....	129

**Chapter 4. Self-Assembly of PS-*b*-P4VP Block Copolymer on Molecularly Functionalized Silicon Substrates: Fabrication of Inorganic Nanostructured Etchmask for Lithographic**

<b>Use</b> .....	<b>136</b>
4.1. Abstract .....	137
4.2. Introduction .....	137
4.3. Experimental .....	140
4.4. Results and Discussion.....	144
4.4.1. Molecular Functionalization with EG .....	144
4.4.2. BCP Self-assembly on Functionalized Surface.....	148
4.4.3. BCP Film Reconstruction with Ethanol .....	155
4.4.4. Iron Oxide(s) Hard Mask Fabrication by Inclusion Technique .....	156
4.4.5. GISAXS of BCP Films at Different Stages .....	160
4.4.6. Fabrication of Silicon Nanopillars .....	162
4.5. Conclusions .....	164
4.6. References .....	164
4.7. Appendix – Chapter 4 .....	168

**Chapter 5. Aligned Silicon Nanofins via the Directed Self-Assembly of PS-*b*-P4VP Block Copolymer and Metal Oxide Enhanced Pattern Transfer.....**

<b>170</b>	<b>171</b>
5.1. Abstract .....	171
5.2. Introduction .....	171
5.3. Experimental .....	174
5.4. Results and Discussion.....	178
5.5. Conclusions .....	193
5.6. References .....	194
5.7. Appendix – Chapter 5 .....	198

**Chapter 6. Solvent vapor annealing of block copolymers in confined topographies: commensurability considerations for nanolithography .....**

<b>220</b>	<b>221</b>
6.1. Abstract .....	221
6.2. Introduction .....	221
6.3. Experimental .....	222
6.4. Results and Discussion.....	226
6.5. Conclusions .....	233
6.6. References .....	233
6.7. Appendix – Chapter 6 .....	236

**Chapter 7. Parallel Arrays of Sub-10 nm Aligned Germanium Nanofins from an “In-situ” Metal Oxide Hardmask using Directed Self-Assembly of Block Copolymers .....**

<b>238</b>	<b>239</b>
7.1. Abstract .....	239
7.2. Introduction .....	240
7.3. Experimental .....	242
7.4. Results and Discussion.....	245
7.5. Conclusions .....	252
7.6. References .....	253

7.7. Appendix – Chapter 7 .....	256
<b>Chapter 8. Conclusions and Future Work .....</b>	<b>261</b>
8.1. Conclusions and Future Work.....	262
8.2. References .....	266

**Common abbreviations and acronyms:**

**AFM:** Atomic Force Microscope

**BCP:** Block Copolymer

**DSA:** Directed Self-Assembly

**EBL:** Electron Beam Lithography

*f*: Block volume fraction

**FTIR:** Fourier Transform Infrared Spectroscopy

**GeOI:** Germanium-on-insulator

**GISAXS:** Grazing Incidence Small Angle X-ray Scattering

**HMDS:** Hexamethyldisilazane

**N:** Degree of polymerization

$\chi$ : Flory-Huggins Interaction Parameter (Chi)

**PDMS:** Poly(dimethylsiloxane)

**PS:** Poly(styrene)

**P4VP:** Poly-4-vinylpyridine

**PEO:** Poly(ethylene oxide)

**PFS:** Poly(ferrocenylsilane)

**PLA:** Poly(lactic) acid

**PMMA:** Poly(methyl methacrylate)

**SEM:** Scanning Electron Microscopy

**Si:** Silicon

**SIS:** Sequential Infiltration Synthesis

**TEM:** Transmission Electron Microscopy

---

*Chapter 1*

---

**Introduction**

## 1.1. Abstract

Block copolymer (BCP) nanolithography and directed self-assembly (DSA) of BCPs has emerged as a realizable complementary tool to aid optical patterning of device elements for future integrated circuit advancements. In this chapter, methods to chemically enhance BCP etch contrast for DSA application and further potential applications of inorganic nanoscale features (*e.g.* semiconductors, dielectrics, metals and metal oxides) are examined. Strategies to modify, infiltrate and controllably deposit inorganic material utilizing neat self-assembled BCP thin films open a rich design space to fabricate functional features in the nanoscale regime. The literature review in this chapter provides the reader with an understanding and overview on innovative ways for the selective inclusion/infiltration or deposition of inorganic moieties in microphase separated BCP nanopatterns. Early initial inclusion methods in the field and exciting contemporary reports to further augment etch contrast in BCPs for pattern transfer application are described. Specifically, the use of evaporation and sputtering methods, atomic layer deposition, sequential infiltration synthesis, metal-salt inclusion and aqueous metal reduction methodologies forming isolated nanofeatures will be highlighted in di-BCP systems. Functionalities and newly reported uses for electronic and non-electronic technologies based on the inherent properties of incorporated inorganic nanostructures using di-BCP templates are highlighted. We also outline the potential for extension of incorporation methods to triblock polymer features for more diverse applications.

## 1.2. Block copolymers

Self-assembly (SA) is a reversible process whereby pre-existing disordered components form a highly ordered arrangement or pattern under the right conditions. It should be

noted that there are two main types of SA; dynamic and static. Static SA involves systems that do not dissipate energy and are at local equilibrium. In contrast, dynamic SA (also referred to as self-organisation) may require energy for an ordered structure to form. This reversible spontaneous process of SA is summarised from the Gibbs Free Energy equation below;<sup>1</sup>

$$\Delta G_{SA} = \Delta H_{SA} - T\Delta S_{SA} \quad \text{Equation 1}$$

$\Delta G_{SA}$  when negative self-assembly is a spontaneous process

$\Delta H_{SA}$  enthalpy change due to interaction between segments of BCP

$T\Delta S_{SA}$  entropy change in process

From equation 1 we can conclude that for a given system above a certain temperature for SA to occur, the enthalpy term must be negative and in excess of the entropy term. Thus for SA to successfully occur, enthalpic forces must dominate.

A large number of reviews are available on BCP synthesis,<sup>2-4</sup> thin film behavior and morphologies for nanopatterning,<sup>5-14</sup> and the fundamental influencing parameters concerning BCPs are detailed here. The simplest form of a BCP is one that contains two polymer blocks covalently connected at their ends *i.e.* a diblock copolymer (di-BCP) as shown in Figure 1.1.<sup>15</sup>

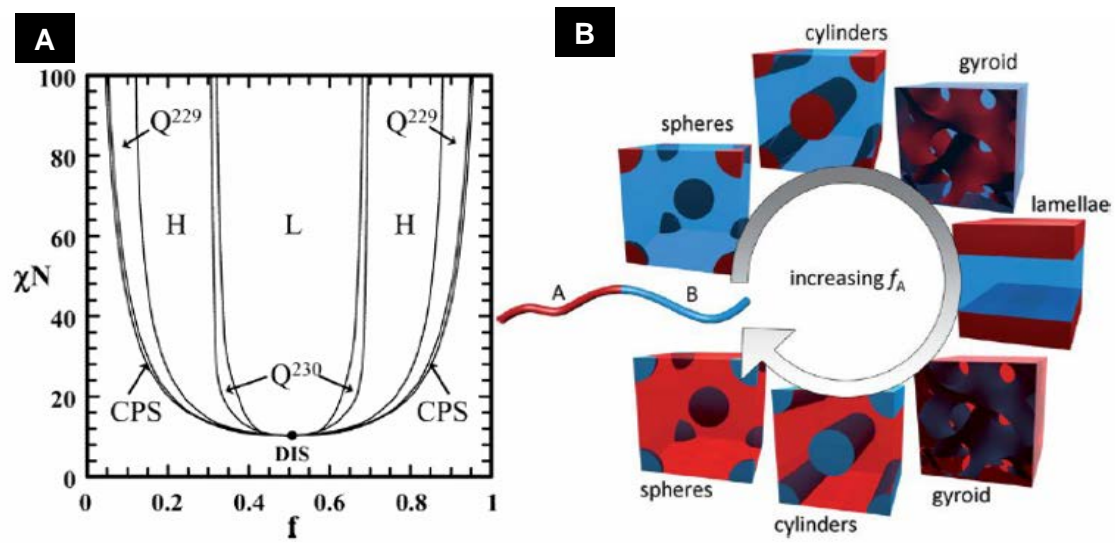


**Figure 1.1.** A. Phase diagram of a diblock copolymer with volume fraction vs  $\chi.N$  as predicted by self-consistent field theory. B. Resulting morphologies on increasing block volume fraction ( $f_A$ ). See text for details. Images reproduced from reference 15.

**Table 1.** Corresponding block percentages and space groups for resulting morphologies of “classical” block copolymers.<sup>16</sup>

Morphology	Space Group	Percentage of block A
<b>Spheres</b>	Im3m	0-21%
<b>Cylinders</b>	p6mm	21-33%
<b>Double Gyroid</b>	Ia3d	33-37%
<b>Double Diamond</b>	pn3m	33-37%
<b>Lamallae</b>	Pm	37%-50%

The block volume fractions ( $f_A$  and  $f_B$ , where  $f_A + f_B = 1$ ) and the polymer-polymer interaction parameter (referred to as the chi factor, Flory-Huggins  $\chi_{AB}$  parameter or simply  $\chi$ ) contribute to resulting morphology and the self-assembly dynamics of di-BCP materials.<sup>17</sup> The  $\chi$  value quantifies the degree of dissimilarity of constituent chains. Di-BCPs have properties that can be utilized for diverse functions which are not accessible from their homopolymer segments. Upon “nanophase separation”, more commonly referred to as microphase separation, di-BCPs can form well-defined nanoscale spherical, cylindrical, gyrodial or lamellar features (see Table 1 and Figure

1.1.A) with increasing  $f$  as shown in Figure 1.1.B. The thermodynamic incompatibility (unfavourable interactions) of the constituent polymer segments is the driving force for microphase separation. Di-BCPs (A-B) form geometries that can be tuned or where one can “dial-in” specific nanoscale dimensions (3-100 nm) via control of the total degree of polymerization ( $N = N_a + N_b$ ) *i.e.* the molecular weight of a BCP.<sup>14</sup>

These factors are represented by equation 2 which describes the free energy of the system:<sup>18</sup>

$$\frac{\Delta G_{\text{mix}}}{k_b T} = \frac{1}{N_A} \ln (f_A) + \frac{1}{N_B} \ln (f_B) + f_A f_B \chi \quad \text{Equation 2}$$

$\Delta G_{\text{mix}}$  = Gibbs free energy

$K_b$  = Boltzmann's constant

$T$  = Temperature

$N_A$  = Polymerisation of segment A

$N_B$  = Polymerisation of segment B

$f_A$  = Volume fraction of block A

$f_B$  = Volume fraction of block B

$\chi$  = Flory-Huggins Interaction Parameter

From equation 2, terms 1 and 2 can be manipulated by the polymerisation of the BCP and relative volume fractions. In contrast term 3,  $\chi$ , is a result of the molecules involved ( $f_A$  and  $f_B$ ) and is directly related to temperature.

The phase diagram displayed in Figure 1.1.A shows the relationship of  $\chi \cdot N$  versus  $f$ . If  $\chi$  and/or  $N$  value are reduced so that  $\chi \cdot N$  is below a critical value, entropic factors will produce a disordered phase. It should be noted that the product of  $\chi$  and  $N$ ,  $\chi \cdot N$ , plays a pivotal role in microphase separation occurring and theoretically a  $\chi \cdot N$  value above  $\sim 10.5$  is needed for ordered morphologies to occur.  $\chi$  is determined by the di-BCP selected while the volume fraction and polymerisation which influence the translational and configurational entropy are determined by the polymerisation stoichiometry. As determined from equation 2,  $\chi$  is a temperature dependent parameter. For an ordered structure at equilibrium, polymer chains of the DBCP will be arranged in minimum free energy configurations.

### 1.3. Motivation and scope

The empirical law known as “Moore’s Law” drives the nanoelectronic industry to continually achieve ever smaller technology nodes for increased electronic device performance.<sup>19</sup> Due to physical limits and prohibitive costs encountered with optical lithography patterning, alternative methodologies are being investigated and scrutinized. Additionally, major semiconductor companies also face challenges to evolve and diversify devices (More than Moore, MtM), together with advanced connectivity (Internet of Things, IOT). It has been reported extensively in recent years the enormous promise that block copolymer (BCP) self-assembly may be promising enough to afford the nanoelectronic industry an alternative patterning technology.<sup>20-24</sup> Highly ordered BCP etch mask arrays with near perfect registration could possibly augment next-generation lithographic processes so as to move industrial scale patterning into the deep nanoscale regime (sub-10 nm) while reducing costs and maintaining throughput for high volume manufacturing (HVM) needs.

Research on BCP materials, enhanced polymer block etch contrast, reducing line edge/width roughness, minimizing defect levels, high-aspect ratio pattern transfer and overall integration for electronic device patterning is being relentlessly developed in pursuit of Moore's Law,<sup>25</sup> a trend followed for continued silicon feature miniaturization over the past 50 years. Top-down optical patterning of substrates to fabricate trenches (graphoepitaxy, hard<sup>26</sup> or soft<sup>27</sup>) and chemically modify polymer interactions at random copolymer brush coated substrate surfaces (chemoepitaxy<sup>28</sup>) to "direct" self-assembly are referred to as directed self-assembly (DSA) of BCPs. DSA of BCPs coupling top-down fabrication with BCP self-assembly provides a powerful synergy to fabricate device related geometries with the potential to further the increased demands of microprocessor and hard disk drive companies. The capacity of DSA of BCPs lies in the technology's conceptual similarities and parallel processing schemes to current device patterning where a light sensitive polymeric based layer (photoresist) is spun on a substrate and is patterned with ultraviolet light to attain device relevant features (*e.g.* line, holes). These patterned resist features are subsequently "pattern transferred" to the underlying material.

There are still outstanding issues with BCP nanolithography patterning for HVM and very large scale integration (VLSI). One major concern is the poor etch contrast between polymer blocks to enable high fidelity device structures following pattern transfer.<sup>29</sup> In this regard, infiltrating self-assembled BCP nanopatterns with inorganic moieties to chemically enhance the pattern is extremely useful. Since most BCP systems are made up primarily of lighter elements (*e.g.* C, H, O, N) and thus have poor etch contrast, incorporating heavier metal containing species has great potential for etch

enhancement. As-synthesized metal containing BCPs have been highlighted recently to circumvent this issue and two reviews are available.<sup>30,31</sup> Therefore, this literature review aims to provide an overview of versatile ex-situ infiltration techniques on as-formed BCP patterns. Ideally, BCP materials should allow a facile highly selective pattern transfer resulting in high aspect ratio features (*i.e.* the ratio of lateral to vertical dimensions) as shown in Figure 1.2.

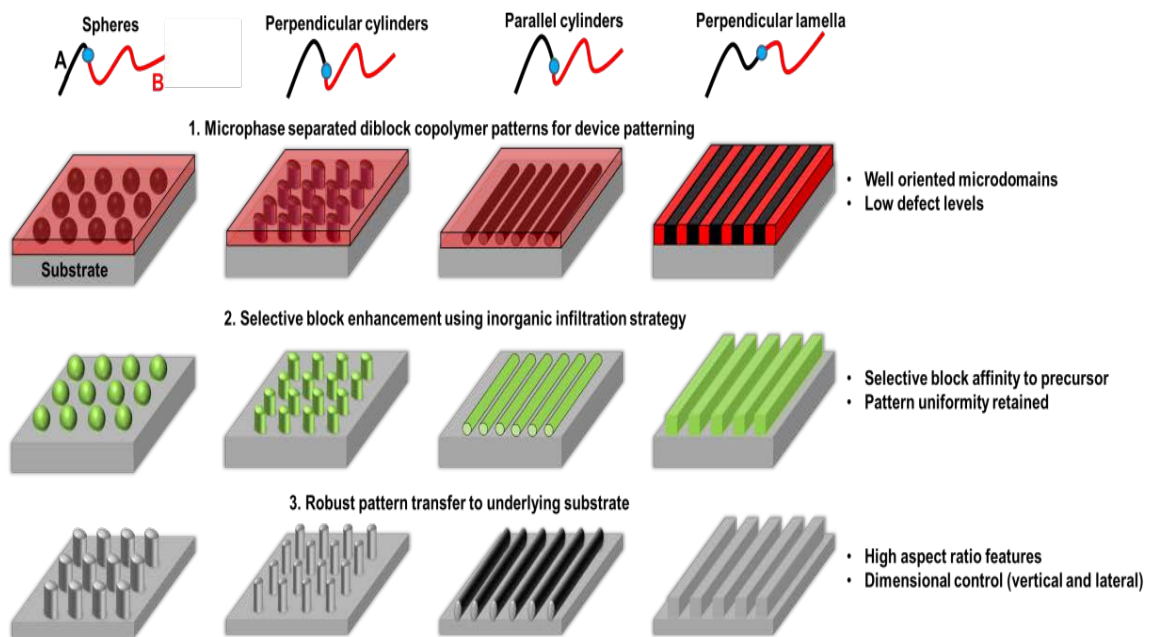


**Figure 1.2.** Schematic representing paths to well-defined high aspect ratio features using di-BCP systems and infiltration techniques. 1. Successful self-assembly of di-BCP system forming ordered arrays. 2. Selective incorporation of one block with inorganic material to enhance etch contrast. Inorganic features at substrate surfaces can also be utilized for other functions (see text for details). 3. Pattern transfer using inorganic etch mask.

The potential of infiltration of “neat” BCPs was outlined in 2006 by Krishnimoorthy *et al.*<sup>7</sup>, “In addition to *in-situ* synthesis of nanoparticles, block-copolymer-derived templates can be used to assemble “preformed” nanoparticles into a variety of ordered arrangements”. This statement referred to only a handful of early demonstrations as we will discuss below. However, at present a diverse range of techniques have established

superb control for directing nanoparticles and inorganic material using neat BCPs. There are a number of reasons that such post BCP self-assembly modifications are advantageous for on-chip etch masks. Firstly, achieving well-defined inorganic nanostructures post self-assembly avoids complexities that can alter kinetic and thermodynamic paths when bonding materials (*e.g.* metal salts, small molecules) with BCPs in solution.<sup>32</sup> Furthermore, the range of BCP materials in solution that can be selectively altered is quite narrow (restricted to electron donating sites in BCP blocks like poly-2-vinylpyridine (P2VP) and poly-4-vinylpyridine (P4VP), or weakly coordinated with polyethylene oxide (PEO) blocks). Consequently, it is difficult to produce well-oriented and ordered microphase separated BCP patterns of technological use with high registration and global coverage. Lastly, morphological changes are also a concerning factor when adding materials in solution that may result in atypical BCP structures following thin film preparation. In this respect, the surface energetics at the polymer/substrate and free interface (polymer/air) must be given special attention for BCP thin films to self-assemble with desired orientation and order with appropriate treatment techniques. Two popular annealing methods for inducing self-assembly and enhancing the long range order of BCPs are solvent vapor annealing<sup>33</sup> and thermal annealing.<sup>8,34</sup> These two annealing methods would presumably behave differently in comparison to accepted annealing protocols for forming thermodynamically stable structures when materials are bonded in solution due to changes including but are not limited to BCP volume fraction, glass-transition temperature, crystallinity, polymer chain mobility, block surface energies and free air/polymer and polymer/substrate interface interactions.

Strategies for enhancing and infiltrating a particular polymer block component have been demonstrated across a range of BCP systems. Beyond on-chip etch mask applications for nanolithography, the alterations to BCP systems enable the formation of hybrid nanoscale materials with novel functionalities and salient work is described in sections below. Through selective infiltration of “foreign” species within BCP microdomains, resulting nanostructures can potentially address a range of electronic, environmental and energy applications in low-cost scalable processes. Although this chapter focuses on di-BCP structures, other linear BCP structures such as triblock polymers (ABA, ABC) and multiblock copolymers [(AB)<sub>n</sub>] can access a myriad of zero, one, two, and three dimensional architectures increasing design space for future materials and could possibly be infiltrated in the same manner as di-BCP copolymers. In a recent article, Ross *et al.*<sup>35</sup> have emphasized the potential of utilizing 3D patterns for batteries, membranes or photovoltaic application as placement of features and defect levels are not as stringent as for integrated circuit application. With this in mind, the ability to replicate 3D BCP patterns using inorganic strategies described in this chapter may allow low-cost high density fabrication practices for nanomanufacturing. We examine some of the most recent methodologies over the past decade as follows; section 1.4: evaporation and sputtering of metals on BCP templates; section 1.5: atomic layer deposition (ALD) and BCP templates; 1.6: sequential infiltration synthesis (SIS) of BCPs; 1.7: spin coating methodologies for metal nanoparticle alignment and metal oxide inclusion with “activated” block copolymer templates, and 1.8: aqueous metal reduction (AMR) and block copolymer nanopatterns. Each section describes reports on as-formed (*i.e.* “neat”) BCP patterns on their etch mask use and functional use. In reviewing the different methodologies for fabricating inorganic material, we also highlight the specific BCP system attributes within sections that allow facile infiltration

due to their inherent chemical properties to form porous templates or their reactivity for chemical reactions with precursor material.

#### 1.4. Evaporation and sputtering of metals on block copolymer templates

Over a decade ago, Park *et al.* demonstrated a high level of control to fabricate hexagonally packed metal dot arrays with an areal density of  $10^{11}$  cm<sup>-2</sup>.<sup>36</sup> A cylinder forming poly(styrene)-*block*-poly(isoprene) (PS-*b*-PI) BCP was employed to form large scale coverage of nanodot patterns to behave as an etch mask. A trilayer pattern-transfer scheme was utilized (top layer of BCP, middle layer of silicon nitride and bottom layer of polyimide) as shown in Figure 1.3. The authors described that the trilayer pattern transfer route was adopted in order to increase aspect ratio of pattern transferred features as previous work displayed an aspect ratio of  $\sim 1$ .<sup>37</sup> Their previous work in 1997 reported the first demonstration of pattern transfer with a BCP, using a sphere forming PS-*b*-poly(butadiene) (PS-*b*-PB) BCP. Two years prior to this experimental pattern transfer evidence, the original concept for adopting BCP films as etch masks for patterning small features was formulated by Mansky *et al.*<sup>38,39</sup> These initial works outlined the requirement for careful attention to BCP selection and chemistry for on-chip etch-mask application. In Park's work, the minor PI block of PS-*b*-PI BCP was removed via ozonolysis and washing of fragments as the carbon-carbon double bond backbone of the PI block is susceptible to fragmentation (similar to the PB block in PS-*b*-PB<sup>37,39</sup>) enabling a porous PS matrix to be formed (Figure 1.3.C). Subsequent RIE processes developed a porous polyimide pattern (Figure 1.3.E). Consecutive evaporation processes of Ti and Au (5 nm/15 nm) were used to in-fill the porous polyimide area (Figure 1.3.F). Following lift-off of the polyimide material, well-ordered Au nanodots were fabricated (Figure 1.3.H and I).

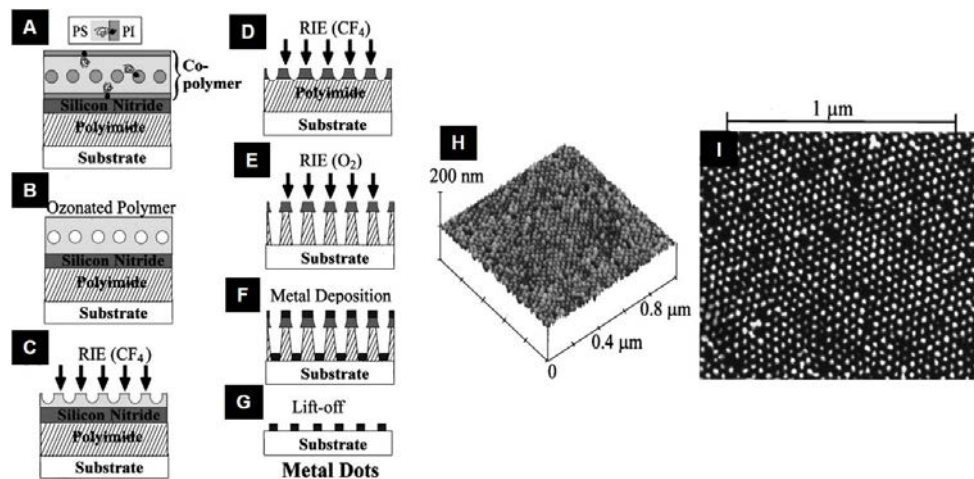


**Figure 1.3.** A-G. Process flow of trilayer pattern transfer strategy using PS-*b*-PI for templating Au nanodots via lift-off. H and I. AFM and SEM images of Au nanodots with an areal density of  $10^{11} \text{ cm}^{-2}$ . Scheme and images reproduced from reference 36.

The above mentioned successes showed the capabilities of BCPs to form both well-defined on-chip etch masks for nanopatterning but more importantly demonstrated a relatively simple process route to allow placement and registration of a metal in the sub-20 nm diameter regime. Following Park's work, further studies using evaporation of metallic material on neat or as-formed BCP films largely concerned PS-*b*-poly(methyl methacrylate) (PS-*b*-PMMA). One such report<sup>40</sup> used a porous PS-*b*-PMMA template where PMMA was selectively removed through UV exposure (and acetic washing) as PMMA is susceptible to scission. Interestingly, with the PS etch mask in place on silicon, dry etch procedures were carried out to roughen the surface of the underlying silicon electrode of a metal oxide semiconductor capacitor thus increasing the device surface area.<sup>41</sup> Additionally, porous PS templates were employed to demonstrate highly ordered Au, Co and Ti nanodot arrays after e-beam evaporation and removal of the PS material.

The earliest works on modification and infiltrating PS-*b*-PMMA BCPs as described<sup>40,41</sup> centred on thermal or e-beam evaporation of metals combined with lift-off procedures. Another example presented by Russell and coworkers<sup>42</sup> using PS-*b*-PMMA templates and Cr evaporation in 2002 demonstrated a similar level of areal density ( $10^{11}$  cm<sup>-2</sup>) to Park's<sup>36</sup> work. PMMA was initially removed via the UV exposure/acetic acid washing protocol generating a porous matrix. Metal evaporation allowed Cr nanodots to be formed after PS matrix removal. Interestingly, the authors also reported on the fabrication of a Cr matrix via an inverse PS-*b*-PMMA system (*i.e.*  $f_{\text{PMMA}} = 0.7$ , PMMA matrix surrounded by PS dots). After selectively removing the PMMA matrix, Cr evaporation (15 nm) enabled a porous Cr matrix to be generated following excess PS and Cr elimination. The work extended the use of BCP templates to act as both negative and positive templates. Succeeding publications on PMMA based etching and lift-off methods have demonstrated graphoepitaxially aligned magnetic Co nanodots using a dry lift-off procedure,<sup>43</sup> fabrication of high-aspect ratio (1:10) Si nanopillars using sputtered Cr,<sup>44</sup> high temperature resistant Au nanoparticles,<sup>45</sup> ultra-small ferromagnetic (Co) nanorings,<sup>46</sup> Ag nanowires (also fabricated via electrochemical etching),<sup>47</sup> selective masked deposition of Fe catalyst particles for carbon nanotube growth,<sup>48</sup> Au and Al nanowire arrays guided by soft graphoepitaxy,<sup>49,50</sup> Al<sub>2</sub>O<sub>3</sub> dot nanopatterning on Cu substrates,<sup>51</sup> silicon nanocrystals,<sup>52</sup> and Ge nanowire fabrication.<sup>53</sup> Another report in 2007 attempted to selectively decorate evaporated Ag on electron-beam lithographically exposed PS-*b*-PMMA BCPs. The authors observed less Ag decoration in electron-beam exposed areas and commented how the methodology could potentially be utilized to tailor a BCP system domain selectivity where an inherent attraction is not present.<sup>54</sup> In 2014, Kreuzer *et al.*<sup>55</sup> outlined an unusual phenomenon whereby either mesoporous Ti films were formed on a low

molecular weight unmodified PS-*b*-PEO template (period of dots ~ 40 nm) or hexagonally arranged Ti dots were formed on a larger molecular weight template (period of dots ~ 100 nm) after electron-beam evaporation of a nominal 10 nm of Ti. The report showed that by choosing a particular template different meso or nano structures could be formed. The work also emphasized that surface chemistry is not the sole dominating factor for selective evaporation and the dimensions of features of a template must also be accounted for.

One work highlighting the elegance and versatility of BCP materials using PS-*b*-poly4-vinyl-pyridine (PS-*b*-P4VP) demonstrated pattern transfer of pores, pillars and rings into silicon oxide via gold evaporated etch masks on a PS-*b*-P4VP template as shown in Figure 1.4.<sup>56</sup> PS-*b*-P<sub>x</sub>VPs ( $x = 2$  or  $4$ ) have received much study owing to the reactive PVP groups for metal or small molecule bonding and their inherently high  $\chi$  (PS-*b*-P2VP,  $\chi \sim 0.18$ ).

The authors took advantage of selective solvent swelling of P4VP to create a “surface reconstructed” or porous film. Glancing angle gold evaporation along with thermal annealing enabled the formation of different Au patterns, *i.e.* depending on thermal annealing temperature and time, Au nanoparticles or rings could be attained due to differing P4VP-Au interactions as shown in Figure 1.4.A-C. The patterns were subsequently used as etch masks to etch into SiO<sub>2</sub> underlayer (Figure 1.4.D-F).

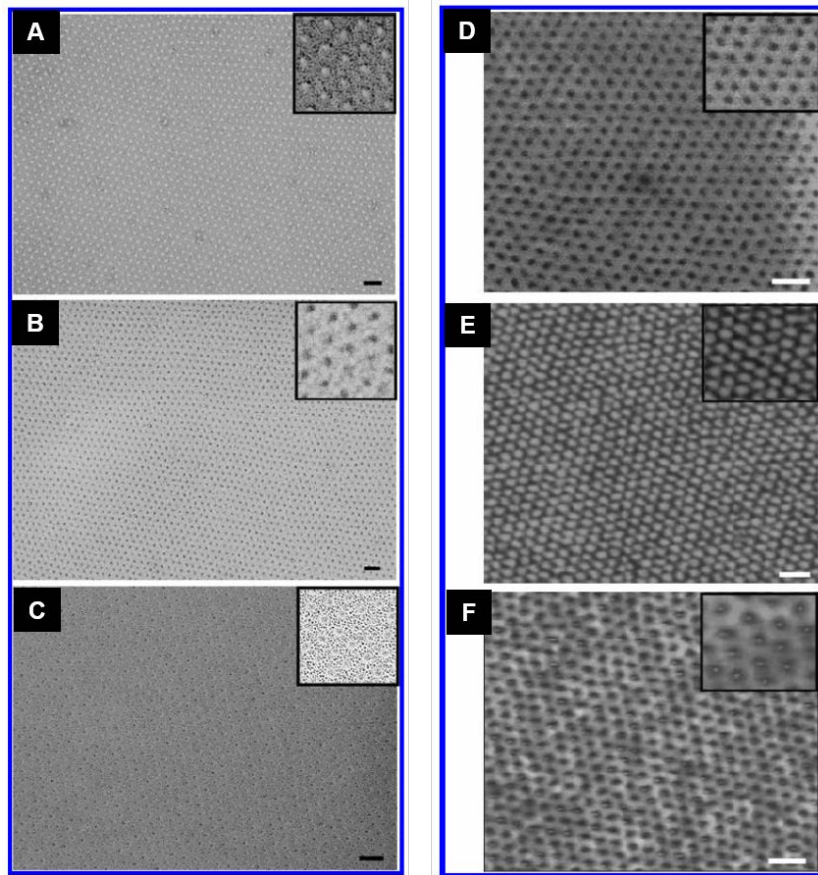


**Figure 1.4.** TEM images of Au decoration via glancing angle evaporation ( $\sim 5^\circ$ ) on surface reconstructed PS-*b*-P4VP films showing Au (A) outside the P4VP pore after evaporation, (B) inside the P4VP pore using  $<0.5$  nm Au layer through thermal annealing at  $115^\circ\text{C}$  for 10 minutes, and (C) having a ring pattern using a Au layer  $>0.5$  nm thermally annealed  $180^\circ\text{C}$  for 30 minutes. (D-F) SEM images following reactive ion etching of etch masks (A-C) into underlying silicon oxide generating (D) pores, (E) pillars, and (F) ring patterns. All scale bars = 100 nm. Images reproduced from reference 56.

The first demonstration of a metal nanodot memory array using a BCP lift-off technique was reported by Hong *et al.*<sup>57</sup> in 2010. Porous PS-*b*-PMMA nanodot patterns were utilized for Cr nanodot fabrication via evaporation and lift-off of the PS template. Subsequent ALD coating of a control oxide ( $\text{Al}_2\text{O}_3$ ) on the Cr nanodots and an evaporated metal gate (Ti/Al layers) were carried out to fabricate the memory device (see Figure 1.5.H-I). The authors reported an “*ultrawide memory window*” (15 V) for their device. Importantly, it was concluded that the density of the device features could certainly be extended beyond the 40 nm period of Cr dots used by the range of “*other*

*copolymer systems with stronger segregation forces*". This is certainly true from today's BCP processes where nanodot templates with periods of 18 nm,<sup>58</sup> 17 nm,<sup>59,60</sup> 12 nm,<sup>61,62</sup> and 10 nm<sup>63</sup> have been fabricated with high  $\chi$  BCP materials.

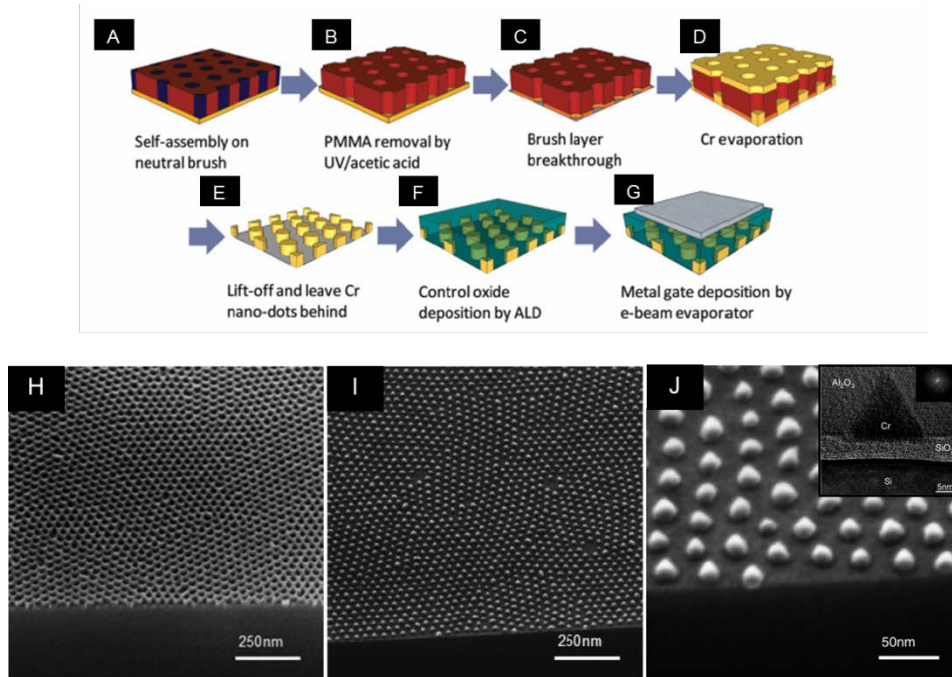


**Figure 1.5.** (A-G) Process flow for metal nanodot memory device. (H) Side-view SEM image of Porous PS matrix following selective PMMA removal. Top-down (I) and side-view (J) SEM images of evaporated Cr nanoarrays using host PS matrix. Inset in (J) shows TEM image of gate oxide on Cr dot. Scheme and images reproduced from reference 57.

An interesting demonstration by Kim *et al.*<sup>64</sup> in 2015 described the use of BCP nanopatterning for triboelectric generator application. Triboelectric nanogenerators have gained interest for energy harvesting and BCP patterning has been proposed due to the associated low device fabrication costs. In Kim's work, PS-*b*-PMMA was spin coated on a Au coated Kapton film producing an arrangement of vertically oriented PMMA cylinders (see Figure 1.6.A) in the PS matrix. Successful thermal evaporation of Au into the porous PS template (via UV/acetic acid protocol) and subsequent lift-off of the PS matrix produced high density Au nanodots. After device fabrication using the

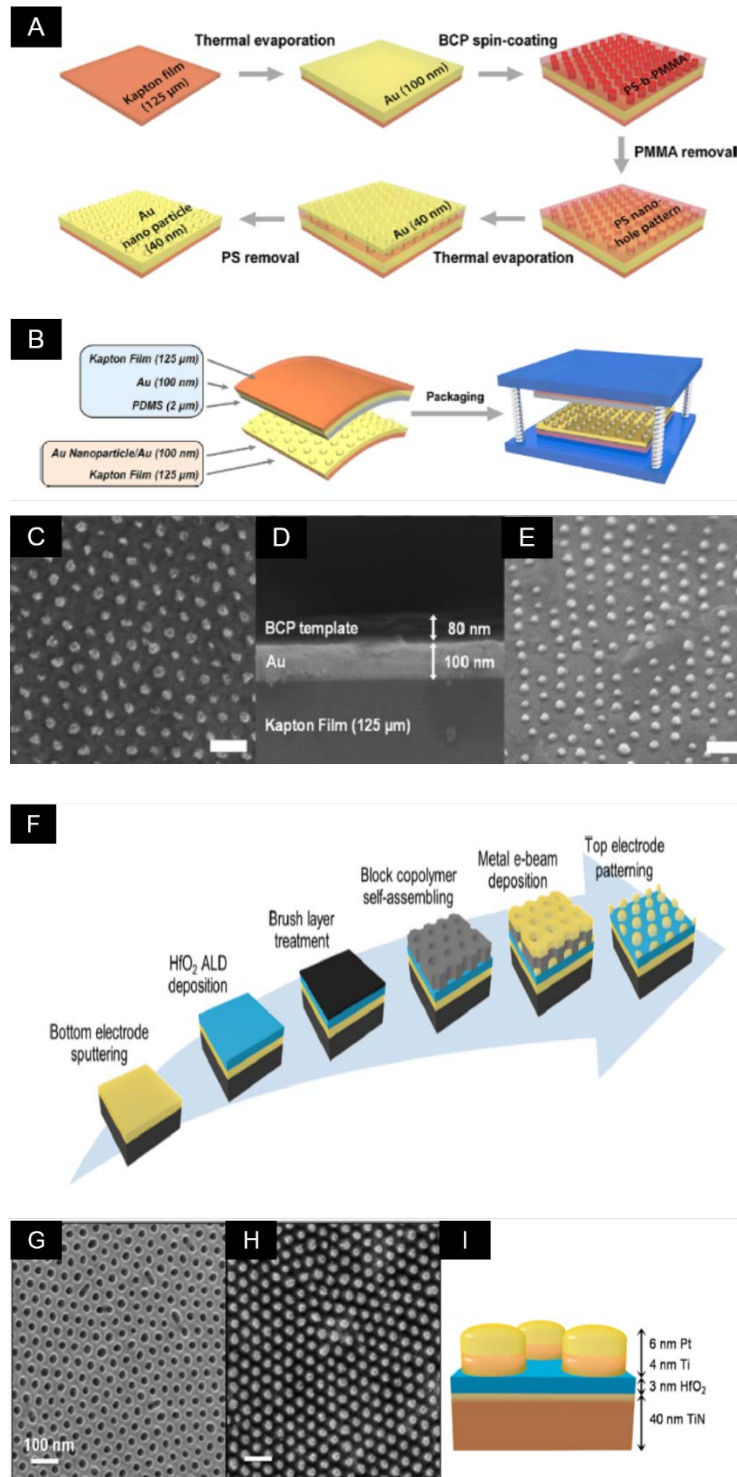


**Figure 1.6.** (A) and (B) show process flow for triboelectric nanogenerators. (C) Top-down SEM and side-view SEM (D,E) of Au nanodots following evaporation for triboelectric device. (A-E) reproduced from reference 64. (F) Process flow for development of bilayer Pt/Ti nanodots on HfO<sub>2</sub>/TiN surface for resistive switching memory application. Top-down SEM image of (G) porous host PS template and (H) Pt/Ti nanodots as shown in (I). (F-I) reproduced from reference 65. All scale bars = 100 nm.

Au nanodots from BCP patterning, current output of the triboelectric nanogenerator increased at least 16 times.

Others have also lately reported device fabrication for memory application using PS-*b*-PMMA templates. Frascaroli *et al.*<sup>65</sup> developed resistive switching in a high-density device using bilayer Pt/Ti nanodots at a density of  $5 \times 10^{10}$  devices  $\text{cm}^{-2}$ . The work highlights the ability of BCPs to address HVM needs where scalability and high device density are necessary, which can be difficult to access with expensive top-down patterning methods alone. Note that the bilayer of Pt/Ti nanodots were patterned on a  $\text{HfO}_2/\text{TiN}$  surface (see Figure 1.6. F-I) and electrically characterized using a conductive atomic force microscope.

Many studies have been published combining BCP dot templates and evaporated metal with a focus on magnetic studies. One-dimensional metal nanowires are also of interest for a plethora of diverse functions including optoelectronic, photonic and solar-cell devices. The above outlined approaches using evaporation and BCP templating generally involve a lift-off procedure. In contrast, excellent work has been shown by Ross and co-workers using PS-*b*-poly(dimethyl siloxane) (PS-*b*-PDMS) templates and radio frequency sputtering of a variety of metals coupled with plasma etching.<sup>66-68</sup> PS-*b*-PDMS is a BCP of major focus in the BCP nanopatterning community due to its high  $\chi$  ( $\chi \sim 0.26$ ) and the PDMS silicon containing backbone producing etch contrast

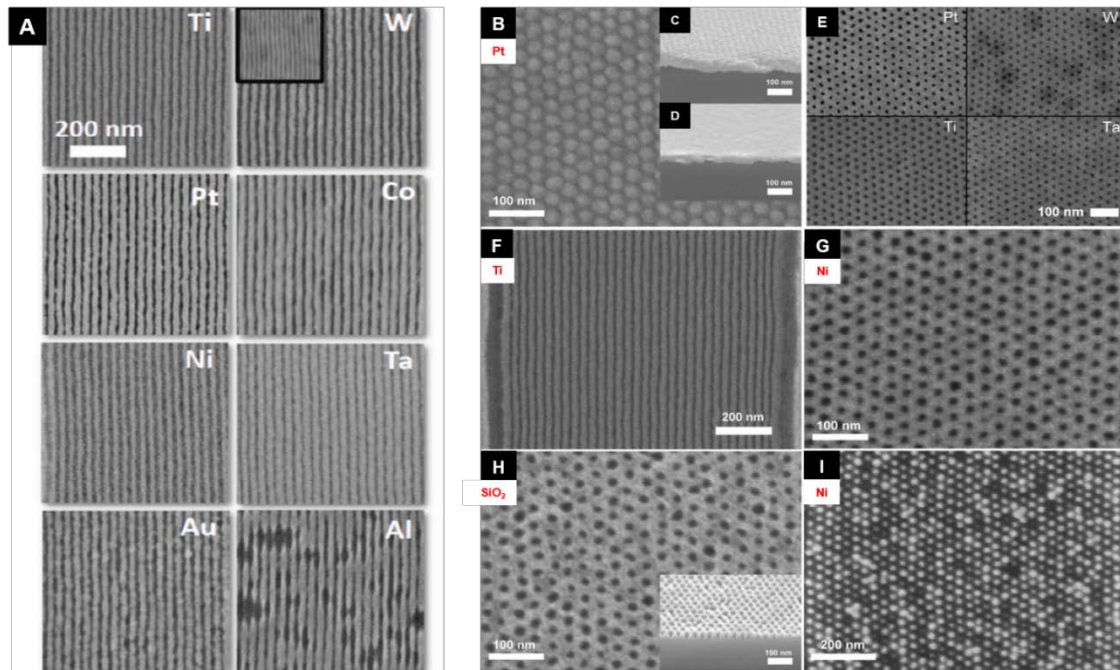


**Figure 1.7.** (A) Top-down SEM images of diverse metallic lines fabricated from robust process using PS-*b*-PMDS templates and metal radio frequency sputtering. (B) Pt deposited on PDMS spheres. Images reproduced from reference 66. (E) Metallic porous films after selective PDMS removal, (F) Ti lines, (G) a nanoporous Ni metallic film, (H) porous SiO<sub>2</sub> following etching using nanoporous metallic film, and (I) Ni nanodots. Images reproduced from reference 68.

when oxidized. After developing well-oriented oxidized PDMS line-space features following selective etching, radio frequency sputtering of Ti, W, Pt, Co, Ni, Ta, Au and Al along with selective dry etching of the sputtered metal led to resulting metal wires with sub-10 nm feature size.<sup>66</sup>

Figure 1.7.A displays SEM data of the respective metals fabricated using this “Damascene-like” process with periods of 17 nm. Importantly, the fabrication process was shown to be robust as studies revealed that the Ni nanowires retained their magnetic properties. A follow up work detailed a similarly impressive level of control in generating nanopore arrays via a sphere forming PS-*b*-PDMS template and radio frequency sputtering for magnetic study (Figure 1.7.B-I).<sup>68</sup>

More recently, Baruth *et al.* also described a “Damascene-like” process by overfilling a porous PS template generated from a cylinder forming PS-*b*-PLA BCP (see Figure 1.8.A and B for process flow and porous PS matrix).<sup>69</sup> After overfilling Ni<sub>80</sub>Fe<sub>20</sub> (permalloy) through molecular beam deposition, planarization using ion beam milling to the PS matrix followed by dry etching enabled the formation of Ni<sub>80</sub>Fe<sub>20</sub> nanodots as shown in Figure 1.8.C. The authors also described a climate controlled process enhancing the ordering PS-*b*-PLA features during self-assembly. A considerable difference in the long range order of the BCP was observed between the two studied annealing environments and thus the resulting evaporated patterned Ni<sub>80</sub>Fe<sub>20</sub> material. Of late, further work on the PS-*b*-PLA system has led to even greater control in the degree of order and thus the resultant incorporated metal material.<sup>58</sup>

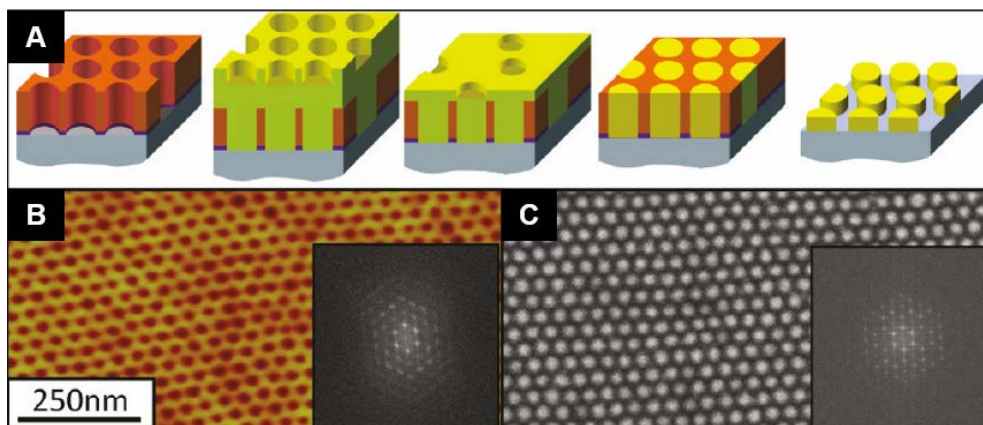


**Figure 1.8.** (A) “Damascene-like” process for the generation of permalloy nanodots using PS-*b*-PLA BCP. (B) Porous PS matrix after PLA etching. (C) SEM image of highly ordered permalloy nanodots fabricated using molecular beam deposition followed Ar ion beam milling. Reproduced from reference 69.

The opening part of Section 1.4. provided an overview of early research of metal incorporation via evaporation (thermal, e-beam) and sputtering using BCP templates as hosts that has catalysed more incorporation techniques to be investigated and led to further achievements. Latterly the work has progressed to achieve finer definition and registration of metals via graphoepitaxial alignment. These last-mentioned works attaining high-quality ordered patterns can partly be attributed to the use of high  $\chi$  (*e.g*

PS-*b*-PDMS and PS-*b*-PLA) materials. It is recognizable in the subsequent sections discussed below that researchers have now expanded their employed techniques to realize inorganic nanostructures with improved placement accuracy and pattern uniformity.

### 1.5. Atomic layer deposition methods and block copolymer templates

Atomic layer deposition (ALD) is a versatile technique for depositing inorganic material for the controlled formation of uniform layers via vapor phase precursors.<sup>70</sup> The systematic nature of ALD cycles enables atomic level precision through self-limiting surface reactions in the deposition of inorganic functional material. Such approaches allow tuning and interface engineering to precisely modify nanoscale BCP features on a large scale. This introductory chapter focuses on techniques that modify nanolithography relevant self-assembled BCP templates (spheres, cylinders, lamella) as opposed to methods that coat or infiltrate kinetically trapped structures like micelles,<sup>71</sup> nanorods,<sup>72</sup> *etc.* It could be argued that ALD alone is not a true “infiltration” technique however it warrants highlighting due to its possible impact for feature size alteration, density multiplication potential and close relationship with SIS (Section 1.6.).

A variety of ALD-BCP practices have emerged that could continue the scaling of complementary metal-oxide semiconductor (CMOS) devices in the future. An interesting article in 2014 by Moon *et al.*<sup>73</sup> introduced a methodology combining ALD alumina coating and a porous PS template (initial periods of 46 nm and 28 nm) to reduce and define periodicities of 14 nm in line space patterns with feature sizes of ~ 5 nm whilst the approach can also lead to period and feature size shrinkage for hole patterns. Figure 1.9. shows SEM images of reduced features enabled through ALD

spacing layers. The methodology possesses great potential for circumventing the size limitations associated with low  $\chi$  BCPs like PS-*b*-PMMA. The enhancement strategy avoids costly lithographic tools and complex processes (such as litho-etch-litho-etch) for pattern multiplication. A uniform 5 nm thick alumina layer was deposited on the PMMA removed PS-*b*-PMMA features (lamella for line space features and perpendicular cylinders for nanohole arrays). This spacer layer was subsequently removed using controlled ICP etching. Additional PS removal and pattern transfer of the robust alumina features resulted in silicon line arrays and nanotubes as shown in Figure 1.9. A similar ALD-BCP approach albeit with larger periods (36 nm) in an earlier reported work in 2010 by researchers at CEA LETI (Grenoble, France) demonstrated the selective removal of PMMA from PS-*b*-PMMA BCP combined with an ALD deposited alumina material to act as a hardmask.<sup>74,75</sup> Through careful tuning of PS surface chemistry, alumina deposition was predominantly formed in the porous regions between PS features. The alumina patterns were then pattern transferred to the underlying substrate producing high-fidelity silicon nanostructures (see Figure 1.9G and H). In the above works, the benefits offered by inorganic inclusion via ALD are clear for density multiplication and enhanced pattern transfer, and it is worthy to note the importance and understanding of dry plasma etching processes tailored for transferring the ALD generated features.

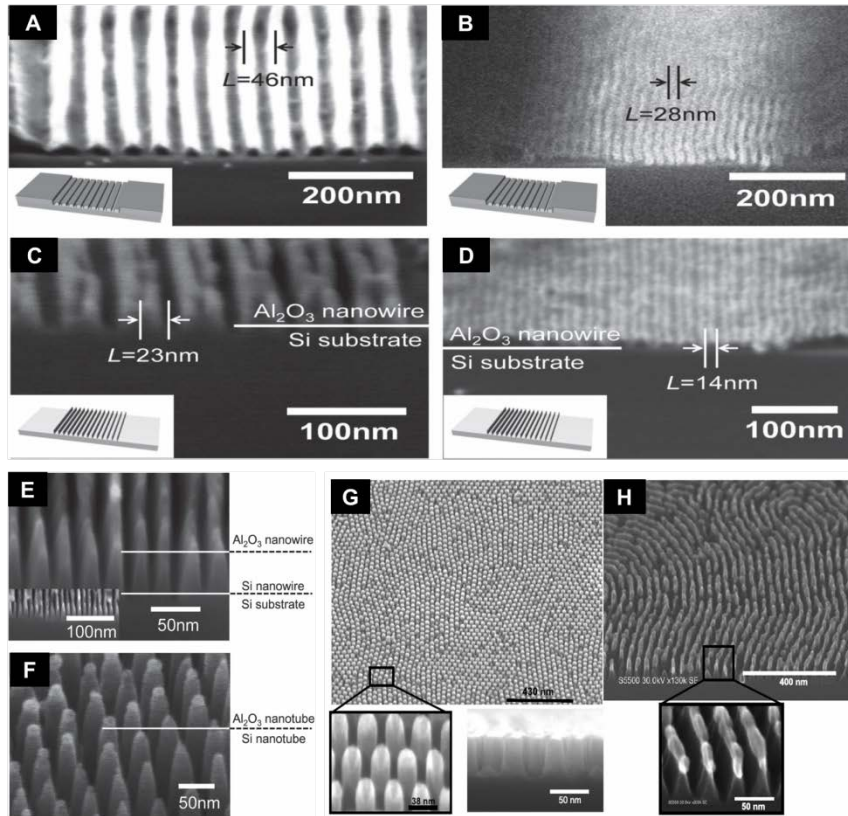


**Figure 1.9.** Side-view SEM images of PS line space templates from PS-*b*-PMMA BCPs with periods of 46 nm (A) and 28 nm (B) respectively. Corresponding alumina nanowire features following ALD spacer deposition, ICP spacer etching and BCP etching producing reduced features at 23 nm (C) and 14 nm (D) periods. (A-D) reproduced from reference 73. (E) Si nanostructure and (F) nanotubes after Si etching. (A-F) reproduced from reference 73. Side view and high resolution SEM images of (G) nanopillars and (H) nanofin features using robust ALD Al<sub>2</sub>O<sub>3</sub> mask patterns for enhanced pattern transfer. (E-H) reproduced from reference 74.

In 2013, a work by Hagglund *et al.*<sup>76</sup> utilized a BCP lift-off approach similar to studies reported in section 1.4 to pattern high density arrays of Au nanodots and SnS<sub>x</sub> or ZnO ALD films were subsequently deposited on the arrays. The ALD deposition was carried out to enhance and analyze the optical effects of the plasmonic arrays. The authors reported a record effective absorption coefficient per volume equivalent thickness which surpassed any previously detailed materials. The work displayed the importance of complementary methods and interdisciplinary study to achieve new fundamental insights at sub-10 nm feature sizes accessible with BCP patterns.

ALD can also be used impressively for inorganic replication of highly oriented thicker BCP templates with great precision. For example, using 500 nm porous PS-*b*-P2VP films Yin *et al.*<sup>77</sup> created titania nanotubes as shown in Figure 1.10.D and E. An important process step for this accomplishment is related to the “reactivity” of the poly-*x*-vinylpyridine ( $x = 2$  or 4) containing BCPs. As mentioned in Section 1.4., when exposed to a selective solvent, PVPs swell and form pores. Depending on conditions, *viz.* time and temperature, the pore size can be tuned and therefore one can alter the diameter of included precursor via pore size tuning as well as precursor loading. Such deep micron thick, well-ordered inorganic features from BCP templates with high porosity may have potential in a number of catalytic, sensor and separation science areas. The approach has been used to deposit metal oxides within membrane features for antireflective application<sup>78</sup> and nanorods for enhanced humidity-sensing<sup>79</sup> designed from PS-*b*-P2VP BCPs. Synthetic methods have advanced endlessly to add functionality to BCPs<sup>14</sup> and BCPs containing an easily removable block to form nanoporous templates for deposition are advantageous. A recent study published illustrates this synergy of BCP functionality and ALD patterning. Initially, a Si containing BCP, PS-*b*-poly(4-(*tert*-butyldimethylsilyl)oxystyrene) (PS-*b*-PSSi)<sup>80</sup> was synthesized and solvent vapor annealing produced PS nanodot arrays surrounded by a majority PSSi matrix (see Figure 1.10F - J). The natural etch contrast of the PSSi allowed selective PS etching to create a nanoporous PSSi template with ~ 200 nm thickness on an organic resist material (SU-8).<sup>81</sup>

Following pattern transfer of the nanopore arrays to the thick underlying cross-linked SU-8 layer, sequential ALD processing and calcination led to highly ordered crystalline anatase titania. Nanolaminate ( $\text{TiO}_2/\text{Al}_2\text{O}_3/\text{TiO}_2$ ) and mixed phase (Ti-O-Ti) nanotube

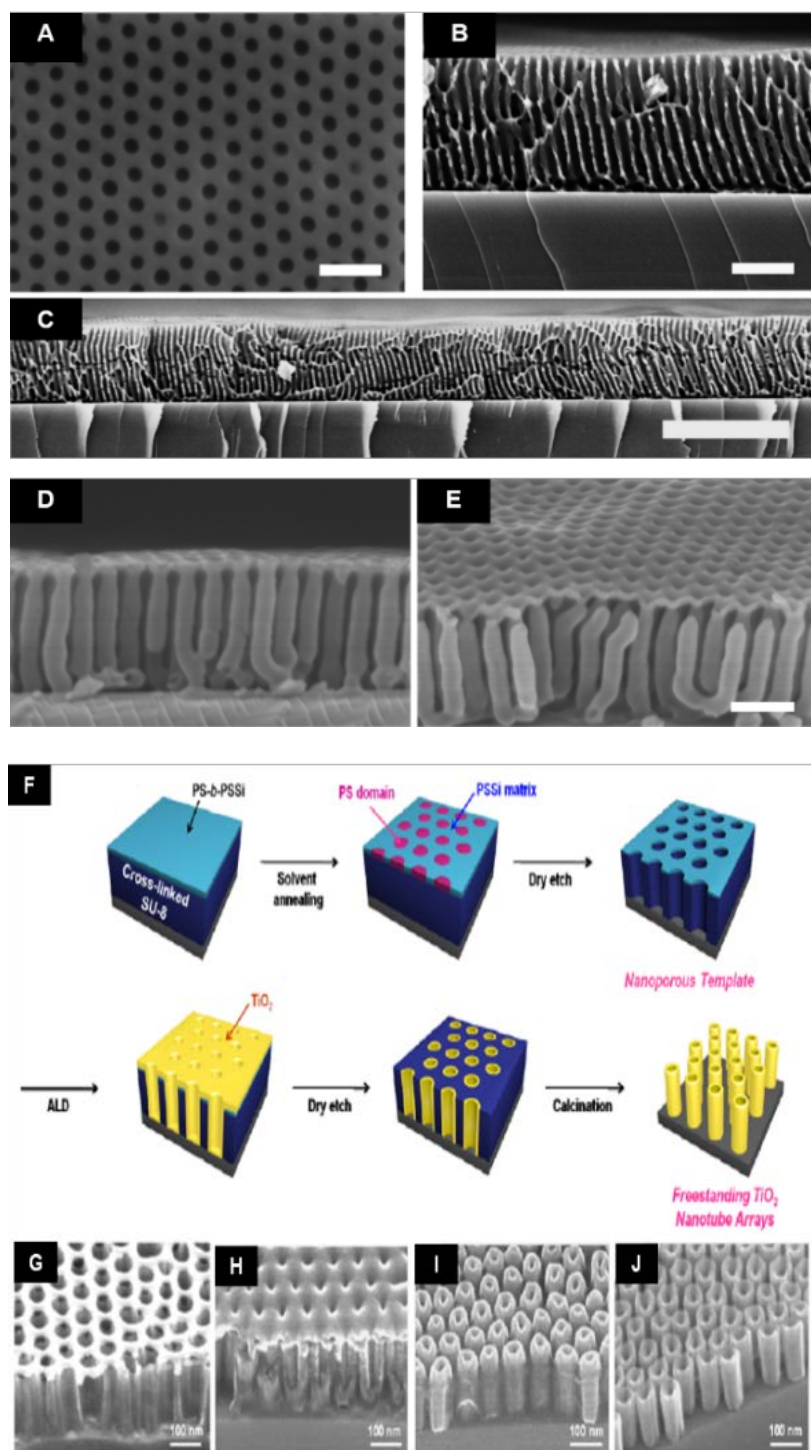


**Figure 1.10.** (A)-(C) 500 nm porous PS-*b*-P2VP nanodot features used as host template for ALD TiO<sub>2</sub> nanotube fabrication (D, E). (A-E) reproduced from reference 77. (F) Scheme for TiO<sub>2</sub> nanotube arrays using PS-*b*-PSSi BCP template. (G) Nanoporous PSSi template, (H) after ALD of 20 nm TiO<sub>2</sub>, (I) after dry etch step, and (J) freestanding TiO<sub>2</sub> nanotube array following calcination to remove organic matrix material. (F-J) reproduced from reference 80.

arrays were also fabricated. The work demonstrated a robust manner for creating hybrid materials circumventing the problematic nature of commonly employed AAO templates that can suffer pattern collapse.

Recently, a functional route combining directed block copolymer self-assembly and ALD was employed to create reduced features of a PS-*b*-PDMS.<sup>82</sup> Tolbert and co-workers described how through using repeated ALD cycles of alumina they reduced spacing of PDMS cylinders from 20 nm to less than 10 nm. The modification allowed the spin coating and alignment within ALD coated PDMS cylinders of 1-D FePt nanocrystals, a useful magnetic material. As highlighted in the work, the ALD coated layer behaves as a protective layer to the underlying polymer pattern since the organic solvents used to spin coat FePt nanoparticles would generally destroy the polymer. Additionally, the alumina layer provides thermal stability (up to 250°C) that allowed FePt particles to exhibit both ferromagnetic and superparamagnetic behavior. The work illustrated the flexibility that DSA of BCPs provides to address not only nanolithographic issues but to enable high density alignment of magnetic material.

As mentioned above, another factor to consider for achieving high control, uniformity and precision of inorganic incorporation is the use of easily etchable blocks in a BCP to create a porous host material. In this regard, one of the best BCPs studied to date has been PS-*b*-poly(lactic acid), also referred to as PS-*b*-polylactide (PS-*b*-PLA).<sup>83</sup> Owing to the degradable PLA component, porous templates can be formed through simple wet etching. Ming-Ho and coworkers have produced excellent 3-D inorganic replicas (*e.g.* silica,<sup>84-86</sup> titania<sup>87</sup>) with PS-*b*-PLA gyroid templating structures via sol-gel reactions for environmental use, drug delivery application and anti-reflection purposes. The work

has been reviewed extensively.<sup>83,88</sup> Recently, Gladfelter and co-workers have published work<sup>89</sup> employing ALD ZnO to achieve smaller feature dimensions using PS-*b*-PLA in a similar fashion to work described above.<sup>82</sup>

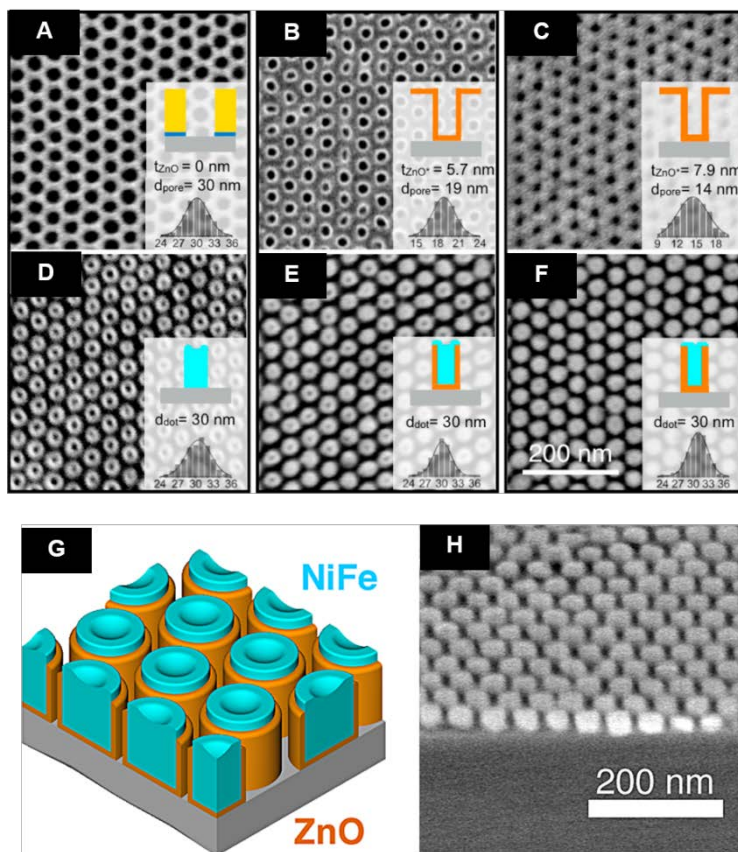


**Figure 1.11.** Top-down SEM images of reduced nanodot tuning through repeated ALD ZnO cycles. (A) Nanoporous PS template after PLA removal, (B) 5.7 nm ZnO coated with a pore size of 19 nm and (C) 7.9 nm ZnO coated with a pore size of 14 nm. (D-F) Corresponding permalloy filling of ZnO nanocrucibles. (G) Graphical representation of ZnO nanocrucibles filled with permalloy material. (H) Side-view SEM of (F). Images adopted from reference 89.

However, this work involved using a porous majority PS matrix template (Figure 1.11.A) generated from a hexagonal forming PS-*b*-PLA BCP to reduce the pore size of perpendicular cylinders. After successfully reducing pore diameter from 30 nm to 14 nm (Figure 1.11.B and C), permalloy ( $\text{Ni}_{80}\text{Fe}_{20}$ ) was evaporated on the ZnO “nanocrucibles” followed by a “Damascene-type” process reported earlier<sup>69</sup> to leave well-ordered ZnO nanocrucibles surrounding the permalloy dots. The material showed

ferromagnetic multidomain/vortex state at larger diameters but at reduced diameters (14 nm) exhibited superparamagnetism.

The combination of BCP nanolithography and conformal coating through ALD enabled high temperature processing to be carried out that might have use for bit patterned media application. As stated earlier, most reports using ALD on copolymer structures have focused on non-linear architectures. This section illustrates the significance of emerging work on the utilization of ordered DSA related BCP patterns coupled with ALD patterning to achieve not only nanolithographic triumphs but also the optimization of the two processes to access alignment of relevant magnetic material and highly porous inorganic designs with potential ultrahigh density bit media, solar cell, environmental and photochemical applications.

### **1.6. Sequential infiltration synthesis of block copolymers**

Peng *et al.*<sup>90</sup> were the first to employ an ALD derived process (in later publications coined sequential infiltration synthesis or SIS) with an asymmetric forming PS-*b*-PMMA BCP system consisting of either nanoposts or cylinders to fabricate metal oxide arrays. As depicted in Figure 1.12. and 1.13., the process involves initial exposure of the PS-*b*-PMMA films to precursor molecules (trimethyl aluminum or titanium tetrachloride/water) possessing an affinity to the reactive PMMA domain. These domains behave as growth sites for subsequent ALD cycles that can be infiltrated with an array of semiconductor and light active materials. It can be noted that the alternative strategy used here avoids using UV exposure/acetic acid washing process described earlier for PMMA elimination although the PMMA microdomain is still the microdomain of infiltration interest. In this first publication in 2010, Al<sub>2</sub>O<sub>3</sub> and TiO<sub>2</sub>

arrays were generated using ALD cycles and feature sizes beyond the original polymer template were enabled through repeated ALD cycles as well as longer precursor exposure times. There are two key achievements through this synergistic ALD-BCP approach. Firstly, the methodology is based on forming inorganic structures within BCP domains rather than at interface boundaries. This is in contrast to other work that coats the outside of polymer materials with ALD. Furthermore, block removal is not necessary and thus an often problematic process step that can induce defects is avoided. In this respect, it may be possible to apply the methodology to reactive sites in BCPs which do not contain an easily removable block. Secondly, the methodology allows a facile way to mimic the original BCP nanopattern without disturbing morphology. Peng's work employed already assembled BCP domains and chemically enhanced the domains via "molecular recognition". The ability to tune and alter the resulting feature sizes without having to adjust the BCP molecular weight is advantageous. However, although SIS provides scope to alter feature sizes one would assume there are upper and lower thresholds for feature size tuning. We state this as presumably at later stages after repeated cycles or higher precursor loads, infiltrated domains may agglomerate during feature formation.

In a follow-up work, Darling, Elam and coworkers demonstrated the fabrication of continuous ZnO, SiO<sub>2</sub> and W line structures with SIS and PS-*b*-PMMA BCP.<sup>91</sup> The application of the SIS practice to such a well-studied BCP system like PS-*b*-PMMA further enhances its possible integration for etch-mask applications, as the metal oxide can be employed as a hardmask to pattern the underlying device material. It is accepted that the etch contrast between PS and PMMA is relatively low and thus this chemical infiltration is an advancement with regard to device processing. Figure 1.12.B-D shows

high-fidelity silicon nanostructures perpendicular and parallel to the substrate plane following pattern transfer using an  $\text{Al}_2\text{O}_3$  hardmask via SIS.<sup>92</sup>

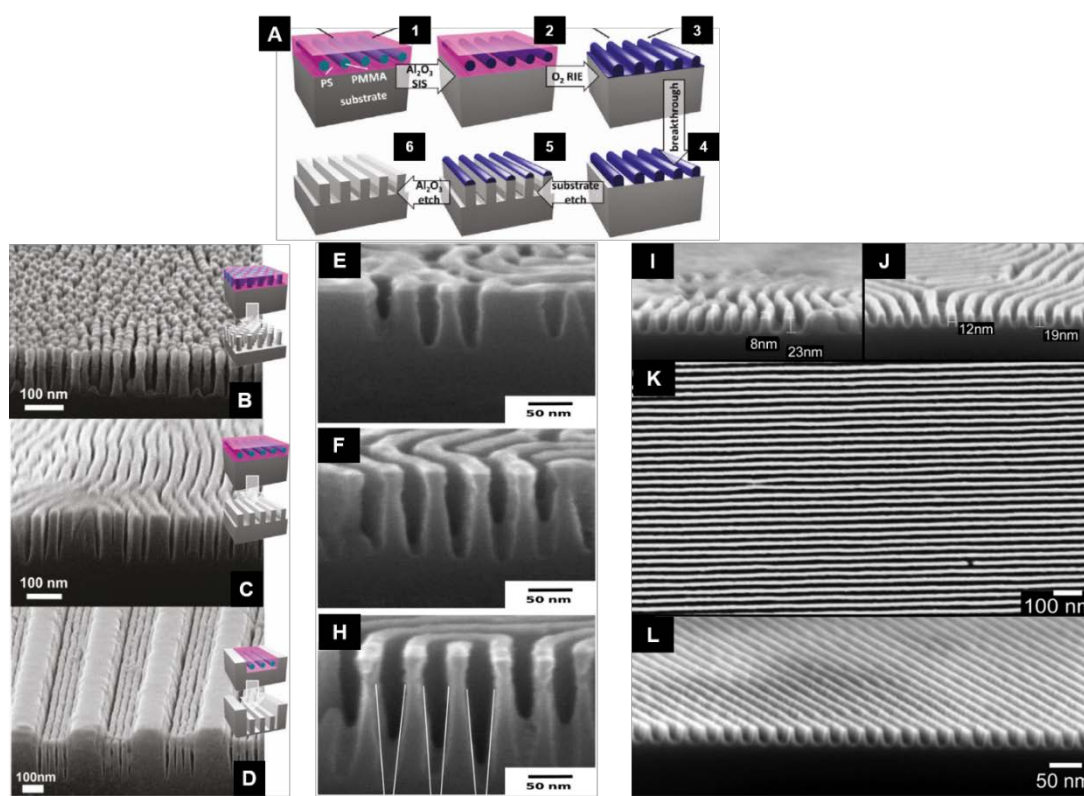


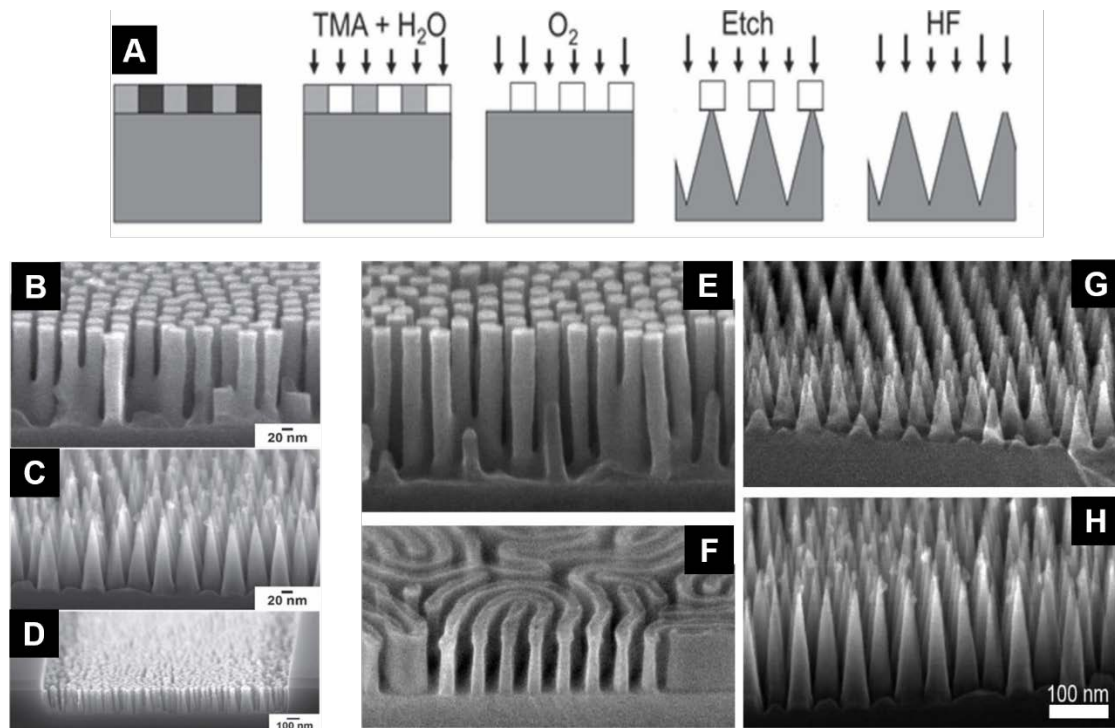
**Figure 1.12.** (A) Process flow for SIS of PS-*b*-PMMA BCPs to enhance etch contrast. (B-D) Cross-section SEM images of silicon nanoposts and nanofins (graphoepitaxy approach) from SIS  $\text{Al}_2\text{O}_3$  mask for enhanced etch contrast. (E-H) Patterned silicon from SIS  $\text{Al}_2\text{O}_3$  mask using lamellar forming PS-*b*-PMMA (period  $\sim 38$  nm) BCP system. (I-L) High quality pattern transfer using SIS  $\text{Al}_2\text{O}_3$  masks coupled with chemoepitaxy schemes for alignment. Images reproduced from references 92-94.

Subsequently, Black and co-workers illustrated high-aspect ratio pattern transfer using the same SIS approach for PS-*b*-PMMA (see Figure 1.12.E-L).<sup>93</sup> Systematic studies were carried out analyzing the  $\text{Al}_2\text{O}_3$  infiltration effect on domains which showed that image quality suffered with higher ALD cycles.<sup>94</sup> They also found that extensive trimethyl aluminium/water exposure cycles or ALD cycles alone damaged the pattern quality. Another report provided a further advance and twist on the SIS technique by simply exposing PS-*b*-PMMA BCPs (cylindrical and lamellar morphologies) to UV light for a short period thus creating activation of reactive sites for precursors.<sup>95</sup>

However, the reactive sites in this case were in the PS component of the BCP in comparison to the PMMA block as described earlier. This simple modification allowed selective infiltration to an alternative block other than PMMA. The ability to switch from PMMA domain infiltration to PS domain infiltration creates further opportunities for the SIS methodology to be adopted. The most prominently studied BCPs other than the “first-generation” PS-*b*-PMMA BCP contain a PS block in most cases *e.g.* PS-*b*-PEO, PS-*b*-PDMS, PS-*b*-P2VP, PS-*b*-P4VP and PS-*b*-PLA. For this reason, alternative block selectivity could be used to write inverse patterns.

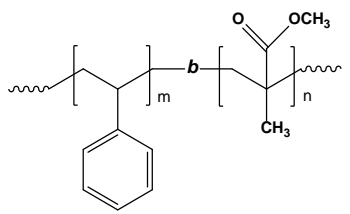
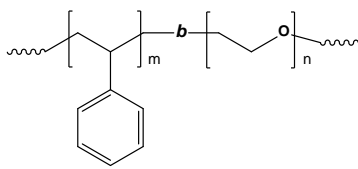
Impressive reports by Checco *et al.*<sup>96,97</sup> and Rahman *et al.*<sup>98,99</sup> has already shown the near future commercial potential of infiltrated BCP technology for everyday use. In one report, Al<sub>2</sub>O<sub>3</sub> features produced via SIS coupled with evaporation and vapor synthesis have been utilized to produce Fe, Si and Ge nanowires for anti-reflection and hydrophobic application.<sup>99</sup> In another work, following the fabrication of cone tipped nanopillars (Figure 1.13.C) superhydrophobicity was observed over large areas.<sup>96</sup> Superhydrophobicity describes the ability of a rough hydrophobic surface to repel water, with criteria including a contact angle greater than 150° and low contact angle hysteresis. Superhydrophobic surfaces designed in this manner hold potential for commercialization however further research in their design to improve overall stability could have serious outcomes for self-cleaning surfaces and energy/heat conservation. The researchers initially formed hexagonally packed PS-*b*-PMMA BCP patterns over large areas. The patterns were then infiltrated with Al<sub>2</sub>O<sub>3</sub> and subsequently pattern transferred to the underlying substrate. Using a highly selective etch that created a tapered sidewall due to lateral silicon etching, water droplet behavior was investigated. Prior to the water droplet testing, octadecyltrichlorosilane was coated on the different

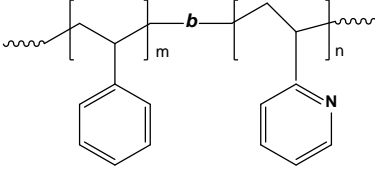
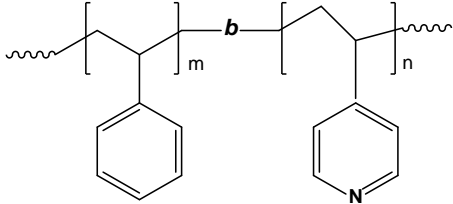
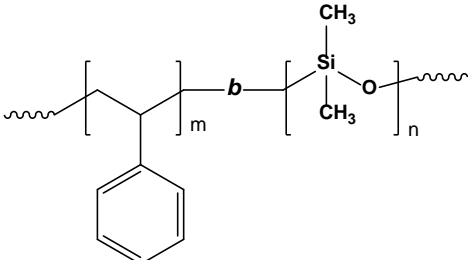
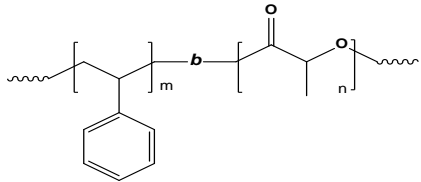
topographies created (spacing varied from 30 – 52 nm for both nanopillars and nanocones). The tapered cone nanopillars proved to be the optimal geometry for superhydrophobicity.



**Figure 1.13.** (A) SIS of PS-*b*-PMMA BCP, followed by plasma and wet etching for nanocone fabrication. (B)-(H) Cross-section SEM images of silicon nanostructures patterned using SIS Al<sub>2</sub>O<sub>3</sub> of PS-*b*-PMMA BCPs (cylinder and lamella) for superhydrophobic application. Images adopted from references 96 and 97.

Table 2. Block copolymers, infiltration techniques and reported functions

Block Copolymer	Infiltration Technique	Resulting Nanostructure	Function/Application
<p><b>PS-<i>b</i>-PMMA</b></p> 	Evaporation/E-beam or Ion beam deposition	Au dots/posts, <sup>40,42,45,64,76</sup> Co posts, <sup>43</sup> Co nanorings, <sup>46</sup> Fe posts, <sup>48</sup> Cr posts, <sup>44,57</sup> aligned Al and Au nanowires, <sup>49</sup> Ge nanowires, <sup>53</sup> Al <sub>2</sub> O <sub>3</sub> dots, <sup>51</sup> Ti/Pt dots <sup>65</sup>	On-chip etch mask, <sup>44</sup> ferromagnetic nanorings, <sup>46</sup> carbon nanotube growth, <sup>48</sup> metal nanodot memory device, <sup>57</sup> triboelectric generator, <sup>62</sup> resistive switching nanodevice, <sup>65</sup> plasmonic, <sup>76</sup>
	Atomic layer deposition	Al <sub>2</sub> O <sub>3</sub> line and hole spacer, <sup>73</sup> Al <sub>2</sub> O <sub>3</sub> wires and posts <sup>74,75</sup>	On-chip etch mask <sup>73-75</sup>
	Sequential Infiltration Synthesis	Al <sub>2</sub> O <sub>3</sub> posts, <sup>90,95,96-100</sup> Al <sub>2</sub> O <sub>3</sub> wires, <sup>90-95</sup> TiO <sub>2</sub> wires, <sup>90</sup> SiO <sub>2</sub> posts, <sup>91</sup> SiO <sub>2</sub> wires, <sup>91</sup> W wires, <sup>91</sup> ZnO posts, <sup>95</sup> ZnO wires <sup>91,95</sup>	On-chip etch mask, <sup>92-94,96,97</sup> SIS procedure for PS block selectivity, <sup>95</sup> superhydrophobicity, <sup>96,97</sup> anti-reflection, <sup>98</sup> nanowire growth, <sup>99</sup> broadband antireflection for Si solar cell <sup>100</sup>
	Spin coating	FePt nanoparticles, <sup>101,102</sup> CdSe nanoparticles, <sup>102</sup> CdSe@ZnS quantum dots, <sup>103</sup> Fe <sub>2</sub> O <sub>3</sub> nanoparticles, <sup>103</sup> 1D ZnO nanorods <sup>103</sup>	Alignment of nanoparticles within BCP grooves, <sup>100,101,103</sup> dual nanopatterning <sup>103</sup>
<p><b>PS-<i>b</i>-PEO</b></p> 	Metal Salt Inclusion	Fe <sub>2</sub> O <sub>3</sub> dots, <sup>104-107</sup> Fe <sub>3</sub> O <sub>4</sub> dots, <sup>104-107</sup> CeO <sub>2</sub> dots, <sup>107,108</sup> CuO dots, <sup>107</sup> lead zirconate titanate dots, <sup>109</sup> Ag dots <sup>110</sup>	On-chip etch mask, <sup>105,106,112</sup> superparamagnetism, <sup>104,106</sup> vertical Si nanowires for neuroelectrode modification, <sup>112</sup> ferroelectric, <sup>109</sup> antimicrobial function <sup>110</sup>
		Fe <sub>2</sub> O <sub>3</sub> , Fe <sub>3</sub> O <sub>4</sub> wires <sup>111</sup>	On-chip etch mask <sup>111</sup>

<b>PS-<i>b</i>-P2VP</b>	Atomic layer deposition	TiO <sub>2</sub> nanotubes <sup>77</sup>	500 nm thick porous TiO <sub>2</sub> nanotubes <sup>77</sup>
	Precursor spin coating	SiO <sub>2</sub> posts <sup>59</sup>	On-chip etch mask, SiO <sub>2</sub> pillars <sup>59</sup>
	Aqueous metal reduction	Au, Pd, Pt, Fe, Co, Cu, Ni wires <sup>113-115</sup>	Aligned metallic lines and density doubling using graphoepitaxy, <sup>113-115</sup> electrical resistivity of Pt wires <sup>113</sup>
<b>PS-<i>b</i>-P4VP</b>	Sputtering	Au decoration <sup>56</sup>	On-chip etch mask, Patterned SiO <sub>2</sub> posts, pillars and rings <sup>56</sup>
	Metal salt inclusion/precursor spin coating	Fe <sub>2</sub> O <sub>3</sub> dots, <sup>116</sup> Fe <sub>3</sub> O <sub>4</sub> dots, <sup>116</sup> Fe <sub>3</sub> O <sub>4</sub> and Al <sub>2</sub> O <sub>3</sub> wires, <sup>117,118</sup> SiO <sub>2</sub> posts, <sup>59,119</sup> SiO <sub>2</sub> wires, <sup>119</sup> HfO <sub>2</sub> wires <sup>132</sup>	On-chip etch mask, Si nanopillars, <sup>116</sup> Si and Ge nanofins, SiO <sub>2</sub> pillars <sup>59</sup>
	Aqueous metal reduction	Fe <sub>2</sub> O <sub>3</sub> nanoparticles, <sup>120</sup> Au dots, Pt dots, Pt/Au dots, Au wires/Au dots, Au wires/Pt dots, Pt wires/Pt dots, <sup>121</sup> Fe-Pt, Co-Pt, Pd-Au, Co-Pd-Pt alloys, <sup>122</sup> Au rings, dots, meshes, double wires, <sup>123</sup> Au wires and meshes <sup>124</sup>	Carbon nanotube growth, <sup>120,122</sup> charge trap memory device, <sup>121</sup> plasmonic <sup>121,123</sup>
<b>PS-<i>b</i>-PDMS</b>	Sputtering	Ti, <sup>66</sup> W, <sup>66,67</sup> Pt, <sup>66</sup> Co, <sup>66</sup> Ni, <sup>66</sup> Ta, <sup>66</sup> Au, <sup>66</sup> Al, <sup>66</sup> Ti wires <sup>68</sup>	Graphoepitaxially aligned inorganic wires <sup>66,67</sup> Electrical and magnetic Ni nanowire properties <sup>66</sup>
	Atomic layer deposition	Pt, W, Ti, Ta, Ni dots <sup>68</sup>	Nanopore on-chip etch mask <sup>68</sup>
		Al <sub>2</sub> O <sub>3</sub> feature reducer <sup>82</sup>	Alignment of FePt nanoparticles <sup>82</sup>
<b>PS-<i>b</i>-PLA</b>	Molecular beam deposition/evaporation	Ni <sub>180</sub> Fe <sub>20</sub> , <sup>69,89</sup> Ni <sup>58</sup>	Ferromagnetism <sup>69,89</sup>
			

A notable report in 2015 showed that the silicon nanotextures could be utilized for solar cell application. Specifically, Rahman *et al.*<sup>100</sup> described that enhanced broadband antireflection in silicon solar cells could be achieved using silicon features with sub-50 nm fabricated via SIS alumina infused PMMA domains of a PS-*b*-PMMA BCP. The practice involved is a facile and low-cost device route to surpass common bulk materials with antireflective silicon nitride coating layers.

Despite the experimental evidence demonstrated thus far for the efficacy of SIS treated materials, little clear understanding of the mechanism(s) has been put forward until now. Using *in-situ* fourier transform infrared analysis Biswas *et al.*<sup>125</sup> ascertained that a two-step mechanism is involved leading to the formation of covalent bonding between carbonyl group of PMMA and aluminium precursor. In general, the first step of SIS involves the exposure of polymer material to TMA. This was found to an extremely quick interaction (180 seconds) but is quite unstable. The formation of stable Al-O linkages will subsequently occur in a slow manner (close to ~ 60 minutes) but is dependent on TMA desorption. Once a high concentration level of the initial physisorbed complex (TMA-C=O) exists, stable covalent Al-O bonds will form. The author's hypothesis on intermediate complex formation was also confirmed by density functional theory calculations. The most significant comment in their study is "*that the TMA purge time is crucial for Al<sub>2</sub>O<sub>3</sub> formation within PMMA*". This is related to the unstable nature of the TMA-PMMA interaction and that short purge times are required in order to augment the formation of Al<sub>2</sub>O<sub>3</sub> in PMMA growth sites. A comprehensive insight of the SIS process in relation to PMMA film thickness and temperature effect was also reported.<sup>126</sup> Such studies to define and understand the complex molecular level interactions are extremely useful if SIS BCP nanolithography methods (and SIS e-

beam, optical resists<sup>127,128</sup>) are to be commercially viable for HVM and VLSI where stringent defect tolerance levels must be satisfied.

### 1.7. Spin coating methodologies for metal nanoparticle alignment and metal oxide inclusion with “activated” block copolymer templates

Spin coating inorganic nanoparticles is an attractive approach for generating functional features as many routes possess the potential for industrial scale processing. Spin coating on modified (*e.g.* photochemically altered, selective solvent swelling) BCP thin films combined with further treatment (*e.g.* thermal annealing, calcination, ozonation) can lead to semiconductor, ferroelectric or magnetic materials in a highly straightforward process. In 2005, Darling *et al.*<sup>101</sup> demonstrated a novel route for the placement of magnetic FePt nanoparticles on vacuum ultraviolet etched PMMA half-cylinder domains in PS-*b*-PMMA system (Figure 1.14.).

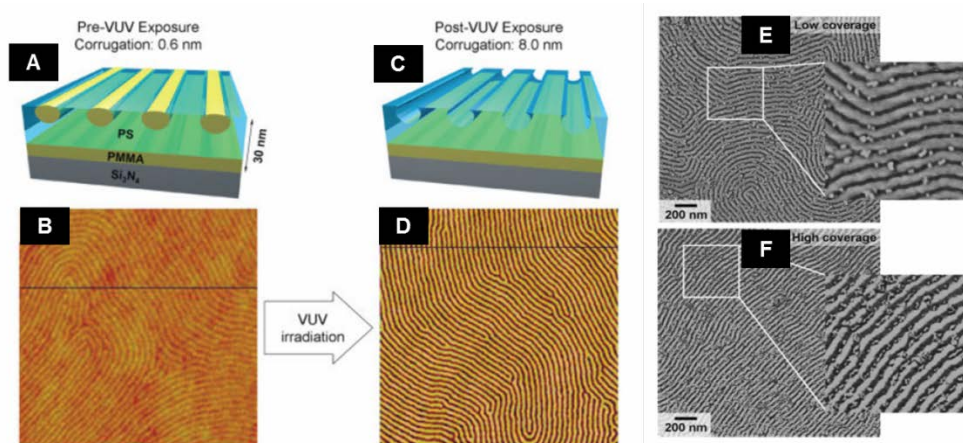


**Figure 1.14.** (A) and (C) show schematic representation of cylinder forming PS-*b*-PMMA films before and after VUV irradiation used to etch PMMA half-cylinders. (B) and (D) are corresponding AFM images (both 2 x 2 μm). Following spin-coating of FePt nanoparticles low coverage (E) and high coverage (F) areas of nanoparticle clusters were identified showing high adsorption to the photochemically altered PMMA domains. Images reproduced from reference 101.

The etched PMMA domains provided a selective channel for oleic-acid capped FePt nanoparticles. Importantly, the resulting functional material length scale was an order

of magnitude smaller than the initial PS-*b*-PMMA template. Darling's work showed the simplicity of spin coating functional material on modified BCP templates.

Moreover, the work highlighted the potential and significance of altering chemistry of self-assembled BCP templates for creating "nanotroughs" and domains for the positioning of nanomaterials. Additional work<sup>102</sup> suggested that the process was physical rather than chemical which expanded the range of nanoparticles that could be aligned in etched microdomain channels.

In 2009, Son *et al.*<sup>103</sup> demonstrated a facile spin-coating process for the placement of nanomaterial including CdSe@ZnS quantum dots, Fe<sub>2</sub>O<sub>3</sub> nanoparticles, and 1-D ZnO nanorods after exposing PS-*b*-PMMA patterns to selective solvents creating surface reconstructed grooves. The authors also managed to create dual patterned films (consisting of CdSe@ZnS quantum dots and Fe<sub>2</sub>O<sub>3</sub> nanoparticles) through electron beam exposure following the first nanoparticle deposition step. One should note the progress of placement and alignment in the recent synergistic approach<sup>82</sup> detailed in section 1 for FePt nanoparticles utilizing ALD modified DSA BCP patterns.

More recently, we have demonstrated a rich variety of metal oxide nanostructures with as-formed self-assembled cylinder forming PS-*b*-PEO and PS-*b*-P4VP BCPs through an "*in-situ*" metal-salt inclusion spin coating methodology. Since cylinder systems can be tailored to enable perpendicular or parallel cylinder orientation through solvent vapor annealing treatment, both metal oxide nanodots and nanowires can be accessed. Initially, neat PS-*b*-PEO or PS-*b*-P4VP templates with enhanced ordering are modified and "activated" through ethanol treatment. The PEO and P4VP blocks selectivity to

ethanol render porous templates for successful metal ion inclusion. Whilst the exact mechanism of pore forming is under debate for these systems, evidence suggests that PEO domains are etched.<sup>111</sup> In contrast, P4VP domains are swollen and collapse within the pores as others have noted.<sup>77</sup> The treatment is proven to be reversible through appropriate treatment for PS-*b*-P4VP BCPs.<sup>56</sup> The “activation” step is crucial for allowing the inorganic salt to be included in the desired location.

Micelle formation can be used to form metal nanoarrays;<sup>129,130</sup> however the associated co-ordination chemistry can be complex, particularly for BCPs not possessing a direct bonding site. Moreover, in technologies such as lithography and fluidics, pattern placement is paramount and therefore micelle formation restricts line space feature formation and high registration being achieved. The spin coating methodology we have employed translates to both perpendicular and parallel cylinder orientations with large scale inclusion and uniformity evident. In initial works, iron oxide (Fe<sub>3</sub>O<sub>4</sub> and Fe<sub>2</sub>O<sub>3</sub>) nanodot arrays were created over large areas following spin coating of a metal nitrate ethanolic solution.<sup>104,116</sup> Following deposition of the metal salt precursors by spin coating, ultraviolet/ozone treatment is carried out to remove the remaining polymer matrix material and oxidize the nitrate precursor. Others have recently adopted a similar approach to form oxides and then thermally annealed films post metal precursor deposition to remove the polymer template.<sup>131</sup> In 2008, Park *et al.*<sup>119</sup> demonstrated silica nanodots and nanowires following spin-coating of a PDMS precursor in selective solvents on surface reconstructed PS-*b*-P4VP films. In our work, the FeO nanodots produced from perpendicularly oriented PEO cylinders were shown to possess superparamagnetism as the features are less than the single domain size of iron oxide (< 20 nm).<sup>104</sup> The methodology has shown the ability to easily change a nanodots size

through simply increasing metal ion concentration without having to change the BCP molecular weight.<sup>107</sup> Additionally, the practice and corresponding superparamagnetism was demonstrated for a series of high and low molecular weight PS-*b*-PEO systems.<sup>106</sup> Thus far, Fe<sub>3</sub>O<sub>4</sub>,<sup>106,116,117</sup> CeO<sub>2</sub>,<sup>107,108</sup> CuO,<sup>107</sup> Al<sub>2</sub>O<sub>3</sub>,<sup>117</sup> HfO<sub>2</sub><sup>132</sup> patterning of nanodot and nanowire features have been developed using the metal salt inclusion methodology and have been shown to be effective on-chip etch masks on silicon (see examples in Figure 1.15.).

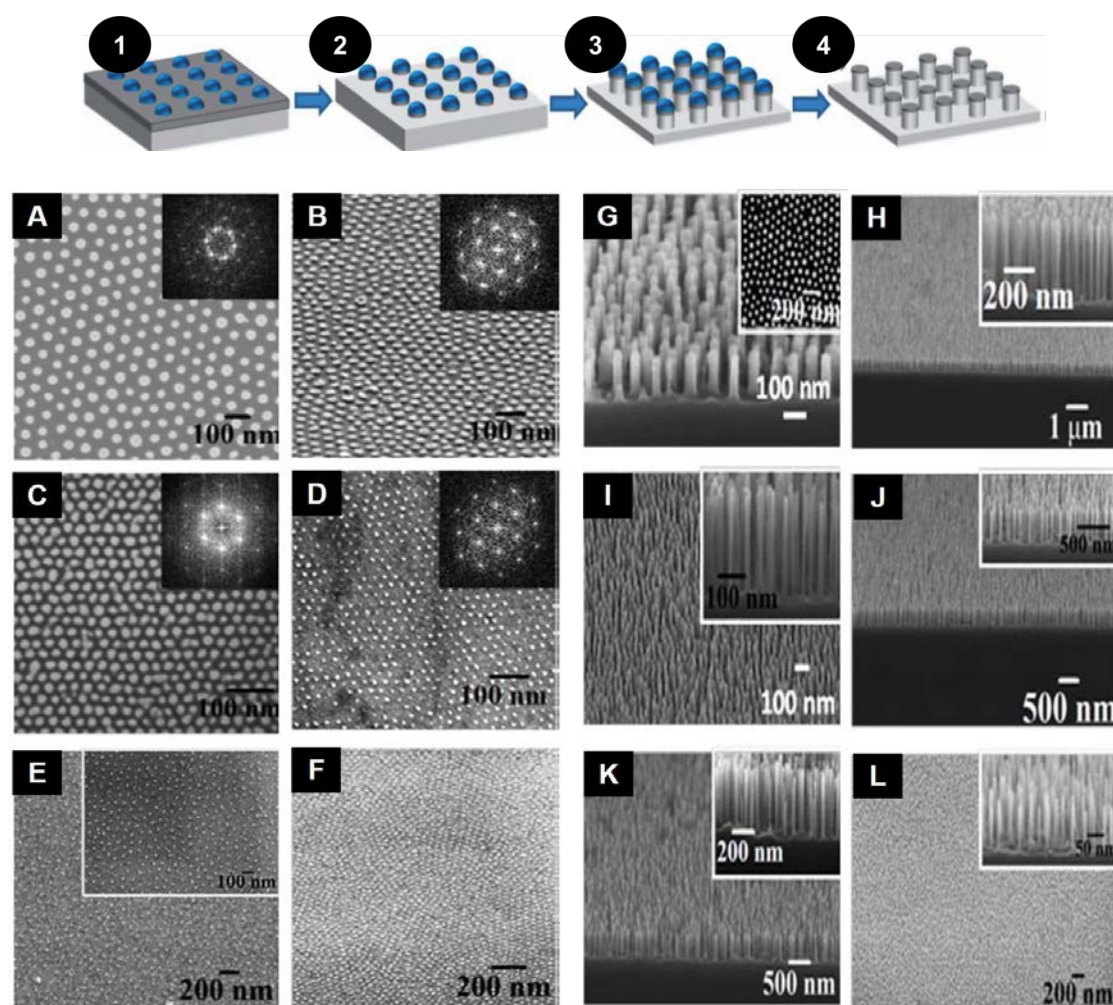


**Figure 1.15.** (1) Metal ion inclusion via spin coating on “activated” PS-*b*-PEO nanodot template (2) Metal oxide nanodots after inclusion and UV/O<sub>3</sub> to oxidize metal ion and remove polymer matrix. (3) Plasma etching to pattern transfer metal oxide etch mask. (4) Resulting high-fidelity silicon nanofeatures. (A-F) Series of top-down SEM images of varying Fe<sub>3</sub>O<sub>4</sub> nanodots with different periods. (G-L) Corresponding structures following pattern transfer of Fe<sub>3</sub>O<sub>4</sub> etch masks forming high-aspect ratio silicon nanowires. Images reproduced from reference 105. See text for application and function.

Silicon nanopillars of 500 nm in height can be obtained following plasma etching metal oxide nanodot patterns.<sup>105,106,116</sup> Additionally, nanowires were developed in the same way for both BCP systems, PS-*b*-PEO and PS-*b*-P4VP, resulting in highly uniform Fe<sub>3</sub>O<sub>4</sub> nanowires with 42 nm (PS-*b*-PEO)<sup>111</sup> and 32 nm (PS-*b*-P4VP)<sup>117</sup> periodicity (see Figure 1.16.). We have also integrated the metal-salt inclusion technique in graphoepitaxy schemes with similar efficacy in PS-*b*-P4VP for patterning aligned Si and Ge nanofins as shown in Figure 1.16. and 1.17.<sup>117,132</sup> “Activated” PS-*b*-P4VP line pattern and metal salt inclusion producing Fe<sub>3</sub>O<sub>4</sub>, Al<sub>2</sub>O<sub>3</sub> and HfO<sub>2</sub> nanowires have been employed as robust on-chip etch masks with similar efficacy for pattern transfer. These achievements are pertinent for DSA technology as pattern transfer fidelity is critical. Patterning magnetic and integrated circuit features via BCP nanolithography with this process offers great potential due to the simplicity and cost-effectiveness.

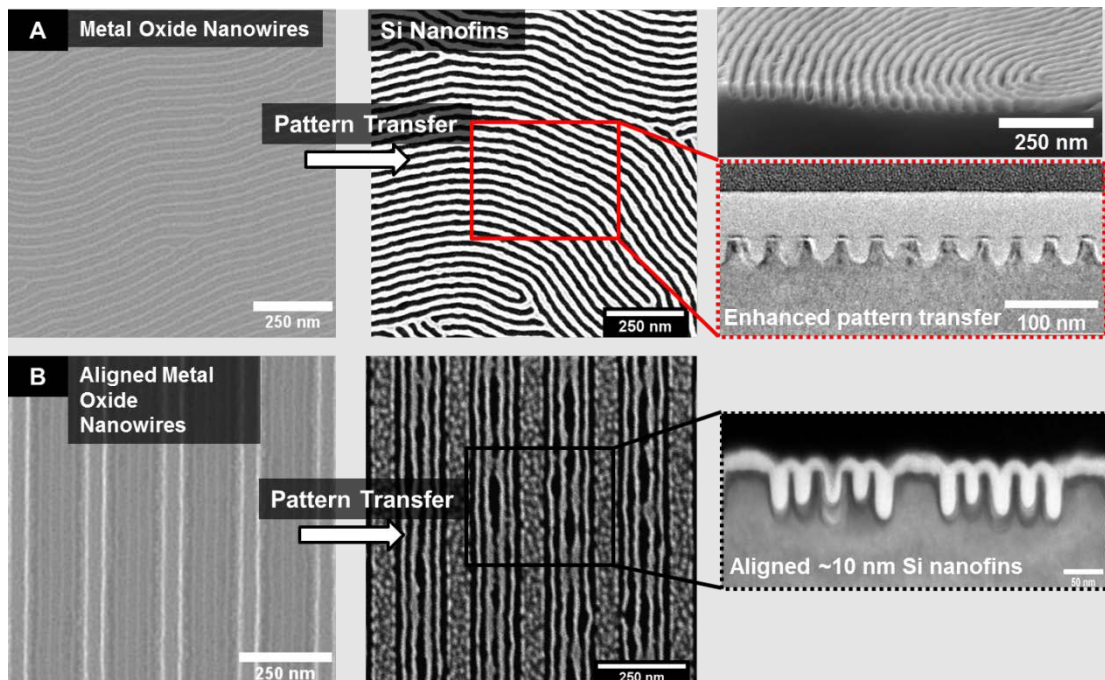


**Figure 1.16.** (A) Alumina metal oxide inclusion in PS-*b*-P4VP BCP for enhanced silicon patterned transfer for line space features (B) Metal-oxide inclusion process integrated with directed self-assembly scheme using graphoepitaxy. Images reproduced from reference 117.

Fabrication of lead zirconate titanate (PZT) nanodots was also achieved via BCP templating that displayed piezoelectric and ferroelectric behavior.<sup>109</sup> The pattern density was calculated to be  $\sim 68 \times 10^9$  nanodots  $\text{cm}^{-2}$ . The ability to template functional material in this fashion with ferroelectric behavior may be of use for future memory devices due to reduced power consumption and faster write speeds than flash memory.

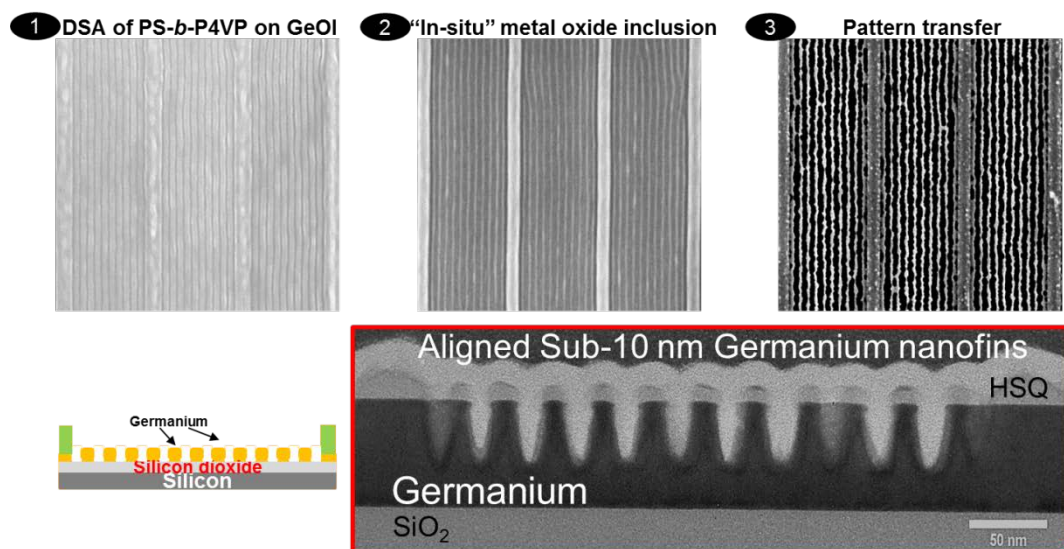


**Figure 1.17.** Fabrication of aligned sub 10-nm germanium nanofins via metal oxide enhanced pattern transfer from PS-*b*-P4VP BCP. Note channel widths in 1-3 are 361 nm. See text for details. Images reproduced from reference 132.

Apart from on-chip etch mask use for achieving ultra-small feature sizes, the high-density metal and metal oxide arrays or resulting high aspect ratio pattern transferred geometries can be applied for biomedical and bioscience related applications. Recently, sub-20 nm vertical Si nanowires (generated from metal salt inclusion with PS-*b*-PEO and subsequent pattern transfer) were shown to reduce electrical impedance and increase conductivity for neuroelectrodes.<sup>112</sup> This is particularly useful for addressing electrode failure or deterioration as the vertical nanowires prevent tissue encapsulation of the electrode *in-situ* and, therefore, leads to longer electrode performance and sensitivity. Additionally, silver nanodots patterned on glass substrates using BCP

templates have shown antimicrobial activity that may be of benefit for food packaging application.<sup>110</sup> The above outlined inorganic nanofeature fabrication routes using “activated” BCP templates and straightforward metal-salt inclusion can access ordered arrangements of diverse inorganic materials. The inorganic features can be pattern transferred for high-aspect ratio structures showing their etch-mask application,<sup>105,111</sup> with resulting Si features also used for biomedical application<sup>112</sup> or inorganic features at substrate surfaces can be utilized to further efforts on magnetic,<sup>104,106</sup> ferroelectric<sup>109</sup> and anti-microbial<sup>110</sup> use in an easy and low cost manner.

### **1.8. Aqueous metal reduction and block copolymer nanopatterns**

Another route encompassing metal inclusion or more appropriately defined aqueous metal reduction involves the immersion of BCP thin films in an acidic metal containing medium. A report in 2007 by Chai *et al.*<sup>113</sup> using a cylindrical forming PS-*b*-P2VP BCP system and aqueous metal reduction developed highly defined Au, Pd and Pt nanowires from metal ion loading and reduction with strict alignment of the initial BCP features directed through graphoepitaxy (see Figure 1.18.). Noble metal nanostructures receive much research interest as their increased scattering and absorption of light at the nanoscale can potentially be used for energy, environmental<sup>133</sup> and biomedicine<sup>134</sup> use. The authors report that for successful metal complexation, an acidic medium is essential. Since the P2VP cylinders are buried within the hydrophobic PS matrix, access for metal ions alone is problematic. Therefore the acidic medium enabled swelling of the cationic P2VP domains which “*pierce and penetrate*” the PS overlayer. The P2VP domains eventually perforate the PS domains as shown in Figure 1.18. leading to mushroom caps. This perforation phenomenon can be attributed to the alteration in pH (<4.5) of the acidic medium and as noted by the authors, mushroom

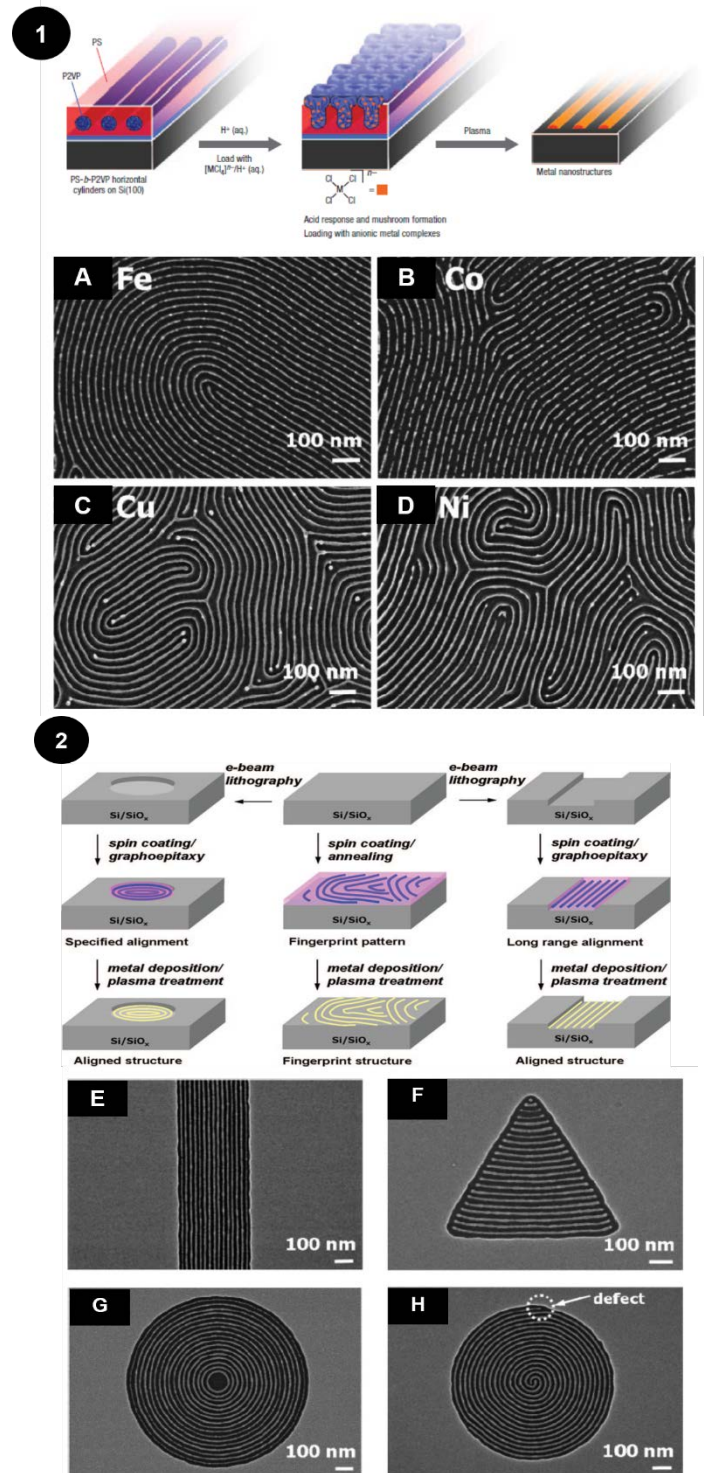


**Figure 1.18.** (1) Scheme of metal ion reduction after immersion of PS-*b*-P2VP films in acidic medium forming mushroom caps followed by O<sub>2</sub> plasma revealing metallic lines. (2) Process flows for graphoepitaxy approaches BCP alignment with different geometries. (A-D) Top-down SEM images of Fe, Co, Cu and Ni metallic lines via aqueous metal reduction and O<sub>2</sub> plasma. (E-H) Aligned Pt features from PS-*b*-P2VP BCP and graphoepitaxy. Schemes and images reproduced from references 112 and 113 respectively.

cap formation was more prominent with HCl (stronger acid) than HF. A follow-up work<sup>114</sup> reinforced the efficacy of the acidic medium for generating a morphological change in the BCP film to allow inclusion of metal ion at the protonated P2VP domains. Figure 1.18. shows an array of metal wires formed via immersion of PS-*b*-P2VP films in metal acidic solutions followed by O<sub>2</sub> plasma treatment. Pd and other noble metal nanoparticle deposition on surface reconstructed films has been utilized by Stamm and co-workers using PS-*b*-P4VP BCP and supramolecular formed systems.<sup>135,136</sup> A recent review<sup>137</sup> is available on the methods used which vary from deposition of pre-synthesized nanoparticles to immersion of neat films in nanoparticles. Following these reports, researchers have followed a similar protocol for developing well-defined metallic features with the PS-*b*-PVP family of BCPs. One interesting publication developed monodisperse Fe<sub>2</sub>O<sub>3</sub> nanoparticles via ordered PS-*b*-P4VP microdomains and highly defined metal deposition provided catalytic sites for vertical carbon nanotube growth (CNT).<sup>120</sup> A detailed study on the loading time of precursor (30 seconds to 40 minutes) allowed the researchers to correlate the mean diameter size of Fe<sub>2</sub>O<sub>3</sub> nanoparticles to number of CNT grown. A work in 2012 by Wu *et al.*<sup>115</sup> demonstrated the true potential of BCP lithography to address ever decreasing technology nodes. The authors reported a method of forming bilayers of cylinder PS-*b*-P2VP structures through controlled swelling conditions. Subsequent Pt metallization of optimized conditions revealed density doubling of both dot and line-space features as shown in Figure 1.19. The process was also demonstrated using graphoepitaxy schemes.

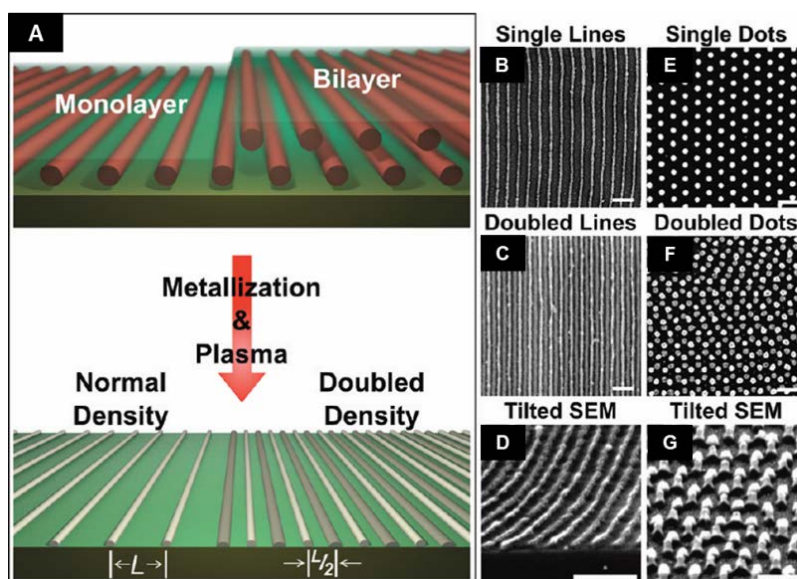


**Figure 1.19.** (A) Process for density doubling using PS-*b*-P2VP BCP templates. (B-G) Resulting density multiplication of Pt features after aqueous metal reduction using bilayer films of PS-*b*-P2VP. Reproduced from reference 114.

More recent publications by Kim and co-workers<sup>121,122</sup> have shown sophisticated methods to form highly intricate and technologically relevant materials for catalytic growth and device fabrication. In both reports, PS-*b*-P4VP BCP self-assembly and cylinder orientation (dots and lines) were tuned via solvent vapor annealing and aqueous metal reduction was used to fabricate metallic features. A multi-level charge trap memory device was presented through Pt-Au binary dot pattern.<sup>121</sup> The Pt-Au binary dot pattern was produced through metallization of vertical cylinder structure that were subsequently used for the self-assembly of a second vertical cylinder layer where metallization was utilized again as shown in Figure 1.20. Additionally, using multicomponent patterns the authors demonstrated the synergy of their features that led to higher extinction over visible and infrared regions. By employing Au nanowire and Pt dots, higher extinction levels were recorded in comparison to either metallic feature alone. The plasmonic capability demonstrated by this work opens many possibilities for light excitation applications.

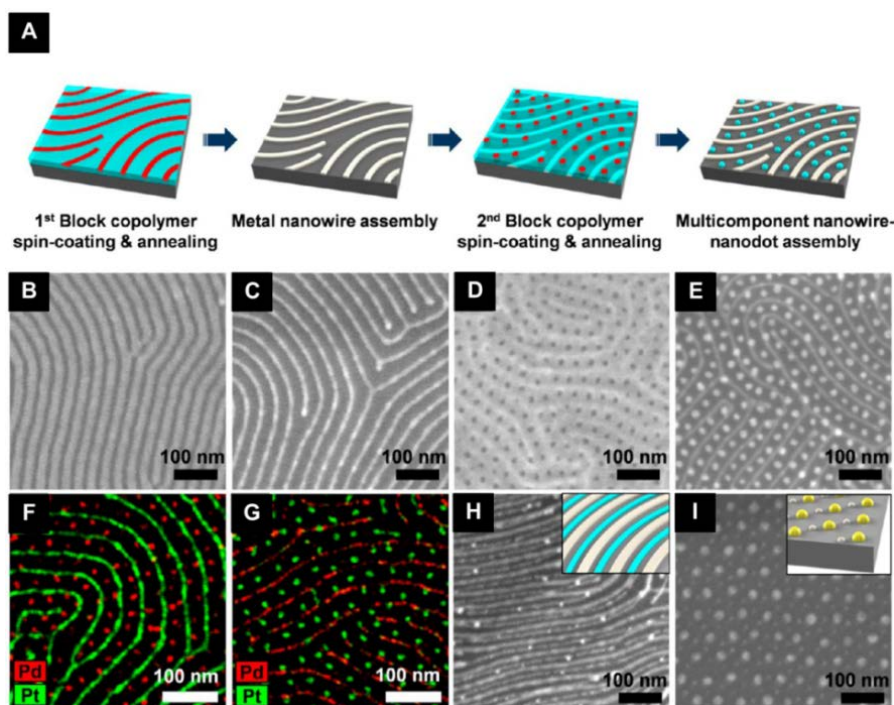


**Figure 1.20.** (A) Steps involved in multicomponent metallic patterns. (B and C) Show SEM images of BCP films and initial Pt nanowire fabrication. (D and E) SEM images of BCP nanodot film on Pt metallic lines, followed by Pd dot formation between metallic lines. (F and G) EDS elemental mapping of metallic nanodot and nanowire patterns. (H and I) SEM images of Pt-Pd nanowire arrays and Au-Pt nanodot arrays. Images reproduced from reference 120.

Note that reports for metallization have used  $O_2$  plasma treatment after metal uptake for removal of polymer matrices to position nanometallic features at substrate surfaces. Thermal annealing, ultraviolet/ozone exposure and solution based (*e.g.* selective solvent sonication or short piranha treatments) could also be used effectively to eliminate PS or polymer matrix material. Aqueous metal reduction was also employed to fabricate dimensionally controlled single crystalline intermetallic nanoalloys such as Fe-Co.<sup>122</sup> The synergistic properties enabled accelerated growth of vertical CNTs. The methodology presented highlighted the precision and accuracy that BCP formation coupled with aqueous metal reduction can allow surpassing problematic nucleation, particle agglomeration or growth kinetic issues of other synthetic procedures. In 2015,

the methodology was utilized for a cylinder PS-*b*-PEO BCP forming TiO<sub>2</sub> structures for photocatalytic degradation of methylene blue dye.<sup>138</sup> AMR has similar features of metal-salt inclusion described in 1.7 however AMR is dictated by chemical interactions that need to be tailored. Metal-salt inclusion largely relies on capillary forces (physical) to replicate BCP templates that have been “activated” and thus may be more useful for a broader range of BCP systems to attain good feature uniformity.

A report by Mun *et al.*<sup>123</sup> has also highlighted the significance of microdomain swelling and its’ effect on resulting structures. The authors used PS-*b*-P4VP thin films to create arrays of diverse patterns including Au nanorings, nanomeshes, and double nanowires. Through careful tuning of BCP film thickness, UV/O<sub>3</sub> etching, or O<sub>2</sub> plasma treatment structures were transformed from conventional dot and line patterns to the above mentioned diverse features as shown in Figure 1.21. The Au patterns were also investigated for their plasmonic properties. The work demonstrated robust patterning processes that can allow the fabrication of intricate metal patterns from simple BCP dot and line patterns.

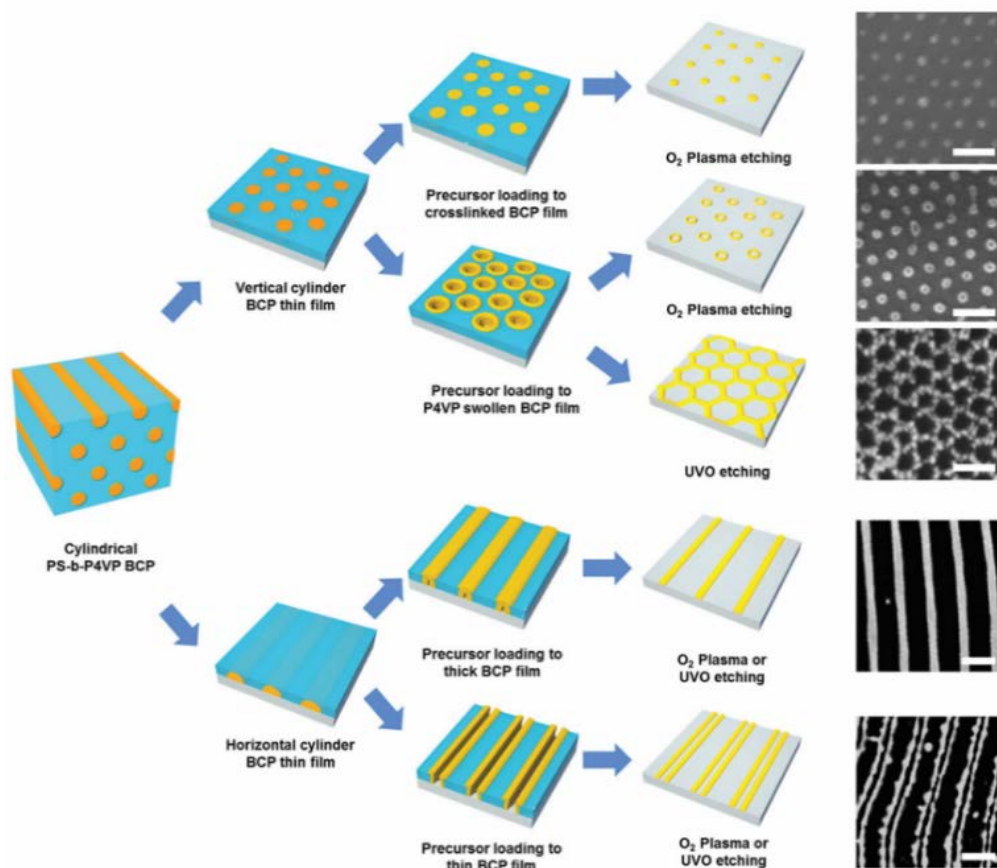


**Figure 1.21.** Schematic summarizing processes used to fabricate diverse Au patterns from dot and line orientation using a PS-*b*-P4VP BCP template. Top-down SEM images of resulting Au nanostructures are shown. Scale bars = 100 nm. Reproduced from reference 122.

### 1.9. Triblock polymers and inorganic incorporation

A linear tri-BCP is made up of three polymer blocks with a particular block repeated twice (*i.e.* A-B-A), while a tri-BTP consists of three distinct polymer segments covalently bonded together (*i.e.* A-B-C).<sup>139</sup> The generic term “tri-BP” is used in parts below for simplicity to refer to block polymers composed of three polymer blocks (A-B-A or A-B-C). Note that the terms tri-BCP and tri-BTP are often used interchangeably in the literature.

The bulk of this chapter has centered on work describing diblock copolymers as these dominate the literature. However more complex systems are receiving interest as they

allow more intricate morphologies and arrangements that could have a number of potential applications. Certainly, where more than one “reactive” block exists, there is the possibility of creating complex heterostructures or controlling *e.g.* feature spacing and arrangement beyond simple diblock limitations. Due to the resulting structural variations, tri-BP features modified via inorganic incorporation techniques outlined in this chapter may be worth serious consideration to open up diverse nano-applications beyond the scope of work reported hitherto on di-BCP systems. Although work is scarce in this area, it is highly worthwhile assessing the potential of these systems for creating inorganic material arrangements. Owing to the complexity of tri-BP features, the potential for sublithographic patterning also deserves attention as recently detailed in an article by de Pablo and co-workers.<sup>140</sup> This section of the chapter is not comprehensive (reflecting the extent of work), but rather provides the reader with an overview of tri-BPs ability to form tantalizing structural variations for nanotechnological uses.

Tri-BPs, both linear and non-linear (star, cyclic) forms can produce dozens of nanoscale architectures with complexity surpassing the basic geometries outlined for di-BCPs (A-B).<sup>141,142</sup> Tri-BPs easily allow square packed and core shell cylinder or sphere arrays that are ideal for bit patterned media application.<sup>143</sup> However, the microphase separation of tri-BTPs is also more complex than a simple di-BCP as three  $\chi$  factors must be considered, *i.e.*  $\chi_{AB}$ ,  $\chi_{BC}$  and  $\chi_{CA}$ . Similarly, three volume fractions contribute to resulting morphologies ( $f_a + f_b + f_c = 1$ ). Figure 1.22. displays and outlines the exotic morphologies possible via self-assembly of a tri-BTP.<sup>144</sup>

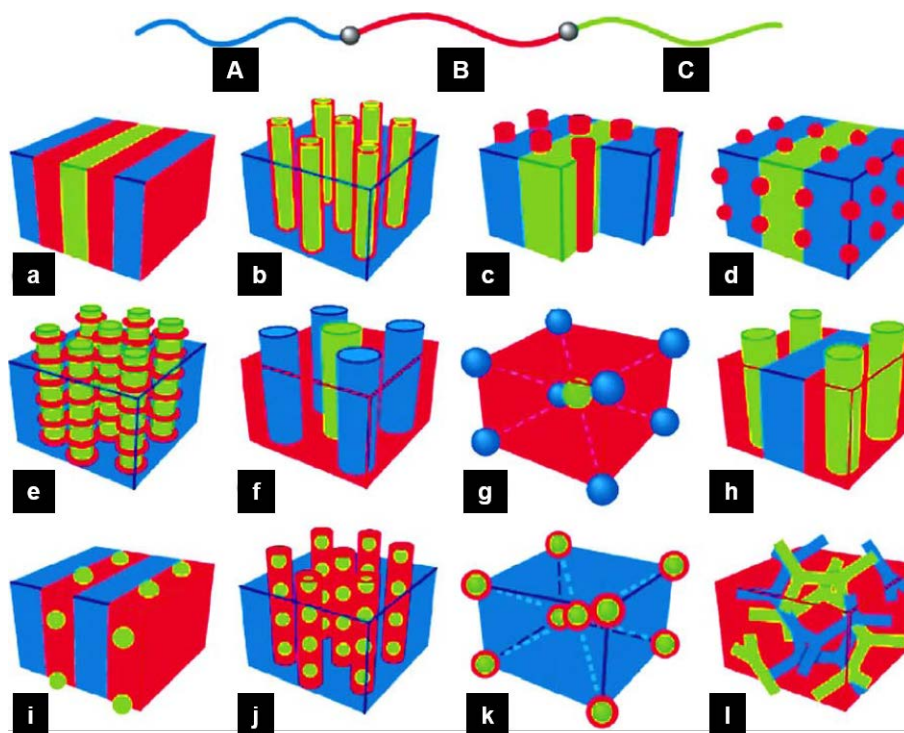


**Figure 1.22.** Schematics show some of the potential morphologies from a tri-block copolymer (A-B-C). Reproduced from reference 143.

Tri-BTPs share similar governing microphase separation criteria as di-BCPs as morphological structures (and dimensions) are dependent on temperature, block volume fraction and molecular weight. However, the order in which a tri-BTP is arranged (A-B-C or B-A-C or C-A-B) plays a crucial role in determining the morphological structure.<sup>145</sup>

Tri-BCPs have been well studied as structure directing agents since the early 1990's for mesoporous silica and aluminosilicate templating. Silica and aluminosilicate frames are of particular interest for uses centered on molecular separation, catalysis, and pollution remediation, amongst other functions.<sup>146</sup> In particular, a common industrial class of A-B-A type tri-BCPs under the trade name Pluronic® (BASF) BCPs have been widely established as structure directing agents owing to the materials amphiphilic nature in aqueous media. Also referred to as “polaxomers”, Pluronic tri-BCPs contain a middle

hydrophobic poly(propyleneoxide) block and hydrophilic polyethylene oxide (PEO) blocks at either side, *i.e.* PPO-*b*-PPE-*b*-PPO (see Figure 1.23.A). Pluronic's also gained interest for mesoporous material templating as shown in Figure 1.23.B owing to the ability for one to manipulate orientation and chain length and resulting channel size surpassing previous employed practices such as evaporation induced self-assembly (EISA).<sup>147</sup> Key reports by Stucky and co-workers outlined the manipulation of these low-cost surfactants for developing silica fibers with large pore sizes,<sup>148</sup> mesoporous silica,<sup>149</sup> and metal oxide frameworks.<sup>150,151</sup> Moreover, Pluronic ® BCPs have also been utilized extensively in gene therapy applications,<sup>152,153</sup> nanomedicine formulations and drug excipients,<sup>154,155</sup> and thermally responsive gels for protein and peptide delivery.<sup>156</sup> It should be noted that excellent work by the Wiesner and Steiner groups have demonstrated the efficacy of BPs (di- and tri-) and sol-gel chemistry as structure directing agents for functional applications, *e.g.* dye-sensitized solar cells, fuel cells and photonics. The applications will not be discussed in this chapter and readers are referred to relevant tutorial and review articles in references 157 and 158.

In more recent reports, evidence of employing tri-BPs beyond structure directing uses are apparent. Interesting, sophisticated and highly relevant device applicable structures are now evident. An early report from 2003 by Ludwigs *et al.*<sup>159</sup> showed the functional capability of a linear tri-BTP system, PS-*block*-P2VP-*block*-poly(*t*-butyl methacrylate) (PS-P2VP-PtBMA). Following solvent vapor annealing of PS-P2VP-PtBMA thin films, a perforated lamella structure within the thin film was obtained. An impressive degree of order was achieved for hexagonally packed dots as shown in Figure 1.23.D. The chemistry of this tri-BTP provided added functionality, as the PtBMA could be removed via UV exposure or could be altered through HCl treatment to form

poly(methacrylic acid) (PMAA). This report also commented on highly ordered pattern formation irrespective of substrate as confirmed by simulation data. This is an important point as this particular PS-P2VP-PtBMA tri-BCP avoided complex brush modifications unlike those required for di-BCP counterparts, *e.g.* PS-*b*-PMMA<sup>160</sup> or PS-*b*-PDMS<sup>161</sup>. In 2006, a report by Bang *et al.*,<sup>162</sup> demonstrated the possibility of A-B-C tri-BPs for high density patterning of defect-free porous films with cylinder diameters as small as 10 nm. The work documented the use of PEO-*b*-PMMA-*b*-PS following solvent vapor annealing. As outlined previously in this chapter, PMMA is extremely susceptible to UV degradation. The midblock of PMMA of PEO-*b*-PMMA-*b*-PS was removed using a brief UV exposure (see Figure 1.23.E). The report was a significant contribution to further extend the work on di-BCP systems. The PEO-*b*-PMMA-*b*-PS tri-BTP effectively surpassed the poor degradability of PS-*b*-PEO BCPs (ethanol exposure has since circumvented this limitation as described herein) while extending long range order that is difficult to attain solely with PS-*b*-PMMA BCP systems. Other tri-BPs of note include those studied by Epps and co-workers focusing on solvent vapor anneal effects in PdS-*b*-PI-*b*-PdS (d = deuterated) films<sup>163</sup>, phase changes due to partial hydrogenation in a PI-*b*-PS-*b*-PMMA system<sup>164</sup>, and the precise placement of gold nanoparticle location in well-ordered PS-*b*-PI-*b*-PS patterns<sup>165</sup>. An endless range of architectures are possible beyond di- and tri-BPs, and recently multiblocks have been suggested to open a “Pandora’s box” of design space by virtue of synthetic polymer advances.<sup>166</sup>

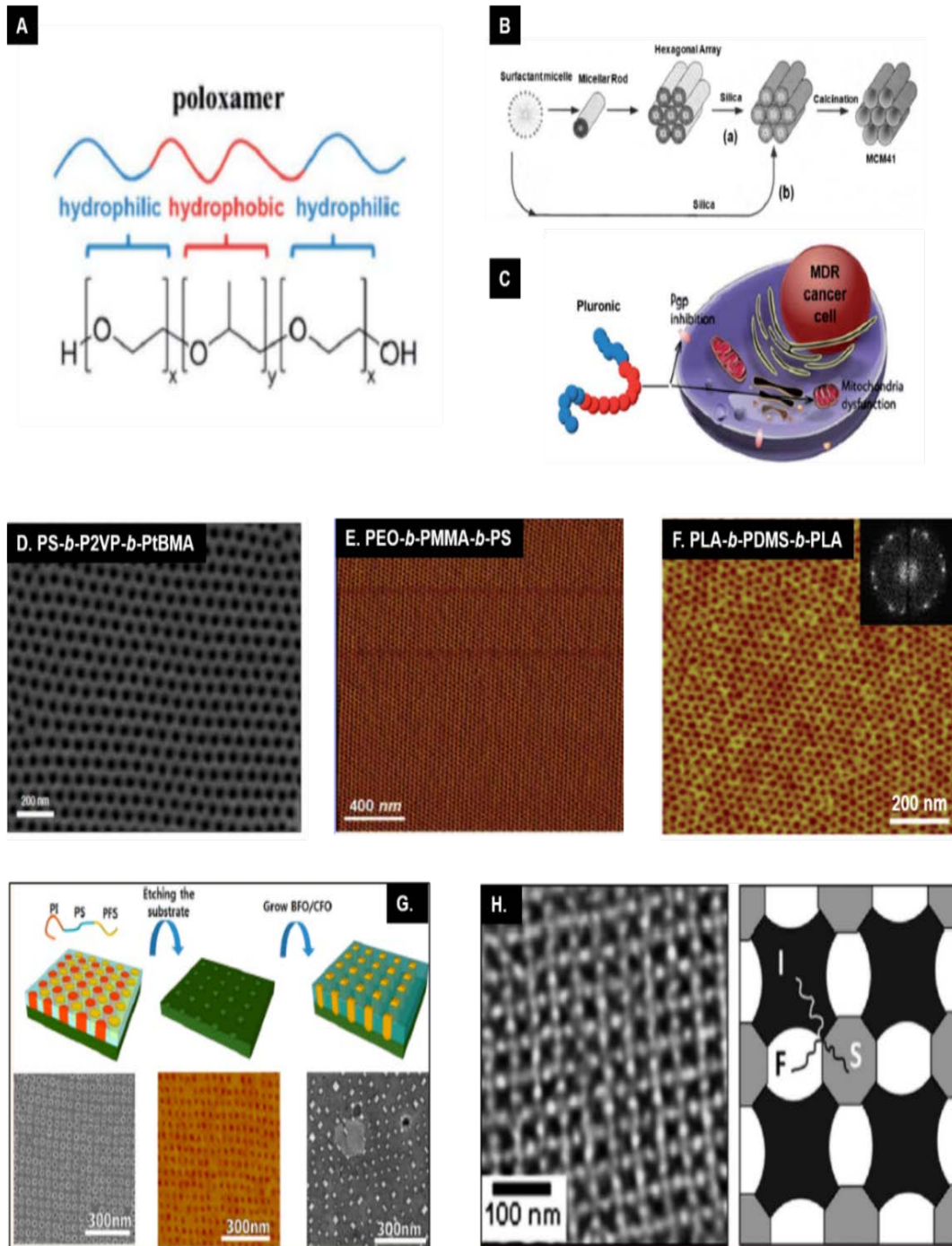


**Figure 1.23.** (A). Chemical structure of PEO-*b*-PPO-*b*-PEO tri-BCP. See text for further details. (B). Synthesis route using Pluronic species for inorganic framework.<sup>167</sup> (C). Bio-application of Pluronic BCP for nanomedicine. Well defined nanodot patterns from PS-*b*-P2VP-*b*-PtBMA (D), PEO-*b*-PMMA-*b*-PS (E), and PLA-*b*-PDMS-*b*-PLA (F). (G) Multiferroic composite growth based on PI-*b*-PS-*b*-PFS, see text for details. (H) SEM image of Archimedean tiling pattern formed through a miktoarm star terpolymer PI-arm-PS-arm-PFS and schematic representation. Images reproduced from reference 155 (A and C), 157 (D), 162 (E), 168 (F), 174 (G), and 176(H).

Publications by Hillmyer and co-workers have illustrated the potential functional capacity of PLA containing tri-BPs with examples for nanolithographic application (using PLA-*b*-PDMS-*b*-PLA<sup>168</sup> - see Figure 1.23.F, and PS-*b*-PI-*b*-PLA<sup>169</sup>), ultrafiltration membranes (using PS-*b*-PI-*b*-PLA<sup>170</sup>), porous linear polyethylene channels (using PLA-*b*-LPE-*b*-PLA<sup>171</sup>), and poly(acrylic acid) coated PS channels (using PS-*b*-PDMA-*b*-PLA<sup>172</sup>). The molecular design routes generated added functionality to basic polymer blocks that can possibly address various membrane and separation science technological challenges. Additionally, the BPs developed with rapidly degradable PLA components combined with the incorporation methods outlined in this chapter could lead to intricate hybrid materials for alternative device uses.

Likewise, Manners, Ross, and co-workers have explored tri-BTPs and miktoarm polymers for etch mask applications and functional use. In 2009, the synthesis and self-assembly of a new tri-BTP was described for developing nanoscale ring patterns.<sup>173</sup> After solvent vapor annealing of a PS-*b*-polyferrocenylsilane-*b*-P2VP (PS-*b*-PFS-*b*-P2VP) BTP, a PS core and PFS shell in a P2VP matrix was developed. PFS, an iron and silicon containing moiety, is particularly useful as a BP component due to its resistance to dry etching. The authors reported the use of PS and P2VP etched films forming robust PFS ring arrays that were subsequently used as lithographic templates for transferring to a PS polymer layer via imprinting. Another work involving a PFS containing tri-BTP, PI-*b*-PS-*b*-PFS, was employed for patterning pits in a Nb-doped SrTiO<sub>3</sub> substrate.<sup>174</sup> These square symmetry pits (period ~ 44 nm) were utilized for nanocomposite growth and fabrication of multiferroic BiFeO<sub>3</sub>-CoFe<sub>2</sub>O<sub>4</sub> material (see Figure 1.23.G). The PI-*b*-PS-*b*-PFS system has also been demonstrated forming square arrays of dot and hole patterns along with combinations of both.<sup>175</sup> More exotic BP

materials including a miktoarm star terpolymer PI-arm-PS-arm-PFS blended with a homopolymer have been explored for patterning Archimedean tilings (see Figure 1.23.H) for nanolithographic application and DSA application.<sup>176,177</sup> The works illustrated a gallery of fascinating structural variations which could potentially be used beyond etch mask applications.

Many of the tri-BP systems mentioned above contain a reactive block like PEO, PI and PVP, or an easily etched block such as PMMA or PLA, all of which can be infiltrated. Such desirable chemical attributes in tri-BP systems further the potential to access bimetallic or trimetallic hybrid systems using innovative incorporation techniques. Additionally, metal containing BPs like PFS systems could easily be altered post self-assembly to add another metal component. Thus far, works on such systems to incorporate further inorganic material are scarce and could enable multi-functionality beyond simple di-BCP arrays.

### **1.10. Summary and Outlook**

Microphase separated BCP films are well-established templates for pattern formation at the nanoscale and have been studied as potential on-chip etch masks for next-generation electronic devices. We have highlighted recent reports that have emerged on BCP film formation for incorporating inorganic material for on-chip etch mask and other functional use. Importantly, the densities and coverages accessible with BCP templates make them a unique a self-assembling material for device fabrication. Whilst many milestones have been achieved, the work to realize non-electronic applications is very much in its' infancy and thus provides scope for further improvement and discovery.

Evaporation and sputtering methods outlined in Section 1.4. have proven quite fruitful for proof of concept in early work on the positional accuracy and manipulation of inorganic material on slight modifications (minor block etching, swelling) of neat BCP templates. It appears that evaporation (thermal or e-beam) and radio frequency sputtering are quite amenable to BCP templates and industrial fabrication processes as high temperatures are not necessary limiting potential damage to BCP morphologies or device performance issues.

The successive sections largely detailed the more recent reports of inorganic inclusion at the nanoscale utilizing BCPs. Many approaches have been employed illustrating the diverse nature and ability of BCPs to incorporate functional material after self-assembly. Interestingly, growth sites (SIS), “activation” (metal-salt inclusion), and acidic media (aqueous metal reduction) have been employed as ways to enhance uptake and overall uniformity for inorganic inclusion. Pattern transfer of high fidelity structures has not been demonstrated with evaporation/sputtering or aqueous metal reduction methods. In contrast, ALD, SIS and metal-salt inclusion practices provide routes for reproducibly generating high-fidelity nanostructures for on-chip etch mask application and therefore one would assume will lead the way for device integration.

The deeper understanding of BCP self-assembly has led to many improvements where microdomains can be dictated and aligned over large scale areas. In the more recent studies (< 5 years) discussed above, one observes a distinct enhancement in BCP ordering and orientation using higher  $\chi$  BCP materials such as PS-P<sub>x</sub>VP (x = 2 or 4), PS-*b*-PDMS and PS-*b*-PLA compared to the low  $\chi$  PS-*b*-PMMA. BCP nanopattern improvements are primarily related to high  $\chi$  factor as line edge roughness is reduced

and microphase separation is more likely to occur. Additionally, knowledge of influencing BCP environmental and processing conditions is continually evolving and more sophisticated annealing protocols are being implemented achieving ultra-fast processing periods (sub-1 minute)<sup>178-180</sup> whilst still retaining superb pattern ordering. Such milestones on BCP control coupled with inorganic infiltration techniques only further enhance the viability of BCP nanopatterning for application in electronic and non-electronic based technologies.

### 1.11. References

- (1) Farrell, R. A.; Fitzgerald, T. G.; Borah, D.; Holmes, J. D.; Morris, M. A. Chemical Interactions and Their Role in the Microphase Separation of Block Copolymer Thin Films. *International Journal of Molecular Sciences* **2009**, *10*, 3671-3712.
- (2) Hadjichristidis, N.; Pitsikalis, M.; Iatrou, H.: Synthesis of block copolymers. In *Block Copolymers I*; Abetz, V., Ed.; Advances in Polymer Science, 2005; Vol. 189; pp 1-124.
- (3) Arslan, H.: *Block and Graft Copolymerization by Controlled/Living Radical Polymerization Methods*, 2012.
- (4) Keddie, D. J. A guide to the synthesis of block copolymers using reversible-addition fragmentation chain transfer (RAFT) polymerization. *Chemical Society Reviews* **2014**, *43*, 496-505.
- (5) Bates, F. S.; Fredrickson, G. H. Block Copolymer Thermodynamics - Theory and Experiment. *Annual Review of Physical Chemistry* **1990**, *41*, 525-557.
- (6) Fasolka, M. J.; Mayes, A. M. Block copolymer thin films: Physics and applications. *Annual Review of Materials Science* **2001**, *31*, 323-355.
- (7) Krishnamoorthy, S.; Hinderling, C.; Heinzlmann, H. Nanoscale patterning with block copolymers. *Materials Today* **2006**, *9*, 40-47.
- (8) Albert, J. N. L.; Epps III, T. H. Self-assembly of block copolymer thin films. *Materials Today* **2010**, *13*, 24-33.
- (9) Kim, H. C.; Park, S. M.; Hinsberg, W. D.; Division, I. R. Block copolymer based nanostructures: Materials, processes, and applications to electronics. *Chemical Reviews* **2010**, *110*, 146-177.
- (10) Kim, B. H.; Kim, J. Y.; Kim, S. O. Directed self-assembly of block copolymers for universal nanopatterning. *Soft Matter* **2013**, *9*, 2780-2786.
- (11) Luo, M.; Epps, T. H. Directed Block Copolymer Thin Film Self-Assembly: Emerging Trends in Nanopattern Fabrication. *Macromolecules* **2013**, *46*, 7567-7579.
- (12) Koo, K.; Ahn, H.; Kim, S.-W.; Ryu, D. Y.; Russell, T. P. Directed self-assembly of block copolymers in the extreme: guiding microdomains from the small to the large. *Soft Matter* **2013**, *9*, 9059-9071.
- (13) Hu, H.; Gopinadhan, M.; Osuji, C. O. Directed self-assembly of block copolymers: a tutorial review of strategies for enabling nanotechnology with soft matter. *Soft Matter* **2014**, *10*, 3867-3889.

- (14) Schacher, F. H.; Rugar, P. A.; Manners, I. Functional block copolymers: Nanostructured materials with emerging applications. *Angewandte Chemie - International Edition* **2012**, *51*, 7898-7921.
- (15) Botiz, I.; Darling, S. B. Optoelectronics using block copolymers. *Materials Today* **2010**, *13*, 42-51.
- (16) Park, C.; Yoon, J.; Thomas, E. L. Enabling nanotechnology with self assembled block copolymer patterns. *Polymer* **2003**, *44*, 6725-6760.
- (17) Lodge, T. P. Block copolymers: Past successes and future challenges. *Macromolecular Chemistry and Physics* **2003**, *204*, 265-273.
- (18) Segalman, R. A. Patterning with block copolymer thin films. *Materials Science & Engineering R-Reports* **2005**, *48*, 191-226.
- (19) Thompson, S. E.; Parthasarathy, S. Moore's law: the future of Si microelectronics. *Materials Today* **2006**, *9*, 20-25.
- (20) Hawker, C. J.; Russell, T. P. Block copolymer lithography: Merging "bottom-up" with "top-down" processes. *MRS Bulletin* **2005**, *30*, 952-966.
- (21) Darling, S. B. Directing the self-assembly of block copolymers. *Progress in Polymer Science* **2007**, *32*, 1152-1204.
- (22) Ross, C. A.; Cheng, J. Y. Patterned magnetic media made by self-assembled block-copolymer lithography. *MRS Bulletin* **2008**, *33*, 838-845.
- (23) Jeong, S.-J.; Kim, J. Y.; Kim, B. H.; Moon, H.-S.; Kim, S. O. Directed self-assembly of block copolymers for next generation nanolithography. *Materials Today* **2013**, *16*, 468-476.
- (24) Morris, M. A. Directed self-assembly of block copolymers for nanocircuitry fabrication. *Microelectronic Engineering* **2015**, *132*, 207-217.
- (25) Moore, G. E. Cramming More Components onto Integrated Circuits. *Electronics* **1965**, *38*, 114-117.
- (26) Tsai, H.; Pitera, J. W.; Miyazoe, H.; Bangsaruntip, S.; Engelmann, S. U.; Liu, C.-C.; Cheng, J. Y.; Bucchignano, J. J.; Klaus, D. P.; Joseph, E. A.; Sanders, D. P.; Colburn, M. E.; Guillorn, M. A. Two-Dimensional Pattern Formation Using Graphoepitaxy of PS-*b*-PMMA Block Copolymers for Advanced FinFET Device and Circuit Fabrication. *ACS Nano* **2014**, *8*, 5227-5232.
- (27) Jeong, S.-J.; Kim, S. O. Ultralarge-area block copolymer lithography via soft graphoepitaxy. *Journal of Materials Chemistry* **2011**, *21*, 5856-5859.
- (28) Stoykovich, M. P.; Müller, M.; Kim, S. O.; Solak, H. H.; Edwards, E. W.; De Pablo, J. J.; Nealey, P. F. Materials Science: Directed assembly of block copolymer blends into nonregular device-oriented structures. *Science* **2005**, *308*, 1442-1446.
- (29) Gu, X.; Gunkel, I.; Russell, T. P. Pattern transfer using block copolymers. *Philosophical Transactions of the Royal Society A: Mathematical, Physical and Engineering Sciences* **2013**, *371*.
- (30) Ramanathan, M.; Tseng, Y.-C.; Ariga, K.; Darling, S. B. Emerging trends in metal-containing block copolymers: synthesis, self-assembly, and nanomanufacturing applications. *Journal of Materials Chemistry C* **2013**, *1*, 2080-2091.
- (31) Nunns, A.; Gwyther, J.; Manners, I. Inorganic block copolymer lithography. *Polymer* **2013**, *54*, 1269-1284.
- (32) Mai, Y.; Eisenberg, A. Self-assembly of block copolymers. *Chemical Society Reviews* **2012**, *41*, 5969-5985.
- (33) Sinturel, C.; Vayer, M.; Morris, M.; Hillmyer, M. A. Solvent Vapor Annealing of Block Polymer Thin Films. *Macromolecules* **2013**, *46*, 5399-5415.
- (34) Bates, C. M.; Maher, M. J.; Janes, D. W.; Ellison, C. J.; Willson, C. G. Block Copolymer Lithography. *Macromolecules* **2013**, *47*, 2-12.

- (35) Ross, C. A.; Berggren, K. K.; Cheng, J. Y.; Jung, Y. S.; Chang, J.-B. Three-Dimensional Nanofabrication by Block Copolymer Self-Assembly. *Advanced Materials* **2014**, *26*, 4386-4396.
- (36) Park, M.; Chaikin, P. M.; Register, R. A.; Adamson, D. H. Large area dense nanoscale patterning of arbitrary surfaces. *Applied Physics Letters* **2001**, *79*, 257-259.
- (37) Park, M.; Harrison, C.; Chaikin, P. M.; Register, R. A.; Adamson, D. H. Block Copolymer Lithography: Periodic Arrays of  $\sim 10^{11}$  Holes in 1 Square Centimeter. *Science* **1997**, *276*, 1401-1404.
- (38) Mansky, P.; Chaikin, P.; Thomas, E. L. Monolayer films of diblock copolymer microdomains for nanolithographic applications. *Journal of Materials Science* **1995**, *30*, 1987-1992.
- (39) Mansky, P.; Harrison, C. K.; Chaikin, P. M.; Register, R. A.; Yao, N. Nanolithographic templates from diblock copolymer thin films. *Applied Physics Letters* **1996**, *68*, 2586-2588.
- (40) Guarini, K. W.; Black, C. T.; Milkove, K. R.; Sandstrom, R. L. Nanoscale patterning using self-assembled polymers for semiconductor applications. *Journal of Vacuum Science & Technology B* **2001**, *19*, 2784-2788.
- (41) Black, C. T.; Guarini, K. W.; Milkove, K. R.; Baker, S. M.; Russell, T. P.; Tuominen, M. T. Integration of self-assembled diblock copolymers for semiconductor capacitor fabrication. *Applied Physics Letters* **2001**, *79*, 409-411.
- (42) Shin, K.; Leach, K. A.; Goldbach, J. T.; Kim, D. H.; Jho, J. Y.; Tuominen, M.; Hawker, C. J.; Russell, T. P. A simple route to metal nanodots and nanoporous metal films. *Nano Letters* **2002**, *2*, 933-936.
- (43) Xiao, S. G.; Yang, X. M.; Edwards, E. W.; La, Y. H.; Nealey, P. F. Graphoepitaxy of cylinder-forming block copolymers for use as templates to pattern magnetic metal dot arrays. *Nanotechnology* **2005**, *16*, S324-S329.
- (44) Gowrishankar, V.; Miller, N.; McGehee, M. D.; Misner, M. J.; Ryu, D. Y.; Russell, T. P.; Drockenmuller, E.; Hawker, C. J. Fabrication of densely packed, well-ordered, high-aspect-ratio silicon nanopillars over large areas using block copolymer lithography. *Thin Solid Films* **2006**, *513*, 289-294.
- (45) Danilo, Z.; Dong Ha, K.; Alexey, P. M.; Sigrid, H.; Roland, S.; Petra, G.; Reinald, H.; Stephan, S.; Craig, J. H.; Thomas, P. R.; Martin, S.; Ulrich, G. High-temperature resistant, ordered gold nanoparticle arrays. *Nanotechnology* **2006**, *17*, 2122.
- (46) Deepak, K. S.; Robert, V. K.; Hongqi, X.; Ting, X.; Thomas, P. R.; Mark, T. T. Arrays of ultrasmall metal rings. *Nanotechnology* **2008**, *19*, 245305.
- (47) Park, S.; Kim, B.; Cirpan, A.; Russell, T. P. Preparation of Metallic Line Patterns from Functional Block Copolymers. *Small* **2009**, *5*, 1343-1348.
- (48) Lee, D. H.; Shin, D. O.; Lee, W. J.; Kim, S. O. Hierarchically Organized Carbon Nanotube Arrays from Self-Assembled Block Copolymer Nanotemplates. *Advanced Materials* **2008**, *20*, 2480-2485.
- (49) Jeong, S.-J.; Kim, J. E.; Moon, H.-S.; Kim, B. H.; Kim, S. M.; Kim, J. B.; Kim, S. O. Soft Graphoepitaxy of Block Copolymer Assembly with Disposable Photoresist Confinement. *Nano Letters* **2009**, *9*, 2300-2305.
- (50) Jeong, S.-J.; Moon, H.-S.; Shin, J.; Kim, B. H.; Shin, D. O.; Kim, J. Y.; Lee, Y.-H.; Kim, J. U.; Kim, S. O. One-Dimensional Metal Nanowire Assembly via Block Copolymer Soft Graphoepitaxy. *Nano Letters* **2010**, *10*, 3500-3505.
- (51) Choi, J. W.; Kim, M.; Safron, N. S.; Arnold, M. S.; Gopalan, P. Transfer of Pre-Assembled Block Copolymer Thin Film to Nanopattern Unconventional Substrates. *ACS Applied Materials & Interfaces* **2014**, *6*, 9442-9448.

- (52) Pellegrino, P.; Perego, M.; Schamm-Chardon, S.; Seguini, G.; Andreozzi, A.; Lupi, F. F.; Castro, C.; Assayag, G. B. Fabrication of well-ordered arrays of silicon nanocrystals using a block copolymer mask. *physica status solidi (a)* **2013**, *210*, 1477-1484.
- (53) Rasappa, S.; Borah, D.; Senthamaraiannan, R.; Faulkner, C. C.; Wang, J. J.; Holmes, J. D.; Morris, M. A. Fabrication of Germanium Nanowire Arrays by Block Copolymer Lithography. *Science of Advanced Materials* **2013**, *5*, 782-787.
- (54) Darling, S. B.; Hoffmann, A. Tuning metal surface diffusion on diblock copolymer films. *Journal of Vacuum Science & Technology A* **2007**, *25*, 1048-1051.
- (55) Kreuzer, M.; Simão, C.; Diaz, A.; Sotomayor Torres, C. M. Formation of Titanium Nanostructures on Block Copolymer Templates with Varying Molecular Weights. *Macromolecules* **2014**, *47*, 8691-8699.
- (56) Park, S.; Wang, J.-Y.; Kim, B.; Russell, T. P. From Nanorings to Nanodots by Patterning with Block Copolymers. *Nano Letters* **2008**, *8*, 1667-1672.
- (57) Hong, A. J.; Liu, C.-C.; Wang, Y.; Kim, J.; Xiu, F.; Ji, S.; Zou, J.; Nealey, P. F.; Wang, K. L. Metal Nanodot Memory by Self-Assembled Block Copolymer Lift-Off. *Nano Letters* **2010**, *10*, 224-229.
- (58) Baruth, A.; Seo, M.; Lin, C. H.; Walster, K.; Shankar, A.; Hillmyer, M. A.; Leighton, C. Optimization of Long-Range Order in Solvent Vapor Annealed Poly(styrene)-*block*-poly(lactide) Thin Films for Nanolithography. *ACS Applied Materials & Interfaces* **2014**.
- (59) Gu, X.; Dorsey, P.; Russell, T. P. High density and large area arrays of silicon oxide pillars with tunable domain size for mask etch applications. *Advanced Materials* **2012**, *24*, 5505-5511.
- (60) Son, J. G.; Gotrik, K. W.; Ross, C. A. High-Aspect-Ratio Perpendicular Orientation of PS-*b*-PDMS Thin Films under Solvent Annealing. *ACS Macro Letters* **2012**, *1*, 1279-1284.
- (61) Huda, M.; Liu, J.; Yin, Y.; Hosaka, S. Fabrication of 5-nm-sized nanodots using self-assembly of polystyrene-poly(dimethylsiloxane). *Japanese Journal of Applied Physics* **2012**, *51*.
- (62) Gu, W.; Xu, J.; Kim, J.-K.; Hong, S. W.; Wei, X.; Yang, X.; Lee, K. Y.; Kuo, D. S.; Xiao, S.; Russell, T. P. Solvent-Assisted Directed Self-Assembly of Spherical Microdomain Block Copolymers to High Areal Density Arrays. *Advanced Materials* **2013**, *25*, 3677-3682.
- (63) Hosaka, S.; Akahane, T.; Huda, M.; Zhang, H.; Yin, Y. Controlling of 6 nm Sized and 10 nm Pitched Dot Arrays Ordered along Narrow Guide Lines Using PS-PDMS Self-Assembly. *ACS Applied Materials & Interfaces* **2014**.
- (64) Kim, D.; Jeon, S.-B.; Kim, J. Y.; Seol, M.-L.; Kim, S. O.; Choi, Y.-K. High-performance nanopattern triboelectric generator by block copolymer lithography. *Nano Energy* **2015**, *12*, 331-338.
- (65) Frascaroli, J.; Brivio, S.; Ferrarese Lupi, F.; Seguini, G.; Boarino, L.; Perego, M.; Spiga, S. Resistive Switching in High-Density Nanodevices Fabricated by Block Copolymer Self-Assembly. *ACS Nano* **2015**, *9*, 2518-2529.
- (66) Jung, Y. S.; Lee, J. H.; Lee, J. Y.; Ross, C. A. Fabrication of Diverse Metallic Nanowire Arrays Based on Block Copolymer Self-Assembly. *Nano Letters* **2010**, *10*, 3722-3726.
- (67) Jung, Y. S.; Chang, J. B.; Verploegen, E.; Berggren, K. K.; Ross, C. A. A Path to Ultranarrow Patterns Using Self-Assembled Lithography. *Nano Letters* **2010**, *10*, 1000-1005.

- (68) Jung, Y. S.; Ross, C. A. Well-Ordered Thin-Film Nanopore Arrays Formed Using a Block-Copolymer Template. *Small* **2009**, *5*, 1654-1659.
- (69) Baruth, A.; Rodwogin, M. D.; Shankar, A.; Erickson, M. J.; Hillmyer, M. A.; Leighton, C. Non-lift-off Block Copolymer Lithography of 25 nm Magnetic Nanodot Arrays. *ACS Applied Materials & Interfaces* **2011**, *3*, 3472-3481.
- (70) Mackus, A. J. M.; Bol, A. A.; Kessels, W. M. M. The use of atomic layer deposition in advanced nanopatterning. *Nanoscale* **2014**, *6*, 10941-10960.
- (71) Suresh, V.; Huang, M. S.; Srinivasan, M. P.; Krishnamoorthy, S. In Situ Synthesis of High Density sub-50 nm ZnO Nanopatterned Arrays Using Diblock Copolymer Templates. *ACS Applied Materials & Interfaces* **2013**, *5*, 5727-5732.
- (72) Wang, Y.; Qin, Y.; Berger, A.; Yau, E.; He, C.; Zhang, L.; Gösele, U.; Knez, M.; Steinhart, M. Nanoscopic Morphologies in Block Copolymer Nanorods as Templates for Atomic-Layer Deposition of Semiconductors. *Advanced Materials* **2009**, *21*, 2763-2766.
- (73) Moon, H.-S.; Kim, J. Y.; Jin, H. M.; Lee, W. J.; Choi, H. J.; Mun, J. H.; Choi, Y. J.; Cha, S. K.; Kwon, S. H.; Kim, S. O. Atomic Layer Deposition Assisted Pattern Multiplication of Block Copolymer Lithography for 5 nm Scale Nanopatterning. *Advanced Functional Materials* **2014**, *24*, 4343-4348.
- (74) Gay, G.; Baron, T.; Agrafeil, C.; Salhi, B.; Chevolleau, T.; Cunge, G.; Grampeix, H.; Tortai, J. H.; Martin, F.; Jalaguier, E.; Salvo, B. D. CMOS compatible strategy based on selective atomic layer deposition of a hard mask for transferring block copolymer lithography patterns. *Nanotechnology* **2010**, *21*, 435301.
- (75) Tallegas, S.; Baron, T.; Gay, G.; Agrafeil, C.; Salhi, B.; Chevolleau, T.; Cunge, G.; Bsiesy, A.; Tiron, R.; Chevalier, X.; Navarro, C.; Aissou, K.; Otsuka, I.; Halila, S.; Fort, S.; Borsali, R. Block copolymer technology applied to nanoelectronics. *physica status solidi (c)* **2013**, *10*, 1195-1206.
- (76) Hägglund, C.; Zeltzer, G.; Ruiz, R.; Thomann, I.; Lee, H.-B.-R.; Brongersma, M. L.; Bent, S. F. Self-Assembly Based Plasmonic Arrays Tuned by Atomic Layer Deposition for Extreme Visible Light Absorption. *Nano Letters* **2013**, *13*, 3352-3357.
- (77) Yin, J.; Yao, X.; Liou, J.-Y.; Sun, W.; Sun, Y.-S.; Wang, Y. Membranes with Highly Ordered Straight Nanopores by Selective Swelling of Fast Perpendicularly Aligned Block Copolymers. *ACS Nano* **2013**, *7*, 9961-9974.
- (78) Yang, J.; Tong, L.; Yang, Y.; Chen, X.; Huang, J.; Chen, R.; Wang, Y. Selective-swelling-induced porous block copolymers and their robust TiO<sub>2</sub> replicas via atomic layer deposition for antireflective applications. *Journal of Materials Chemistry C* **2013**, *1*, 5133-5141.
- (79) Li, F.; Yao, X.; Wang, Z.; Xing, W.; Jin, W.; Huang, J.; Wang, Y. Highly Porous Metal Oxide Networks of Interconnected Nanotubes by Atomic Layer Deposition. *Nano Letters* **2012**, *12*, 5033-5038.
- (80) Kim, S. M.; Ku, S. J.; Jo, G. C.; Bak, C. H.; Kim, J.-B. Fabrication of versatile nanoporous templates with high aspect ratios by incorporation of Si-containing block copolymer into the lithographic bilayer system. *Polymer* **2012**, *53*, 2283-2289.
- (81) Se Jin, K.; Gyeong Cheon, J.; Chang Hong, B.; Su Min, K.; Yu Ri, S.; Kwang Ho, K.; Se Hun, K.; Jin-Baek, K. Highly ordered freestanding titanium oxide nanotube arrays using Si-containing block copolymer lithography and atomic layer deposition. *Nanotechnology* **2013**, *24*, 085301.
- (82) Schelhas, L. T.; Farrell, R. A.; Halim, U.; Tolbert, S. H. Directed Self-Assembly as a Route to Ferromagnetic and Superparamagnetic Nanoparticle Arrays. *Advanced Functional Materials* **2014**, *24*, 6956-6962.

- (83) She, M.-S.; Lo, T.-Y.; Hsueh, H.-Y.; Ho, R.-M. Nanostructured thin films of degradable block copolymers and their applications. *NPG Asia Mater* **2013**, *5*, e42.
- (84) Hsueh, H.-Y.; Chen, H.-Y.; She, M.-S.; Chen, C.-K.; Ho, R.-M.; Gwo, S.; Hasegawa, H.; Thomas, E. L. Inorganic Gyroid with Exceptionally Low Refractive Index from Block Copolymer Templating. *Nano Letters* **2010**, *10*, 4994-5000.
- (85) Lee, H.-C.; Hsueh, H.-Y.; Jeng, U. S.; Ho, R.-M. Functionalized Nanoporous Gyroid SiO<sub>2</sub> with Double-Stimuli-Responsive Properties as Environment-Selective Delivery Systems. *Macromolecules* **2014**, *47*, 3041-3051.
- (86) Wang, H.-F.; Yu, L.-H.; Wang, X.-B.; Ho, R.-M. A Facile Method To Fabricate Double Gyroid as a Polymer Template for Nanohybrids. *Macromolecules* **2014**, *47*, 7993-8001.
- (87) Hsueh, H.-Y.; Ho, R.-M. Bicontinuous Ceramics with High Surface Area from Block Copolymer Templates. *Langmuir* **2012**, *28*, 8518-8529.
- (88) Hsueh, H.-Y.; Yao, C.-T.; Ho, R.-M. Well-ordered nanohybrids and nanoporous materials from gyroid block copolymer templates. *Chemical Society Reviews* **2015**.
- (89) Lin, C.-H.; Polisetty, S.; O'Brien, L.; Baruth, A.; Hillmyer, M. A.; Leighton, C.; Gladfelter, W. L. Size-Tuned ZnO Nanocrucible Arrays for Magnetic Nanodot Synthesis via Atomic Layer Deposition-Assisted Block Polymer Lithography. *ACS Nano* **2015**, *9*, 1379-1387.
- (90) Peng, Q.; Tseng, Y.-C.; Darling, S. B.; Elam, J. W. Nanoscopic Patterned Materials with Tunable Dimensions via Atomic Layer Deposition on Block Copolymers. *Advanced Materials* **2010**, *22*, 5129-5133.
- (91) Peng, Q.; Tseng, Y.-C.; Darling, S. B.; Elam, J. W. A Route to Nanoscopic Materials via Sequential Infiltration Synthesis on Block Copolymer Templates. *ACS Nano* **2011**, *5*, 4600-4606.
- (92) Tseng, Y.-C.; Peng, Q.; Ocola, L. E.; Elam, J. W.; Darling, S. B. Enhanced Block Copolymer Lithography Using Sequential Infiltration Synthesis. *The Journal of Physical Chemistry C* **2011**, *115*, 17725-17729.
- (93) Johnston, D. E.; Lu, M.; Black, C. T. Plasma etch transfer of self-assembled polymer patterns. *MOEMS* **2012**, *11*, 031306.
- (94) Ruiz, R.; Wan, L.; Lille, J.; Patel, K. C.; Dobisz, E.; Johnston, D. E.; Kisslinger, K.; Black, C. T. Image quality and pattern transfer in directed self assembly with block-selective atomic layer deposition. *Journal of Vacuum Science & Technology B* **2012**, *30*, 06F202.
- (95) Kamcev, J.; Germack, D. S.; Nykypanchuk, D.; Grubbs, R. B.; Nam, C.-Y.; Black, C. T. Chemically Enhancing Block Copolymers for Block-Selective Synthesis of Self-Assembled Metal Oxide Nanostructures. *ACS Nano* **2012**, *7*, 339-346.
- (96) Checco, A.; Rahman, A.; Black, C. T. Robust Superhydrophobicity in Large-Area Nanostructured Surfaces Defined by Block-Copolymer Self Assembly. *Advanced Materials* **2014**, *26*, 886-891.
- (97) Checco, A.; Ocko, B. M.; Rahman, A.; Black, C. T.; Tasinkevych, M.; Giacomello, A.; Dietrich, S. Collapse and Reversibility of the Superhydrophobic State on Nanotextured Surfaces. *Physical Review Letters* **2014**, *112*, 216101.
- (98) Rahman, A.; Liu, M.; Black, C. T. Block copolymer self assembly for design and vapor-phase synthesis of nanostructured antireflective surfaces. *Journal of Vacuum Science & Technology B* **2014**, *32*.
- (99) Rahman, A.; Black, C. T. Block Copolymer Self Assembly for Design and Vapor Phase Synthesis of One-Dimensional Nanostructured Materials. *Micro- and Nanotechnology Sensors, Systems, and Applications VI* **2014**, 9083.

- (100) Rahman, A.; Ashraf, A.; Xin, H.; Tong, X.; Sutter, P.; Eisaman, M. D.; Black, C. T. Sub-50-nm self-assembled nanotextures for enhanced broadband antireflection in silicon solar cells. *Nat Commun* **2015**, *6*.
- (101) Darling, S. B.; Yufa, N. A.; Cisse, A. L.; Bader, S. D.; Sibener, S. J. Self-Organization of FePt Nanoparticles on Photochemically Modified Diblock Copolymer Templates. *Advanced Materials* **2005**, *17*, 2446-2450.
- (102) Darling, S. B. Mechanism for hierarchical self-assembly of nanoparticles on scaffolds derived from block copolymers. *Surface Science* **2007**, *601*, 2555-2561.
- (103) Son, J. G.; Bae, W. K.; Kang, H.; Nealey, P. F.; Char, K. Placement Control of Nanomaterial Arrays on the Surface-Reconstructed Block Copolymer Thin Films. *ACS Nano* **2009**, *3*, 3927-3934.
- (104) Ghoshal, T.; Maity, T.; Godsell, J. F.; Roy, S.; Morris, M. A. Large Scale Monodisperse Hexagonal Arrays of Superparamagnetic Iron Oxides Nanodots: A Facile Block Copolymer Inclusion Method. *Advanced Materials* **2012**, *24*, 2390-2397.
- (105) Ghoshal, T.; Senthamaraiannan, R.; Shaw, M. T.; Holmes, J. D.; Morris, M. A. "In situ" hard mask materials: a new methodology for creation of vertical silicon nanopillar and nanowire arrays. *Nanoscale* **2012**, *4*, 7743-7750.
- (106) Ghoshal, T.; Maity, T.; Senthamaraiannan, R.; Shaw, M. T.; Carolan, P.; Holmes, J. D.; Roy, S.; Morris, M. A. Size and space controlled hexagonal arrays of superparamagnetic iron oxide nanodots: magnetic studies and application. *Scientific Reports* **2013**, *3*.
- (107) Ghoshal, T.; Shaw, M. T.; Bolger, C. T.; Holmes, J. D.; Morris, M. A. A general method for controlled nanopatterning of oxide dots: a microphase separated block copolymer platform. *Journal of Materials Chemistry* **2012**, *22*, 12083-12089.
- (108) Ghoshal, T.; Fleming, P. G.; Holmes, J. D.; Morris, M. A. The stability of "Ce<sub>2</sub>O<sub>3</sub>" nanodots in ambient conditions: a study using block copolymer templated structures. *Journal of Materials Chemistry* **2012**, *22*, 22949-22957.
- (109) Varghese, J.; Ghoshal, T.; Deepak, N.; O'Regan, C.; Whatmore, R. W.; Morris, M. A.; Holmes, J. D. Fabrication of Arrays of Lead Zirconate Titanate (PZT) Nanodots via Block Copolymer Self-Assembly. *Chemistry of Materials* **2013**, *25*, 1458-1463.
- (110) Azlin-Hasim, S.; Cruz-Romero, M. C.; Ghoshal, T.; Morris, M. A.; Cummins, E.; Kerry, J. P. Application of silver nanodots for potential use in antimicrobial packaging applications. *Innovative Food Science & Emerging Technologies* **2015**, *27*, 136-143.
- (111) Ghoshal, T.; Senthamaraiannan, R.; Shaw, M. T.; Holmes, J. D.; Morris, M. A. Fabrication of ordered, large scale, horizontally-aligned Si nanowire arrays based on an in situ hard mask block copolymer approach. *Advanced Materials* **2014**, *26*, 1207-1216.
- (112) Mokarian-Tabari, P.; Vallejo-Giraldo, C.; Fernandez-Yague, M.; Cummins, C.; Morris, M. A.; Biggs, M. J. P. Nanoscale neuroelectrode modification via sub-20 nm silicon nanowires through self-assembly of block copolymers. *Journal of Materials Science-Materials in Medicine* **2015**, *26*.
- (113) Chai, J.; Wang, D.; Fan, X.; Buriak, J. M. Assembly of aligned linear metallic patterns on silicon. *Nature Nanotechnology* **2007**, *2*, 500-506.
- (114) Chai, J.; Buriak, J. M. Using Cylindrical Domains of Block Copolymers To Self-Assemble and Align Metallic Nanowires. *ACS Nano* **2008**, *2*, 489-501.
- (115) Wu, N. L. Y.; Zhang, X.; Murphy, J. N.; Chai, J.; Harris, K. D.; Buriak, J. M. Density Doubling of Block Copolymer Templated Features. *Nano Letters* **2012**, *12*, 264-268.

- (116) Cummins, C.; Borah, D.; Rasappa, S.; Chaudhari, A.; Ghoshal, T.; O'Driscoll, B. M. D.; Carolan, P.; Petkov, N.; Holmes, J. D.; Morris, M. A. Self-assembly of polystyrene-*block*-poly(4-vinylpyridine) block copolymer on molecularly functionalized silicon substrates: fabrication of inorganic nanostructured etchmask for lithographic use. *Journal of Materials Chemistry C* **2013**, *1*, 7941-7951.
- (117) Cummins, C.; Gangnaik, A.; Kelly, R. A.; Borah, D.; O'Connell, J.; Petkov, N.; Georgiev, Y. M.; Holmes, J. D.; Morris, M. A. Aligned silicon nanofins via the directed self-assembly of PS-*b*-P4VP block copolymer and metal oxide enhanced pattern transfer. *Nanoscale* **2015**, *7*, 6712-6721.
- (118) Cummins, C.; Kelly, R. A.; Gangnaik, A.; Georgiev, Y. M.; Petkov, N.; Holmes, J. D.; Morris, M. A. Solvent Vapor Annealing of Block Copolymers in Confined Topographies: Commensurability Considerations for Nanolithography. *Macromolecular Rapid Communications* **2015**, *36*, 762-767.
- (119) Park, S.; Kim, B.; Wang, J. Y.; Russell, T. P. Fabrication of Highly Ordered Silicon Oxide Dots and Stripes from Block Copolymer Thin Films. *Advanced Materials* **2008**, *20*, 681-685.
- (120) Shin, D. O.; Lee, D. H.; Moon, H. S.; Jeong, S. J.; Kim, J. Y.; Mun, J. H.; Cho, H.; Park, S.; Kim, S. O. Sub-Nanometer Level Size Tuning of a Monodisperse Nanoparticle Array Via Block Copolymer Lithography. *Advanced Functional Materials* **2011**, *21*, 250-254.
- (121) Shin, D. O.; Mun, J. H.; Hwang, G.-T.; Yoon, J. M.; Kim, J. Y.; Yun, J. M.; Yang, Y.-B.; Oh, Y.; Lee, J. Y.; Shin, J.; Lee, K. J.; Park, S.; Kim, J. U.; Kim, S. O. Multicomponent Nanopatterns by Directed Block Copolymer Self-Assembly. *ACS Nano* **2013**, *7*, 8899-8907.
- (122) Mun, J. H.; Chang, Y. H.; Shin, D. O.; Yoon, J. M.; Choi, D. S.; Lee, K.-M.; Kim, J. Y.; Cha, S. K.; Lee, J. Y.; Jeong, J.-R.; Kim, Y.-H.; Kim, S. O. Monodisperse Pattern Nanoalloying for Synergistic Intermetallic Catalysis. *Nano Letters* **2013**, *13*, 5720-5726.
- (123) Mun, J. H.; Cha, S. K.; Kim, H.; Moon, H.-S.; Kim, J. Y.; Jin, H. M.; Choi, Y. J.; Baek, J. E.; Shin, J.; Kim, S. O. Nanodomain Swelling Block Copolymer Lithography for Morphology Tunable Metal Nanopatterning. *Small* **2014**, *10*, 3742-3749.
- (124) Park, W. I.; Tong, S.; Liu, Y.; Jung, I. W.; Roelofs, A.; Hong, S. Tunable and rapid self-assembly of block copolymers using mixed solvent vapors. *Nanoscale* **2014**, *6*, 15216-15221.
- (125) Biswas, M.; Libera, J. A.; Darling, S. B.; Elam, J. W. New Insight into the Mechanism of Sequential Infiltration Synthesis from Infrared Spectroscopy. *Chemistry of Materials* **2014**, *26*, 6135-6141.
- (126) Biswas, M.; Libera, J. A.; Darling, S. B.; Elam, J. W. Kinetics for the Sequential Infiltration Synthesis of Alumina in Poly(methyl methacrylate): An Infrared Spectroscopic Study. *The Journal of Physical Chemistry C* **2015**.
- (127) Tseng, Y.-C.; Peng, Q.; Ocola, L. E.; Czaplowski, D. A.; Elam, J. W.; Darling, S. B. Enhanced polymeric lithography resists via sequential infiltration synthesis. *Journal of Materials Chemistry* **2011**, *21*, 11722-11725.
- (128) Tseng, Y.-C.; Mane, A. U.; Elam, J. W.; Darling, S. B. Enhanced Lithographic Imaging Layer Meets Semiconductor Manufacturing Specification a Decade Early. *Advanced Materials* **2012**, *24*, 2608-2613.
- (129) Cho, H.; Park, H.; Park, S.; Choi, H.; Huang, H.; Chang, T. Development of various PS-*b*-P4VP micellar morphologies: Fabrication of inorganic nanostructures from micellar templates. *Journal of Colloid and Interface Science* **2011**, *356*, 1-7.

- (130) Cho, H.; Park, H.; Russell, T. P.; Park, S. Precise placements of metal nanoparticles from reversible block copolymer nanostructures. *Journal of Materials Chemistry* **2010**, *20*, 5047-5051.
- (131) Roulet, M.; Vayer, M.; Sinturel, C. A simple route to ordered metal oxide nanoparticle arrays using block copolymer thin films. *European Polymer Journal* **2013**, *49*, 3897-3903.
- (132) Cummins, C.; Gangnaik, A.; Kelly, R. A.; Hydes, A. J.; O'Connell, J.; Petkov, N.; Georgiev, Y. M.; Borah, D.; Holmes, J. D.; Morris, M. A. Parallel Arrays of Sub-10 nm Aligned Germanium Nanofins from an In Situ Metal Oxide Hardmask using Directed Self-Assembly of Block Copolymers. *Chemistry of Materials* **2015**, *27* (17), 6091-6096.
- (133) Li, J.; Zhao, T.; Chen, T.; Liu, Y.; Ong, C. N.; Xie, J. Engineering noble metal nanomaterials for environmental applications. *Nanoscale* **2015**.
- (134) Jain, P. K.; Huang, X.; El-Sayed, I. H.; El-Sayed, M. A. Noble Metals on the Nanoscale: Optical and Photothermal Properties and Some Applications in Imaging, Sensing, Biology, and Medicine. *Accounts of Chemical Research* **2008**, *41*, 1578-1586.
- (135) Bhoje Gowd, E.; Nandan, B.; Vyas, M. K.; Bigall, N. C.; Eychmüller, A.; Schlörb, H.; Stamm, M. Highly ordered palladium nanodots and nanowires from switchable block copolymer thin films. *Nanotechnology* **2009**, *20*.
- (136) Nandan, B.; Gowd, E. B.; Bigall, N. C.; Eychmüller, A.; Formanek, P.; Simon, P.; Stamm, M. Arrays of Inorganic Nanodots and Nanowires Using Nanotemplates Based on Switchable Block Copolymer Supramolecular Assemblies. *Advanced Functional Materials* **2009**, *19*, 2805-2811.
- (137) Bigall, N. C.; Nandan, B.; Gowd, E. B.; Horechyy, A.; Eychmüller, A. High-Resolution Metal Nanopatterning by Means of Switchable Block Copolymer Templates. *ACS Applied Materials & Interfaces* **2015**.
- (138) Mayeda, M. K.; Hayat, J.; Epps, T. H.; Lauterbach, J. Metal oxide arrays from block copolymer thin film templates. *Journal of Materials Chemistry A* **2015**, *3*, 7822-7829.
- (139) Fernyhough, C. M.; Pantazis, D.; Pispas, S.; Hadjichristidis, N. The micellar behavior of linear triblock terpolymers of styrene (S), isoprene (I), and methyl methacrylate (MMA) in selective solvents for PS and PMMA. *European Polymer Journal* **2004**, *40*, 237-244.
- (140) Nagpal, U.; Detcheverry, F. A.; Nealey, P. F.; de Pablo, J. J. Morphologies of Linear Triblock Copolymers from Monte Carlo Simulations. *Macromolecules* **2011**, *44*, 5490-5497.
- (141) Hadjichristidis, N.; Iatrou, H.; Pitsikalis, M.; Pispas, S.; Avgeropoulos, A. Linear and non-linear triblock terpolymers. Synthesis, self-assembly in selective solvents and in bulk. *Progress in Polymer Science* **2005**, *30*, 725-782.
- (142) Hadjichristidis, N.; Hirao, A.; Tezuka, Y.; DuPrez, F.: *Complex Macromolecular Architectures: Synthesis, Characterization, and Self-Assembly*; Wiley, 2011.
- (143) Ross, C. A.; Jung, Y. S.; Chuang, V. P.; Son, J. G.; Gotrik, K. W.; Mickiewicz, R. A.; Yang, J. K. W.; Chang, J. B.; Berggren, K. K.; Gwyther, J.; Manners, I. In *Tilte2010; Engineering, P. o. S.-T. I. S. f. O.s.*
- (144) Bates, F. S.; Fredrickson, G. H. Block copolymers - Designer soft materials. *Physics Today* **1999**, *52*, 32-38.
- (145) Zheng, W.; Wang, Z.-G. Morphology of ABC Triblock Copolymers. *Macromolecules* **1995**, *28*, 7215-7223.

- (146) Davis, M. E. Ordered porous materials for emerging applications. *Nature* **2002**, *417*, 813-821.
- (147) Farrell, R. A.; Petkov, N.; Morris, M. A.; Holmes, J. D. Self-assembled templates for the generation of arrays of 1-dimensional nanostructures: From molecules to devices. *Journal of Colloid and Interface Science* **2010**, *349*, 449-472.
- (148) Yang, P.; Zhao, D.; Chmelka, B. F.; Stucky, G. D. Triblock-Copolymer-Directed Syntheses of Large-Pore Mesoporous Silica Fibers. *Chemistry of Materials* **1998**, *10*, 2033-2036.
- (149) Zhao, D.; Huo, Q.; Feng, J.; Chmelka, B. F.; Stucky, G. D. Nonionic Triblock and Star Diblock Copolymer and Oligomeric Surfactant Syntheses of Highly Ordered, Hydrothermally Stable, Mesoporous Silica Structures. *Journal of the American Chemical Society* **1998**, *120*, 6024-6036.
- (150) Yang, P.; Zhao, D.; Margolese, D. I.; Chmelka, B. F.; Stucky, G. D. Generalized syntheses of large-pore mesoporous metal oxides with semicrystalline frameworks. *Nature* **1998**, *396*, 152-155.
- (151) Yang, P. D.; Deng, T.; Zhao, D. Y.; Feng, P. Y.; Pine, D.; Chmelka, B. F.; Whitesides, G. M.; Stucky, G. D. Hierarchically ordered oxides. *Science* **1998**, *282*, 2244-2246.
- (152) Kabanov, A. V.; Lemieux, P.; Vinogradov, S.; Alakhov, V. Pluronic® block copolymers: novel functional molecules for gene therapy. *Advanced Drug Delivery Reviews* **2002**, *54*, 223-233.
- (153) Fusco, S.; Borzacchiello, A.; Netti, P. A. Perspectives on: PEO-PPO-PEO triblock copolymers and their biomedical applications. *Journal of Bioactive and Compatible Polymers* **2006**, *21*, 149-164.
- (154) Batrakova, E. V.; Kabanov, A. V. Pluronic block copolymers: Evolution of drug delivery concept from inert nanocarriers to biological response modifiers. *Journal of Controlled Release* **2008**, *130*, 98-106.
- (155) Pitto-Barry, A.; Barry, N. P. E. Pluronic® block-copolymers in medicine: from chemical and biological versatility to rationalisation and clinical advances. *Polymer Chemistry* **2014**, *5*, 3291-3297.
- (156) Bromberg, L. E.; Ron, E. S. Temperature-responsive gels and thermogelling polymer matrices for protein and peptide delivery. *Advanced Drug Delivery Reviews* **1998**, *31*, 197-221.
- (157) Orilall, M. C.; Wiesner, U. Block copolymer based composition and morphology control in nanostructured hybrid materials for energy conversion and storage: solar cells, batteries, and fuel cells. *Chemical Society Reviews* **2011**, *40*, 520-535.
- (158) Stefik, M.; Guldin, S.; Vignolini, S.; Wiesner, U.; Steiner, U. Block copolymer self-assembly for nanophotonics. *Chemical Society Reviews* **2015**.
- (159) Ludwigs, S.; Boker, A.; Voronov, A.; Rehse, N.; Magerle, R.; Krausch, G. Self-assembly of functional nanostructures from ABC triblock copolymers. *Nat Mater* **2003**, *2*, 744-747.
- (160) Zucchi, I. A.; Poliani, E.; Perego, M. Microdomain orientation dependence on thickness in thin films of cylinder-forming PS-*b*-PMMA. *Nanotechnology* **2010**, *21*.
- (161) Borah, D.; Rasappa, S.; Senthamaraiannan, R.; Holmes, J. D.; Morris, M. A. Tuning PDMS Brush Chemistry by UV-O<sub>3</sub> Exposure for PS-*b*-PDMS Microphase Separation and Directed Self-assembly. *Langmuir* **2013**, *29*, 8959-8968.
- (162) Bang, J.; Kim, S. H.; Drockenmuller, E.; Misner, M. J.; Russell, T. P.; Hawker, C. J. Defect-Free Nanoporous Thin Films from ABC Triblock Copolymers. *Journal of the American Chemical Society* **2006**, *128*, 7622-7629.

- (163) Albert, J. N. L.; Young, W.-S.; Lewis, R. L.; Bogart, T. D.; Smith, J. R.; Epps, T. H. Systematic Study on the Effect of Solvent Removal Rate on the Morphology of Solvent Vapor Annealed ABA Triblock Copolymer Thin Films. *ACS Nano* **2011**, *6*, 459-466.
- (164) Tureau, M. S.; Epps, T. H. Effect of Partial Hydrogenation on the Phase Behavior of Poly(isoprene-*b*-styrene-*b*-methyl methacrylate) Triblock Copolymers. *Macromolecules* **2012**, *45*, 8347-8355.
- (165) Mayeda, M. K.; Kuan, W.-F.; Young, W.-S.; Lauterbach, J. A.; Epps, T. H. Controlling Particle Location with Mixed Surface Functionalities in Block Copolymer Thin Films. *Chemistry of Materials* **2012**, *24*, 2627-2634.
- (166) Bates, F. S.; Hillmyer, M. A.; Lodge, T. P.; Bates, C. M.; Delaney, K. T.; Fredrickson, G. H. Multiblock Polymers: Panacea or Pandora's Box? *Science* **2012**, *336*, 434-440.
- (167) Beck, J. S.; Vartuli, J. C.; Roth, W. J.; Leonowicz, M. E.; Kresge, C. T.; Schmitt, K. D.; Chu, C. T. W.; Olson, D. H.; Sheppard, E. W. A new family of mesoporous molecular sieves prepared with liquid crystal templates. *Journal of the American Chemical Society* **1992**, *114*, 10834-10843.
- (168) Rodwogin, M. D.; Spanjers, C. S.; Leighton, C.; Hillmyer, M. A. Polylactide-Poly(dimethylsiloxane)-Polylactide Triblock Copolymers as Multifunctional Materials for Nanolithographic Applications. *ACS Nano* **2010**, *4*, 725-732.
- (169) Kubo, T.; Wang, R. F.; Olson, D. A.; Rodwogin, M.; Hillmyer, M. A.; Leighton, C. Spontaneous alignment of self-assembled ABC triblock terpolymers for large-area nanolithography. *Applied Physics Letters* **2008**, *93*.
- (170) Querelle, S. E.; Jackson, E. A.; Cussler, E. L.; Hillmyer, M. A. Ultrafiltration Membranes with a Thin Poly(styrene)-*b*-poly(isoprene) Selective Layer. *ACS Applied Materials & Interfaces* **2013**, *5*, 5044-5050.
- (171) Pitet, L. M.; Amendt, M. A.; Hillmyer, M. A. Nanoporous Linear Polyethylene from a Block Polymer Precursor. *Journal of the American Chemical Society* **2010**, *132*, 8230-8231.
- (172) Rzayev, J.; Hillmyer, M. A. Nanochannel Array Plastics with Tailored Surface Chemistry. *Journal of the American Chemical Society* **2005**, *127*, 13373-13379.
- (173) Chuang, V. P.; Ross, C. A.; Gwyther, J.; Manners, I. Self-Assembled Nanoscale Ring Arrays from a Polystyrene-*b*-polyferrocenylsilane-*b*-poly(2-vinylpyridine) Triblock Terpolymer Thin Film. *Advanced Materials* **2009**, *21*, 3789-3793.
- (174) Choi, H. K.; Aimon, N. M.; Kim, D. H.; Sun, X. Y.; Gwyther, J.; Manners, I.; Ross, C. A. Hierarchical Templating of a BiFeO<sub>3</sub>-CoFe<sub>2</sub>O<sub>4</sub> Multiferroic Nanocomposite by a Triblock Terpolymer Film. *ACS Nano* **2014**, *8*, 9248-9254.
- (175) Choi, H. K.; Gwyther, J.; Manners, I.; Ross, C. A. Square Arrays of Holes and Dots Patterned from a Linear ABC Triblock Terpolymer. *ACS Nano* **2012**, *6*, 8342-8348.
- (176) Aissou, K.; Choi, H. K.; Nunns, A.; Manners, I.; Ross, C. A. Ordered Nanoscale Archimedean Tilings of a Templated 3-Miktoarm Star Terpolymer. *Nano Letters* **2013**, *13*, 835-839.
- (177) Aissou, K.; Nunns, A.; Manners, I.; Ross, C. A. Square and Rectangular Symmetry Tiles from Bulk and Thin Film 3-Miktoarm Star Terpolymers. *Small* **2013**, *9*, 4077-4084.

- (178) Zhang, X.; Murphy, J. N.; Wu, N. L. Y.; Harris, K. D.; Buriak, J. M. Rapid Assembly of Nanolines with Precisely Controlled Spacing from Binary Blends of Block Copolymers. *Macromolecules* **2011**, *44*, 9752-9757.
- (179) Park, W. I.; Kim, J. M.; Jeong, J. W.; Jung, Y. S. Deep-Nanoscale Pattern Engineering by Immersion-Induced Self-Assembly. *ACS Nano* **2014**, *8*, 10009-10018.
- (180) Mokarian-Tabari, P.; Cummins, C.; Rasappa, S.; Simao, C.; Sotomayor Torres, C. M.; Holmes, J. D.; Morris, M. A. Study of the Kinetics and Mechanism of Rapid Self-Assembly in Block Copolymer Thin Films during Solvo-Microwave Annealing. *Langmuir* **2014**, *30*, 10728-10739.

---

*Chapter 2*

---

**Selective Etching of Polylactic Acid in Poly(styrene)-*block*-poly(D,L)lactide Diblock Copolymer for Nanoscale Patterning**

## 2.1. Abstract

Self-assembled thin films of a lamellar-forming polystyrene-*block*-poly(D,L)lactide (PS-*b*-PLA) block copolymer (BCP) contain a “reactive” block that can be readily removed to provide a template for substrate pattern formation. In this chapter, various methods of PLA removal were studied with a view to develop the system as an on-chip etch mask for substrate patterning. Solvo-microwave annealing was used to induce microphase separation in PS-*b*-PLA BCP with a periodicity of 34 nm ( $L_0$ ) on silicon and silicon on insulator (SOI) substrates. Wet etches based on alkaline and enzymatic solutions were studied in depth. Fourier transform infrared (FTIR) analysis showed that basic hydrolysis using sodium hydroxide (NaOH) or ammonium hydroxide (NH<sub>4</sub>OH) solutions resulted in greater PLA removal in comparison to an enzymatic approach using Proteinase K in a Tris-HCl buffer solution. However, in the enzymatic approach, the characteristic self-assembled fingerprint patterns were retained with less damage. Comparison to a dry etch procedure using a reactive ion etch (RIE) technique was made. A detailed study of the etch rate of PS and PLA homopolymer and PS-*b*-PLA shows depending on DC bias, the etch selectivity of PLA and PS  $\left(\frac{dPLA}{dPS}\right)$  can be almost doubled from 1.7 at DC bias 145 V to 3 at DC bias 270 V.

## 2.2. Introduction

Block copolymers (BCPs) consist of two chemically incompatible polymers covalently bonded that can microphase separate into well-arranged nanoscale features of significant nanotechnological importance.<sup>1-5</sup> By altering molecular weights and volume fractions of the BCP components, the periodicity of the resulting morphology can be controlled and the pattern can be developed for a particular function. In recent years, there has been

much interest in BCPs for nanolithography use due to these tuneable characteristics.<sup>6,7</sup> With the ability to achieve sub-10 nm feature sizes<sup>8,9</sup> and integrated circuit relevant geometries through directed self-assembly,<sup>10-12</sup> BCPs are a possible alternative methodology for further extension of Moore's Law.

One of the key processes in a strategy for developing high density device structures from BCPs is pattern transfer where the "soft" mask is transferred to the underlying substrate. It is highly desirable to have a BCP system where one block can be readily removed (etched) to form a topographic pattern resistant block acting as an on-chip mask for subsequent substrate etching. This process is well demonstrated for the polystyrene-*block*-polymethylmethacrylate (PS-*b*-PMMA) system using reactive ion etching (RIE).<sup>13-17</sup> Controlled wet etching can also be effective and because of its simplicity may be practical as a general method to create periodic porous nanochannels<sup>18</sup> for inclusion of functional material for applications in optical, medical or sensing technologies.

The development of processes for selective block removal and/or subsequent pattern transfer is challenging and several solutions have been trialled. An "*in situ*" inclusion technique recently showed the effectiveness of metal oxide etch masks as size and dimensional control were demonstrated for silicon nanopillar and nanowire fabrication.<sup>19-21</sup> Polystyrene-*block*-polydimethylsiloxane (PS-*b*-PDMS) has also been intensely studied as the silicon backbone of the PDMS block provides natural etch contrast and can form a robust template for pattern transfer purposes.<sup>8</sup> Polystyrene-*block*-polylactide (PS-*b*-PLA) is another BCP of considerable potential as an etch mask or porous forming template. Firstly, PS-*b*-PLA has a high Flory Huggins interaction parameter ( $\chi = 0.233$ )<sup>22</sup> which makes smaller feature sizes more accessible. Secondly,

PS-*b*-PLA has similar block surface energies avoiding wetting layer formation at the polymer/air interface. Lastly, the ease of removal of the aliphatic polyester PLA makes the system ideal for attaining high etch contrast. PLA has been etched most commonly using a mild NaOH solution.<sup>23-26</sup> It has also been suggested that a PLA wetting layer exists at the polymer/substrate interface and this can cause delamination without suitable surface treatment.<sup>27,28</sup> This approach of substrate modification was recently used for a bottlebrush PS-*b*-PLA where an enzyme was used for PLA degradation to replicate biological conditions.<sup>29</sup>

This chapter demonstrates the applicability of PS-*b*-PLA in pattern transfer through the use of a highly selective dry etch procedure to remove the PLA block and enable silicon nanowire fabrication. Three wet etch routes to remove PLA were also studied. The often used NaOH was shown to result in over etching. This led to development of an NH<sub>4</sub>OH and methanol etch system. We also report extension of established enzymatic PLA degradation in biomedical studies<sup>30-34</sup> to degradation of the PLA block in PS-*b*-PLA system. As mentioned, the dry etching of PLA could be performed with a high degree of selectivity leading to large area removal of PLA with the structure of the original pattern being retained. The etch selectivity of PS and PLA was measured in a controlled way by manipulating the DC bias indirectly during the RIE process.

### 2.3. Experimental

**Materials.** Planar substrates used were highly polished single-crystal silicon <100> wafers (*p*- type) with a native oxide layer of ~2 nm. No attempt was taken to remove the native oxide of a few nm depth. Silicon on insulator (SOI) substrates employed contained a 140 nm box layer on bulk silicon, followed by a gate oxide with a thickness of 1.2 nm,

a 50 nm device active layer, and finally a 20 nm silicon dioxide layer. Polystyrene-*block*-Polylactide (referred to as PS-*b*-PLA, note that PLA is in the DL form) was purchased from Polymer Source, Inc., Canada, with a total number average molecular weight of  $M_n = 40.5 \text{ kg mol}^{-1}$  ( $M_{nPS} = 21 \text{ kg mol}^{-1}$ ;  $M_{nPLA} = 19.5 \text{ kg mol}^{-1}$ ,  $f_{PS} = 0.53$ ), a polydispersity index of 1.15 and was used as received. Hydroxyl terminated polystyrene (PS-OH) was purchased from Polymer Source, Inc., Canada, with a total number average molecular weight of  $M_n = 6 \text{ kg mol}^{-1}$ , a polydispersity index of 1.05 and was used as received. PS and PLA homopolymer ( $M_{nPS} = 16 \text{ kg mol}^{-1}$  with a polydispersity index of 1.03 and  $M_{nPLA} = 16 \text{ kg mol}^{-1}$  with a polydispersity index of 1.30) were both purchased from Polymer Source, Inc., Canada. Proteinase K (from *Tritirachium album* lyophilized powder), sodium hydroxide beads, ruthenium (III) chloride hydrate, ammonium hydroxide (28.0-30.0%  $\text{NH}_3$  basis), methanol (anhydrous, 99.8%), chloroform (HPLC grade,  $\geq 99.9\%$ , contains 0.5-1.0% ethanol as stabilizer), tetrahydrofuran (THF) (HPLC grade,  $\geq 99.9\%$ ) and sodium hypochlorite solution (reagent grade, chlorine 10-15 %) were all purchased from Sigma Aldrich. Ruthenium tetroxide ( $\text{RuO}_4$ ) was prepared as described elsewhere<sup>35</sup> and staining was carried out for 1 minute.

**Substrate cleaning, PS-OH brush modification, BCP preparation, homopolymer preparation and deposition.** Substrates were cut into pieces that allowed for horizontal placement in microwave tube. Initial experiments involved cleaning substrates using UV/ozone for 30 minutes before solvo-microwave annealing. All UV/Ozone treatments were performed in a PSD Pro Series Digital UV Ozone System, Novascan Technologies, Inc. However, when BCP films prepared on UV/ozone cleaned substrates were wet etched delamination of the film resulted. Thus, substrates were modified with a PS-OH brush to promote more stable films. Further examination on substrate surface

modification is discussed below. For PS-OH brush modified surfaces, substrates (Si or SOI) were degreased by ultrasonication in acetone and isopropanol (IPA) solutions for 5 minutes each, dried in flowing nitrogen gas and baked for 2 minutes at 180 °C in an ambient atmosphere to remove any residual IPA. This was followed by cleaning in a piranha solution (1:3 v/v 30% H<sub>2</sub>O<sub>2</sub>:H<sub>2</sub>SO<sub>4</sub>) (*Safety caution: May cause explosion in contact with organic material!*) at 100 °C for 60 minutes, rinsed with deionized water (resistivity  $\geq 18$  M $\Omega$ /cm) several times and dried under nitrogen flow. 1 weight % PS-OH solutions in toluene were then spin coated at 2000 rpm for 30 seconds. After spin coating, substrates were annealed at 180°C for 6 hours. PS-OH treated substrates were rinsed in toluene for 10 minutes twice to remove any excess polymer that had not grafted fully to the substrate surface. After washing, substrates were blown dry with nitrogen gas. An ellipsometry measurement shows a 2 nm brush layer is formed. 2 weight % PS-*b*-PLA solutions were made using chloroform whereby the solution was sonicated for 30 minutes to ensure full dissolution. Following dissolution, BCP solution was spin coated on the PS-OH brush modified surfaces at 2000 rpm for 30 seconds. For homopolymer dry etch studies only, 3 weight % chloroform solutions of PS and PLA films were prepared and spin coated at 2000 rpm on UV/ozone cleaned silicon substrates.

**Microwave annealing process.** Please note that a comprehensive study has been published on the solvo-microwave annealing of this PS-*b*-PLA system.<sup>36</sup> Following deposition of the BCP solution at 2000 rpm for 30 seconds, patterns were developed after samples were placed in the sample holder (*i.e.* microwave tube) and then placed in the microwave (CEM model). Note that the experimental setup including the microwave holder and the microwave synthesizer can be viewed elsewhere.<sup>8</sup> Power was set at 300 W, while ramp rate was set for 3 minutes, and temperature was set to 55°C with THF as solvent in the sample holder. Annealing time varied from 15 seconds to 2 minutes.

**PLA etching methods. Alkaline route 1;** A 0.05 M NaOH (60:40, water:methanol) solution was prepared at room temperature. The solution was given sufficient time (~ 15 minutes) in order to fully dissolve. Microwave annealed PS-*b*-PLA films were then immersed in the solution for a range of time periods. After removal, films were washed twice with deionized water/methanol for 5 minutes. **Alkaline route 2;** NH<sub>4</sub>OH/Methanol (1:2) solution was prepared at room temperature. The same procedure as NaOH approach was followed for immersion and washing of the film. **Enzymatic route;** The degradation solution here composed of 1 mg of Proteinase K dissolved in 5 ml of Tris-HCl buffer (pH = 8.6). The solution was placed in an oil bath and left heat to 37 °C. Once the desired temperature was reached, and stable for a period of time, the PS-*b*-PLA films were immersed for various times (from 15 minutes to 24 hours). Following degradation, the film was removed and washed twice in deionized water for 5 minutes. All films were washed as described above and were dried under nitrogen flow to ensure complete removal of PLA fragments that were degraded.

**Dry etch tools and recipes.** Dry etching of the PS-*b*-PLA films was performed in an Oxford Instruments Plasmatech in RIE mode using a mixture of argon and oxygen gas. Flows rates were set at 15 sccm for argon and 10 sccm for oxygen gas. Process pressure was 12 mTorr while radio frequency power was 40 W. The value of DC bias was varied between 145V – 270V which is a critical parameter by altering process pressure. The DC bias variation proved to be a critical parameter for result consistency. This is discussed in detail in the results and discussion section. **Pattern Transfer;** The remaining PS etch mask was pattern transferred to the underlying silicon substrate using a combination of sulphur hexafluoride (SF<sub>6</sub>) and trifluoromethane (CHF<sub>3</sub>) gasses in an STS AOE inductively coupled plasma (ICP) etcher.<sup>17</sup> The residual PS stripes following the pattern transfer were removed by O<sub>2</sub> plasma.

**Characterization.** Film Thickness. BCP film thicknesses were measured with a spectroscopic ellipsometer “J.A. Woollam Ellipsometer” at a fixed angle of incidence of  $70^\circ$ , on at least five different places on the sample and was averaged as the film thickness. A three layer model ( $\text{SiO}_2$  + polymer brush + BCP) for total BCP film was used to simulate experimental data. Atomic Force Microscopy (AFM). AFM (Park systems, XE-100) was operated in AC (tapping) mode under ambient conditions using silicon microcantilever probe tips with a force constant of  $42 \text{ N m}^{-1}$ . Topographic and phase images were recorded simultaneously. AFM was employed to monitor the progression of each etch route and since AFM cannot define the exact depth etched in the PS-*b*-PLA samples, etch values quoted here are nominal. However, the relative magnitude of the etch depth observed agreed with cross section SEM measurements and so could be used for comparative purposes. Scanning Electron Microscopy (SEM). SEM images were obtained by a FEI Helios Nanolab 600i system at an accelerating voltage of 5 kV and at a working distance of 4 mm. Cross section SEM images involved cleaving the substrate in half and positioning the substrate perpendicular to the incident beam of electrons. The stage was then tilted at  $20^\circ$ . Fourier Transform Infrared (FTIR) Spectroscopy. An IR660, Varian infrared spectrometer was used to record the FTIR spectra. The FTIR was operated in ATR mode. The measurements were performed in the spectral range of  $4000\text{--}400 \text{ cm}^{-1}$ , with a resolution of  $4 \text{ cm}^{-1}$  and data averaged over 32 scans. This characterization was carried out to see the effect of the etch routes on degradation of the PLA composition.

## 2.4. Results and discussion

### 2.4.1 Self-Assembly and Surface Modification.

Microwave annealing is an emerging technique for inducing microphase separation in BCPs in a quick, easy and low cost manner. Buriak and co-workers<sup>37</sup> published the seminal work illustrating its flexibility for the rapid self-assembly of PS-*b*-PMMA and PS-*b*-P2VP (polystyrene-*block*-poly2-vinylpyridine) BCPs. Borah *et al.* recently demonstrated microwave annealing without the use of solvents for self-assembly of PS-*b*-PMMA<sup>38</sup> and PS-*b*-PDMS<sup>8,38</sup> block copolymer systems. Here solvo-microwave annealing was used to generate highly ordered lamellar PS-*b*-PLA patterns (see experimental for details). A fingerprint pattern with a periodicity of 34 nm ( $L_0$ ) was formed (see Figure 2.1a). The solvo-microwave annealed films had a thickness of 200 nm following self-assembly. The initial self-assembled pattern in Figure 2.1a is the PS-*b*-PLA film without any etching and is characteristic of films used for wet and dry etching procedures below. Due to the similar surface energies of PS and PLA ( $\gamma_{s\text{ PS}} = 42.0 \text{ mJ m}^{-2}$ ,  $\gamma_{s\text{ PLA}} = 36.0\text{--}41.1 \text{ mJ m}^{-2}$ ),<sup>27</sup> a preference for either block at the polymer/air interface does not exist and since a neutral solvent THF (solubility parameters for PS, PLA and THF are  $18.5 \text{ MPa}^{1/2}$ ,  $18.5 \text{ MPa}^{1/2}$  and  $16.8 \text{ MPa}^{1/2}$  respectively)<sup>39</sup> was used for annealing, perpendicular lamellar patterns were observed. THF was introduced to enable self-assembly as the polymer chains are mobilized by the solvent vapor during the rapid annealing process. Microwave annealing was carried out without solvent but did not produce microphase separated patterns. Dewetting is not an issue like other high  $\chi$  BCP materials such as PS-*b*-PDMS where the large surface energy difference between the blocks results in preferential wetting at polymer/substrate and polymer/air interfaces.<sup>40,41</sup> The PS-*b*-PLA film shows complete surface coverage (See Appendix – Chapter 2, Figure S2.7.1). For SEM characterization of the microphase separated structure, staining with

$\text{RuO}_4$  was used to enhance the domain contrast between PS and PLA. Figure 2.1b shows a cross section SEM image of the self-assembled PS-*b*-PLA pattern where PS domains appear bright in comparison to the dark PLA domains. The image provides evidence for the extension of the lamellar through the entire film.

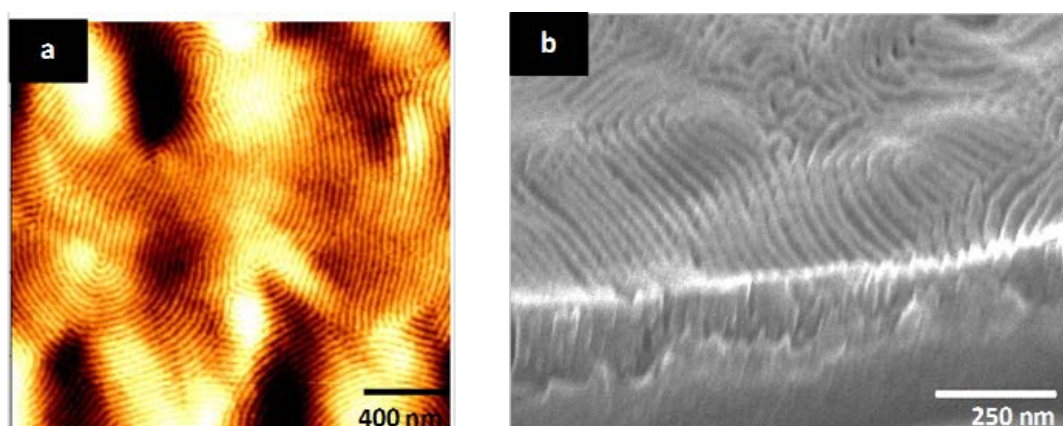


**Figure 2.1.** (a) AFM topography image of microphase separated PS-*b*-PLA structure on UV/ozone cleaned silicon substrate after solvo-microwave annealing for 60 seconds in the presence of THF at 55°C. Film thickness was measured at ~ 200 nm. (b) Cross section SEM image of the initially microphase separated structure on silicon following staining with  $\text{RuO}_4$ .

It should be noted that initial experiments involving exposure of the films to NaOH solutions of varying concentration resulted in immediate delamination of the BCP thin film after immersion. We believe this is due to the formation of a PLA wetting layer at the polymer-substrate interface as shown in Figure 2.2.a. This wetting mechanism has been postulated in previous work<sup>27</sup> and is probably due to strong polar interactions of PLA with the native silicon oxide layer. Thus, degradation of the PLA wetting layer in NaOH leads to detachment of the polymer film and delamination. To avoid this problem, a PS-OH brush layer was grafted to piranha cleaned Si or SOI substrates using thermal annealing enabling better adhesion of the polymer film through the increased PS block interaction with the treated surface. Polymer brushes are commonly used to control microdomain orientation<sup>8,38</sup> but the functionalization used here did not modify the pattern

formation significantly and was successful in promoting effective selective etching even in harsh conditions. We believe the brush aids layer homogeneity and thus the increased PS block interaction with the modified substrate allows wet etching to be carried without film delamination. As mentioned, the existence of a PLA wetting layer is speculated due to the dramatic loss of film during wet etching. We are unable to determine the existence of a thick BCP wetting layer (*i.e.* PS wetting layer) when the PS-OH brush is used for surface functionalization. Since we speculate the absence of a thick PS wetting layer, our illustration in Figure 2.2b shows a PS-OH brush modification layer enabling PS-*b*-PLA self-assembly comparable to non-treated substrates, *i.e.* domains are ordered perpendicular to substrate.

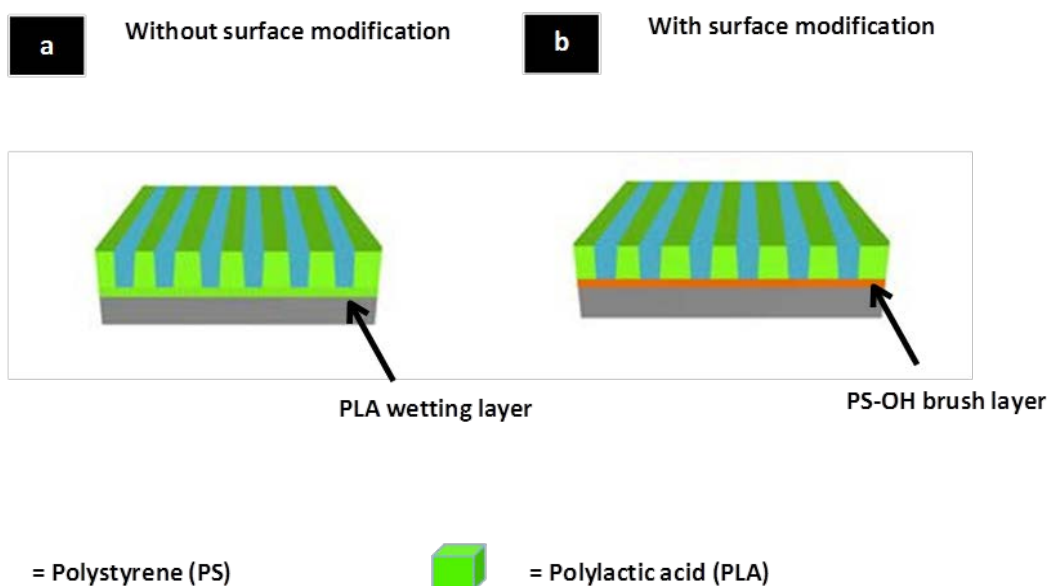


**Figure 2.2.** Graphical representation of interfacial interaction of PS-*b*-PLA with different substrate chemistries, (a) after UV/O<sub>3</sub> treatment only and (b) after piranha cleaning plus grafting of PS-OH brush.

#### 2.4.2. PLA Degradation with Sodium Hydroxide Route.

Hillmyer and coworkers have shown that basic hydrolysis is suitable for the removal of the PLA block in asymmetric PS-*b*-PLA systems.<sup>23-25,27,28,39,42</sup> Figure 2.3 displays AFM and SEM data following the etching of a PS-*b*-PLA film with 0.05 M NaOH for 5

minutes. The solution degraded 6.5 nm on average of PLA from the AFM line profile.

Figure 2.4 shows

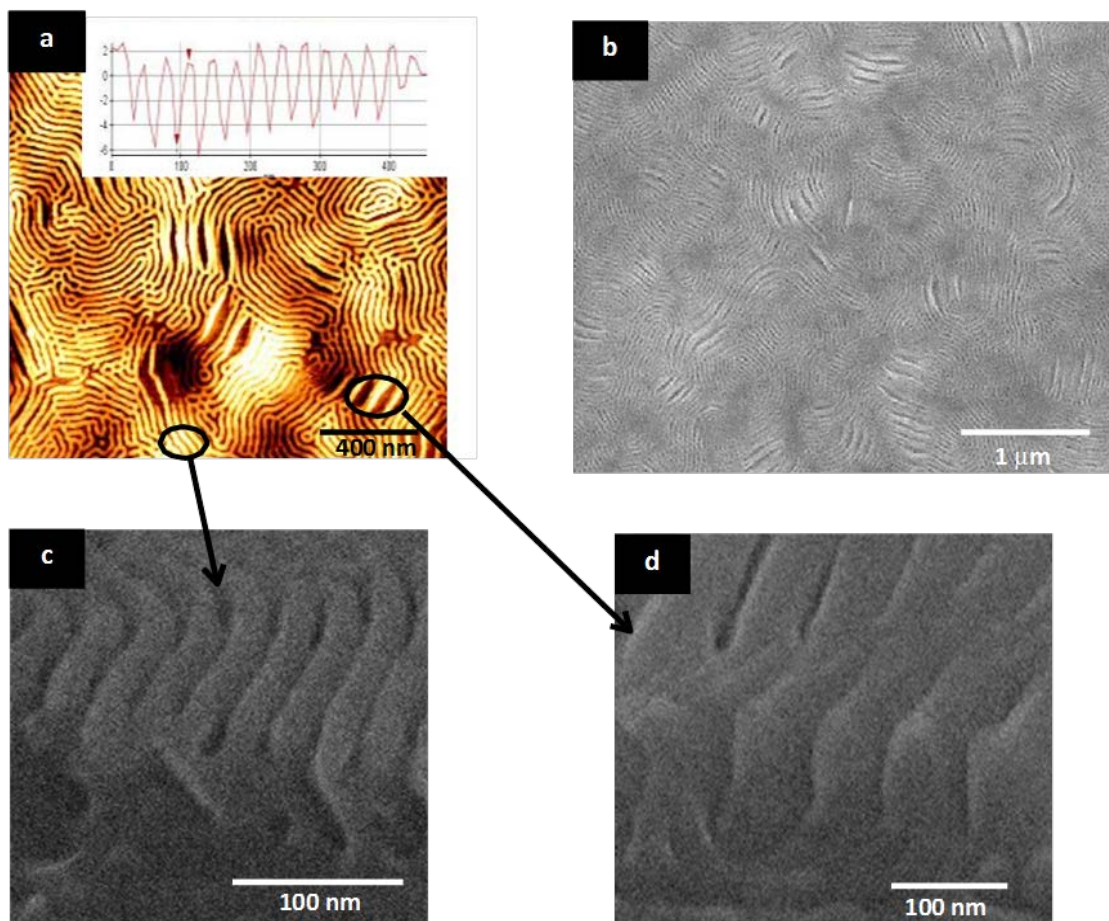


**Figure 2.3.** (a) AFM topographic image ( $2 \times 2 \mu\text{m}$ ) after 5 minutes etching with 0.05 M sodium hydroxide/methanol solution. Inset shows AFM line profile estimating PLA degradation of 6.5 nm. (b) Low resolution top down SEM image of (a). (c) Cross section SEM image showing an area that has retained the periodicity (34 nm) of the original pattern. (d) Cross section SEM image of a region where PS lines have coalesced.

SEM data of etching PS-*b*-PLA films with 0.05 M NaOH for 15, 30 and 45 minutes respectively. (See corresponding AFM data in Figure S2.7.2). 10 nm of PLA was etched on average with 15 minutes treatment (see Figure S2.7.3). Etching the films for 30 and 45 minutes resulted in degradation and damage to the film pattern. This suggests that a 5 to 15 minute treatment period is the optimum process window for the NaOH etch solution for degrading PLA.

The concentration of the NaOH solution (0.05M) is ten times less than previously reported for hexagonal forming PS-*b*-PLA systems,<sup>23,39,42</sup> yet considerable structure deformation was observed. Using a 0.5 M NaOH solution and exposure times of 5 minutes led to complete removal of the pattern formed and this suggests that lamellar patterns are more susceptible to pattern destruction during selective removal of PLA. This could be due to a number of factors. The hexagonal phase may have greater structural integrity due to the honeycomb like structure of PS that remains after removal. The crystallinity of PLA is an important factor that can define the etch degradation rate. PLA etched in some previous studies<sup>43,44</sup> were of a highly crystalline PLLA form compared to the amorphous PLA in our system. The PLA here is in the DL isomeric or racemic form. The crystalline form is probably less soluble due to the crystalline stabilization energy<sup>45</sup> and amorphous regions allow water uptake more readily.<sup>46</sup> Finally, because the films here are relatively thick, the PS fin-like structures may have little mechanical robustness and collapse into one another. This merging of features can be seen in Figures 2.3, Figure 2.4.a-c and 2.5b and c. Specifically, Figure 2.3c illustrates the success of PLA removal whilst retaining the microphase separated periodicity of 34 nm. In contrast, some areas as shown in Figure 2.3d reveal merging of the PS fin-like structures with a periodicity of 70 nm.

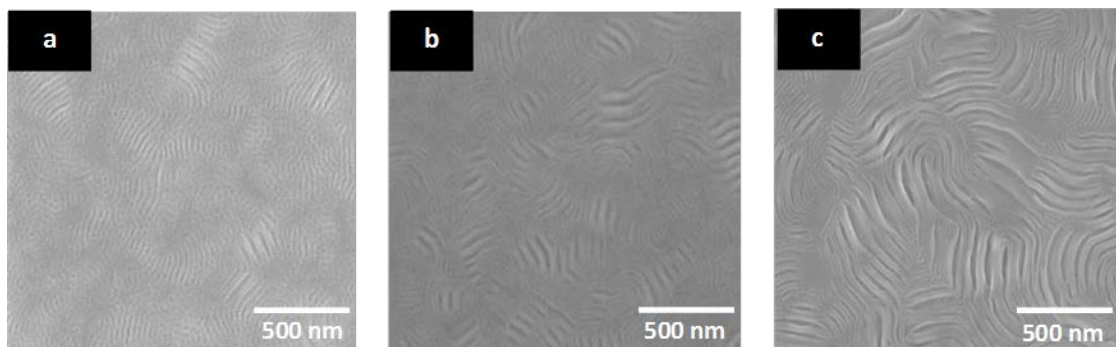


**Figure 2.4.** Top down SEM images of partial PLA degradation using 0.05 M sodium hydroxide/methanol solution. (a) 15 minutes immersion (b) 30 minutes immersion (c) 45 minutes immersion.

### 2.4.3. PLA Degradation with Ammonium Hydroxide Route.

Because of the sensitivity of the system to caustic solutions, an alternative alkaline solution was sought. In basic aqueous solutions like NaOH solutions described above, PLA is vulnerable to main chain cleavage leading to the degradation of PLA and water uptake.<sup>47</sup> Subsequently, hydrolysis of -C-O- ester bonds occurs.<sup>48</sup> Thus, a solution of ammonium hydroxide and methanol to reduce the rate of hydrolysis was investigated. Figure 2.5 shows top down SEM images of this approach using etch times of 10, 20 and 30 minutes respectively. (See Figure S2.7.4 for corresponding AFM data). Excellent etch contrast is observed similar to the PS-*b*-PLA films treated with the NaOH solutions. However, isolated regions of pattern collapse are first observed after 20 minutes of etchant exposure as shown in Figure 2.5b (note that the inset in b shows varying periodicity of the PS fin-like structures as seen above for the NaOH route). The amount of PLA removed after 30 minutes etching with NH<sub>4</sub>OH solution was estimated to be 15 nm from AFM line profile (see Figure S2.7.6) suggesting significant PLA removal. The top down SEM image in Figure 2.5c confirms coalescence of PS lines and the apparent domain size has increased considerably. A contributing factor to this coalescence is the high aspect ratio of the polymer films. Since the films are quite thick (~200 nm), they are

not mechanically robust enough, and thus with the increased aspect ratio following PLA removal the PS lines will collapse into one another. This has also been previously demonstrated for thick PS-*b*-PMMA films during wet etching.<sup>49</sup>

The loss of the pattern quality on extended etching could be attributed to autocatalysis (*i.e.* product catalysed reaction<sup>50</sup>). Autocatalysis in PLA is caused by initial hydrolysis yielding carboxylic acid terminated chains that subsequently catalyse ester hydrolysis. For PDLLA, autocatalysis occurs faster within a PDLLA structure than at the surface<sup>48</sup> and this might account for the delamination observed in the non-brush coated substrates as well merging of the PS features rather than simple thinning of the structures. Note that little surface etching is observed.

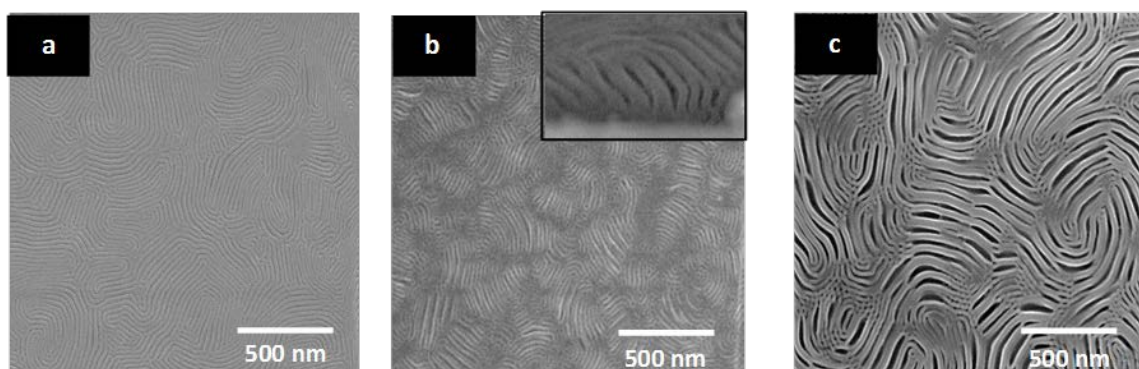


**Figure 2.5.** Top down SEM images of partial PLA degradation using an ammonium hydroxide/methanol solution. (a) 10 minutes immersion (b) 20 minutes immersion (c) 30 minutes immersion. Inset in (b) shows cross section of film.

An AFM line profile obtained prior to etching shows the PS domains have a width of 23 nm for self-assembled patterns. However, after a sample was exposed to the  $\text{NH}_4\text{OH}$  etch for 30 minutes, the domain width doubled to 46 nm, a periodicity consistent with merging of two adjacent PS lines as described earlier.

#### 2.4.4. PLA Degradation with Enzymatic Route.

Whilst both alkaline solutions showed promise as PLA etchants, they both showed extensive pattern damage at extended periods prior to complete PLA removal. For successful use in pattern transfer both complete removal and low damage are prerequisites so that low line edge roughness and good aspect ratio are achieved. Thus, an alternative methodology of biodegradation was examined. PLA is a polymer that can be degraded through the action and metabolism of microorganisms yielding non-toxic products.<sup>51</sup> Although we have described this method here as enzymatic, it should be noted that degradation using Proteinase K combines both enzymatic and chemical hydrolysis.<sup>52</sup> This enzymatic approach is novel since PLA biodegradation is common in food science and biomedicine but has yet to be employed with diblock copolymers. Following documented conditions<sup>26,53</sup> to mimic a biological environment, we used Proteinase K enzyme in a Tris-HCl buffer solution (pH = 8.6) at 37°C. Top down SEM images following different exposure times to the enzymatic environment are shown in Figure 2.6 (See Figure S2.7.6 for corresponding AFM data). Although the rate of PLA removal is significantly less than for the basic hydrolysis etches, the SEM data are of high quality consistent with a highly homogeneous etch over the whole of the surface. Additionally, after 45 minutes of etching the polymer film retained the characteristic fingerprint pattern with little sign of damage (Figure 5c). FTIR data confirms that at least 50% of PLA is removed in the bulk film.

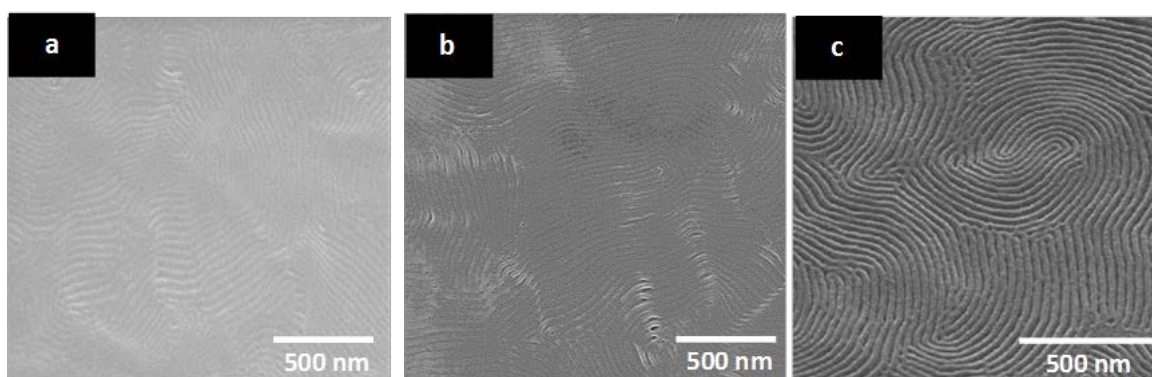


**Figure 2.6.** Top down SEM images of PS-*b*-PLA samples after immersion in a Proteinase K/Tris-HCl buffer (pH=8.6) solution at 37°C for (a) 15 minutes (b) 30 minutes (c) 45 minutes. Note SEM image (c) is at a tilt of 45°.

Further enzymatic degradation studies were carried out at extended etch periods. Exposing the film for 1 hour to the enzymatic conditions produced good porous templates with 5 nm of PLA removed over large areas as shown in Figure 2.7a. Indeed, non-destructive removal of PLA with Proteinase K could be observed for up to 3 hours when extensive damage can be seen as the PLA concentration became very low (see SEM images Figure S2.7.8 a-e).

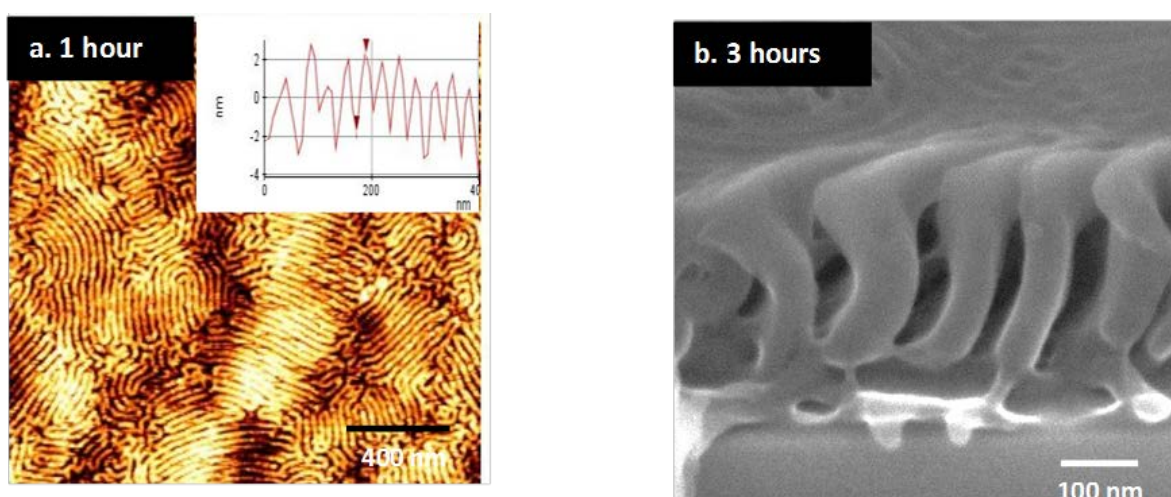


**Figure 2.7.** (a) AFM topographic image (2x2  $\mu\text{m}$ ) after 60 minutes etching with Proteinase K/Tris-HCl buffer (pH=8.6) solution at 37°C. Inset shows estimated 5 nm etched from AFM line profile. (b) Cross section SEM image after immersing in Proteinase K Tris-HCl buffer solution for 3 hours.

The cross section SEM of the sample etched in the Proteinase K solution for 3 hours is shown in Figure 2.7b revealing the PS topography after PLA removal. As observed previously for extended etching with the alkaline solutions described above, merging of the PS structures is seen in isolated areas.

#### 2.4.5. Dry Etch Studies and Route for PLA removal.

A dry etch process was also optimized to selectively remove an estimated 10 nm of PLA as determined from AFM line profiles. In Figure 2.8, AFM images a-c highlight the stepwise removal of PLA using a combination of argon and oxygen plasma with a reactive ion etcher (see experimental for details). The AFM topographic images are of high quality and show little damage over large areas.

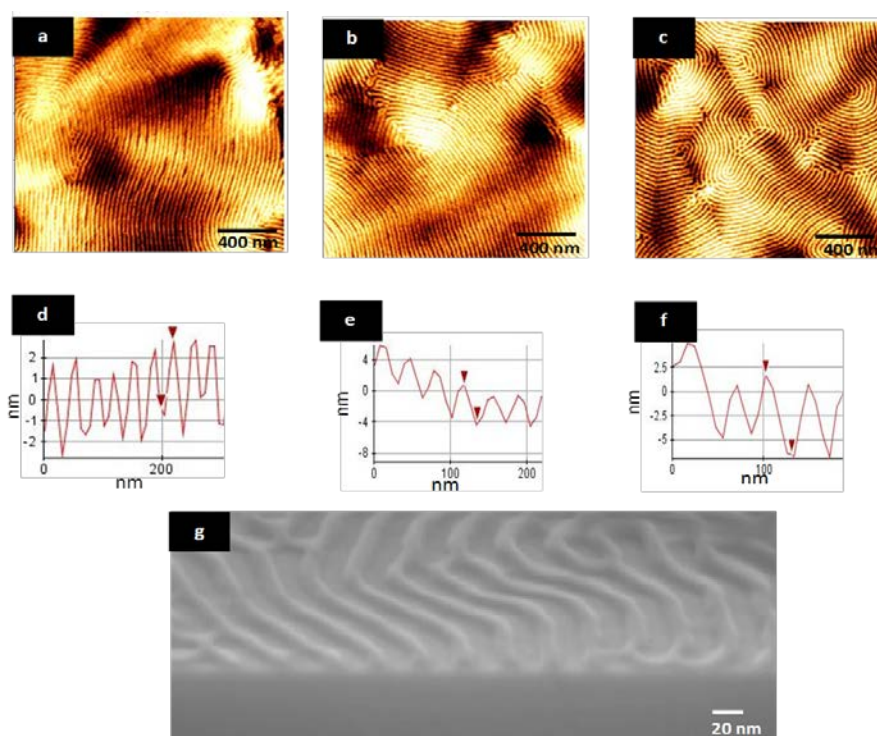


**Figure 2.8.** AFM topographic images ( $2 \times 2 \mu\text{m}$ ) after the selective removal of PLA using a reactive ion etching combination of argon and oxygen gas. Dry etching was carried out for (a) 10 seconds, (b) 15 seconds and (c) 20 seconds. (d) – (f) are AFM line profiles of etch depth of (a) – (c). (g) Cross section SEM image of PS-*b*-PLA film after 20 seconds RIE.

Figure 2.8d-f shows the corresponding line profiles of AFM images a-c. The resulting dry etch structures show a highly selective etch. PLA is etched at a faster rate than PS due to the presence of oxygen in PLA. It has been calculated from our experimental studies that the etch selectivity for PS-*b*-PLA is 1:5 (PS:PLA) which is significantly greater than that quoted for the PS-*b*-PMMA system (ranges from 1.5-2.5).<sup>54</sup> In comparison to the wet etch methodologies carried out here, the dry etch process is extremely quick, highly selective and non-destructive to the PS component. The cross section SEM image in Figure 2.8g highlights this as a well-defined PS soft mask template has been created following RIE for 20 seconds.

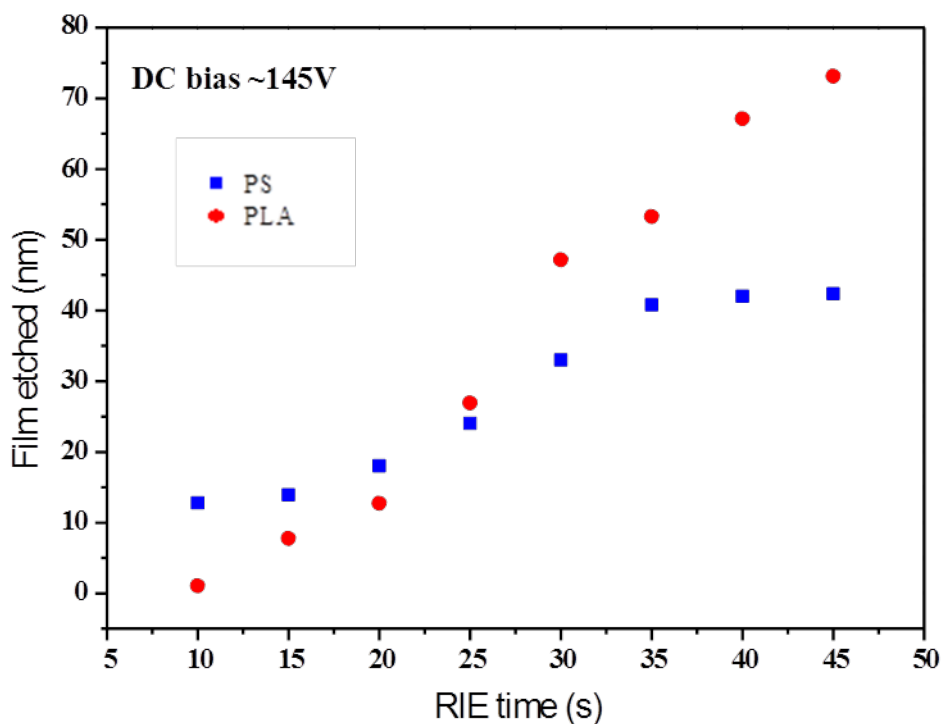
Detailed etching experiments on homopolymers (PS and PLA) and diblock copolymer (PS-*b*-PLA) thin films were carried out to understand the removal rates and behavior of films following the dry etch procedures. The etch rate of polymers has been demonstrated to be related to sputtering factor.<sup>55</sup> Since carbon has a small sputtering yield, the etching of carbon in a polymeric species will be the slowest and therefore is a rate determining step. Etch rate is inversely proportional to the number of carbon atoms. In comparison, the number of oxygen atoms in a monomer enhance the etch rate according to the Ohnishi parameter determined from equation 1:<sup>55</sup>

$$v \propto \frac{N}{N_C - N_O}$$

equation.1

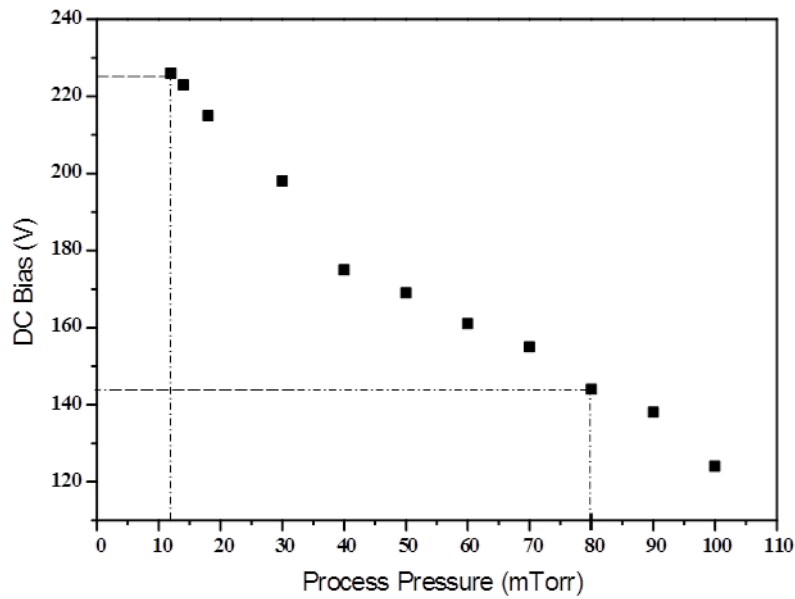
$v$  is the etch rate,  $N$  is the total number of atoms in a monomer unit while  $N_C$  and  $N_O$  are the number of carbon and oxygen atoms in a particular monomer unit. Since the number of carbon and oxygen atoms in PLA ( $C_3H_6O_3$ ) are the same, the etch rate of PLA cannot be calculated theoretically. PS and PLA homopolymer etch rates have been determined

in this work experimentally (See Figure 2.9). Although the etch rate of PS is higher at the beginning, the PLA etch rate increases at a later stage ( $t > 20$  s). This higher etch rate of PLA is correlated to the presence as well as the amount of oxygen atoms in the monomer.



**Figure 2.9.** The etch rate of PS and PLA homopolymers in RIE at DC bias 145 V. Initially PLA shows slower etch rate due to high sputtering yield C=O group, but after 20 seconds when the C=O bond is broken, PLA is etched faster than PS.

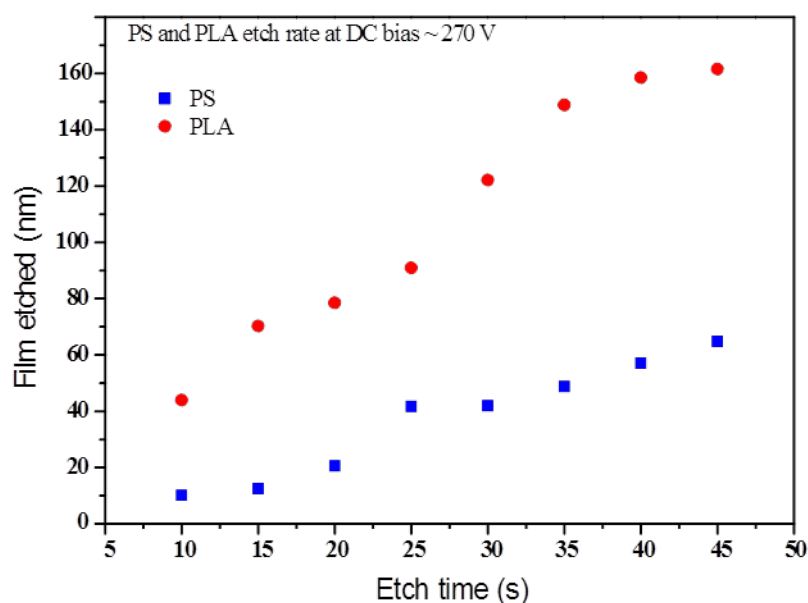
The RIE etch experiment was performed at different DC bias values. DC bias is a byproduct of the etch process and usually cannot be changed as a variable parameter. However, DC bias which occurs due to the imbalance of ion current and electron current is inversely proportional to process pressure ( $DC_{bias} \propto \frac{1}{p^2}$ ). Considering this relationship, by varying the process pressure the DC bias can be altered and tuned appropriately. The DC bias has been systematically tailored in our work (See Figure 2.10) by changing the process pressure.



**Figure 2.10.** Calibration of DC bias via process pressure. Increasing the process pressure reduces DC bias. A Good control and monitoring the DC bias is critical for stability and consistency of the results in RIE etch process.

At higher DC bias values, the PLA etch rate is higher than PS even when samples are etched for short periods. Figure 2.11 shows the PS and PLA rate at DC bias 270 V, where PLA is removed faster at all times during the etch. For example at  $t = 35$  s, PLA is removed three times faster than PS.

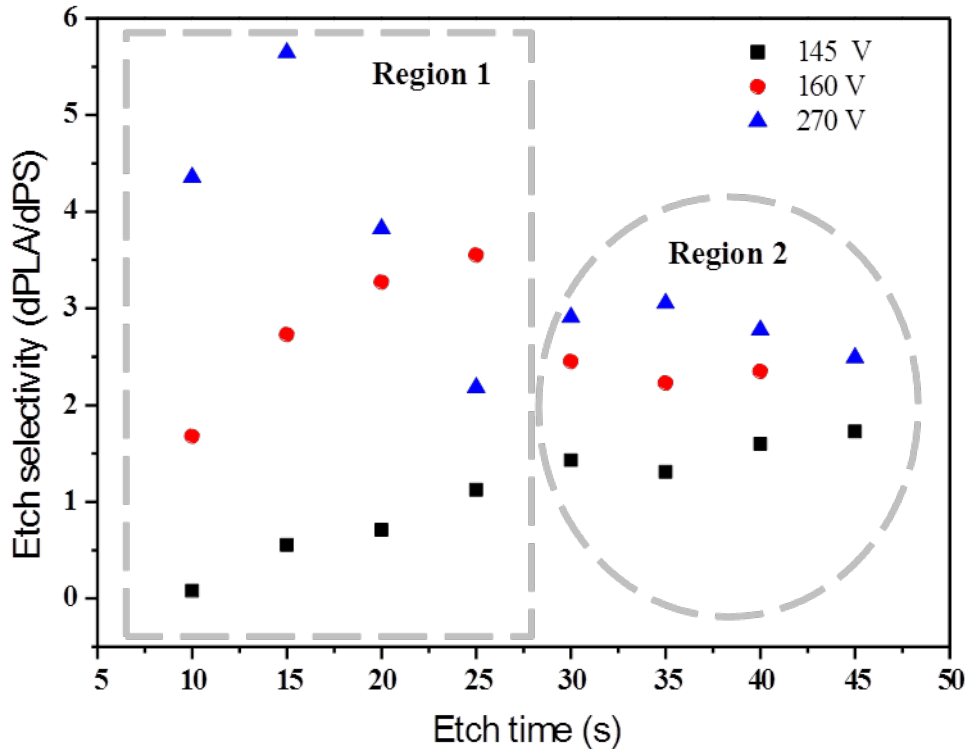
However, our results show the etch selectivity is not independent from DC bias (see Figure 2.12). Note that the etch selectivity relationship outlined in this work between PS and PLA is the ratio of PLA film removed to the etched PS layer at a given time  $\left(\frac{dPLA}{dPS}\right)$ . Depending on DC bias, different trends can be observed from our experimental data (see Figure 2.12). At lower DC bias (145 V) the etch selectivity of PS and PLA increases over time, but the increment is not dramatic and the selectivity is 1.7 at its maximum. More notably after 25 s (at DC bias 145 V), the etch selectivity remains more or less constant.



**Figure 2.11.** PS and PLA homopolymer etch rate at DC bias ~ 270 V.

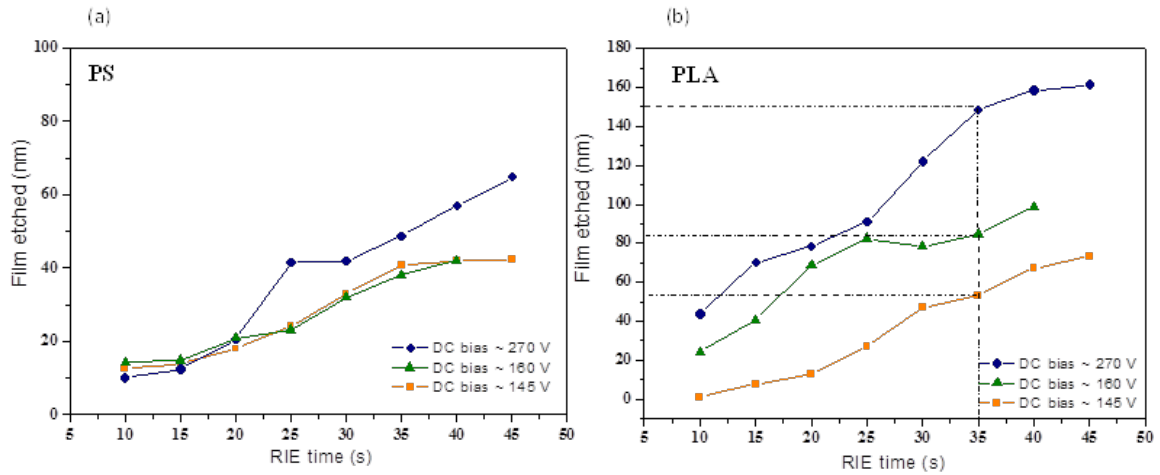
However at higher DC bias *i.e.* 270 V, it seems there are two apparent regions. At  $t < 25$  s, there is no clear trend. This is possibly due to the fact that at higher DC bias, the voltage fluctuates a lot at the beginning of RIE etch process, before it settles to the final value. This is due to higher imbalance of ions and electrons at the negative cycle of the voltage. At lower DC bias, the dispute is less predominant. For instance, in Figure 2.12, at DC bias 160 V and  $t < 25$  s, there is a systematic increase in etch selectivity of PS and PLA with time. This trend is also seen at DC bias 145 V (*i.e.* at  $t < 25$  s), but the etch rate is slower. More notably, in Figure 2.12 at  $t > 25$  s denoted as region 2, the etch selectivity is higher at increased DC bias values, but it remains almost constant or with a very little change over time for all different values of DC bias. This evidently shows the effect of DC bias on etch selectivity; at shorter times, where the DC bias is fluctuating more frequently (region 1 in Figure 2.12) the film removal rate changes with time. At longer etch times (region 2), when the DC bias is steady, the polymer films thin at nearly a constant rate. However, in region 2, the etch selectivity at any given time is greater for

higher values of DC bias. This could be due to the higher resistivity of PS to the etch conditions in comparison to PLA.



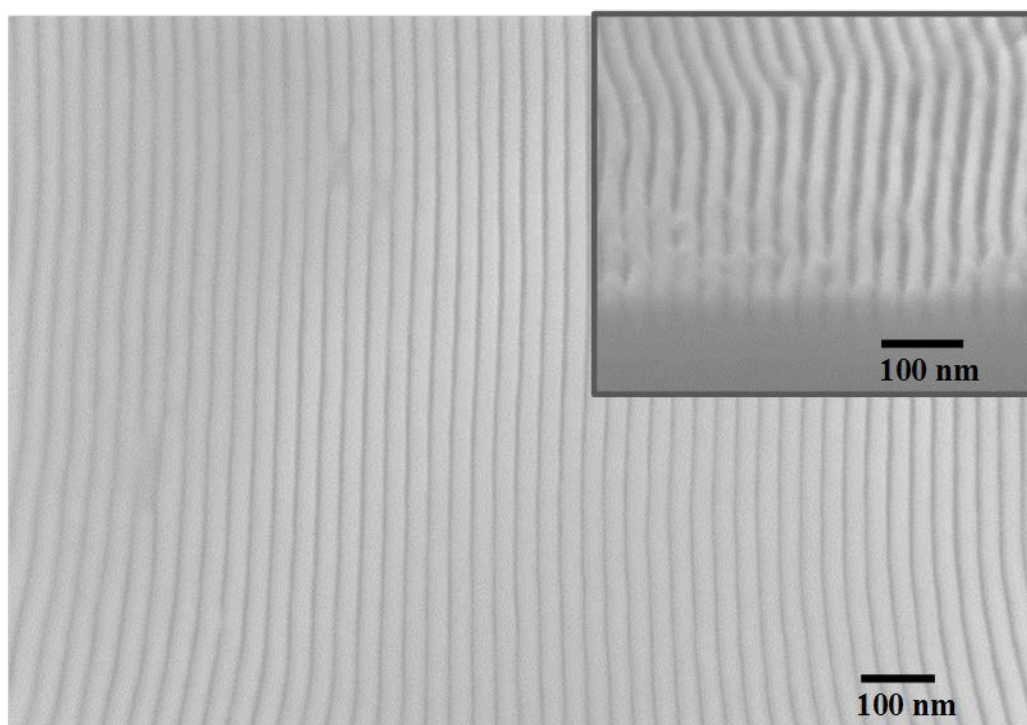
**Figure 2.12.** The effect of DC bias on etch selectivity of PS and PLA homopolymers. The fluctuation of DC bias at the beginning of RIE etch leads to unstable etch selectivity (region 1). The effect is more noticeable for higher values of DC bias (270 V in region 1). At longer times when the fluctuation is less, the etch selectivity remains mostly unchanged at any given DC bias (region 2). However, the etch selectivity is greater at higher DC bias values.

Figure 2.13a and b compares the etch rate of PS and PLA as a function of DC bias. PS etch rate is very similar at all DC bias values in particular at 145 and 160 V. For instance, at  $t = 35$  s, increasing the DC bias to 270 V etches the PS film for an extra 10 nm only (Figure 2.13a). In contrast, the etch rate of PLA is very sensitive to the DC bias. Increasing the DC bias from 145 V to 160 V and to 270 V removes PLA layers much more effectively, from 53 nm to 83 nm and 148 nm respectively, almost three times more.



**Figure 2.13.** The effect of DC bias on etch rate. (a) PS and (b) PLA homopolymers at DC bias of 145, 260 and 270 V. The effect of DC bias is more pronounced on PLA than the PS homopolymer.

Figure 2.14 shows silicon nanowires following pattern transfer using the PS soft mask template created from the selective dry etch process (further details are provided in the experimental section). The top-down image in Figure 2.14 shows uniform silicon nanowires with 16 nm feature size. Furthermore the inset reveals structures with high fidelity and a uniform etch. The etch contrast of the original polymer template is low (Figure 2.8g) from the dry etch but the resulting nanowires show high uniformity and fidelity. However the porous templates created are also ideal for metal oxide inclusion or metal evaporation techniques for fabricating a hard mask enabling higher fidelity structures to be developed following a pattern transfer process.



**Figure 2.14.** Top down SEM image of silicon nanowires following pattern transfer of PS soft mask template. Inset shows cross section SEM revealing uniformity of silicon nanostructures.

#### 2.4.6. FTIR studies of etch routes.

FTIR studies of specific films were made and illustrative data are provided here in Figure 2.15 for each of the different etch routes. The characteristic PLA peak (C=O) is observed at  $1758\text{ cm}^{-1}$ .<sup>22,56</sup> Other features in agreement with literature<sup>57</sup> include the C-H stretch at  $3000\text{ cm}^{-1}$  from the methyl/methylene groups as well as the bands in the region  $1300\text{-}950\text{ cm}^{-1}$  corresponding to the ester linkage (-CO-O-) but are not shown for the sake of brevity. (See Figure S2.7.9). The main PLA peak (C=O) is completely absent from the film that was immersed in the NaOH solution for 45 minutes and therefore the majority of PLA had been removed leaving a topographical PS pattern.

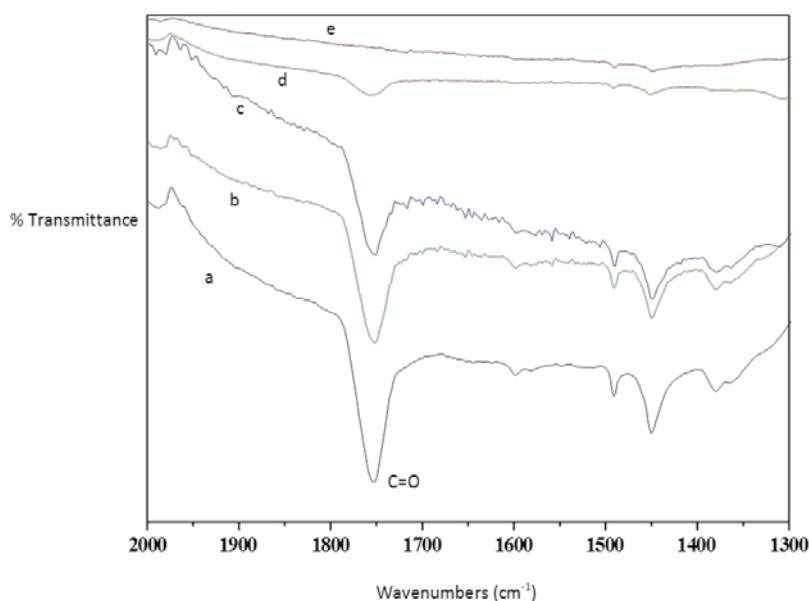


**Figure 2.15.** FTIR spectrum showing different etch routes. (a) PS-*b*-PLA film after microphase separation and prior to etching (black line), (b) following 60 minutes immersion with enzymatic approach (green), (c) 30 minutes exposure with ammonium hydroxide solution (blue), (d) 20 seconds etching with argon/oxygen RIE combination (orange) and (e) 45 minutes immersion in 0.05 M sodium hydroxide solution (red).

A similar result was found for the PS-*b*-PLA sample that had been dry etched for 20 seconds, although the reduced PLA peak suggests the existence of residual PLA material. In comparison, the 30 minute NH<sub>4</sub>OH/methanol route indicates significant PLA retention. As might be expected, Proteinase K removes PLA at a slower rate due to the associated non-aggressive nature of a biological species and is reflected in the spectrum showing the most retention of PLA of all the etch techniques. The data in the spectrum is from the film that had been treated with the enzymatic buffer solution for 1 hour that shows only partial PLA removal.

## 2.5. Conclusions

Symmetric PS-*b*-PLA can form well-ordered microphase separated structures on silicon or SOI substrates under solvo-microwave annealing. Rather unexpectedly, even quite

thick films of 200 nm form vertical lamellae despite the modified substrate interfaces favoring either PLA or PS interactions. These lamellae structures can provide robust structures as lithographic masks or porous templates if the PLA component can be readily removed. Sodium hydroxide, ammonium hydroxide and Proteinase K can all be used to form regular topographical PS patterns. These methods are also environmentally friendly. FTIR data confirmed that the NaOH and NH<sub>4</sub>OH routes removed PLA to a greater degree than the Proteinase K approach. NaOH is the most rapid of the wet etches and Proteinase K the slowest but overall Proteinase K produces less damage. It appears that autocatalytic decomposition is the cause of the greater damage in the base catalyzed etches. Crystallinity is also an issue and the PLA form and its' crystallinity will need to be considered when choosing an appropriate treatment so as to optimize the removal of PLA. All wet etches show very high etch selectivity. SEM evidence reveals PLA removal greater than 50 nm for each route following treatment for a short time period. Thinner films will be studied in the future for the wet etches in order to avoid line collapse which was a possible contributing factor to the loss of pattern quality. Because of the local variations in the thick polymer films in this work, the patterns produced are inhomogeneous. The wet etch methods are not comparable to the pattern quality achieved using the dry etch (RIE) which show excellent homogeneity. Very little damage can be seen with this anisotropic etch and this is probably due to the obvious lack of any autocatalytic effects. The etch selectivity of PS and PLA homopolymer  $\left(\frac{dPLA}{dPS}\right)$  is greatly affected by DC bias during RIE plasma process. We have demonstrated  $\left(\frac{dPLA}{dPS}\right)$  can change from 1.7 to 3 in the range of 145- 270 V DC bias. PS is more resistant to DC bias due to the lack of oxygen atoms in its structure. In comparison, PLA is etched faster due to the presence of oxygen. However, at lower DC bias it takes longer to break C=O bond

in PLA which has a high sputtering yield. At higher DC bias when the C=O bond is broken easier PLA etch rate accelerate while PS etch rate does not show the same dramatic effect. This is the main reason for variation in etch selectivity between PS and PLA homopolymers. By calibrating the DC bias via process pressure, we have optimized the etch condition for PS-*b*-PLA. The dry etch is probably more consistent with producing lithographic processes but the wet etch methods might be more likely to be used for technologies such as membrane fabrication, low cost sensor manufacture or polymeric bio-scaffolds requiring large area substrate production at low capital and operating costs.

## 2.6. References

- (1) Park, C.; Yoon, J.; Thomas, E. L. Enabling nanotechnology with self assembled block copolymer patterns. *Polymer* **2003**, *44*, 6725-6760.
- (2) Black, C. T.; Ruiz, R.; Breyta, G.; Cheng, J. Y.; Colburn, M. E.; Guarini, K. W.; Kim, H. C.; Zhang, Y. Polymer self assembly in semiconductor microelectronics. *IBM Journal of Research and Development* **2007**, *51*, 605-633.
- (3) Hamley, I. W. Nanostructure fabrication using block copolymers. *Nanotechnology* **2003**, *14*, R39-R54.
- (4) Ross, C. A.; Cheng, J. Y. Patterned magnetic media made by self-assembled block-copolymer lithography. *MRS Bulletin* **2008**, *33*, 838-845.
- (5) Botiz, I.; Darling, S. B. Optoelectronics using block copolymers. *Materials Today* **2010**, *13*, 42-51.
- (6) Bates, C. M.; Maher, M. J.; Janes, D. W.; Ellison, C. J.; Willson, C. G. Block Copolymer Lithography. *Macromolecules* **2013**, *47*, 2-12.
- (7) Luo, M.; Epps, T. H. Directed Block Copolymer Thin Film Self-Assembly: Emerging Trends in Nanopattern Fabrication. *Macromolecules* **2013**, *46*, 7567-7579.
- (8) Borah, D.; Shaw, M. T.; Holmes, J. D.; Morris, M. A. Sub-10 nm Feature Size PS-*b*-PDMS Block Copolymer Structures Fabricated by a Microwave-Assisted Solvothermal Process. *ACS Applied Materials & Interfaces* **2013**, *5*, 2004-2012.
- (9) Cushen, J. D.; Otsuka, I.; Bates, C. M.; Halila, S.; Fort, S.; Rochas, C.; Easley, J. A.; Rausch, E. L.; Thio, A.; Borsali, R.; Willson, C. G.; Ellison, C. J. Oligosaccharide/Silicon-Containing Block Copolymers with 5 nm Features for Lithographic Applications. *ACS Nano* **2012**, *6*, 3424-3433.
- (10) Liu, G.; Thomas, C. S.; Craig, G. S. W.; Nealey, P. F. Integration of Density Multiplication in the Formation of Device-Oriented Structures by Directed Assembly of Block Copolymer-Homopolymer Blends. *Advanced Functional Materials* **2010**, *20*, 1251-1257.

- (11) Stoykovich, M. P.; Müller, M.; Kim, S. O.; Solak, H. H.; Edwards, E. W.; De Pablo, J. J.; Nealey, P. F. Materials Science: Directed assembly of block copolymer blends into nonregular device-oriented structures. *Science* **2005**, *308*, 1442-1446.
- (12) Stoykovich, M. P.; Kang, H.; Daoulas, K. C.; Liu, G.; Liu, C.-C.; de Pablo, J. J.; Müller, M.; Nealey, P. F. Directed Self-Assembly of Block Copolymers for Nanolithography: Fabrication of Isolated Features and Essential Integrated Circuit Geometries. *ACS Nano* **2007**, *1*, 168-175.
- (13) Farrell, R. A.; Petkov, N.; Shaw, M. T.; Djara, V.; Holmes, J. D.; Morris, M. A. Monitoring PMMA Elimination by Reactive Ion Etching from a Lamellar PS-*b*-PMMA Thin Film by ex Situ TEM Methods. *Macromolecules* **2010**, *43*, 8651-8655.
- (14) Rasappa, S.; Borah, D.; Senthamarikannan, R.; Faulkner, C. C.; Shaw, M. T.; Gleeson, P.; Holmes, J. D.; Morris, M. A. Block copolymer lithography: Feature size control and extension by an over-etch technique. *Thin Solid Films* **2012**, *522*, 318-323.
- (15) Farrell, R. A.; Kinahan, N. T.; Hansel, S.; Stuen, K. O.; Petkov, N.; Shaw, M. T.; West, L. E.; Djara, V.; Dunne, R. J.; Varona, O. G.; Gleeson, P. G.; Jung, S. J.; Kim, H. Y.; Kolešnik, M. M.; Lutz, T.; Murray, C. P.; Holmes, J. D.; Nealey, P. F.; Duesberg, G. S.; Krstić, V.; Morris, M. A. Large-scale parallel arrays of silicon nanowires via block copolymer directed self-assembly. *Nanoscale* **2012**, *4*, 3228-3236.
- (16) Ting, Y.-H.; Park, S.-M.; Liu, C.-C.; Liu, X.; Himpsel, F. J.; Nealey, P. F.; Wendt, A. E. Plasma etch removal of poly(methyl methacrylate) in block copolymer lithography. *Journal of Vacuum Science & Technology B: Microelectronics and Nanometer Structures* **2008**, *26*, 1684-1689.
- (17) Borah, D.; Shaw, M. T.; Rasappa, S.; Farrell, R. A.; Mahony, C. O.; Faulkner, C. M.; Bosea, M.; Gleeson, P.; Holmes, J. D.; Morris, M. A. Plasma etch technologies for the development of ultra-small feature size transistor devices. *Journal of Physics D: Applied Physics* **2011**, *44*, 174012.
- (18) Hillmyer, M.: Nanoporous Materials from Block Copolymer Precursors. In *Block Copolymers II*; Abetz, V., Ed.; Advances in Polymer Science; Springer Berlin Heidelberg, **2005**; Vol. 190; pp 137-181.
- (19) Ghoshal, T.; Senthamarikannan, R.; Shaw, M. T.; Holmes, J. D.; Morris, M. A. "In situ" hard mask materials: a new methodology for creation of vertical silicon nanopillar and nanowire arrays. *Nanoscale* **2012**, *4*, 7743-7750.
- (20) Ghoshal, T.; Maity, T.; Senthamarikannan, R.; Shaw, M. T.; Carolan, P.; Holmes, J. D.; Roy, S.; Morris, M. A. Size and space controlled hexagonal arrays of superparamagnetic iron oxide nanodots: magnetic studies and application. *Scientific Reports* **2013**, *3*.
- (21) Ghoshal, T.; Senthamarikannan, R.; Shaw, M. T.; Holmes, J. D.; Morris, M. A. Fabrication of ordered, large scale, horizontally-aligned Si nanowire arrays based on an in situ hard mask block copolymer approach. *Advanced Materials* **2014**, *26*, 1207-1216.
- (22) Keen, I.; Yu, A.; Cheng, H.-H.; Jack, K. S.; Nicholson, T. M.; Whittaker, A. K.; Blakey, I. Control of the Orientation of Symmetric Poly(styrene)-*block*-poly(d,l-lactide) Block Copolymers Using Statistical Copolymers of Dissimilar Composition. *Langmuir* **2012**, *28*, 15876-15888.
- (23) Zalusky, A. S.; Olayo-Valles, R.; Wolf, J. H.; Hillmyer, M. A. Ordered Nanoporous Polymers from Polystyrene-Polylactide Block Copolymers. *Journal of the American Chemical Society* **2002**, *124*, 12761-12773.
- (24) Crossland, E. J. W.; Ludwigs, S.; Hillmyer, M. A.; Steiner, U. Freestanding nanowire arrays from soft-etch block copolymer templates. *Soft Matter* **2007**, *3*, 94-98.

- (25) Crossland, E. J. W.; Cunha, P.; Scroggins, S.; Moratti, S.; Yurchenko, O.; Steiner, U.; Hillmyer, M. A.; Ludwigs, S. Soft-Etch Mesoporous Hole-Conducting Block Copolymer Templates. *ACS Nano* **2010**, *4*, 962-966.
- (26) Bolton, J.; Bailey, T. S.; Rzayev, J. Large Pore Size Nanoporous Materials from the Self-Assembly of Asymmetric Bottlebrush Block Copolymers. *Nano Letters* **2011**, *11*, 998-1001.
- (27) Olayo-Valles, R.; Guo, S. W.; Lund, M. S.; Leighton, C.; Hillmyer, M. A. Perpendicular domain orientation in thin films of polystyrene - Polylactide diblock copolymers. *Macromolecules* **2005**, *38*, 10101-10108.
- (28) Baruth, A.; Rodwogin, M. D.; Shankar, A.; Erickson, M. J.; Hillmyer, M. A.; Leighton, C. Non-lift-off Block Copolymer Lithography of 25 nm Magnetic Nanodot Arrays. *ACS Applied Materials & Interfaces* **2011**, *3*, 3472-3481.
- (29) Han, W.; Byun, M.; Zhao, L.; Rzayev, J.; Lin, Z. Q. Controlled evaporative self-assembly of hierarchically structured bottlebrush block copolymer with nanochannels. *Journal of Materials Chemistry* **2011**, *21*, 14248-14253.
- (30) Torres, A.; Li, S. M.; Roussos, S.; Vert, M. Degradation of L- and DL-Lactic acid oligomers in the presence of fusarium moniliforme and pseudomonas putida. *Journal of Environmental Polymer Degradation* **1996**, *4*, 213-223.
- (31) Li, S.; Molina, I.; Bueno Martinez, M.; Vert, M. Hydrolytic and enzymatic degradations of physically crosslinked hydrogels prepared from PLA/PEO/PLA triblock copolymers. *Journal of Materials Science: Materials in Medicine* **2002**, *13*, 81-86.
- (32) Tsuji, H.; Kidokoro, Y.; Mochizuki, M. Enzymatic degradation of poly(L-lactic acid) fibers: Effects of small drawing. *Journal of Applied Polymer Science* **2007**, *103*, 2064-2071.
- (33) Fukushima, K.; Abbate, C.; Tabuani, D.; Gennari, M.; Camino, G. Biodegradation of poly(lactic acid) and its nanocomposites. *Polymer Degradation and Stability* **2009**, *94*, 1646-1655.
- (34) Cai, H.; Dave, V.; Gross, R. A.; McCarthy, S. P. Effects of physical aging, crystallinity, and orientation on the enzymatic degradation of poly(lactic acid). *Journal of Polymer Science Part B: Polymer Physics* **1996**, *34*, 2701-2708.
- (35) Haubruge, H. G.; Jonas, A. M.; Legras, R. Staining of poly(ethylene terephthalate) by ruthenium tetroxide. *Polymer* **2003**, *44*, 3229-3234.
- (36) Mokarian-Tabari, P.; Cummins, C.; Rasappa, S.; Simao, C.; Sotomayor Torres, C. M.; Holmes, J. D.; Morris, M. A. Study of the Kinetics and Mechanism of Rapid Self-Assembly in Block Copolymer Thin Films during Solvo-Microwave Annealing. *Langmuir* **2014**, *30*, 10728-10739.
- (37) Zhang, X.; Harris, K. D.; Wu, N. L. Y.; Murphy, J. N.; Buriak, J. M. Fast Assembly of Ordered Block Copolymer Nanostructures through Microwave Annealing. *ACS Nano* **2010**, *4*, 7021-7029.
- (38) Borah, D.; SenthamaraiKannan, R.; Rasappa, S.; Kosmala, B.; Holmes, J. D.; Morris, M. A. Swift Nanopattern Formation of PS-*b*-PMMA and PS-*b*-PDMS Block Copolymer Films Using a Microwave Assisted Technique. *ACS Nano* **2013**, *7*, 6583-6596.
- (39) Vayer, M.; Hillmyer, M. A.; Dirany, M.; Thevenin, G.; Erre, R.; Sinturel, C. Perpendicular orientation of cylindrical domains upon solvent annealing thin films of polystyrene-*b*-polylactide. *Thin Solid Films* **2010**, *518*, 3710-3715.
- (40) Borah, D.; Rasappa, S.; SenthamaraiKannan, R.; Kosmala, B.; Shaw, M. T.; Holmes, J. D.; Morris, M. A. Orientation and Alignment Control of Microphase-Separated PS-*b*-PDMS Substrate Patterns via Polymer Brush Chemistry. *ACS Applied Materials & Interfaces* **2012**, *5*, 88-97.

- (41) Borah, D.; Rasappa, S.; Senthamaraikannan, R.; Holmes, J. D.; Morris, M. A. Tuning PDMS Brush Chemistry by UV–O<sub>3</sub> Exposure for PS-*b*-PDMS Microphase Separation and Directed Self-assembly. *Langmuir* **2013**, *29*, 8959-8968.
- (42) Vayer, M.; Nguyen, T. H.; Grosso, D.; Boissiere, C.; Hillmyer, M. A.; Sinturel, C. Characterization of Nanoporous Polystyrene Thin Films by Environmental Ellipsometric Porosimetry. *Macromolecules* **2011**, *44*, 8892-8897.
- (43) Lo, K.-H.; Chen, M.-C.; Ho, R.-M.; Sung, H.-W. Pore-Filling Nanoporous Templates from Degradable Block Copolymers for Nanoscale Drug Delivery. *ACS Nano* **2009**, *3*, 2660-2666.
- (44) Hsueh, H.-Y.; Ho, R.-M. Bicontinuous Ceramics with High Surface Area from Block Copolymer Templates. *Langmuir* **2012**, *28*, 8518-8529.
- (45) Garlotta, D. A Literature Review of Poly(Lactic Acid). *Journal of Polymers and the Environment* **2001**, *9*, 63-84.
- (46) Tabi, T.; Sajo, I. E.; Szabo, F.; Luyt, A. S.; Kovacs, J. G. Crystalline structure of annealed polylactic acid and its relation to processing. *Express Polymer Letters* **2010**, *4*, 659-668.
- (47) Zalusky, A. S.; Olayo-Valles, R.; Taylor, C. J.; Hillmyer, M. A. Mesoporous Polystyrene Monoliths. *Journal of the American Chemical Society* **2001**, *123*, 1519-1520.
- (48) de Jong, S. J.; Arias, E. R.; Rijkers, D. T. S.; van Nostrum, C. F.; Kettenes-van den Bosch, J. J.; Hennink, W. E. New insights into the hydrolytic degradation of poly(lactic acid): participation of the alcohol terminus. *Polymer* **2001**, *42*, 2795-2802.
- (49) Liu, C.-C.; Nealey, P. F.; Ting, Y.-H.; Wendt, A. E. Pattern transfer using poly(styrene-*block*-methyl methacrylate) copolymer films and reactive ion etching. *Journal of Vacuum Science & Technology B* **2007**, *25*, 1963-1968.
- (50) Siparsky, G.; Voorhees, K.; Miao, F. Hydrolysis of Polylactic Acid (PLA) and Polycaprolactone (PCL) in Aqueous Acetonitrile Solutions: Autocatalysis. *Journal of Environmental Polymer Degradation* **1998**, *6*, 31-41.
- (51) Chen, Y.; Zhou, S.; Li, Q. Mathematical modeling of degradation for bulk-erosive polymers: Applications in tissue engineering scaffolds and drug delivery systems. *Acta Biomaterialia* **2011**, *7*, 1140-1149.
- (52) Nugroho, P.; Mitomo, H.: *Study of Biodegradation and Improvement of Heat Stability of Poly(lactic acid) by Irradiation at High Temperature*: Malaysian Polymer Journal, 2008; Vol. 3. pp. 27-37.
- (53) Zhao, L.; Byun, M.; Rzayev, J.; Lin, Z. Polystyrene–Polylactide Bottlebrush Block Copolymer at the Air/Water Interface. *Macromolecules* **2009**, *42*, 9027-9033.
- (54) Cheng, H.-H.; Keen, I.; Yu, A.; Chuang, Y.-M.; Blakey, I.; Jack, K. S.; Leeson, M. J.; Younkin, T. R.; Whittaker, A. K. In *Tilte* 2012.
- (55) Gokan, H.; Esho, S.; Ohnishi, Y. Dry etch resistance of organic materials. *Journal of the Electrochemical Society* **1983**, *130*, 143-146.
- (56) Amendt, M. A.; Roerdink, M.; Moench, S.; Phillip, W. A.; Cussler, E. L.; Hillmyer, M. A. Functionalized Nanoporous Membranes from Reactive Triblock Polymers. *Australian Journal of Chemistry* **2011**, *64*, 1074-1082.
- (57) Kaitian, X.; Kozluca, A.; Denkbass, E. B.; Piskin, E. Poly (D,L-lactic acid) homopolymers: Synthesis and characterization. *Turkish Journal of Chemistry* **1996**, *20*, 43-53.

## 2.7. Appendix – Chapter 2

### Selective Etching of Polylactic Acid in Poly(styrene)-*block*-poly(D,L)lactide Diblock Copolymer for Nanoscale Patterning

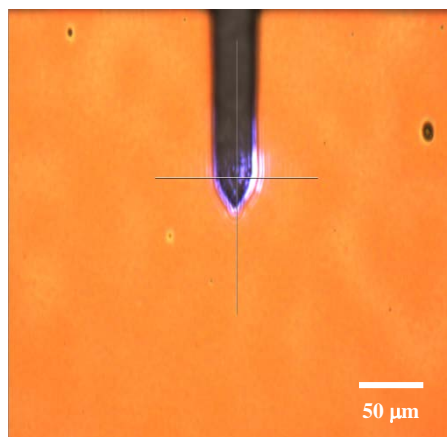


**Figure S2.7.1.** Optical image of PS-*b*-PLA film surface after solvo-microwave annealing showing high surface coverage.

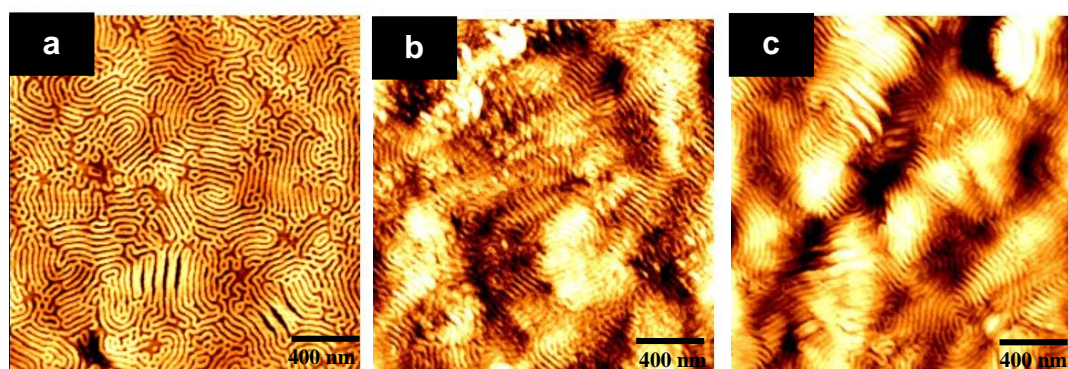


**Figure S2.7.2.** AFM topographic images ( $2 \times 2 \mu\text{m}$ ) of partial PLA degradation using 0.05 M sodium hydroxide/methanol solution. (a) 15 minutes immersion (b) 30 minutes immersion (c) 45 minutes immersion.

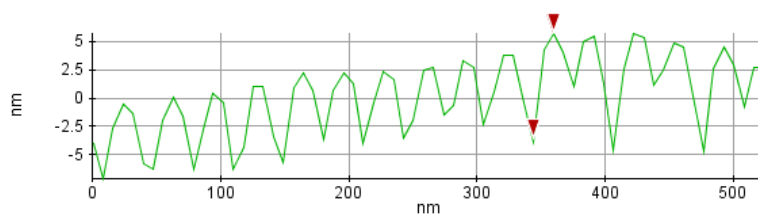


**Figure S2.7.3.** AFM line profile after 15 minutes etching in 0.05 M NaOH solution, estimated 10 nm PLA etched.

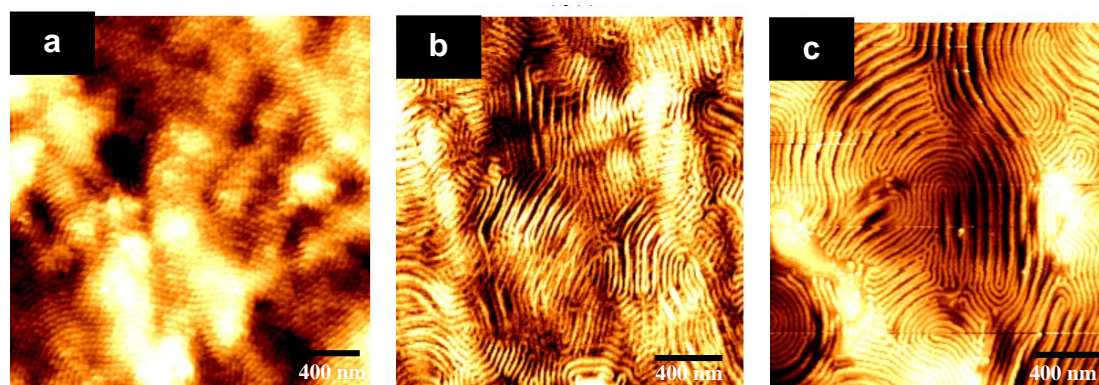


**Figure S2.7.4.** AFM topographic images ( $2 \times 2 \mu\text{m}$ ) of partial PLA degradation using an ammonium hydroxide/methanol solution. (a) 10 minutes immersion (b) 20 minutes immersion (c) 30 minutes immersion.

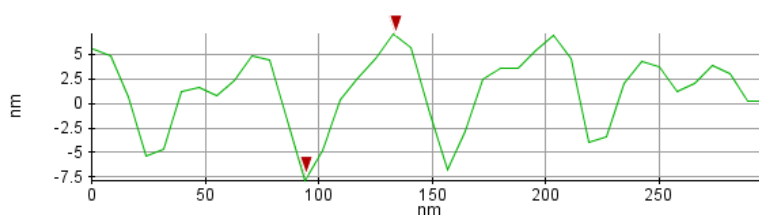


**Figure S2.7.5.** AFM line profile after 30 minutes etching in ammonium hydroxide solution, estimated 15 nm PLA etched.

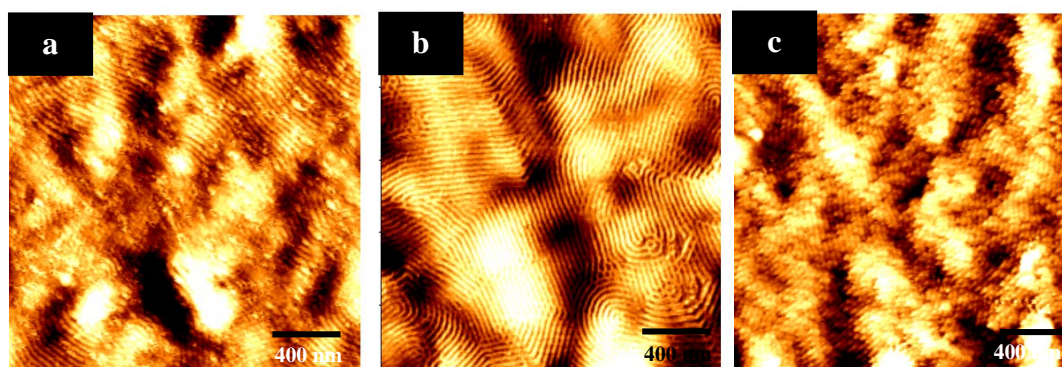


**Figure S2.7.6.** AFM topographic images (2x2  $\mu\text{m}$ ) of partial PLA degradation using a Proteinase K/Tris-HCl buffer (pH=8.6) solution at 37°C. (a) 15 minutes immersion (b) 30 minutes immersion (c) 45 minutes immersion.

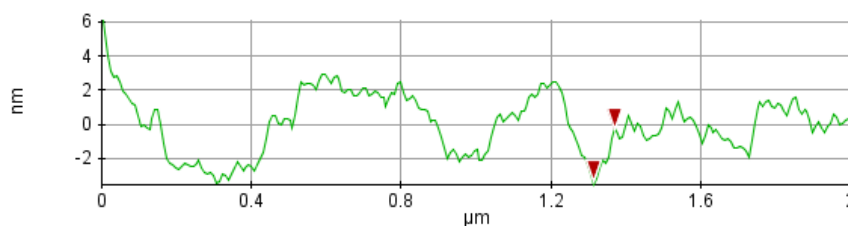


**Figure S2.7.7.** AFM line profile after 45 minutes etching in Proteinase K solution, estimated 3 nm PLA etched.

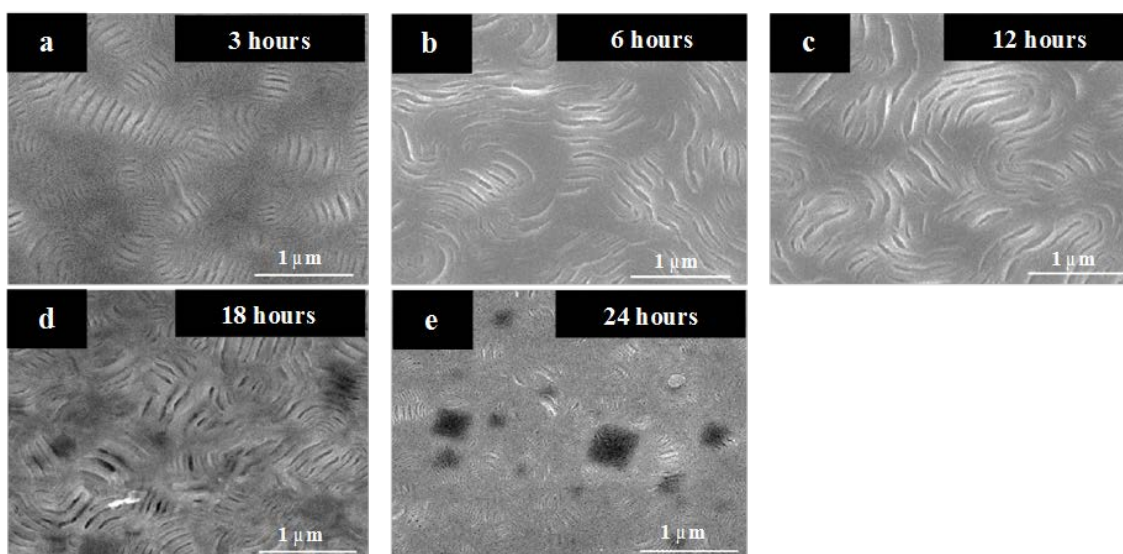


**Figure S2.7.8.** SEM images of extended enzyme etching with Proteinase K for (a) 3 hours, (b) 6 hours, (c) 12 hours, (d) 18 hours and (e) 24 hours.

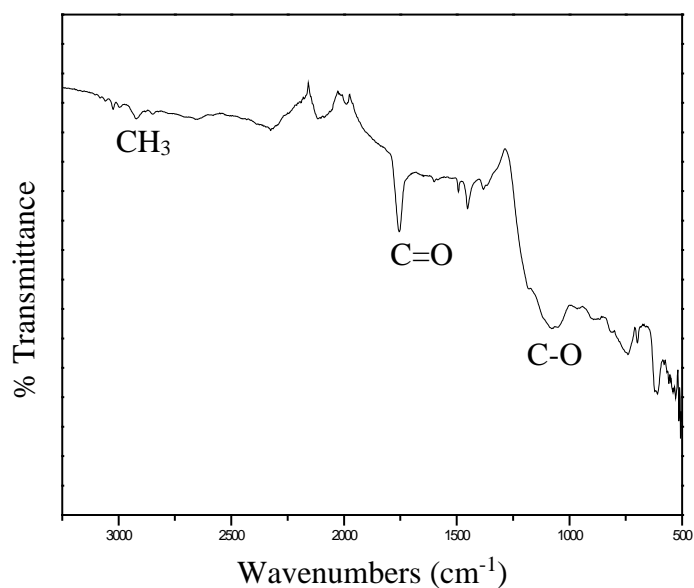


**Figure S2.7.9.** FTIR spectrum between 3500 cm<sup>-1</sup> to 500 cm<sup>-1</sup> showing characteristic PLA peaks. This is the complete FTIR spectrum of line a from Figure 2.15. showing the characteristic peaks in PS-*b*-PDLLA film. Note that this spectrum is of a self-assembled PS-*b*-PLA pattern and is without any etching.

---

## *Chapter 3*

---

**Directed self-assembly of lamellar forming poly(styrene)-*block*-poly(D,L-lactide) block copolymer thin films via solvo-thermal vapor annealing for on-chip etch mask application**

### 3.1. Abstract

Solvo-thermal vapor annealing (STVA) was employed to induce microphase separation in a lamellar forming semicrystalline block copolymer (BCP) thin film containing a rapidly degradable block. Directed self-assembly of poly(styrene)-*block*-poly(D,L-lactide) (PS-*b*-PLA) BCP films via topographically patterned silicon nitride was demonstrated with alignment over macroscopic areas. Interestingly, we observed lamellar patterns aligned parallel as well as perpendicular to graphoepitaxial guiding patterns. PS-*b*-PLA BCP microphase separated with high a degree of order in an atmosphere of tetrahydrofuran (THF) with an elevated vapor pressure (at ca. 40-60°C). Grazing incidence small angle X-ray scattering (GISAXS) measurements of PS-*b*-PLA films reveals the through-film uniformity of perpendicular domains after STVA. Lamellar perpendicular orientation was observed on both hydrophilic and relatively hydrophobic surfaces with a periodicity of  $\sim 32.5$  nm ( $L_0$ ). The rapid removal of the PLA domains is demonstrated using a mild basic solution for the development of a well-defined PS mask template. GISAXS data reveals the through-film uniformity is retained following wet etching. The results in this chapter demonstrate highly oriented PS-*b*-PLA microdomains after a short annealing period and facile PLA removal forming porous on-chip etch masks for nanolithography application.

### 3.2. Introduction

Nanoscale patterning of thin films using BCP self-assembly is a facile and low cost route to form well-registered and highly defined domains from 3-100 nm.<sup>1</sup> Depending on the BCP compositional design, arrangements with lamellar, spherical, cylindrical, and gyroidal geometries can be developed over arbitrarily large areas. Desired length scales of geometries from a few tens of nanometres to a hundred nanometres can be accessed

via alternating volume fraction ( $f$ ) and through tailoring of the BCP chain lengths, *i.e.* degree of polymerization ( $N$ ). Such complex yet ordered nanodomains provide an ideal platform for use in neuroprosthetic technologies,<sup>2</sup> membrane/filtration systems,<sup>3,4</sup> magnetic storage devices<sup>5,6</sup> and photovoltaics.<sup>7,8</sup> Another potential application has focused on using BCP templates as on-chip etch masks for next-generation lithography.<sup>9</sup>

Directed self-assembly (DSA) of BCPs is a promising candidate for augmenting the lithographic patterning process to enable higher computing speed and reduced power consumption per device function (*i.e.* Moore's Law).<sup>10</sup> Two key challenges in the BCP nanolithography field include the placement and registration of features and the ability to define ultra-small critical dimensions. Graphoepitaxy is used to obtain long range order and alignment of BCP features via trenches lithographically defined prior to BCP deposition and self-assembly.<sup>11-14</sup> Similarly, chemoepitaxy developed by Nealey and co-workers demonstrates extreme precision by using lithographically defined chemical patterns to control PS-*b*-poly(methyl methacrylate, PMMA) assembly and alignment.<sup>15,16</sup> Low line edge roughness of resulting pattern transferred nanostructures, high areal density and ease of processing (and similarity to industry patterning) are some of the main attributes that have placed graphoepitaxy and chemoepitaxy at the forefront of alternative patterning methodologies. BCP material criteria beyond the "first generation" PS-*b*-PMMA include a BCP possessing a high Flory-Huggins interaction parameter (*i.e.*  $\chi$ ) and high etch contrast to allow sub-10 nm critical dimensions (CD) to be attained following pattern transfer. New BCP materials possessing a high  $\chi$  have been reported of late which can access sub-10 nm feature sizes.<sup>17-21</sup>

Shear force,<sup>22</sup> magnetic fields<sup>23</sup> and thermal annealing<sup>24</sup> are routinely employed for the self-assembly of BCP thin film morphologies. More recently, microwave irradiation was

shown to induce self-assembly in a range of high  $\chi$  BCPs in sub-2 minute processes.<sup>25-29</sup> Controlling BCP nanodomain orientation is paramount for a particular technological application. In this regard, solvent vapor annealing (SVA) has been utilized to induce self-assembly and manipulate microdomain orientation.<sup>30</sup> SVA is a technique that plasticizes polymer material and the solvent-polymer interaction reduces the diffusive energy barrier promoting microphase separation at lower temperatures.<sup>31</sup> Despite its widespread use the interpretation and exact mechanism(s) of the SVA method is not fully understood. Various mechanisms have been postulated from empirical evidence. Gu *et al.*<sup>32,33</sup> have recently provided an insight on poly(styrene)-*block*-poly(2-vinylpyridine) (PS-*b*-P2VP) BCPs and highlight the importance of taking into account the processing conditions such as swelling ratio of BCP films and solvent removal rates during SVA. The work by Gu *et al.* further emphasizes the benefits of GISAXS as a characterization method that has also been carried out on other BCP systems regarding swelling effects.<sup>34,35</sup> Likewise, Mokarian *et al.*<sup>36</sup> employed an *in-situ* time-resolved light scattering device to observe a “flipping” phenomenon in hexagonal forming PS-*block*-polyethylenoxide (PS-*b*-PEO) films that was related to vapor pressure threshold value. In addition to using a solvent to impart mobility in a BCP, combining the solvent vapors with temperature to increase vapor pressure also enhances the ordering dynamics of BCPs.<sup>31,37</sup> The complex interplay of surface energetics and confinement effects of BCPs in thin film form requires extensive solvent analysis. Each polymer block swells at different rates depending on the selectivity of the exposed solvent. Screening of solvent molecules occurs at the interface of the two blocks of a BCP as defined by equation 1 below.<sup>36,38</sup>

$$\chi_{\text{eff}} = \chi(1 - \Phi_s) \quad (1)$$

where  $\chi_{\text{eff}}$  and  $\chi$  are the Flory-Huggins interaction parameters in the presence and absence of the solvent. Parameter  $\Phi_s$  is the volume fraction of solvent. From equation 1, solvent uptake by the polymer film will reduce the overall  $\chi$  of the system, however solvent use is required to reduce the glass transition of the PS block enabling microphase separation.<sup>38</sup> Lamellar PS-*b*-PLA studies to date have focused mainly on thermal annealing.<sup>39,40</sup> Keen *et al.*<sup>40</sup> have demonstrated DSA of PS-*b*-PLA with sub-10 nm feature sizes and outlined key contributions on the relationship between defect levels and degree of frustration of polymer chains under confinement.

We present a systematic study using AFM data complemented by GISAXS analysis on the STVA behavior and microphase separation of a near symmetric forming PS-*b*-PLA BCP. We show through STVA the microphase separation of PS-*b*-PLA (21,000 g mol<sup>-1</sup> - 19,500 g mol<sup>-1</sup>) BCP system and the DSA of line patterns on topographically patterned silicon nitride substrates. GISAXS provided an interesting insight on the interior orientation of the PS-*b*-PLA films following STVA. Our studies showed that microphase separated BCP patterns were attained only through increasing THF vapor pressure using a higher processing temperature. Periodicity ( $L_0$ ) of the microphase domains was measured at 32 nm. Morphological changes were observed in films of  $\sim 1.47 L_0$  ( $\sim 48$  nm) up to 45-60 minutes with PS-*b*-PLA possessing patterns with long average line lengths. Wet etching of the PLA component in PS-*b*-PLA films is also detailed showing a high degree of selectivity.

### 3.3. Experimental

**Materials.** Polystyrene-*block*-polylactide (referred to as PS-*b*-PLA, but note that PLA is in the DL form) was purchased from Polymer Source, Inc., Canada, with a total number

average molecular weight of  $M_n = 40.5 \text{ kg mol}^{-1}$  ( $M_{nPS} = 21 \text{ kg mol}^{-1}$ ;  $M_{nPLA} = 19.5 \text{ kg mol}^{-1}$ ,  $f_{PS} = 0.53$ ), a polydispersity index of 1.15 and was used without further purification or treatment. The planar substrates used were highly polished single-crystal silicon  $\langle 100 \rangle$  wafers (p-type) with a native oxide layer of 2 nm. Silicon nitride ( $\text{Si}_3\text{N}_4$ ) substrates used composed of a low pressure chemical vapor deposition deposited  $\text{Si}_3\text{N}_4$  coated substrate (resistivity,  $\rho = 1 \times 10^{14}$  to  $1 \times 10^{16} \text{ } \Omega \text{ cm}$ ) on p-type silicon  $\langle 100 \rangle$  with a surface  $\text{SiO}_2$  layer  $\sim 7$  nm thick. Topographically patterned  $\text{Si}_3\text{N}_4$  substrates with pitches in the range of 50–500 nm, variable mesa widths of 30–700 nm, and depth of  $\sim 50$ –60 nm were fabricated via 193 nm UV-lithography and processed by means of conventional mask and etch techniques. SEM and TEM characterization of the  $\text{Si}_3\text{N}_4$  substrates can be found elsewhere.<sup>27</sup> Sulfuric acid (ACS reagent, 95.0–98.0%), hydrogen peroxide (containing inhibitor, 30 wt. % in  $\text{H}_2\text{O}$ , ACS reagent), methanol (for HPLC,  $\geq 99.9\%$ ) chloroform (HPLC grade,  $\geq 99.9\%$ , contains 0.5–1.0% ethanol as stabilizer), toluene (for HPLC, 99.9%), tetrahydrofuran (THF) (HPLC grade,  $\geq 99.9\%$ ), hexamethyldisilazane, sodium hydroxide (purum p.a.,  $\geq 98.0\%$  (T), beads), ruthenium(III) chloride hydrate, and sodium hypochlorite solution (6–14% active chlorine basis) were all purchased from Sigma Aldrich.

**Substrate Cleaning, Block Copolymer Preparation and Deposition.** Substrates were cut into  $2.0 \text{ cm}^2$  pieces and were cleaned in a piranha solution (1 : 3 v/v 30%  $\text{H}_2\text{O}_2$  :  $\text{H}_2\text{SO}_4$ ) (Caution – piranha solution may cause explosion in contact with organic material) at  $100^\circ\text{C}$  for 30 minutes, rinsed with DI waters several times and dried using nitrogen gas. Following this, the freshly piranha cleaned substrates were sonicated with chloroform (*i.e.* BCP casting solvent) for 10 minutes. Substrates that were functionalized with a hexamethyldisilazane (HMDS) layer were first sonicated with acetone followed by methanol (20 minutes sonication in each). After sonication, the substrates were

immersed in a solution of toluene:HMDS (1:5) for ~16 hours, as described previously in the literature.<sup>41</sup> 0.5 wt % solutions of PS-*b*-PLA were prepared in chloroform and subsequently sonicated for 30 minutes. Following complete dissolution, PS-*b*-PLA solution was spin coated on piranha cleaned silicon substrates at 2000 rpm for 30 seconds. 0.5 wt % PS-*b*-PLA solutions were spin coated on HMDS treated silicon in the same manner. Note that the HMDS step was carried out so that film delamination was avoided via promotion of PS adhesion onto the HMDS functionalized substrate. Following PS-*b*-PLA deposition, solvent vapor annealing (SVA) treatment was carried out. Films were placed inside a glass jar (150 ml) with a small vial containing ~1 ml of THF solvent for up to 60 minutes. This was the standard protocol for all temperatures; room temperature, 40°C and 55°C were examined. Prior to STVA films at room temperature, the vial containing THF solvent was placed inside the annealing jar for up to 20 minutes before sample to ensure a saturated THF atmosphere was reached. Following the desired SVA or STVA period, the film was removed immediately and solvent was allowed to evaporate at ambient conditions before characterization.

**Grazing Incidence Small Angle X-Ray Scattering (GISAXS).** GISAXS experiments were performed at 8 KeV at an incidence angle of 0.22° (above the critical angle of the film, probing inside the film and just at the critical angle of silicon). All patterns are an average of about 10 frames, to reduce the signal to noise ratio.

**PLA block degradation/etch.** A 0.01M NaOH (60:40, water:methanol) solution was prepared at room temperature. The solution was given sufficient time (~15 minutes) in order to fully dissolve. STVA PS-*b*-PLA films were then immersed in the basic solution for up to 5 minutes. After removal from the degradation solution, films were washed twice with deionized water and blown dry under nitrogen. Etching of thicker PS-*b*-PLA films formed via “solvo-microwave” annealing is detailed in a prior publication.<sup>42</sup>

**Characterization. Film Thickness.** BCP film thicknesses were measured with a spectroscopic ellipsometer “J.A. Woollam Ellipsometer” at a fixed angle of incidence of  $70^\circ$ , on at least five different places on the sample and was averaged as the film thickness. A layer model ( $\text{SiO}_2 + \text{BCP}$ ) for total BCP film was used to simulate experimental data.

**Atomic Force Microscopy (AFM).** AFM (Park systems, XE-100) was operated in AC (tapping) mode under ambient conditions using silicon microcantilever probe tips with a force constant of  $42 \text{ N m}^{-1}$ . Topographic and phase images were recorded simultaneously.

**Scanning Electron Microscopy (SEM).** SEM images were obtained by a FEI Helios Nanolab 600i system at an accelerating voltage of 5 kV and at a working distance of 4 mm. Cross-section SEM images involved cleaving the substrate in half and positioning the substrate perpendicular to the incident beam of electrons. The stage was then tilted at  $20^\circ$  to  $30^\circ$ .

**Fourier Transform-Infrared (FT-IR) Spectroscopy.** An IR660, Varian infrared spectrometer was used to record the FT-IR spectra. The FT-IR was operated in ATR mode during measurements. The measurements were performed in the spectral range of  $4000$  to  $400 \text{ cm}^{-1}$ , with a resolution of  $1 \text{ cm}^{-1}$  and data averaged over 32 scans. FT-IR was employed to analyze films before and after etching the PLA block of the PS-*b*-PLA BCP.

### 3.4. Results and Discussion

#### 3.4.1. Microphase separation of PS-*b*-PLA BCP

In general, calculating solubility differences between a polymer and a particular solvent will provide a reasonable indication of miscibility. When  $|\delta_{\text{polymer}} - \delta_{\text{solvent}}| < 2.5$   $[\text{MPa}]^{1/2}$ , then during SVA a solvent will diffuse into a polymer.<sup>43</sup> Free volume is subsequently created in the polymer network which decreases the glass transition temperature ( $T_g$ ) of the polymer enhancing chain mobility. Solubility parameters for PS,

PLA and THF are 18.8, 22.2 and 19.4 [MPa]<sup>1/2</sup> respectively.<sup>44-46</sup> THF is a relatively neutral solvent for both PS and PLA blocks (see calculation in Appendix – Chapter 3 Table 3.7.S1) and was employed as our SVA solvent. We also investigated chloroform as a SVA solvent as this was used as the spin casting solvent. Despite similar polymer-solvent interactions to THF, microphase separation was not observed in the process window studied (see appendix Figure S3.7.1). We believe the neutral interface created at the polymer/air interface when SVA with THF allows perpendicular orientation of the lamellar microdomains as others have also noted in their experiments for similar systems.<sup>47,48</sup> Thin films of PS-*b*-PLA were initially prepared on silicon substrates following piranha cleaning. To induce self-assembly, films were exposed to THF vapors at 55°C for up to 50 minutes. The as-cast film of 0.5 wt% PS-*b*-PLA chloroform solution spun on silicon is shown in Figure 3.1a. A near featureless film is observed. The initial as-cast film thickness was measured at 47.05 nm ± 0.11 nm. Samples STVA with THF for 15, 30 and 45 at 55°C are shown in Figure 3.1b-d. One can see that self-assembly occurring after 15 minutes and that fully developed domains with extended average line lengths are observed after 45 minutes SVA. The perpendicular domains in Figure 3.1d have a 32.5 nm periodicity ( $L_0$ ). After swelling of the film for 45 minutes with THF vapor at 55°C (Figure 3.1d), the dried film thickness was almost the same as the as-cast film at 48 nm ± 0.16 nm. Table 1 displays thicknesses for as-cast and STVA annealed films on piranha cleaned and HMDS functionalized silicon substrates.

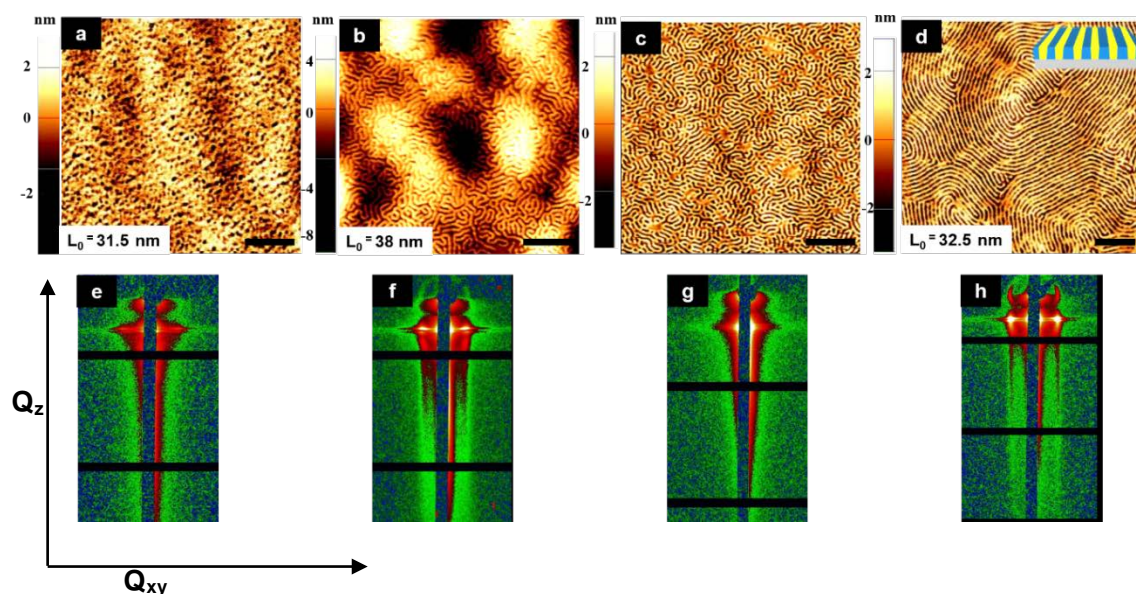


**Figure 3.1.** AFM topographic images of PS-*b*-PLA BCP films (a) as-cast and after solvent vapor annealing with THF @ 55°C after (b) 15 minutes, (c) 30 minutes and (d) 45 minutes. Scale bars represent 400 nm.  $L_0$  in (a), (b), and (d) represent the repeat periodicity calculated from GISAXS measurements. (e-h) Corresponding GISAXS patterns for (a) – (d).

Detailed GISAXS analysis was carried out on the above STVA films (Figure 3.1a-d). The as-cast, 15 minute and 45 minute treated films exhibited a correlation peak with at least one order as seen in GISAXS patterns in Figure 3.1 (e), (f) and (h). One observes a large disorder in the as-cast film (Figure 3.1e) in the in plane correlation which is consistent with AFM image in Figure 3.1a. GISAXS data of the PS-*b*-PLA film displayed in Figure 3.1c also provides us with more information for this pitch size decrease. As the corresponding GISAXS data reveals in Figure 3.1g, we observe no correlation within the plane of the substrate in comparison to first order peaks observed in Figure 3.1f and h. The corresponding AFM image in Figure 3.1c also reveals a complex structure of short lamella lines and possible perforated lamella (antidots). Only after a certain time we observe a stable equilibrium structure with highly oriented vertical lamella sheets (Figure 3.1d). The GISAXS image with strong Bragg rods in Figure 3.1h for the 45 minute film experiment reveals an elongation in the  $q_z$  axis, *i.e.* domains oriented perpendicular to

the substrate. This is in agreement with the AFM image in Figure 3.1d. We observed a notable difference between microdomain pitches at 15 minutes STVA ( $38 \pm 0.2$  nm) whilst 45 minutes STVA samples possessed a pitch of  $32.5 \pm 0.2$  nm.

**Table 1.** Contact angle of silicon after different treatment techniques and film thickness of PS-*b*-PLA BCP material after casting and solvent vapor annealing.

Material	Contact angle	As cast film thickness	Thickness after SVA for 45 minutes
Piranha cleaned Si + chloroform sonication	~25°	-	-
HMDS treated Si	~70°	-	-
0.5 wt % PS- <i>b</i> -PLA on piranha cleaned Si	-	47.05 nm $\pm$ 0.11 nm	48.92 nm $\pm$ 0.16 nm
0.5 wt % PS- <i>b</i> -PLA on HMDS treated Si	-	47.83 nm $\pm$ 0.05 nm	47.98 nm $\pm$ 0.05 nm

As time proceeds, we then observe a decrease in microdomain pitch but enhanced average line lengths (Figure 3.1d) with the removal of solvent and the film reaching a metastable state. The through film uniformity of this pattern is also confirmed by the GISAXS analysis. One could also claim that the morphologies achieved in the swollen state during STVA have been retained upon evaporation (dry state) as they are quite distinct from each other. This has recently been shown for asymmetric PS-*b*-PLA by Sinturel *et al.*<sup>35</sup>

Our investigation also examined films over a range of temperatures while exposed to solvent vapor and without solvent vapor, *i.e.* thermal annealing. Films were subsequently exposed to a polar and non-polar solvent (THF and CHCl<sub>3</sub>) at room temperature and at 40°C and 55°C to increase solvent vapor pressure in an attempt to achieve microphase separation via enhanced chain mobility. Microphase separation was not observed by

AFM analysis with films SVA with chloroform (data is displayed and discussed in appendix table 3.7.S2 and Figure S3.7.1). Likewise, self-assembly was not observed for films thermally annealed at 40°C or at 55°C (see appendix Figure S3.7.2). These particular temperatures were used as they are close to 2 times and 4 times the vapor pressure of neutral solvent THF that forms well-defined PS-*b*-PLA films. Thermal annealing alone produced no microphase separation in our study, and THF solvent vapor exposure at RT also showed no signs of microphase separated morphologies. In comparison, with elevated vapor pressures at 40°C and 55°C, we observe distinct lamellar patterns in PS-*b*-PLA BCP films.

#### 3.4.2. Directed Self-Assembly of PS-*b*-PLA via Topographic Substrates.

For BCP materials to realize their nanolithographic potential, integration with top-down lithographically patterned substrates must be demonstrated.<sup>10</sup> We have employed Si<sub>3</sub>N<sub>4</sub> trenched substrates (see experimental for fabrication details) to graphoepitaxially align PS-*b*-PLA films. Note that the use of “orientation” below refers to PS and PLA domains relative to the substrate while “alignment” is in reference to the features relative to the guiding sidewall geometry. Also results presented in Figure 3.3 and 3.4 below were processed in the same manner (film thickness, STVA time and temperature). Figure 3.2 shows SEM images of resulting alignments which are also represented schematically. Figure 3.3a shows a top-down SEM image of self-assembled PS-*b*-PLA pattern formation on an open area of the Si<sub>3</sub>N<sub>4</sub> substrate following the optimized SVA conditions discussed above. PS domains appear dark while PLA domains are bright due to RuO<sub>4</sub> staining for SEM contrast purposes. Figure 3.3b reveals the perpendicular alignment of PS-*b*-PLA features to the Si<sub>3</sub>N<sub>4</sub> sidewalls as represented in Figure 3.2A. The channel dimensions (dark) are ~50 nm (1.53) L<sub>0</sub> wide while the mesa dimensions (bright) are ~

140 nm.  $L_0$  measured in the channels is similar as that measured on planar silicon and open areas of the  $\text{Si}_3\text{N}_4$  substrates at  $\sim 32.5$  nm. The perpendicular alignment preference of the domains to the sidewalls is also revealed in Figure 3.3c and d with channel width dimensions slightly wider at  $\sim 130$  nm ( $4 L_0$ ) and  $\sim 150$  nm ( $4.61 L_0$ ) while mesa dimensions are  $\sim 70$  nm and  $\sim 96$  nm respectively.

This orientation of the domains is due to the neutral sidewalls. Additionally, despite channel widths ranging from  $\sim 50$  nm to  $\sim 150$  nm the perpendicular orientation is retained. We assume that the neutrality of the graphoepitaxy sidewalls favors a perpendicular registration although this evolution of orientation is surprising in comparison to graphoepitaxial alignment in general. However, if one compares the near identical surface energies of the constituent blocks,  $\gamma^{\text{PS}} = 42 \text{ mJ m}^{-2}$  and  $\gamma^{\text{PLA}} 36.0\text{--}41.1 \text{ mJ m}^{-2}$ ,<sup>29,39</sup> the perpendicular alignment to guiding features may be expected as neither block has a wetting preference. Other reports have shown similar alignment results in graphoepitaxy schemes and were as a result of surface chemistry interactions,<sup>49</sup> solvent anneal conditions,<sup>50</sup> mesa widths<sup>50</sup> or film thickness.<sup>51</sup> Here it appears that the neutral sidewalls and confinement of PS-*b*-PLA material favors perpendicular alignment. Also it is possible that PS and PLA domains are oriented parallel to the substrate surface on the mesas and we cannot observe patterns by SEM.

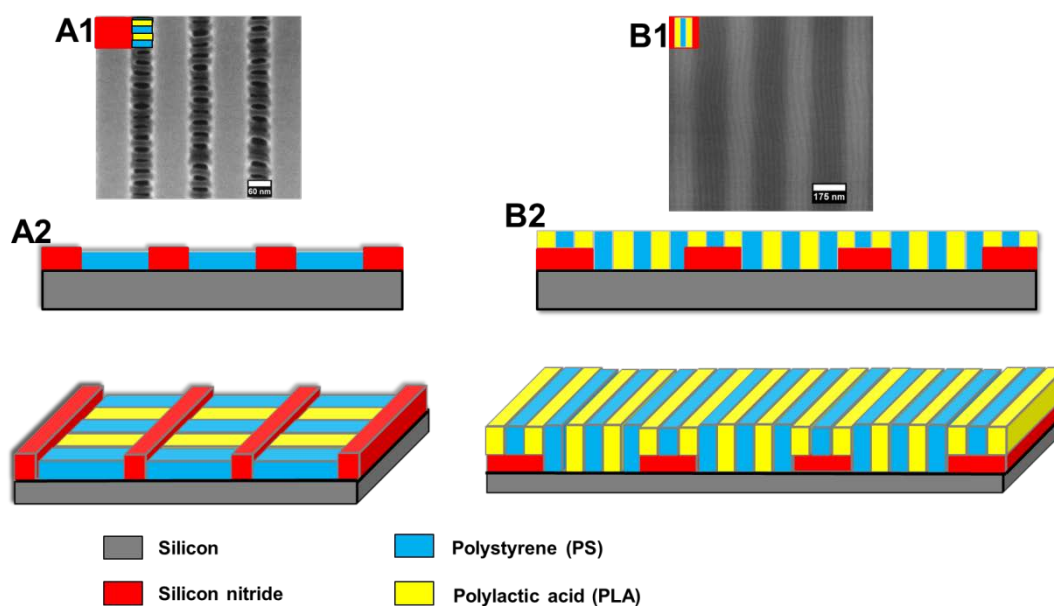


**Figure 3.2.** A. SEM of PS-*b*-PLA perpendicular alignment to silicon nitride sidewalls. B. SEM of PS-*b*-PLA over-flowing channels and aligning parallel to sidewalls. A2 and B2 below SEM images show schemes of both alignments from side-view perspectives.

A further evolution of alignment direction of PS and PLA domains to sidewall features was also observed. Figure 3.4 shows different channel (trench) and mesa dimensions that produced parallel alignment to sidewalls for the PS-*b*-PLA films over macroscopic areas. Notably, the area shows PS-*b*-PLA material that aligned parallel to channel sidewalls. The dimensions of the mesa ( $\sim 96\text{-}500\text{ nm}$ ) and the channels ( $\sim 140\text{-}175\text{ nm}$ , *i.e.*  $4.3 > L_0 < 5.4$ ) in Figure 3.4a-d are slightly wider than those displayed in Figure 3.3b-d. If one considers the graphical representation in Figure 3.2, it is possible that the overflow of PS-*b*-PLA has resulted in the alignment change of microdomains. We believe that the perpendicular alignment observed in Figure 3.4 possibly arises due to the confined domains, and it may be possible that PS-*b*-PLA is residing parallel to the substrate on the mesa and thus is not seen on SEM analysis.

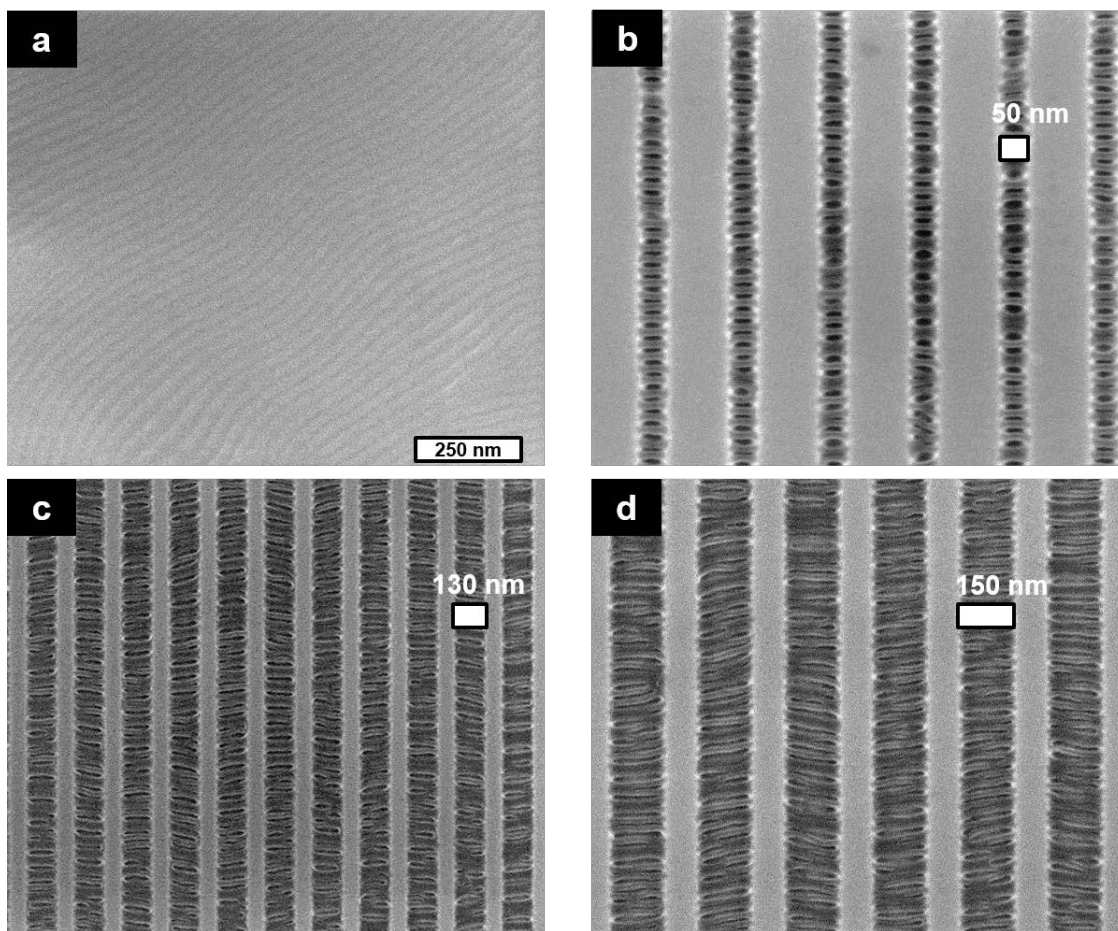


**Figure 3.3.** (a) Top-down SEM image of PS-*b*-PLA self-assembly on open area of Si<sub>3</sub>N<sub>4</sub> patterned substrate. (b) – (d) Top-down SEM images of perpendicular alignment of domains to Si<sub>3</sub>N<sub>4</sub> sidewalls after STVA with THF @ 55°C. Darker areas represent the channels and bright areas are the mesas. Silicon nitride channel widths are marked in respective images. Films were stained with RuO<sub>4</sub> vapors to enhance contrast. PS domains appear dark and PLA domains are bright.

The graphoepitaxy process produces defect-free patterns over large areas however further study is required to dictate the alignment direction of PS-*b*-PLA relative to guiding features. The use of polymer brushes at channel bases as used for BCPs with similar block surface energies such as PS-*b*-PMMA may be necessary for lamellar PS-*b*-PLA BCP.<sup>52</sup> Analysing film thickness and commensurability is also critical for future work.

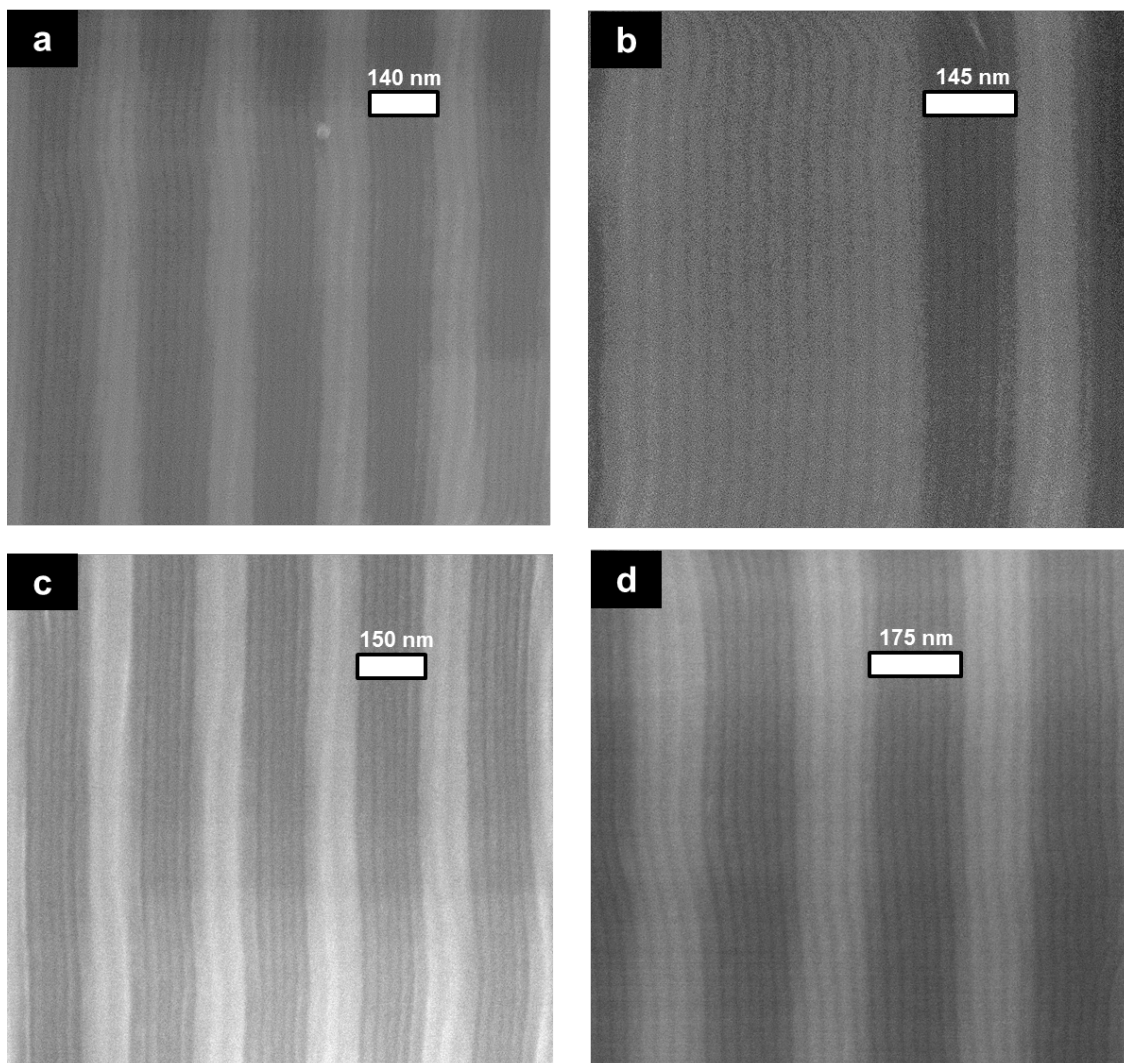


**Figure 3.4.** (a) to (d) Top-down SEM images showing directed assembly of PS-*b*-PLA films after STVA with THF @ 55°C with domain alignment parallel to sidewalls Silicon nitride channels widths are marked in respective images.

### 3.4.3. Contributing factors to fast self-assembly

A number of factors contribute to the self-assembly of this PS-*b*-PLA system and the organized features observed. Firstly, the PS-*b*-PLA diblock copolymer possesses a high  $\chi$  ( $\chi$  @ 55°C ~ 0.187). The  $\chi$  value for PS-*b*-PLA here is over four times higher than the well-studied PS-*b*-PMMA ( $\chi$  ~ 0.043 at 25°C) system. The Flory-Huggins interaction parameter ( $\chi$ ) for PS-*b*-PLA was determined from equation 2 below which was previously established experimentally;<sup>53</sup>

$$\chi(T) = (98.1) T^{-1} - 0.112 \quad (2)$$

where  $T$  represents absolute temperature. Additionally, after determining  $\chi$  at the different process temperatures employed here (see table 2), the corresponding  $\chi N$  values were calculated.  $\chi N > 10.495$  is the minimum threshold figure for microphase separation to occur in BCP films.<sup>54</sup> The PS-*b*-PLA BCP used here has a  $\chi N$  value of 91.57, 84.06 and 78.20 at 23°C, 40°C, and 55°C respectively. These  $\chi N$  values are well above the minimum threshold and are in the strong-segregation regime.<sup>54</sup>

**Table 2.** Characteristics of PS-*b*-PLA block copolymer used in this study.

Block Copolymer	Molecular Weight (kg mol <sup>-1</sup> )	Pitch - AFM	Pitch - GISAXS	$\chi$ @ 23°C	$\chi$ @ 40°C	$\chi$ @ 55°C
PS- <i>b</i> -PLA	21-19.5	~33.7nm	~32.5nm	~ 0.219	~ 0.201	~ 0.187

As mentioned above, an inherent property of the PS-*b*-PLA system is the similar surface energies of the constituent PS and PLA blocks. PS-*b*-PLA is one of the few BCPs that exhibit non-preferential free surface interactions. Neutralization of the free surface has been established of late by Willson, Ellison and co-workers across a range of high  $\chi$  silicon containing BCPs with low pitch.<sup>18,21</sup> Considering these contributing interfacial phenomena, one can assume that a relatively neutral substrate/polymer interface combined with a neutralized free surface for PS-*b*-PLA will lead to perpendicular orientation of the lamella domains.<sup>48</sup> Since the surface energies of PS-*b*-PLA allow a neutral substrate polymer interface, controlling the polymer/air interface can be established via neutral SVA. As we have demonstrated, THF exposure provides a neutralized free interface to enable highly defined lamellar domains to orient perpendicular to the substrate surface. This is observed from the highly developed PS-*b*-PLA domains seen in Figure 3.1d described above.

Figure 3.5 displays a graph of increasing THF vapor pressure due to increasing temperature. The insets (a-c) show surface structures following SVA annealing with THF at room temperature (*i.e.* 23°C), 40°C and 55°C for 45 minutes. We believe that employing temperature while SVA with THF for this particular PS-*b*-PLA system enables and enhances phase segregation for two reasons. Firstly, the increased vapor pressure provides more THF molecules to penetrate into the polymer network more rapidly than at room temperature. PS-*b*-PLA films exposed to THF vapor at room temperature (THF vapour pressure = 19.79 kPa) showed no distinct microphase separation while films SVA at 40°C (THF vapour pressure = 40.22 kPa) and 55°C (THF vapour pressure = 70.03 kPa) revealed well-defined domains. The importance of vapor pressure and ability to enhance the dynamics of self-assembly has been highlighted by our group for this system previously.<sup>29</sup> Secondly, as is well demonstrated, thermal annealing alone enables the microphase separation of BCP above  $T_g$ . Considering that exposure of polymer films to solvents lowers the  $T_g$  of BCP systems, the simultaneous treatment of a THF vaporized PS-*b*-PLA film even at low temperatures should be sufficient for reorganization of polymer chains. We speculate that this is the primary reason for observing such well-defined domains at 40°C. The  $T_g$  of PS and PLA in this system is reported as 98°C and 49°C respectively from the supplier (see experimental for further details). Solvent exposure using a miscible solvent combined with a temperature (40°C) below the reported  $T_g$  provides more mobility to the PS and PLA block. All images from RT, 40°C and 55°C are shown for comparison in Figure S3.7.3.

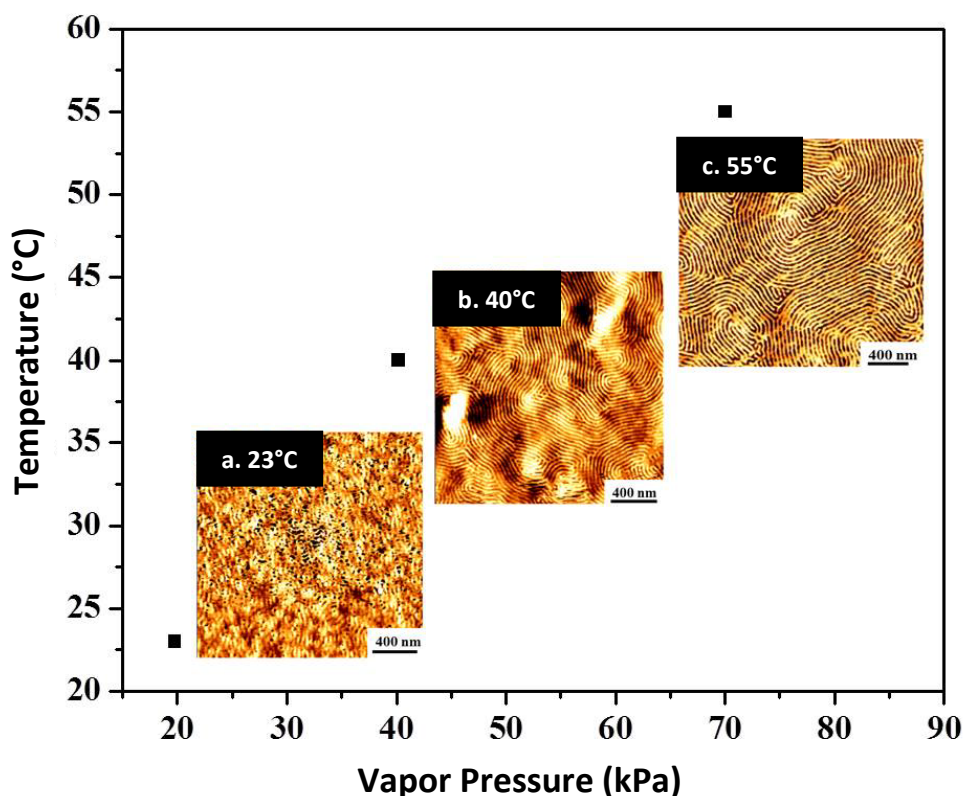


**Figure 3.5.** Graph reflecting correlation of THF vapor pressure with increasing temperature. PS-*b*-PLA self-assembly was induced via increasing THF vapor pressure with increased temperature. Insets (b) and (c) shows highly ordered PS-*b*-PLA domains after SVA with THF @ 40°C and 55°C respectively, while (a) shows no phase separation was observed at room temperature (*i.e.* 23°C).

#### 3.4.4. PLA block removal forming PS mask template

We have previously speculated the existence of a PLA wetting layer at the polymer/substrate interface with this PS-*b*-PLA BCP system that leads to delamination of the film during wet etching.<sup>42</sup> It may be present due to the polar interaction of the PLA block and the native oxide layer on silicon.<sup>55</sup> To overcome the wetting layer formation that leads to delamination of the film, PS-OH brush or HMDS functionalization allows for wet etching to be carried out without delamination of the polymer film.<sup>41,42</sup> To demonstrate the delamination of a PS-*b*-PLA film on a non-brush substrate we used a film with thickness close to ~ 210 nm so that a color change or detachment of the polymer film could be easily observed by naked eye following a brief etch in a 0.01M NaOH

solution. The picture of the original self-assembled 2 wt % film is shown in appendix Figure 3.7.5a. Appendix Figure 3.7.5b shows the same film following etching in a 0.5 M sodium hydroxide solution at room temperature. One observes a drastic color change due to the loss of the polymer film. This simple observation shows that lamellar PS-*b*-PLA films are susceptible to delamination owing to the PLA wetting layer at the polymer-substrate interface. We carried out the same experiment after spin coating a 2 wt % PS-*b*-PLA solution on a HMDS functionalized substrate. It should be noted the microphase separation is not affected greatly when using the modified surface as shown in Figure 3.6a for 0.5wt % PS-*b*-PLA on HMDS silicon. Interestingly, we observed complete detachment of the PS homopolymer film from the piranha cleaned silicon following etching. This shows that PS-*b*-PLA BCP on piranha cleaned silicon may not solely be due to a PLA wetting layer but weak PS interactions. Therefore a HMDS functionalization step results in a stronger adherence and thus enables wet etching of the PS-*b*-PLA BCP to be carried out.

For effective PLA etching, a 0.5 wt % PS-*b*-PLA film on a HMDS modified silicon substrate was etched using a 0.01M sodium hydroxide solution for 5 minutes. From our previous work, we have evaluated different routes and established issues that required further examination.<sup>42</sup> Previously, we discussed that thinner polymer films would be examined and this has been demonstrated here. Figure 3.6a reveals well-developed microphase separated PS-*b*-PLA pattern on HMDS functionalized silicon following SVA with THF at 55°C for 45 minutes. Etching with 0.01M NaOH solution enabled porous PS templates after 5 minutes. Figure 3.6b shows cross-section SEM image of PS soft mask template after PLA removal via wet etching. The image shows that PS-fin collapse after PLA removal is not evident and reveals the high selectivity of the etch and its'

homogeneity over the film surface. The use of a low concentration basic solution for PLA must be noted to avoid roughness. Over-etching is facile with this system as the carboxylic acid backbone of the PLA block is susceptible to chain scission.

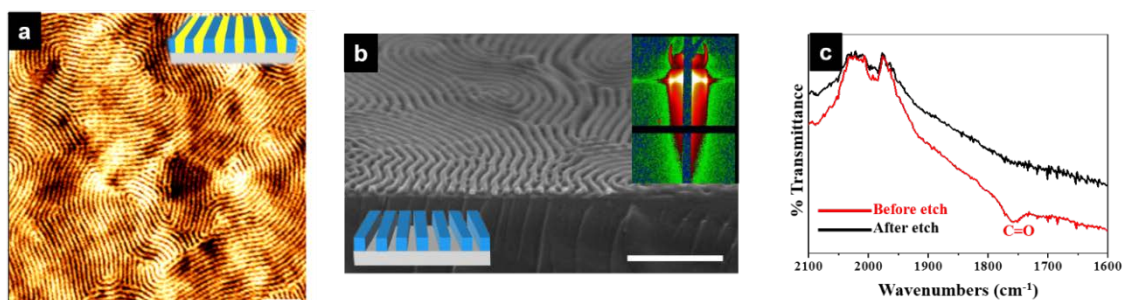


**Figure 3.6.** (a) AFM image of thin film of PS-*b*-PLA self-assembly on HMDS functionalized silicon following 45 minutes STVA. (b) Cross-section SEM of etched PS-*b*-PLA film following 5 minute immersion of film in 0.01 M NaOH solution. Inset in (b) shows corresponding GISAXS pattern retaining the same order as the initial self-assembled film. (c) FT-IR data of film before and after etch treatment showing removal of PLA component. (a) and (b) scale bars represent 250 nm.

Moreover, after the initial chain scission, auto-catalytic effects accelerate the degradation process. The low concentration and short treatment time enabled effective PLA removal without any damage to the overall structure. Etching a thin BCP film also avoids line collapse that can occur due to the high aspect ratio of one domain relative to the nanodomain being removed.<sup>42</sup> Such a scenario in thick films generally results in collapsing of the remaining domains and merging of features. The GISAXS inset also shows that the highly ordered vertical nature of the microdomains is retained, similar to initial PS-*b*-PLA film (Figure 3.6d). FT-IR data provided in Figure 3.6c confirms that PLA has been fully etched. The characteristic C=O peak occurring at 1758 cm<sup>-1</sup> for the PLA backbone is present in the unetched film while the after etch film (5 minutes in 0.01M NaOH solution) shows the absence of this feature.

### 3.5. Conclusions

Chapter 3 outlined a methodology using the solvo-thermal vapor annealing process for the microphase separation of a symmetric PS-*b*-PLA BCP in a short processing period. Parameters influencing the self-assembly kinetics were examined and GISAXS data confirmed that uniform films with high order were formed after optimum annealing. The PS-*b*-PLA BCP thin films developed in this work are of low aspect ratio avoiding line collapse and image quality issues in order to optimize their nanolithographic potential. For pattern transfer purposes, we have also demonstrated highly PLA selective wet and dry etches that can be carried out in a rapid, cheap and reproducible manner. Additionally, directed self-assembly of line space feature were shown over large areas. The work presented in this chapter illustrates the applicability of a high  $\chi$  BCP with a rapidly degradable block for high etch contrast. However, careful substrate surface modifications will be required to controllably align PS-*b*-PLA microdomains to a surface plane to meet DSA requirements.

### 3.6. References

- (1) Segalman, R. A. Patterning with block copolymer thin films. *Materials Science & Engineering R-Reports* **2005**, *48*, 191-226.
- (2) Mokarian-Tabari, P.; Vallejo-Giraldo, C.; Fernandez-Yague, M.; Cummins, C.; Morris, M. A.; Biggs, M. J. P. Nanoscale neuroelectrode modification via sub-20 nm silicon nanowires through self-assembly of block copolymers. *Journal of Materials Science-Materials in Medicine* **2015**, *26*.
- (3) Phillip, W. A.; O'Neill, B.; Rodwogin, M.; Hillmyer, M. A.; Cussler, E. L. Self-Assembled Block Copolymer Thin Films as Water Filtration Membranes. *ACS Applied Materials & Interfaces* **2010**, *2*, 847-853.
- (4) Yin, J.; Yao, X.; Liou, J.-Y.; Sun, W.; Sun, Y.-S.; Wang, Y. Membranes with Highly Ordered Straight Nanopores by Selective Swelling of Fast Perpendicularly Aligned Block Copolymers. *ACS Nano* **2013**, *7*, 9961-9974.
- (5) Xiao, S. G.; Yang, X. M.; Edwards, E. W.; La, Y. H.; Nealey, P. F. Graphoepitaxy of cylinder-forming block copolymers for use as templates to pattern magnetic metal dot arrays. *Nanotechnology* **2005**, *16*, S324-S329.
- (6) Ross, C. A.; Jung, Y. S.; Chuang, V. P.; Son, J. G.; Gotrik, K. W.; Mickiewicz, R. A.; Yang, J. K. W.; Chang, J. B.; Berggren, K. K.; Gwyther, J.; Manners, I. Templated

- self-assembly of Si-containing block copolymers for nanoscale device fabrication, **2010**, *Proceedings of SPIE*, 7637, 76370H.
- (7) Crossland, E. J. W.; Kamperman, M.; Nedelcu, M.; Ducati, C.; Wiesner, U.; Smilgies, D. M.; Toombes, G. E. S.; Hillmyer, M. A.; Ludwigs, S.; Steiner, U.; Snaith, H. J. A Bicontinuous Double Gyroid Hybrid Solar Cell. *Nano Letters* **2008**, *9*, 2807-2812.
- (8) Mulherin, R. C.; Jung, S.; Huettner, S.; Johnson, K.; Kohn, P.; Sommer, M.; Allard, S.; Scherf, U.; Greenham, N. C. Ternary Photovoltaic Blends Incorporating an All-Conjugated Donor-Acceptor Diblock Copolymer. *Nano Letters* **2011**, *11*, 4846-4851.
- (9) Bang, J.; Jeong, U.; Ryu, D. Y.; Russell, T. P.; Hawker, C. Block copolymer nanolithography: Translation of molecular level control to nanoscale patterns. *Advanced Materials* **2009**, *21*, 4769-4792.
- (10) Morris, M. A. Directed self-assembly of block copolymers for nanocircuitry fabrication. *Microelectronic Engineering* **2015**, *132*, 207-217.
- (11) Han, E.; Kang, H.; Liu, C.-C.; Nealey, P. F.; Gopalan, P. Graphoepitaxial Assembly of Symmetric Block Copolymers on Weakly Preferential Substrates. *Advanced Materials* **2010**, *22*, 4325-4329.
- (12) Farrell, R. A.; Kinahan, N. T.; Hansel, S.; Stuenkel, K. O.; Petkov, N.; Shaw, M. T.; West, L. E.; Djara, V.; Dunne, R. J.; Varona, O. G.; Gleeson, P. G.; Jung, S. J.; Kim, H. Y.; Kolešnik, M. M.; Lutz, T.; Murray, C. P.; Holmes, J. D.; Nealey, P. F.; Duesberg, G. S.; Krstić, V.; Morris, M. A. Large-scale parallel arrays of silicon nanowires via block copolymer directed self-assembly. *Nanoscale* **2012**, *4*, 3228-3236.
- (13) Moon, H.-S.; Shin, D. O.; Kim, B. H.; Jin, H. M.; Lee, S.; Lee, M. G.; Kim, S. O. Large-area, highly oriented lamellar block copolymer nanopatterning directed by graphoepitaxially assembled cylinder nanopatterns. *Journal of Materials Chemistry* **2012**, *22*, 6307-6310.
- (14) Cummins, C.; Gangnaik, A.; Kelly, R. A.; Borah, D.; O'Connell, J.; Petkov, N.; Georgiev, Y. M.; Holmes, J. D.; Morris, M. A. Aligned silicon nanofins via the directed self-assembly of PS-*b*-P4VP block copolymer and metal oxide enhanced pattern transfer. *Nanoscale* **2015**, *7*, 6712-6721.
- (15) Kim, S. O.; Solak, H. H.; Stoykovich, M. P.; Ferrier, N. J.; de Pablo, J. J.; Nealey, P. F. Epitaxial self-assembly of block copolymers on lithographically defined nanopatterned substrates. *Nature* **2003**, *424*, 411-414.
- (16) Delgadillo, P. A. R.; Gronheid, R.; Thode, C. J.; Wu, H.; Cao, Y.; Neisser, M.; Somervell, M.; Nafus, K.; Nealey, P. F. Implementation of a chemo-epitaxy flow for directed self-assembly on 300-mm wafer processing equipment. *Journal of Micro/Nanolithography, MEMS, and MOEMS* **2012**, *11*, 031302.
- (17) Bates, C. M.; Seshimo, T.; Maher, M. J.; Durand, W. J.; Cushen, J. D.; Dean, L. M.; Blachut, G.; Ellison, C. J.; Willson, C. G. Polarity-Switching Top Coats Enable Orientation of Sub-10-nm Block Copolymer Domains. *Science* **2012**, *338*, 775-779.
- (18) Cushen, J. D.; Otsuka, I.; Bates, C. M.; Halila, S.; Fort, S.; Rochas, C.; Easley, J. A.; Rausch, E. L.; Thio, A.; Borsali, R.; Willson, C. G.; Ellison, C. J. Oligosaccharide/Silicon-Containing Block Copolymers with 5 nm Features for Lithographic Applications. *ACS Nano* **2012**, *6*, 3424-3433.
- (19) Cushen, J. D.; Bates, C. M.; Rausch, E. L.; Dean, L. M.; Zhou, S. X.; Willson, C. G.; Ellison, C. J. Thin Film Self-Assembly of Poly(trimethylsilylstyrene-*b*-d,l-lactide) with Sub-10 nm Domains. *Macromolecules* **2012**, *45*, 8722-8728.
- (20) Pitet, L. M.; Wuister, S. F.; Peeters, E.; Kramer, E. J.; Hawker, C. J.; Meijer, E. W. Well-Organized Dense Arrays of Nanodomains in Thin Films of

- Poly(dimethylsiloxane)-*b*-poly(lactide) Diblock Copolymers. *Macromolecules* **2013**, *46*, 8289-8295.
- (21) Cushen, J. D.; Wan, L.; Pandav, G.; Mitra, I.; Stein, G. E.; Ganesan, V.; Ruiz, R.; Grant Willson, C.; Ellison, C. J. Ordering poly(trimethylsilyl styrene)-*block*-D,L-lactide) block copolymers in thin films by solvent annealing using a mixture of domain-selective solvents. *Journal of Polymer Science Part B: Polymer Physics* **2014**, *52*, 36-45.
- (22) Angelescu, D. E.; Waller, J. H.; Adamson, D. H.; Deshpande, P.; Chou, S. Y.; Register, R. A.; Chaikin, P. M. Macroscopic Orientation of Block Copolymer Cylinders in Single-Layer Films by Shearing. *Advanced Materials* **2004**, *16*, 1736-1740.
- (23) Gopinadhan, M.; Deshmukh, P.; Choo, Y.; Majewski, P. W.; Bakajin, O.; Elimelech, M.; Kasi, R. M.; Osuji, C. O. Thermally Switchable Aligned Nanopores by Magnetic-Field Directed Self-Assembly of Block Copolymers. *Advanced Materials* **2014**, *26*, 5148-5154.
- (24) Ryu, D. Y.; Ham, S.; Kim, E.; Jeong, U.; Hawker, C. J.; Russell, T. P. Cylindrical microdomain orientation of PS-*b*-PMMA on the balanced interfacial interactions: Composition effect of block copolymers. *Macromolecules* **2009**, *42*, 4902-4906.
- (25) Zhang, X.; Harris, K. D.; Wu, N. L. Y.; Murphy, J. N.; Buriak, J. M. Fast Assembly of Ordered Block Copolymer Nanostructures through Microwave Annealing. *ACS Nano* **2010**, *4*, 7021-7029.
- (26) Zhang, X.; Murphy, J. N.; Wu, N. L. Y.; Harris, K. D.; Buriak, J. M. Rapid Assembly of Nanolines with Precisely Controlled Spacing from Binary Blends of Block Copolymers. *Macromolecules* **2011**, *44*, 9752-9757.
- (27) Borah, D.; Shaw, M. T.; Holmes, J. D.; Morris, M. A. Sub-10 nm Feature Size PS-*b*-PDMS Block Copolymer Structures Fabricated by a Microwave-Assisted Solvothermal Process. *ACS Applied Materials & Interfaces* **2013**, *5*, 2004-2012.
- (28) Borah, D.; Sentharamaikannan, R.; Rasappa, S.; Kosmala, B.; Holmes, J. D.; Morris, M. A. Swift Nanopattern Formation of PS-*b*-PMMA and PS-*b*-PDMS Block Copolymer Films Using a Microwave Assisted Technique. *ACS Nano* **2013**, *7*, 6583-6596.
- (29) Mokarian-Tabari, P.; Cummins, C.; Rasappa, S.; Simao, C.; Sotomayor Torres, C. M.; Holmes, J. D.; Morris, M. A. Study of the Kinetics and Mechanism of Rapid Self-Assembly in Block Copolymer Thin Films during Solvo-Microwave Annealing. *Langmuir* **2014**, *30*, 10728-10739.
- (30) Sinturel, C.; Vayer, M.; Morris, M.; Hillmyer, M. A. Solvent Vapor Annealing of Block Polymer Thin Films. *Macromolecules* **2013**, *46*, 5399-5415.
- (31) Gotrik, K. W.; Ross, C. A. Solvothermal Annealing of Block Copolymer Thin Films. *Nano Letters* **2013**, *13*, 5117-5122.
- (32) Gu, X.; Gunkel, I.; Hexemer, A.; Gu, W.; Russell, T. P. An In Situ Grazing Incidence X-Ray Scattering Study of Block Copolymer Thin Films During Solvent Vapor Annealing. *Advanced Materials* **2014**, *26*, 273-281.
- (33) Gu, X.; Gunkel, I.; Hexemer, A.; Russell, T. Solvent vapor annealing of block copolymer thin films: removal of processing history. *Colloid and Polymer Science* **2014**, *292*, 1795-1802.
- (34) Paik, M. Y.; Bosworth, J. K.; Smilges, D.-M.; Schwartz, E. L.; Andre, X.; Ober, C. K. Reversible Morphology Control in Block Copolymer Films via Solvent Vapor Processing: An in Situ GISAXS Study. *Macromolecules* **2010**, *43*, 4253-4260.
- (35) Sinturel, C.; Grosso, D.; Boudot, M.; Amenitsch, H.; Hillmyer, M. A.; Pineau, A.; Vayer, M. Structural Transitions in Asymmetric Poly(styrene)-*block*-Poly(lactide) Thin Films Induced by Solvent Vapor Exposure. *ACS Applied Materials & Interfaces* **2014**, *6*, 12146-12152.

- (36) Mokarian-Tabari, P.; Collins, T. W.; Holmes, J. D.; Morris, M. A. Cyclical "Flipping" of Morphology in Block Copolymer Thin Films. *ACS Nano* **2011**, *5*, 4617-4623.
- (37) Park, W. I.; Tong, S.; Liu, Y.; Jung, I. W.; Roelofs, A.; Hong, S. Tunable and rapid self-assembly of block copolymers using mixed solvent vapors. *Nanoscale* **2014**, *6*, 15216-15221.
- (38) She, M.-S.; Lo, T.-Y.; Ho, R.-M. Controlled Ordering of Block Copolymer Gyroid Thin Films by Solvent Annealing. *Macromolecules* **2013**, *47*, 175-182.
- (39) Keen, I.; Yu, A.; Cheng, H.-H.; Jack, K. S.; Nicholson, T. M.; Whittaker, A. K.; Blakey, I. Control of the Orientation of Symmetric Poly(styrene)-*block*-poly(d,l-lactide) Block Copolymers Using Statistical Copolymers of Dissimilar Composition. *Langmuir* **2012**, *28*, 15876-15888.
- (40) Keen, I.; Cheng, H.-H.; Yu, A.; Jack, K. S.; Younkin, T. R.; Leeson, M. J.; Whittaker, A. K.; Blakey, I. Behavior of Lamellar Forming Block Copolymers under Nanoconfinement: Implications for Topography Directed Self-Assembly of Sub-10 nm Structures. *Macromolecules* **2013**, *47*, 276-283.
- (41) Baruth, A.; Rodwogin, M. D.; Shankar, A.; Erickson, M. J.; Hillmyer, M. A.; Leighton, C. Non-lift-off Block Copolymer Lithography of 25 nm Magnetic Nanodot Arrays. *ACS Applied Materials & Interfaces* **2011**, *3*, 3472-3481.
- (42) Cummins, C.; Mokarian-Tabari, P.; Holmes, J. D.; Morris, M. A. Selective etching of polylactic acid in poly(styrene)-*block*-poly(d,l)lactide diblock copolymer for nanoscale patterning. *Journal of Applied Polymer Science* **2014**, *131*.
- (43) Gotrik, K. W.; Hannon, A. F.; Son, J. G.; Keller, B.; Alexander-Katz, A.; Ross, C. A. Morphology control in block copolymer films using mixed solvent vapors. *ACS Nano* **2012**, *6*, 8052-8059.
- (44) McKenna, F. H. a. G. B. Physical Properties of Polymers Handbook. *AIP Press* **1996**, 379-400.
- (45) Ho, R. M.; Tseng, W. H.; Fan, H. W.; Chiang, Y. W.; Lin, C. C.; Ko, B. T.; Huang, B. H. Solvent-induced microdomain orientation in polystyrene-*b*-poly (L-lactide) diblock copolymer thin films for nanopatterning. *Polymer* **2005**, *46*, 9362-9377.
- (46) Hou, X.; Li, Q.; Cao, A. Solvent annealing-induced microphase-separation of polystyrene-*b*-polylactide block copolymer aimed at preparation of ordered nanoparticles/block copolymer hybrid thin film. *J Polym Res* **2014**, *21*, 1-15.
- (47) Vayer, M.; Hillmyer, M. A.; Dirany, M.; Thevenin, G.; Erre, R.; Sinturel, C. Perpendicular orientation of cylindrical domains upon solvent annealing thin films of polystyrene-*b*-polylactide. *Thin Solid Films* **2010**, *518*, 3710-3715.
- (48) Hong, S. W.; Gu, W.; Huh, J.; Sveinbjornsson, B. R.; Jeong, G.; Grubbs, R. H.; Russell, T. P. On the Self-Assembly of Brush Block Copolymers in Thin Films. *ACS Nano* **2013**, *7*, 9684-9692.
- (49) Borah, D.; Simao, C. D.; Senthamaraiannan, R.; Rasappa, S.; Francone, A.; Lorret, O.; Salaun, M.; Kosmala, B.; Kehagias, N.; Zelsmann, M.; Sotomayor-Torres, C. M.; Morris, M. A. Soft-graphoepitaxy using nanoimprinted polyhedral oligomeric silsesquioxane substrates for the directed self-assembly of PS-*b*-PDMS. *European Polymer Journal* **2013**, *49*, 3512-3521.
- (50) Jung, Y. S.; Ross, C. A. Orientation-Controlled Self-Assembled Nanolithography Using a Polystyrene-Polydimethylsiloxane Block Copolymer. *Nano Letters* **2007**, *7*, 2046-2050.

- (51) Jeong, S.-J.; Moon, H.-S.; Shin, J.; Kim, B. H.; Shin, D. O.; Kim, J. Y.; Lee, Y.-H.; Kim, J. U.; Kim, S. O. One-Dimensional Metal Nanowire Assembly via Block Copolymer Soft Graphoepitaxy. *Nano Letters* **2010**, *10*, 3500-3505.
- (52) Borah, D.; Rassapa, S.; Shaw, M. T.; Hobbs, R. G.; Petkov, N.; Schmidt, M.; Holmes, J. D.; Morris, M. A. Directed self-assembly of PS-*b*-PMMA block copolymer using HSQ lines for translational alignment. *Journal of Materials Chemistry C* **2013**, *1*, 1192-1196.
- (53) Zalusky, A. S.; Olayo-Valles, R.; Wolf, J. H.; Hillmyer, M. A. Ordered Nanoporous Polymers from Polystyrene-Polylactide Block Copolymers. *Journal of the American Chemical Society* **2002**, *124*, 12761-12773.
- (54) Koo, K.; Ahn, H.; Kim, S.-W.; Ryu, D. Y.; Russell, T. P. Directed self-assembly of block copolymers in the extreme: guiding microdomains from the small to the large. *Soft Matter* **2013**, *9*, 9059-9071.
- (55) Olayo-Valles, R.; Guo, S. W.; Lund, M. S.; Leighton, C.; Hillmyer, M. A. Perpendicular domain orientation in thin films of polystyrene - Polylactide diblock copolymers. *Macromolecules* **2005**, *38*, 10101-10108.

### 3.7. Appendix – Chapter 3

#### Directed self-assembly of lamellar forming poly(styrene)-*block*-poly(D,L-lactide) block copolymer thin films via solvo-thermal vapor annealing for on-chip etch mask application

The selectivity of THF for the PS-*b*-PLA (21 kg mol<sup>-1</sup> -19.5 kg mol<sup>-1</sup>) BCP can be defined by the expression,  $\chi = V_s(\delta_s - \delta_p)^2 / RT + 0.34$ ,<sup>1</sup> where  $V_s$  is the molar volume of the solvent,  $R$  is the gas constant,  $T$  is the Kelvin temperature, and  $\delta_s$  and  $\delta_p$  are the solubility parameters for solvent and polymer, respectively. As described in the chapter, the solubility parameters for PS, PLA and THF are 18.8, 22.2 and 19.4 [MPa]<sup>1/2</sup> while  $V_s$  for THF is 81.7 cm<sup>3</sup>.<sup>2</sup> From the calculations in table 3.7.S1 we see that THF is almost neutral for PS-*b*-PLA since  $\chi_{PS-THF}$  and  $\chi_{PLA-THF}$  values are close to 0.5. Since  $\chi_{PS-THF}$  is below 0.5, *i.e.* a good solvent, THF possesses a slight PS selectivity. The calculations also show that temperature does not affect the polymer-solvent selectivity greatly although there is a reduction in the  $\chi_{PLA-THF}$  value from 0.60 (at 23°C) to 0.57 (at 55°C), thus temperature improves the selectivity of the solvent for the PLA block. Chloroform (CHCl<sub>3</sub>, PS-*b*-PLA casting solvent) was also investigated as a choice solvent for the

solvent vapor annealing process and polymer-solvent interactions are summarized in

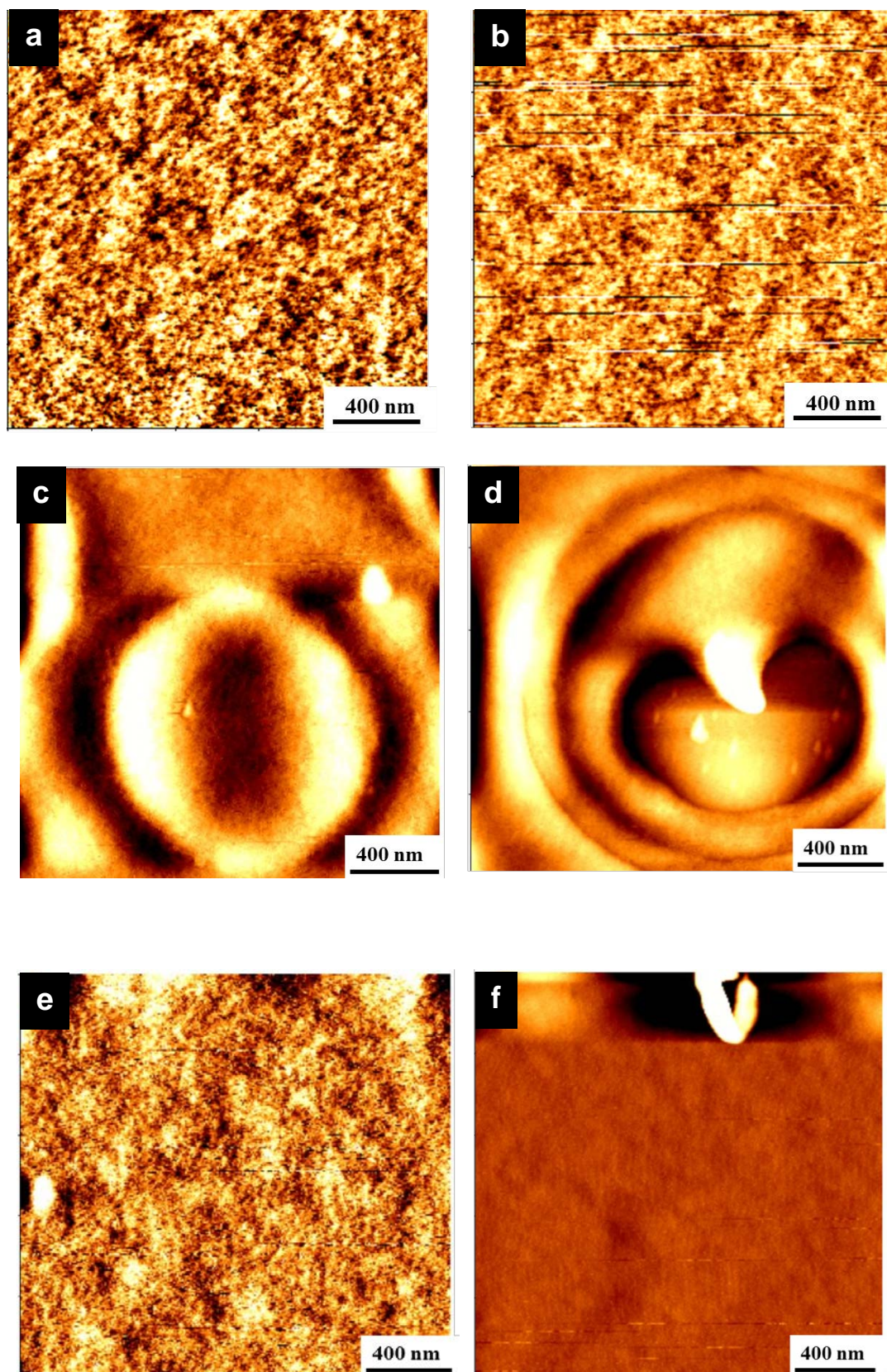
Table 3.7.S2.  $V_s$  for  $\text{CHCl}_3$  is  $80.7 \text{ cm}^3$ .

**Table 3.7.S1.** Polymer-solvent (P-S) interaction parameter ( $\chi_{\text{P-S}}$ ) for PS-*b*-PLA and THF solvent.

Temperature	$\chi_{\text{PS-THF}}$	$\chi_{\text{PLA-THF}}$
23°C	0.35	0.60
40°C	0.35	0.59
55°C	0.35	0.57

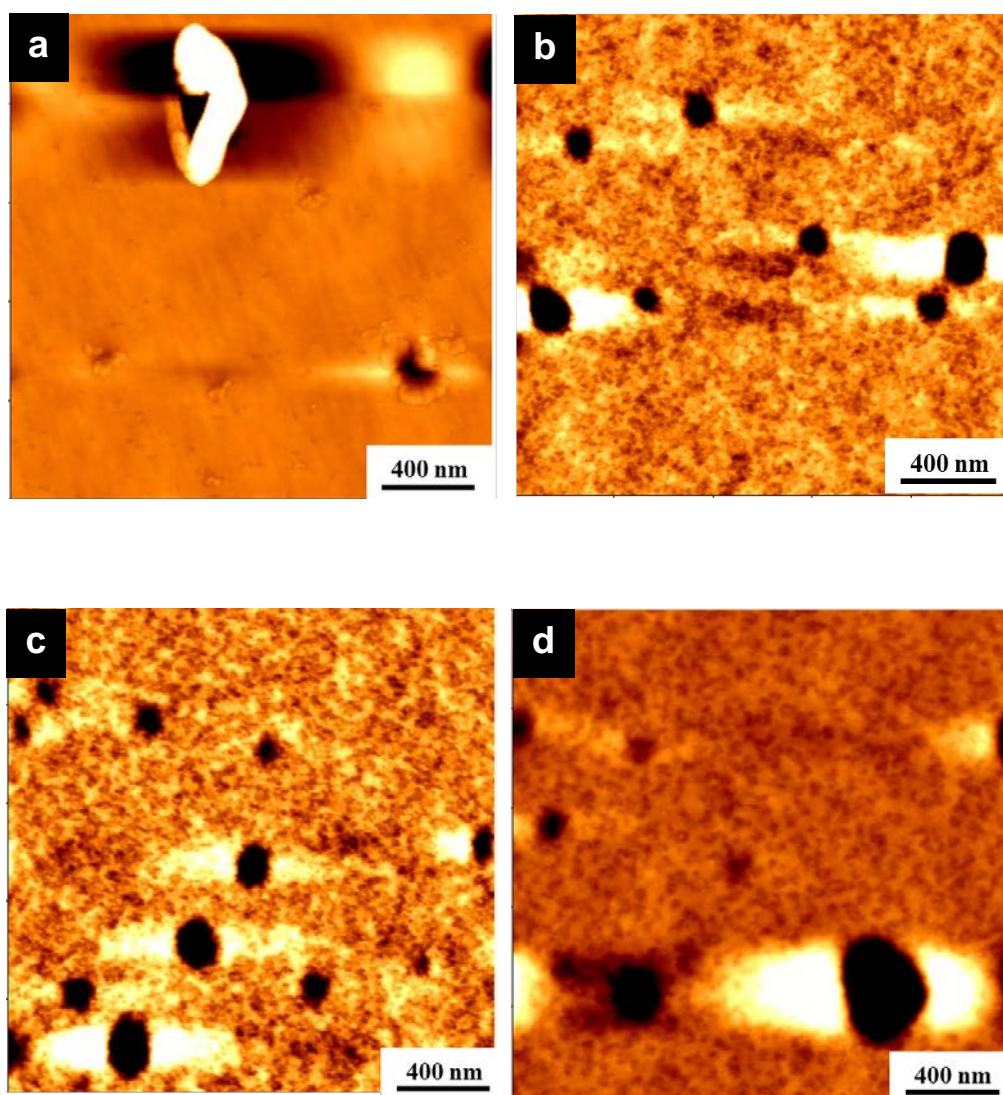
**Table 3.7.S2.** Polymer-solvent (P-S) interaction parameter ( $\chi_{\text{P-S}}$ ) for PS-*b*-PLA and  $\text{CHCl}_3$  solvent.

Temperature	$\chi_{\text{PS-THF}}$	$\chi_{\text{PLA-CHCl}_3}$
23°C	0.34	0.68
40°C	0.34	0.64
55°C	0.34	0.62

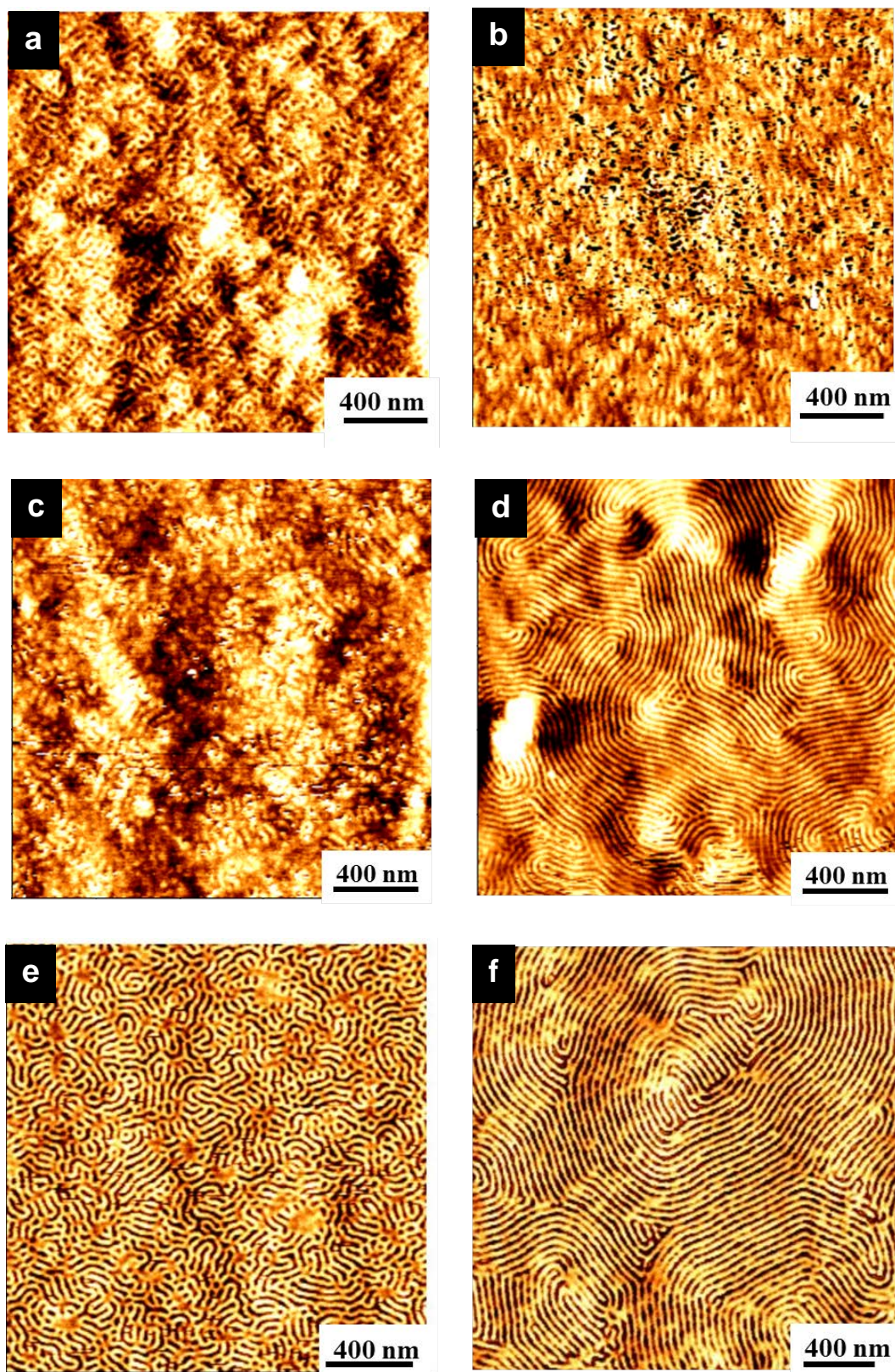


**Figure S3.7.1.** AFM topographic images of 0.5 wt % PS-*b*-PLA (21k-19.5k) thin films on silicon after (a) 30 minutes solvent vapor annealing (SVA) with chloroform ( $\text{CHCl}_3$ ) at room temperature, (b) 60 minutes SVA with  $\text{CHCl}_3$  at room temperature, (c) 30

minutes SVA with  $\text{CHCl}_3$  at  $40^\circ\text{C}$ , (d) 60 minutes SVA with  $\text{CHCl}_3$  at  $40^\circ\text{C}$ , (e) 30 minutes SVA with  $\text{CHCl}_3$  at  $55^\circ\text{C}$ , (f) 60 minutes SVA with  $\text{CHCl}_3$  at  $55^\circ\text{C}$ .

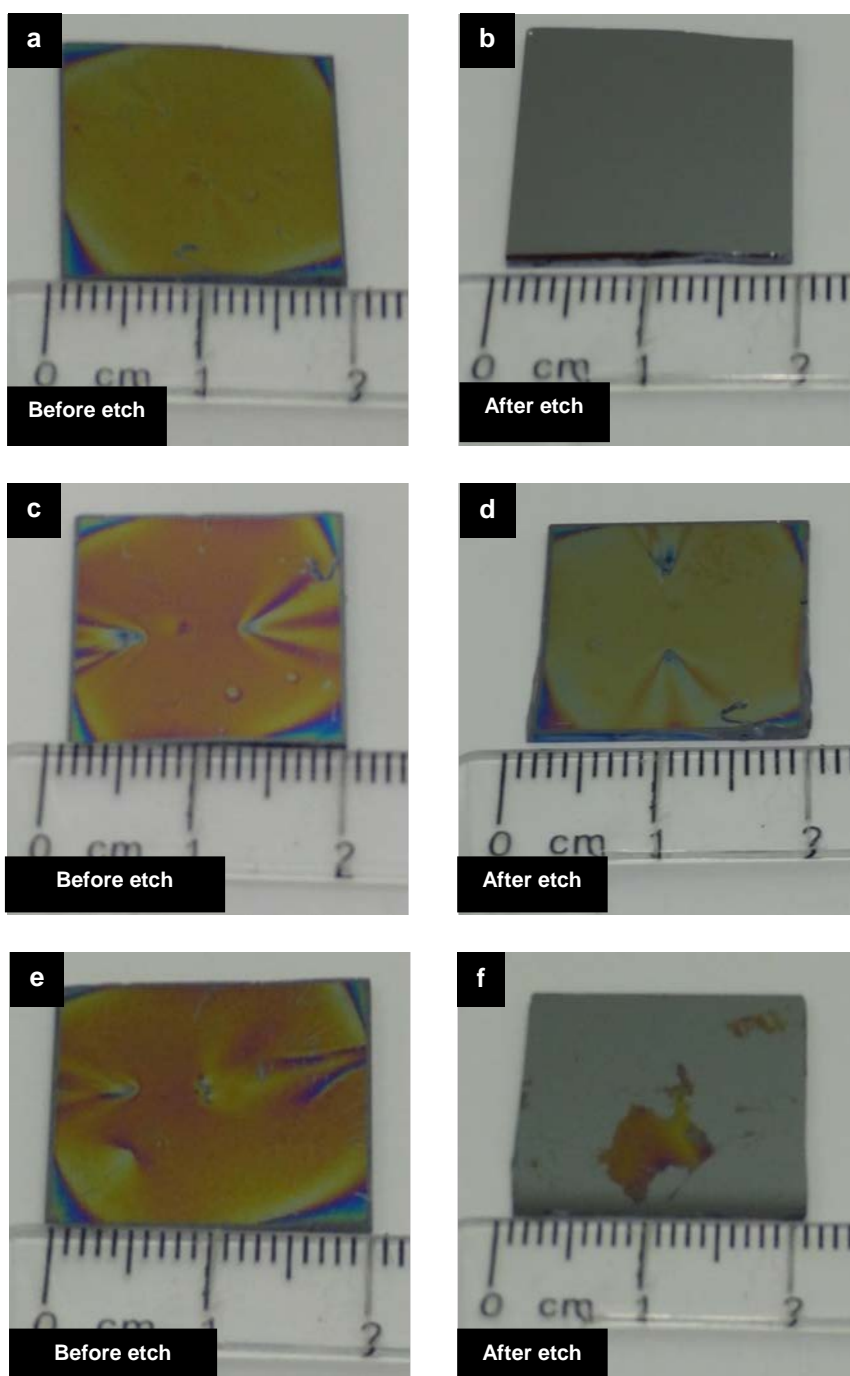


**Figure S3.7.2.** AFM topographic images of 0.5 wt % PS-*b*-PLA (21k-19.5k) thin films on silicon after (a) 30 minutes thermal annealing at  $40^\circ\text{C}$  (b) 60 minutes thermal annealing at  $40^\circ\text{C}$  (c) 30 minutes thermal annealing at  $55^\circ\text{C}$  (d) 60 minutes thermal annealing at  $55^\circ\text{C}$ . Microphase separation is not observed in any of the samples. Notably, hole formation is observed in each image (a) to (d). These were generally  $1 L_o$  ( $\sim 34$  nm) from AFM line profiles.



**Figure S3.7.3.** Atomic force microscopy topographic images of 0.5 wt % PS-*b*-PLA (21k-19.5k) thin films on silicon after (a) 30 minutes SVA with THF at room temperature, (b) 45 minutes SVA with THF at room temperature, (c) 30 minutes SVA with THF at 40°C, (d) 45 minutes SVA with THF at 40°C, (e) 30 minutes SVA with THF

at 55°C, (f) 45 minutes SVA with THF at 55°C. Figure S3.7.3 (e) and (f) also appear in chapter 3 (*i.e.* Figure 3.1) and are included here for comparison purposes.



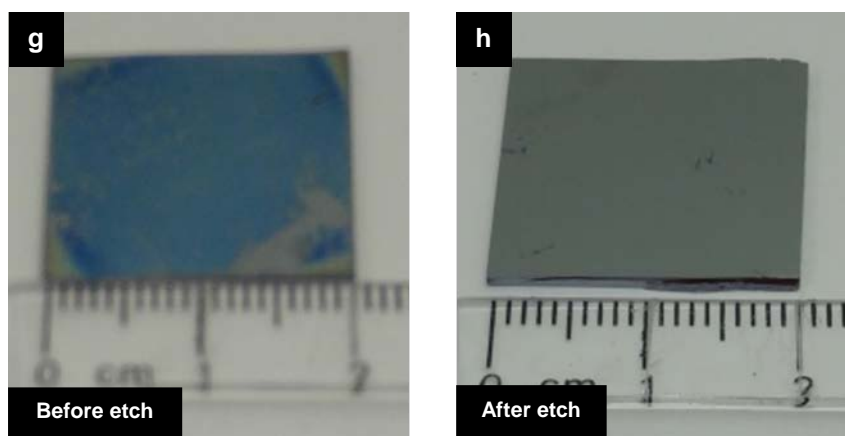


**Figure S3.7.4.** (a) Picture of  $2 \times 2 \text{ cm}^2$  silicon substrate piranha cleaned and sonicated for 10 minutes with  $\text{CHCl}_3$ . A 2 wt % PS-*b*-PLA (21k-19.5k) thin film was subsequently spun cast and then SVA with THF for 60 minutes at  $55^\circ\text{C}$ . (b) Shows sample from (a) after 5 minutes etching with 0.01M sodium hydroxide solution. (water:methanol, 60:40). It is clear that a surface wetting layer exists due to the complete film delamination. (c) Picture of  $2 \times 2 \text{ cm}^2$  HMDS silicon substrate with a 2 wt % PS-*b*-PLA (21k-19.5k) thin film spun cast and then SVA with THF for 60 minutes at  $55^\circ\text{C}$ . (d) Shows PS-*b*-PLA HMDS silicon sample from (c) after 5 minutes etching with 0.01M sodium hydroxide solution. (water:methanol, 60:40). The HMDS functionalization promotes a stronger adhesion of the block copolymer film with the underlying silicon substrate. (e) 2 wt% PS homopolymer film spun cast on  $2 \times 2 \text{ cm}^2$  silicon substrate that was initially piranha cleaned and sonicated for 10 minutes with  $\text{CHCl}_3$ . The 2 wt% PS homopolymer film was SVA for 60 minutes at  $55^\circ\text{C}$ . (f) The PS (22k) homopolymer showed near complete film delamination after 0.01M sodium hydroxide etching for 5 minutes. As can be seen from the picture, only a small portion of the original PS film was retained. (g) 2 wt% PLA (16k) homopolymer film spun cast on  $2 \times 2 \text{ cm}^2$  silicon substrate that was initially piranha cleaned and sonicated for 10 minutes with  $\text{CHCl}_3$ . The 2 wt% PS homopolymer film was SVA for 60 minutes at  $55^\circ\text{C}$ . (h) Following etching the film showed complete delamination as one would expect with the highly susceptible PLA component exposed to basic conditions.

### 3.8. References

- (1) McKenna, F. H. a. G. B. Physical Properties of Polymers Handbook. AIP Press **1996**, 379-400.
- (2) Hansen, C. M. Hansen solubility parameters: a user's handbook. CRC Press **2007**.

---

*Chapter 4*

---

**Self-Assembly of PS-*b*-P4VP Block Copolymer on Molecularly Functionalized Silicon Substrates: Fabrication of Inorganic Nanostructured Etchmask for Lithographic Use**

## 4.1. Abstract

Block copolymers (BCPs) are seen as a possible cost effective complementary technique to traditional lithography currently used in the semiconductor industry. This unconventional approach has received increased attention in recent years as a process capable of facilitating the ever decreasing device size demanded. Control over microdomain orientation and enhancing long range order are key aspects for the utility of BCPs for future lithographic purposes. This chapter provides an efficient route for the fabrication of highly ordered nanostructures suitable for such application. We investigate the significant effect of surface treatment regarding the self-assembly process of polystyrene-*block*-poly(4-vinylpyridine) (PS-*b*-P4VP) by employing an ethylene glycol layer, producing well defined perpendicular P4VP cylinders with long range order over large surface areas. Nanopores are generated through surface reconstruction using a preferential solvent, which allows for the incorporation of an inorganic moiety. Treatment of this pattern with UV/Ozone leads to formation of well-ordered iron oxide nanodots with a pitch of ~26 nm. Furthermore, high aspect ratio silicon nanopillars result following pattern transfer.

## 4.2. Introduction

In an effort to enable the desired feature size of future electronics, block copolymers (BCPs) have been the focus of intense research for the past decade, as outlined in numerous reviews.<sup>1-6</sup> BCPs now offer a promising alternative to the traditional “top-down” fabrication methods due to their processing advantages as well as from an economic standpoint. Owing to diffraction limits, issues with lithography methods have been well documented, as the semiconductor industry now seek a robust high throughput approach. The flexibility offered through the self-assembly of BCPs make these materials

ideal candidates for a wide range of applications and are not solely limited to lithography. However, paramount to their success in the electronics field is to produce high quality structures with long range order which possess few defects after pattern transfer.<sup>7,8</sup> BCPs consist of two monomer components that differ both physically and chemically and when microphase separated give rise to fascinating architectures. One such useful morphology is hexagonally packed cylinders, whereby when the minority block is removed or swollen creates nanopores which can be utilized for the deposition of metal nanoparticles (NPs). Smaller domain dimensions can be produced by lowering the molecular weight of the constituent BCP components and these tunable characteristics highlight the importance of BCPs in the future allowing for the development of ultra-high density storage media.

Dewetting is a major problem encountered with BCPs which prevents pattern formation, limits correlation length and leads to defects. Altering surface energies plays a significant role in controlling both wetting layer and morphologies of BCPs.<sup>9-11</sup> Polystyrene-*block*-polymethylmethacrylate (PS-*b*-PMMA) has been one of the most intensely studied BCPs to date, and various methodologies have been employed to control self-assembly. In asymmetric PS-*b*-PMMA, where PMMA is the minority block, the PMMA block has a preferential interaction with the oxide layers on the silicon substrate, and thus leads to in plane cylinders. To overcome this, the generation of cylinders normal to the surface has been allowed through the use of random copolymer brushes to “neutralize” the surface,<sup>12,13</sup> as well as PS-OH brushes to modify surface energy of the silicon substrate.<sup>14</sup> Recently, Kim *et al* have implemented a similar methodology by adding PS-OH homopolymer to a BCP (polystyrene-*block*-polyethyleneoxide (PS-*b*-PEO) solution resulting in highly ordered microdomains with a reduced process time in comparison to long annealing periods required for usual substrate chemistry modifications.<sup>15</sup> With

regard to polystyrene-*block*-poly(4-vinylpyridine) (PS-*b*-P4VP), control over microdomain orientation has previously been demonstrated by hydrogen bonding small molecules such as 3-Pentadecylphenol (PDP), 2-(4'-Hydroxybenzeneazo)benzoic acid (HABA) and 1-Pyrenbutyric acid (PBA) to P4VP.<sup>16-20</sup> These routes typically take a number of days for hydrogen bonding to successfully take place, adding to the complexity of the overall process. A fundamental challenge for BCPs applicability for integrated circuit integration is the successful transfer of the resulting pattern from the microphase separated BCP to the underlying substrate. To ensure that the pattern is transferred properly etch contrast is required. This can be done by wet etching the BCP, so the minority block is removed or through surface reconstruction whereby nanopores are also produced after exposure to a preferential solvent that induces swelling. Alternatively, plasma assisted etching [reactive ion etching (RIE) or inductively coupled plasma (ICP)], also known as dry etching, is a powerful tool for the selective etch of a minor component and etch directionality leads to ideal templates for pattern transfer as detailed in recent etch studies by Borah *et al.*<sup>21,22</sup>

To generate highly ordered silicon nanostructures with few defects a hard mask (such as Fe<sub>2</sub>O<sub>3</sub>) can also be employed, fabricated using the minority block removal/swelling previously detailed and then followed by the addition of a metal complex. Surface reconstruction has been demonstrated in PS-*b*-P4VP systems using a preferential solvent like ethanol,<sup>23,24</sup> and has been reported in PS-*b*-PMMA BCPs using acetic acid.<sup>25</sup> The resulting nanopores allow for the deposition of various particles with wide ranging functions. With PS-*b*-P4VP, NP inclusion can be done either by depositing the NPs after the self-assembly process or inclusion of the desired ratio of NP to the diblock copolymer solution before spin coating. For example, well-ordered micelle and cylindrical

microdomains have been reported in PS-*b*-P4VP BCPs for metal inclusion to fabricate arrays of iron nanocatalysts,<sup>26</sup> copper nanocatalysts,<sup>27</sup> titania NPs,<sup>28</sup> and iron platinum NPs.<sup>29</sup>

This chapter describes a simple surface modification method (having a short processing time, ~ 1 hour) - using a silicon oxide surface functionalized with an ethylene glycol layer and detail its subsequent effects for controlling the self-assembly process in asymmetric PS-*b*-P4VP as well as increasing surface coverage of the resulting morphology through solvent annealing. This increased surface coverage have beneficial implications for transistor devices but also for other electronic devices such as passive on-chip capacitors whose storage capacity is dependent on area.<sup>30</sup> Our investigation also highlights the role that temperature has in producing highly oriented and well-ordered patterns. Using the surface reconstruction strategy which created a nanoporous template we deposited an iron nitrate ethanol solution that was immediately followed by UV/Ozone exposure to remove the polymer matrix surrounding the nanodot array. Significantly we have shown that this BCP system with a hard mask led to a greater depth profile following pattern transfer.

### 4.3. Experimental

**Materials.** Planar substrates used were highly polished single-crystal silicon <100> wafers (p- type) with a native oxide layer of ~ 2 nm. No attempt was taken to remove the native oxide of a few nm depths. Polystyrene-block-Poly(4-vinylpyridine) was purchased from Polymer Source, Inc., Canada, with a molecular weight of  $M_n = 33.5 \text{ kg mol}^{-1}$  ( $M_{nPS} = 24 \text{ kg mol}^{-1}$ ;  $M_{nP4VP} = 9.5 \text{ kg mol}^{-1}$ ;  $f_{PS} = 0.70$ ), a polydispersity ( $M_w/M_n$ ) of 1.10 (where,  $M_n$  and  $M_w$  are number average and weight average molecular weights)

and was used without further purification. Iron (III) nitrate nonahydrate ( $\text{Fe}_2(\text{NO}_3)_3 \cdot 9\text{H}_2\text{O}$ ), ethylene glycol (EG,  $\text{CH}_2(\text{OH})\text{CH}_2(\text{OH})$ , 95.0%), toluene (99.8%, anhydrous), tetrahydrofuran (THF) (99.8%, anhydrous), ethanol (dehydrated, 200 proof), acetone (99.0%, anhydrous), iso-propanol (IPA) (99.0%, anhydrous), sulphuric acid (98.0%) and hydrogen peroxide (30.0%) were purchased from Sigma-Aldrich and used without further purification unless otherwise stated. De-ionized (DI) water was used wherever necessary.

**Substrate Cleaning, Activation and Modification with EG.** Substrates were cut into  $2.0 \text{ cm}^2$  pieces and then degreased by ultrasonication in acetone and IPA solutions for 5 minutes each, dried in flowing  $\text{N}_2$  gas and baked for 2 minutes at  $120^\circ\text{C}$  in an ambient atmosphere to remove any residual IPA. This was followed by cleaning in a piranha solution (1:3 v/v 30%  $\text{H}_2\text{O}_2$ : $\text{H}_2\text{SO}_4$ ) (CAUTION! May cause explosion in contact with organic material!) at  $100^\circ\text{C}$  for 60 min, rinsed with DI water (resistivity  $\geq 18 \text{ M}\Omega/\text{cm}$ ) several times, acetone, ethanol and dried under  $\text{N}_2$  flow. Piranha activation removes any organic contaminant, greases and creates hydroxyl groups on the silicon substrates. Solution of ethylene glycol (EG) 5 % (v/v) was prepared in ethanol and was stirred at room temperature ( $\sim 23^\circ\text{C}$ ) for 2 hours to ensure complete mixing. The hydroxylated substrates (by piranha solution as mentioned above) were immediately coated with ethylene glycol by spin-coating (P6700 Series Spin-coater, Speciality Coating Systems, Inc., USA) at 1000 rpm for 30 s. Samples were air dried at room temperature ( $\sim 23^\circ\text{C}$ ) for 30 minutes, washed with absolute ethanol and then dried under a stream of nitrogen. Films survived repeated rinses in ethanol as observed by XPS and FTIR.

**BCP Film Preparation and Solvent Anneal.** The polymer was dissolved in a toluene: THF (80: 20) mixture to yield 0.5 wt. % solution and left stirring for 12 hours to ensure complete dissolution. BCP films were prepared by spin coating the polymer solution onto

the substrates at 3000 rpm for 30 seconds. Following deposition, the PS-*b*-P4VP generated thin films were exposed to a saturated THF environment at different temperatures viz., 40 °C, 50 °C and 60 °C. Solvent annealing was carried out in the conventional manner with a small vial containing 8-10 ml of annealing solvent placed inside a glass jar (150 ml) with BCP sample for different time periods. Samples were removed from the glass jars after the desired anneal time and allowed to evaporate the trapped solvent at ambient conditions.

**BCP Film Reconstruction with Ethanol.** Surface reconstruction was carried out by immersing the solvent annealed thin film in ethanol for 20 minutes. After this immersion period, the sample was removed and dried under nitrogen flow. This provided enough time for swelling of the P4VP domains to enable reconstruction of a nanoporous film for subsequent deposition of iron nitrate solution.

**Iron Oxide Nanopattern Development.**  $\text{Fe}_2(\text{NO}_3)_3 \cdot 9\text{H}_2\text{O}$  solution of 0.3 wt.% was prepared in ethanol and spin-coated onto the ethanol reconstructed film at 3000 rpm for 30 seconds. UV/Ozone treatment was used to oxidize the precursor and remove polymer. Samples were UV/Ozone treated in a UV/Ozone system (PSD Pro Series Digital UV Ozone System; Novascan Technologies, Inc., USA). The UV source is two low-pressure mercury vapor grid lamps. Both lamps have an output current of 0.8-0.95 A and power of 65-100 W, as reported by the manufacturer, and have strong emissions at both wavelengths of UV radiation (184.9 nm and 253.7 nm). Samples were placed at a distance of about 4 mm from the UV source and exposed to UV irradiation. The system produces highly reactive ozone gas from oxygen that is present within the chamber. Samples were exposed to UV/Ozone for 3 hours to oxidize the inorganic precursor and remove the PS template. The inorganic nanostructure was further calcined in a muffle furnace (EFL 11/14B CARBOLITE) at 800 °C for 1 hour to verify the thermal stability.

**Pattern Transfer by Plasma Etching.** The FeOxide(s) nanodots fabricated from the BCP template were used as an etch mask for pattern transfer. The silicon etch was performed using CHF<sub>3</sub> (80 sccm) and SF<sub>6</sub> (15 sccm) gases for 12 seconds with an inductively coupled plasma (ICP) and reactive ion etching (RIE) powers of 1200 W and 30 W, respectively, at 2.0 Pa with a helium backside cooling pressure of 1.3 kPa to transfer the patterns into the underlying substrate. The etching process was accomplished in an OIPT Plasmalab System100 ICP180 etch tool.

**Characterization.** Static contact angles ( $\theta_a$ ) of deionized water was measured at ambient temperature using a Data Physics Contact Angle (model: OCA15) goniometer. Contact angles were measured on the opposite edges of at least five drops and averaged. The values were reproducible to within 1.5°. BCP film thicknesses were measured with a spectroscopic ellipsometer “Plasmos SD2000 Ellipsometer” at a fixed angle of incidence of 70°, on at least five different places on the sample and was reported as the film thickness result. A two layer model (SiO<sub>2</sub> + EG) for EG modified surface and a three layer model (SiO<sub>2</sub> + EG + BCP) for total BCP films were used to simulate experimental data. An IR660, Varian infrared spectrometer was used to record the FTIR spectra. The measurements were performed in the spectral range of 4000-500 cm<sup>-1</sup>, with a resolution of 4 cm<sup>-1</sup> and data averaged over 32 scans. X-ray Photoelectron Spectroscopy (XPS) was performed on Vacuum Science Workshop CLASS100 high performance hemispherical analyser using Al K $\alpha$  ( $h\nu = 1486.6$  eV) mono X-ray source. Spectra were obtained at a take-off angle of 15°. Samples were loaded into the vacuum chamber within 1 hour after being prepared and were subjected to XPS analysis. Photoemission peak positions were corrected to C 1s at a binding energy of 284.8 eV. GISAXS and reflectometry data were obtained from beamline I07 at Diamond Light Source Ltd (Didcot, Oxfordshire, U.K.). GISAXS flight tube (purpose built) and Pilatus 2M detector were used for GISAXS

measurements. Atomic Force Microscope (SPM, Park systems, XE-100) was operated in AC (tapping) mode under ambient conditions using silicon microcantilever probe tips with a constant of  $42 \text{ N m}^{-1}$  and a scanning force of  $0.11 \text{ nN}$ . Topographic and phase images were recorded simultaneously. SEM images were obtained by a high resolution ( $< 1 \text{ nm}$ ) Field Emission Zeiss Ultra Plus-SEM with a Gemini® column operating at an accelerating voltage of  $5 \text{ kV}$ . EDX data and images were obtained using Helios Nanolab DB FIB using HAADF detector in STEM mode. The TEM lamella specimen were prepared by the Helios NanoLab DB FIB and were analysed by JEOL 2100 high resolution transmission electron microscope operating at an accelerating voltage of  $200 \text{ kV}$ .

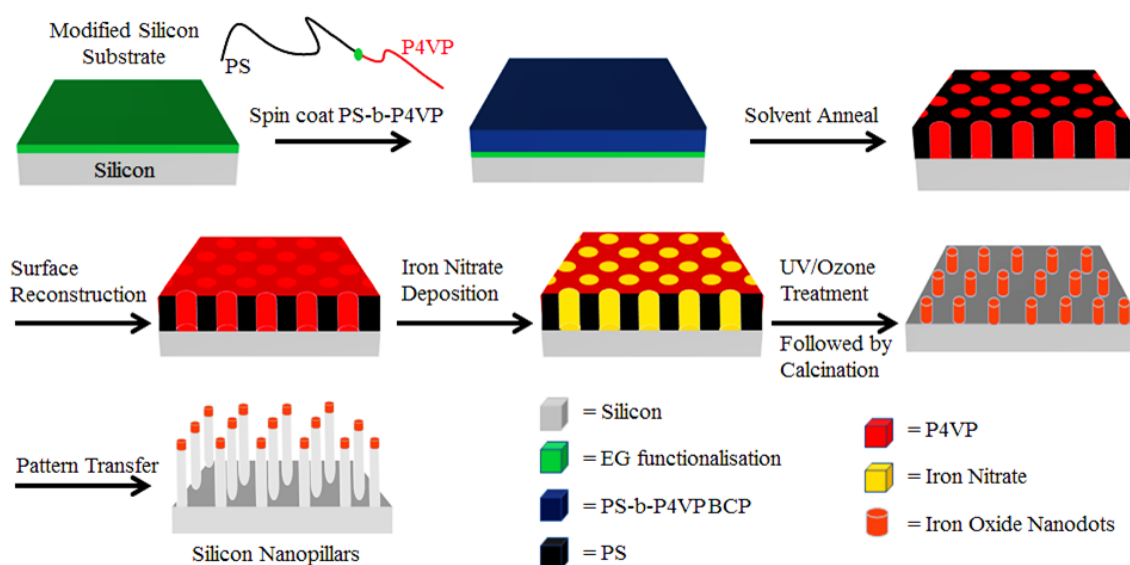


**Figure 4.1.** Details of the process flow of BCP self-assembly on silicon substrates functionalized with EG, film reconstruction with ethanol, iron oxide hard mask fabrication and subsequent plasma etching to fabricate silicon nanopillars.

## 4.4. Results and Discussion

### 4.4.1. Molecular Functionalization with EG

For successful BCP integration in next generation electronics novel approaches are required both for control of self-assembly and for reducing present defect formation

densities. Figure 4.1. details the silicon substrate cleaning, modification with EG and the BCP microphase separation steps. The hydrophilic nature of this EG coated film enables the perpendicular orientation of P4VP hexagonally packed cylinders owing to the preferential interaction with P4VP block in PS-*b*-P4VP. This alteration in substrate surface chemistry aids the self-assembly in forming patterns with a high degree of order that is absent from non-modified silicon substrates (see below).

Prior to BCP film formation, the EG functionalized surface was fully characterized by AFM imaging, contact angle measurement, film thickness by ellipsometry, FTIR, and XPS. The AFM scan of the EG treated surface is presented in Figure 4.2a and reveals a fairly uniform surface with occasional particulate contamination which is however, not seen after BCP deposition (see below). We believe this is multi-layer formation due to strong hydroxyl bonding between EG molecules. We suggest that the multi-layers are re-dissolved in the BCP casting solution but are not re-deposited because of excellent coverage of the BCP on the molecular layer. These observations support the hypothesis of uniform surface functionalization. The attachment of EG at the substrate surface had a marked effect on the water contact angle of the surface. The contact angle of the piranha treated surfaces was measured at  $\sim 27^\circ$ . The static water contact angle of EG modified silicon substrate was found to be  $36^\circ$ , thus portraying the hydrophilic nature of the EG monolayers. We further characterized the EG functionalized surface using ellipsometry and the thickness was measured 1.72 nm. It should be stressed that this technique cannot be used to predict the film density and as such EG coverage, but gives evidence of the functionalization process.

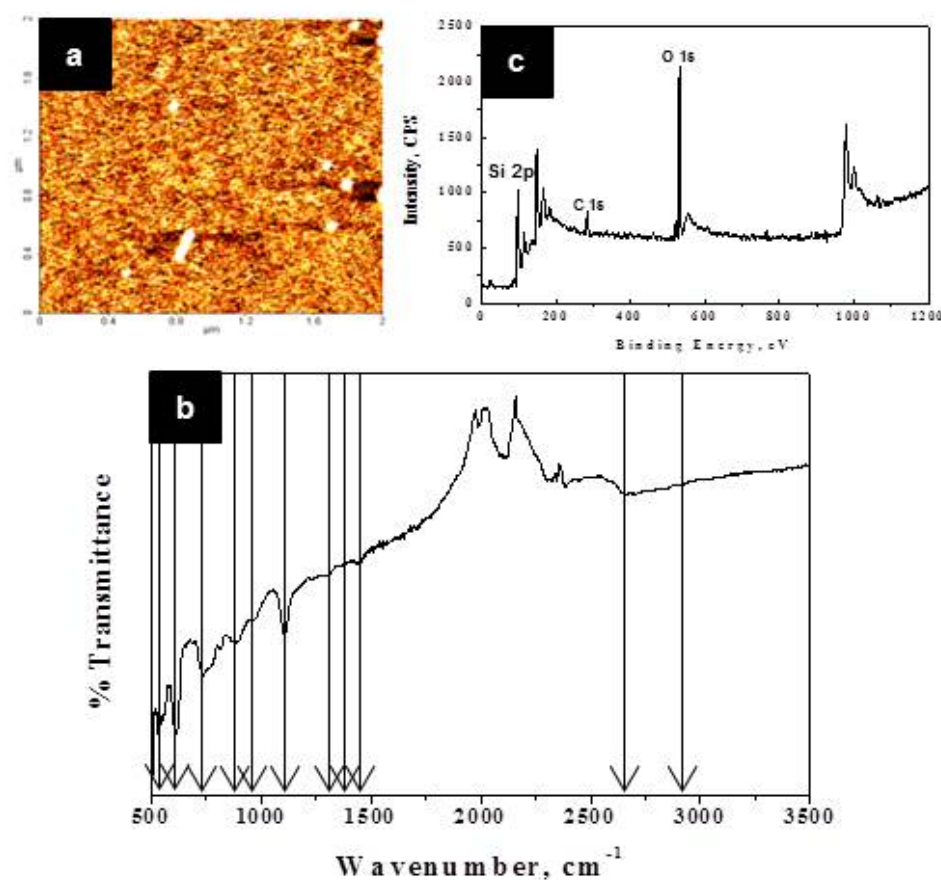


**Figure 4.2.** AFM topography image (2-D) (a), FTIR spectrum (b) and XPS spectrum (c) of EG functionalized silicon substrate.

The FTIR spectrum of EG functionalized surface presented in Figure 4.2b shows a very broad, intense OH valence vibration band near  $2600\text{ cm}^{-1}$ . All of the OH deformational and skeletal bands are slightly shifted to lower wavelength region compared to the liquid phase EG bands and these shifts are consistent with grafting of EG-OH onto the silicon substrate via hydrogen bonding. Besides the simple stretching vibrational mode, two additional deformational vibrational modes are readily observed in the spectra at  $1420\text{ cm}^{-1}$  and  $723\text{ cm}^{-1}$ . The assignment of the skeletal valence and  $\text{CH}_2$  deformation vibrations in EG is not facile but comparison to simple molecular hydrocarbon molecules can be useful.<sup>31</sup> Thus, from Figure 4.2b, the peaks due to  $\text{CH}_2$  deformation are observed are  $2942\text{ cm}^{-1}$  ( $\nu\text{CH}_2$ ),  $1420\text{ cm}^{-1}$  ( $\delta\text{CH}_2$ ),  $1326\text{ cm}^{-1}$  ( $\gamma\text{CH}_2$ ),  $1268\text{ cm}^{-1}$  ( $\tau\text{CH}_2$ ) and  $923$

$\text{cm}^{-1}$  ( $\rho\text{CH}_2$ ). The peak at  $1420\text{ cm}^{-1}$  is overlapped with the hydroxyl deformation peak assigned above. The two skeletal valance vibrations in EG can be assigned to peaks at  $854\text{ cm}^{-1}$  and  $1097\text{ cm}^{-1}$ , respectively, of which the lower frequency probably has more C-C character and the other more C-O character. Two other features at  $530\text{ cm}^{-1}$  and  $603\text{ cm}^{-1}$  can be assigned O-C-C and O-C-C-O vibrational modes, respectively. All of the features are consistent with EG attachment to the surface. The EG functionalized silicon substrate was further assessed using XPS analysis and data are presented in Figure 4.2c. Well-resolved C *1s* (284.9 eV), O *1s* (533.0 eV) and Si *2p* (98.5 eV) features are readily observed (note these values are charge corrected values so the Si *2p* peak is observed at 98.5 eV consistent with other studies of silicon wafers). The C *1s* feature is consistent with adsorbed features such as adsorbed ethanol.<sup>32</sup> The O *1s* is similar to that expected of hydroxyl species in the presence of strong hydrogen bonding.<sup>32,33</sup>

As detailed above, the silicon substrate with a thin native oxide layer was piranha activated prior to EG deposition. Piranha activation results in the formation of surface OH groups as can be seen from the very low water contact angle ( $27^\circ$ ) on the substrate surface. EG solution in ethanol was spin-coated on the activated surface and exposed in ambient conditions at room temperature ( $\sim 23\text{ }^\circ\text{C}$ ) prior to use. Since the sample was not annealed, it is highly unlikely that condensation reactions between the silanol-OH and EG-OH groups occurred. Instead, it appears that the EG molecules were attached to the substrate surface through hydrogen bonding as suggested by XPS and FTIR. The rather low water contact angle suggests that only one hydroxyl group is used to bond to the surface with the second hydroxyl group available for surface reaction. The availability of one of the OH groups is consistent with the areas of multilayer formation seen in the AFM analysis. It should be noted that the assignment of hydrogen bonding mechanism

rather than a condensation reaction of EG-OH groups and surface silanol-OH groups is only partly supported by the XPS, FTIR and contact angle measurements and detailed work may be required. However, we do think this is a valid mechanism as although the EG is strongly bound enough to resist removal during ethanol washes (and subsequent film deposition), however; all traces of EG are lost upon heating to temperatures above 100 °C in vacuum.

#### 4.4.2. BCP Self-assembly on Functionalized Surface

By tailoring the surface energy through this simple surface chemistry modification we have developed highly oriented stable microdomains with reduced defect densities as evidenced from the topographic image shown in Figure 4.3-4.6. The periodicity of these domains is 26 nm (cylinder diameter = 20 nm). Thin films of PS-*b*-P4VP (24k-9.5k) were generated after spin coating from a 0.5 wt.% BCP solution in toluene/THF mixture (see experimental for further details) onto the EG treated silicon substrate and solvent annealed in a THF atmosphere at 50 °C. Park *et al.*<sup>34-36</sup> as well as Shin *et al.*<sup>37</sup> have demonstrated the effectiveness of developing BCP templates from a mixed solvent environment with asymmetric PS-*b*-P4VP. In some cases even after spin coating ordered morphologies were obtained, which were improved upon solvent annealing (see Appendix – Chapter 4, Figure S4.7.1). In this study, THF which is a slightly PS selective solvent was used for annealing thin films. The ability of THF to greatly improve lateral ordering has previously been discussed.<sup>38</sup>

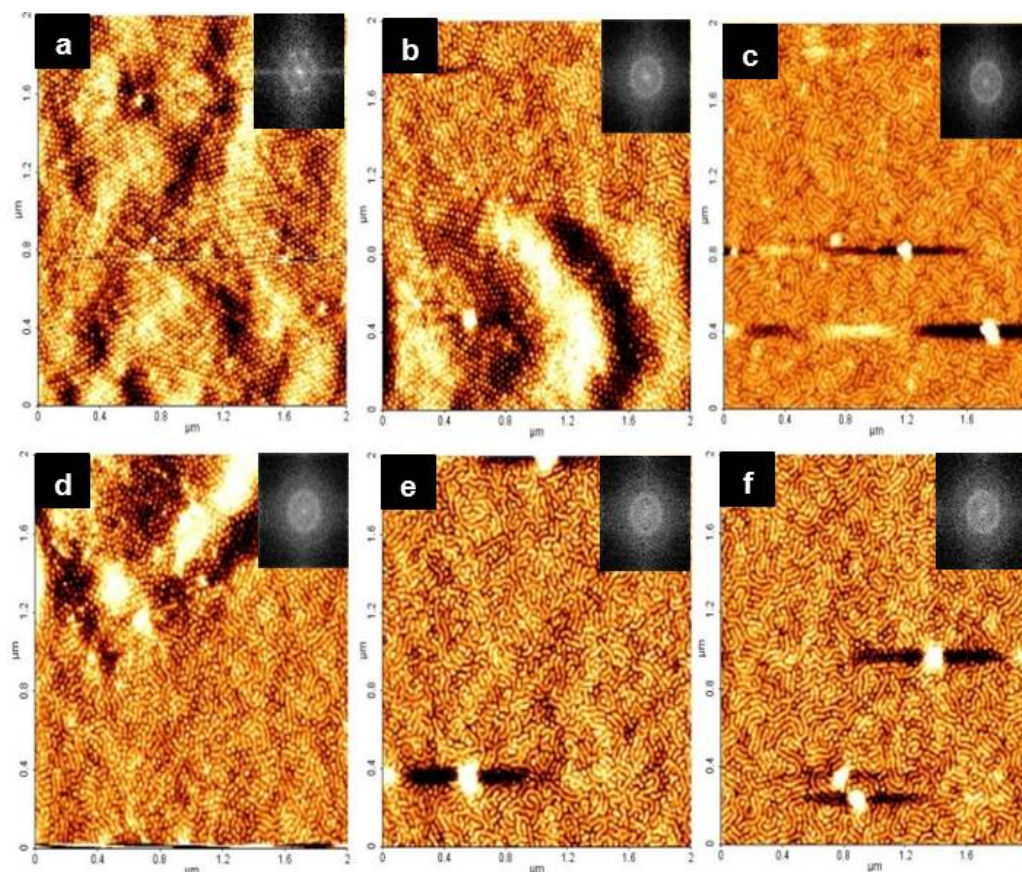


**Figure 4.3.** AFM topography images of PS-*b*-P4VP thin films on toluene cleaned bulk silicon substrates (a - 2 hours, b - 4 hours, c - 6 hours) and EG treated substrates (d - 2 hours, e - 4 hours, f - 6 hours) annealed in THF atmosphere at  $\sim 17$  °C (room temperature). FFT patterns inset show the difference in the degree of order.

Although most hexagonal forming PS-*b*-P4VP systems that have been studied are annealed at room temperature ( $\sim 20$  °C) in a nitrogen atmosphere, this produced a combination of mostly poorly ordered perpendicular and parallel cylinders with macroscale dewetting as well as defects in phase separated areas irrespective of the anneal conditions considered (Figure 4.3). Instead a range of temperatures were investigated to yield the most ordered morphology and increasing the temperature provides sufficient driving force for microphase separation to take place forming ordered patterns that is not evident at lower temperatures.

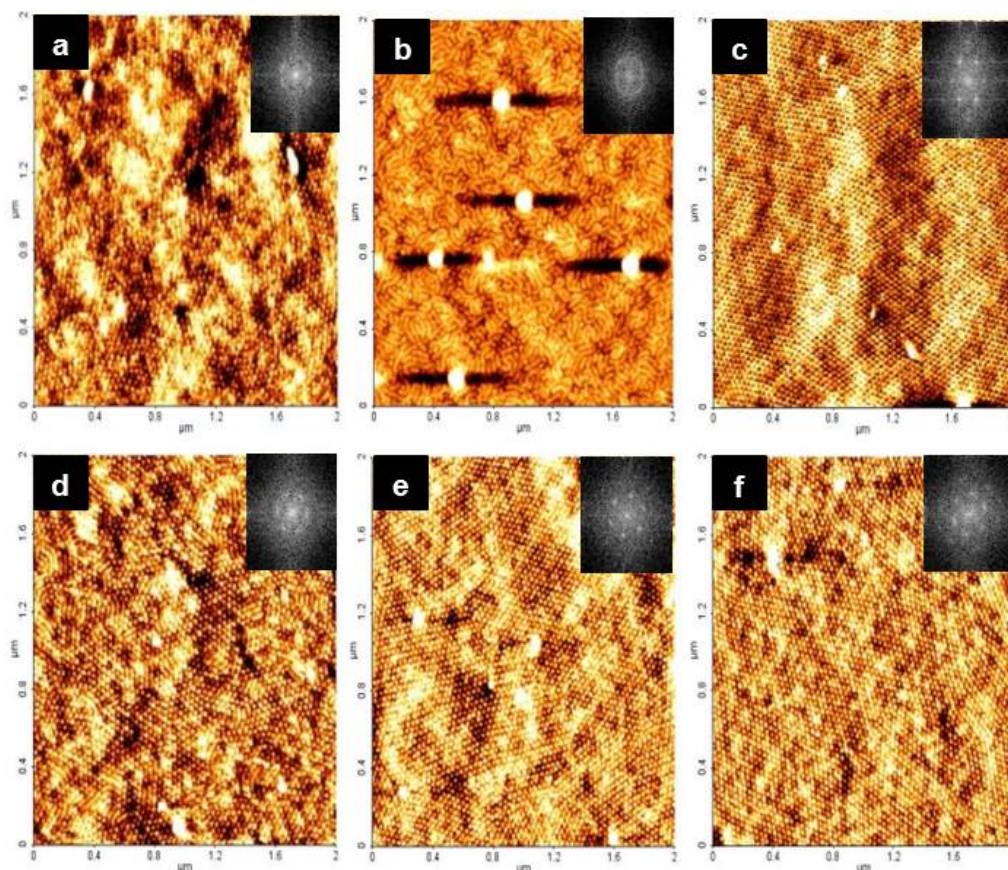


**Figure 4.4.** AFM topography images of PS-*b*-P4VP thin films on toluene cleaned bulk silicon substrates (a - 2 hours, b - 4 hours, c - 6 hours) and EG treated substrates (d - 2 hours, e - 4 hours, f - 6 hours) annealed in THF atmosphere at 40 °C. FFT patterns inset show the difference in the degree of order.

Both toluene cleaned and EG treated substrates showed evidence of both parallel and perpendicular cylinders at different stages of the annealing process. A study of the evolution of morphology of PS-*b*-P4VP was examined over 2, 4 and 6 hour periods at 40 °C, 50 °C and 60 °C in a THF atmosphere. Annealing carried out at 40 °C on toluene cleaned substrates is shown in Figure 4.4a-c. Well-developed microdomains were produced after 2 hours annealing, however; surface coverage was poor in comparison to the microdomains produced on EG functionalized substrates at 40 °C. All AFM images for EG samples taken at 40 °C show highly ordered domains as represented by the FFT inset in Figure 4.4d-f. Samples annealed for 6 hours at 50 °C gave highly uniform films

with high surface coverage and ordered arrays (See Appendix Figure S4.7.2). However, it should be noted that the processing window for these film characteristics are not limited to one specific time and temperature for EG samples. Furthermore, it was found that those films annealed for this time period did not exhibit both perpendicular and parallel cylindrical orientation. Figure 4.5c shows the resulting pattern from a PS-*b*-P4VP film on toluene only cleaned substrates annealed at 50 °C for 6 hours. The corresponding BCP film on an EG treated sample annealed for 6 hours at 50 °C gave the best ordered perpendicular microdomain orientation. Furthermore, it was found that those films annealed for this time period did not show any mixed cylindrical orientation. This comparison illustrates the ability that EG has to wet the substrate sufficiently resulting in enhanced surface coverage (See Figure S4.7.2). Films which were annealed in the same solvent annealing condition but at an elevated temperature of 60 °C are shown in Figure 4.6a-f. With the elevated temperature and longer annealing periods (especially 4 and 6 hours) good perpendicular domains were developed. With regard to toluene cleaned substrates only, all annealing temperatures showed macroscale dewetting as well as defects. It was generally observed that discrete holes formed in the non-EG treated substrate surface, a phenomenon associated with thin film destabilization by intermolecular forces.

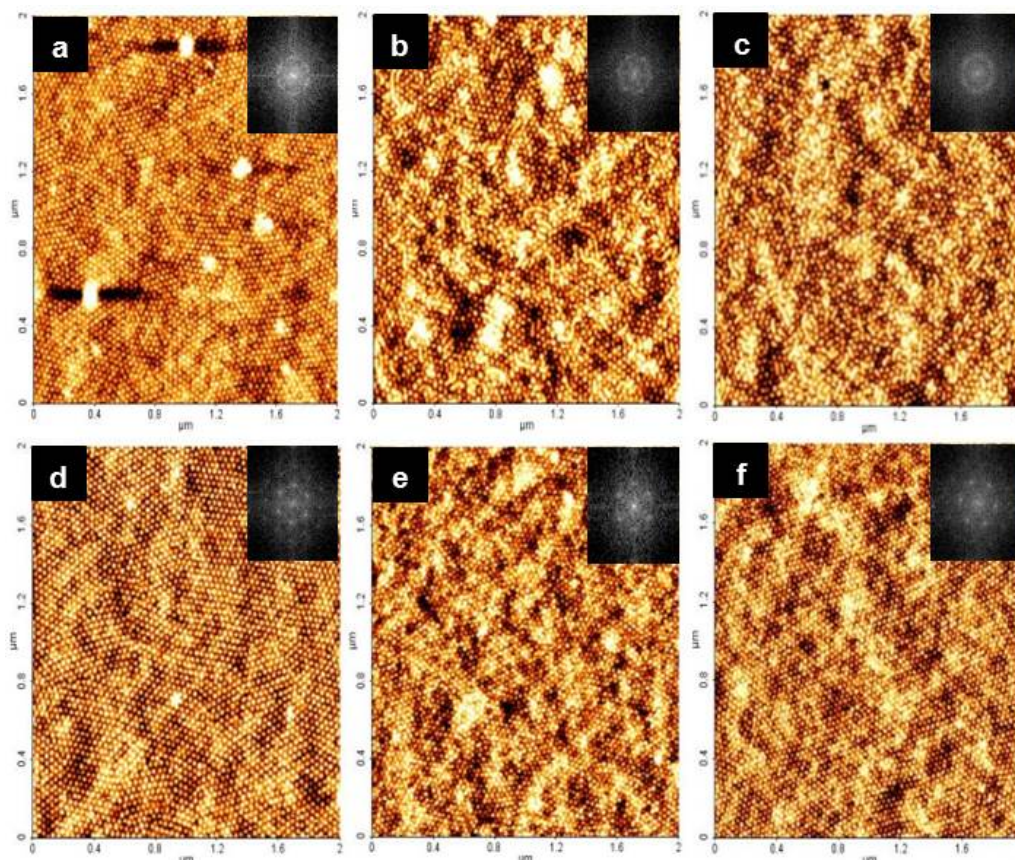


**Figure 4.5.** AFM topography images of PS-*b*-P4VP thin films on toluene cleaned bulk silicon substrates (a – 2 hours, b – 4 hours, c – 6 hours) and EG treated substrates (d – 2 hours, e – 4 hours, f – 6 hours) annealed in THF atmosphere at 50 °C. FFT patterns inset show the difference in the degree of order.

Since hole growth in thin films is significantly influenced by both interfacial and hydrodynamic forces we believe the toluene only cleaned substrates produce more defects and hole growth due to these intermolecular forces with a bare silicon surface in comparison to substrates that were chemically functionalized with EG.<sup>39</sup> Also both a mixture of perpendicular and parallel cylinders has yet to be shown in asymmetric PS-*b*-P4VP when annealed in a THF atmosphere. We employed THF only but THF/Toluene (80:20) was also studied and produced the same results. This work shows how the patterns are not thermodynamically stable as the structure can change between all perpendicular cylinders and a mixture of both perpendicular and parallel cylinders. We

suggest that this mixed orientation results from a swelling/deswelling process as described by Mokarian *et al.* for PS-*b*-PEO systems.<sup>40</sup> Our observation for this PS-*b*-P4VP system does not show time or structural fluctuations as dramatic as the PS-*b*-PEO system mentioned but show similarities that suggest a film thinning effect also occurring and therefore, the release of excess solvent causes a brief rearrangement of cylinders. So, in summary, we found that 6 hours of annealing in a THF atmosphere at 50 °C gave the most consistent pattern that could be utilized for our intended purpose.

The solubility of the BCP blocks in a particular solvent and the rate of solvent evaporation causes the microphase separation as well as orientation of the microdomains. Solvent swelling of a BCP film to a solvent vapor results in swelling the BCP film with solvent vapors and confers enough mobility for the BCP to reorganize. The miscibility between a polymer and a solvent is governed by the polymer (P)-solvent (S) interaction parameter  $\chi_{P-S}$ .<sup>41</sup> The selectivity of THF for the PS-*b*-P4VP BCP can be defined by the expression,  $\chi = V_s (\delta_s - \delta_p)^2 / RT + 0.34$ ,<sup>42</sup> where  $V_s$  is the molar volume of the solvent,  $R$  is the gas constant,  $T$  is the temperature, and  $\delta_s$  and  $\delta_p$  are the solubility parameters for

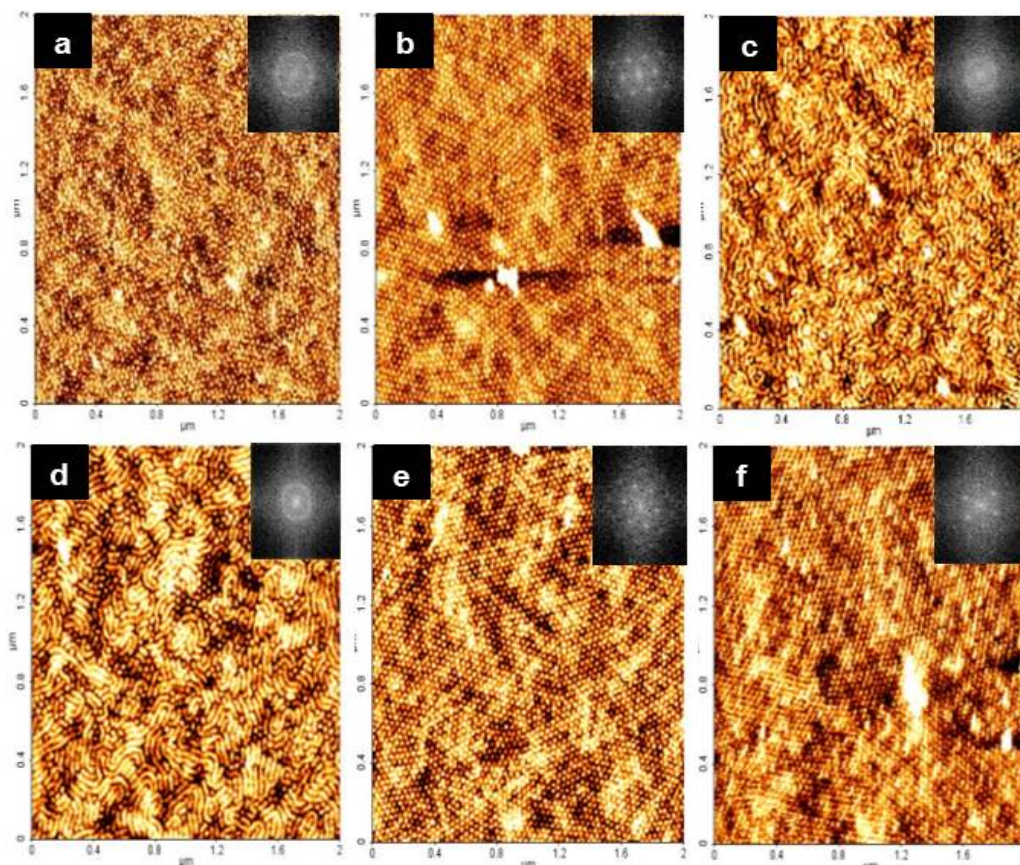


**Figure 4.6.** AFM topography images of PS-*b*-P4VP thin films on toluene cleaned bulk silicon substrates (a – 2 hours, b – 4 hours, c – 6 hours) and EG treated substrates (d – 2 hours, e – 4 hours, f – 6 hours) annealed in THF atmosphere at 60 °C. FFT patterns inset show the difference in the degree of order.

solvent and polymer, respectively. From literature,  $V_s$  for THF is 81.7 cm<sup>3</sup>,  $\delta_s$  for PS, PVP, and THF are 18.6, 22.2, and 16.8 (MPa)<sup>1/2</sup>, respectively.<sup>43</sup> Data calculated at various temperatures are presented in Table 1. Considering the Flory-Huggins criterion for complete solvent-polymer miscibility, i.e.,  $\chi_{P-S} < 0.5$ , it appears that THF is a good solvent for PS and a poor solvent for PVP at the four temperatures (Table 1). There are minor variations in the values of  $\chi_{PS-THF}$  and  $\chi_{PVP-THF}$ , both of which slightly decreases with an increase in temperature and infers a decrease in the degree of immiscibility of the polymer with the solvent. It should be noted that the mechanism(s) of solvent swelling is not well understood. Peng *et al.*,<sup>44</sup> while studying solvent annealing of PS-*b*-PMMA

in acetone vapor at room temperature observed the vapor molecules attract the PMMA block toward the surface of the film. The effect of selectivity and evaporation rate of solvents on morphology change in PS-*b*-P4VP films was studied by Park *et al.*<sup>45</sup> and observed a morphology change from a dimple type to cylindrical microdomains oriented perpendicular to surface with increasing THF concentration or as the solvent became less selective for PS. In the present investigation, we believe the substrate interaction of P4VP with ethylene glycol along with the solvent annealing conditions (i.e. solvent and temperature used) thereby draw the PVP block to the surface through the PS-rich layer.

**Table 1** Polymer (P)-Solvent (S) interaction parameters ( $\chi_{P-S}$ )

Temperature /°C	$\chi_{P-S}$	
	$\chi_{PS-THF}$	$\chi_{P4VP-THF}$
17	0.450	1.328
40	0.442	1.255
50	0.439	1.227
60	0.436	1.201

#### 4.4.3. BCP Film Reconstruction with Ethanol

Surface reconstruction was performed on the solvent annealed sample to facilitate the incorporation of metal nanoparticles. This is possible through the use of a solvent which is non-selective for the majority block, PS in this work, but highly selective for the minor block, P4VP. Samples were immersed for 20 minutes in ethanol and were then dried under nitrogen flow. The process leaves the pattern unchanged but yields a useful highly ordered nanoporous film since P4VP is drawn to the surface as seen in Figure 4.7a. Figure 4.7b shows a cross-section SEM image (tilt 20°) of the surface reconstructed film revealing well-defined nanopores. The TEM cross-sections in Figure 4.7c clearly show that the nanopores are limited to the surface and resides on a thick (20 nm) PS matrix.

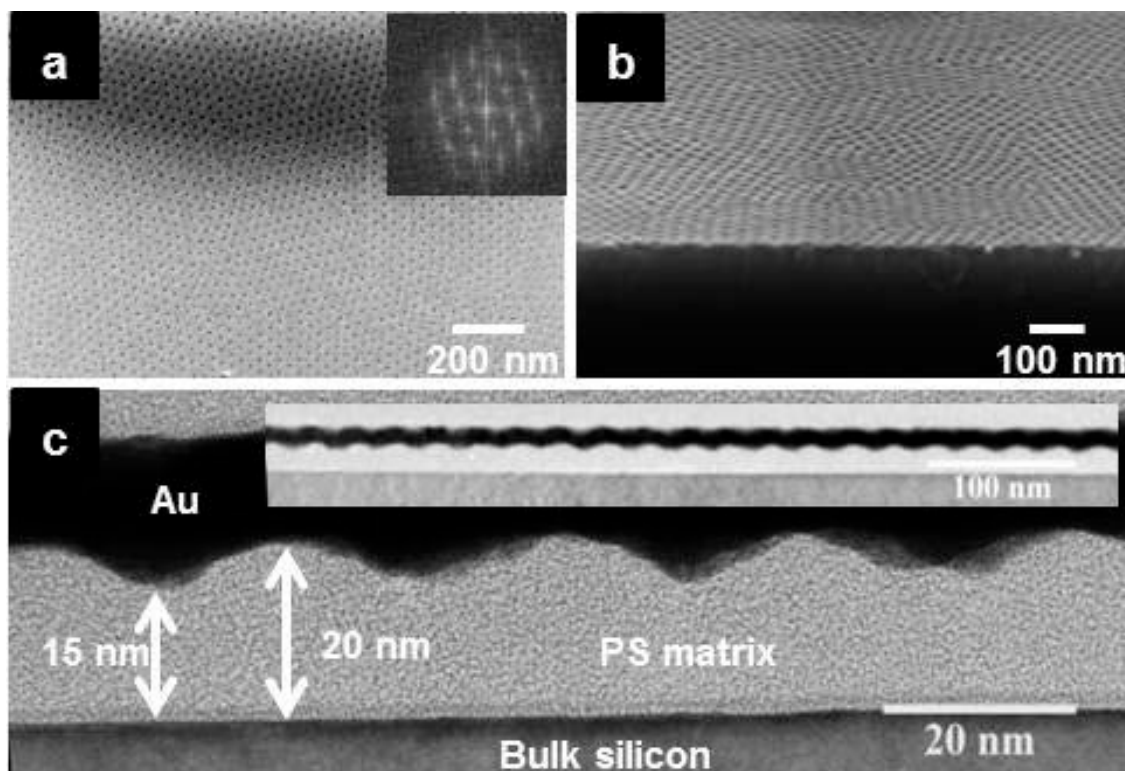


**Figure 4.7.** Top-down (a) and 20° tilted (b) SEM images of surface reconstructed PS-*b*-P4VP film (see experimental section for details). Corresponding FFT pattern inset (a) shows the high degree of order. (c) Cross-section TEM image of nanoporous template (inset a low-resolution cross-section TEM image).

#### 4.4.4. Iron Oxide(s) Hard Mask Fabrication by Inclusion Technique

Following surface reconstruction, the spin coating of a low concentration (0.3 wt. %) iron nitrate solution in ethanol was carried out to fill the nanoporous structure. To prevent overloading of the pores, a low concentration of metal nitrate solution was employed. Metal deposition from nitrate solutions is a straight forward process as recently outlined in work by Ghoshal *et al.*<sup>46,47</sup> However, in the fabrication of a hardmask it is vital that overloading of the pores is avoided, as it will affect the pattern transfer process afterwards whereby excess iron oxide(s) will be formed on the PS matrix leading to non-uniform etching of the underlying silicon substrate.

Post iron nitrate deposition, UV/Ozone treatment was carried out for a 3 hour period which led to the formation of oxide(s) nanodot material and allowed for the removal of the organic polymer matrix. Evidence of FeOxide(s) material is provided in Figure 4.8a-c which shows an AFM topography and top-down SEM images of the well-ordered FeOxide(s) nanodots resembling the template previously represented by PS-*b*-P4VP BCP. Diameter of these nanodots can be manipulated by altering the initial concentration of the iron nitrate solution. FeOxide(s) nanodots were also examined by calcination in air at 800 °C for 1 hour to show thermal stability. The top-down SEM image in Figure 4.8c shows large area of FeOxide(s) nanodots without any change in periodicity or diameter.

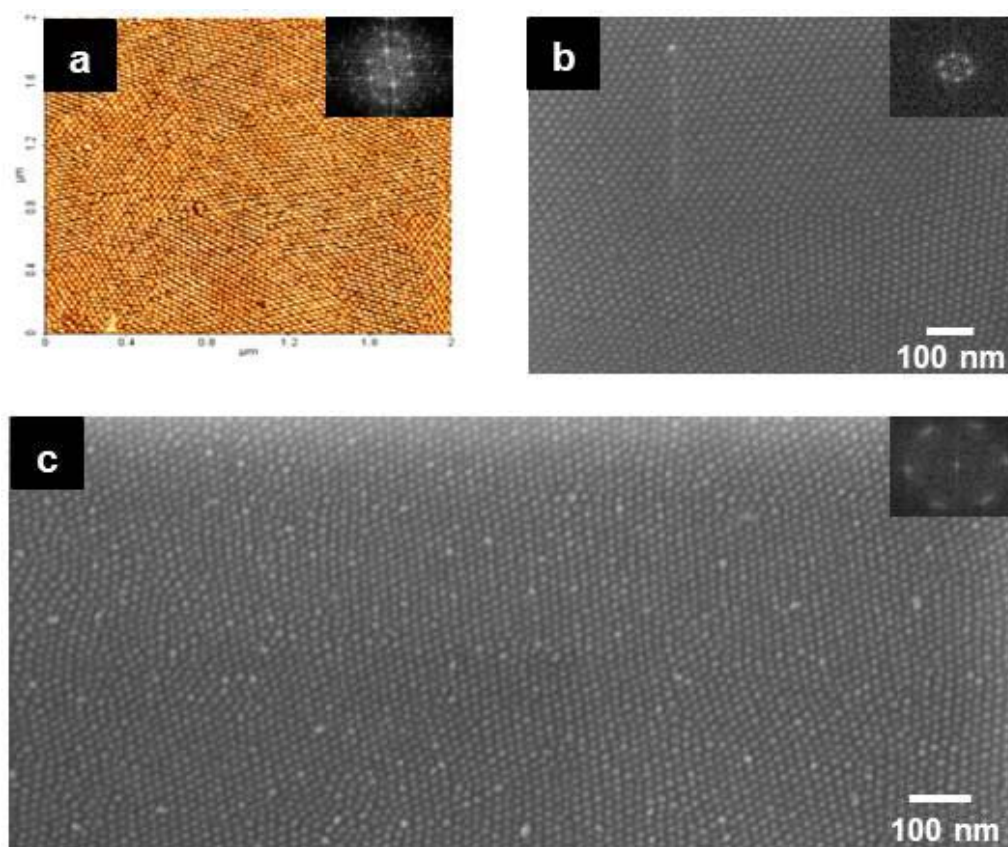


**Figure 4.8.** AFM topography image (a), top-down high resolution SEM image (b) of iron oxide nanodots obtained after UV/Ozone treatment for 3 hours. (c) The iron oxide nanodot patterns obtained from the UV/Ozone treated film after calcination at 800°C for 1 hour.

Analysis of FTIR spectra of various BCP films after microphase separation provides significant information about the behaviour of the film at various stages of FeOxide(s) nanodots fabrication as shown in Figure 4.9. The intense peak observed at  $1110\text{ cm}^{-1}$  can be assigned to Si-O-Si stretching<sup>48</sup> in all the spectra originating from the native SiO<sub>2</sub> layer of the silicon substrate. The stretching of the C-O bonds in PVP which is of interest in the present context can be identified at  $970\text{ cm}^{-1}$  for the BCP films<sup>49</sup> after microphase separation and ethanol reconstruction. This signature PVP peak is of very low intensity in the iron nitrate loaded film and could be due to the interaction of metal ion with the PVP block. UV/Ozone treatment of the iron nitrate loaded film leads to the complete burn out of the polymer and as such the absence of the PVP peak. It clearly indicates the existence of metal ion-PVP interaction and does indeed evidence the inclusion of iron nitrate into the porous BCP film.

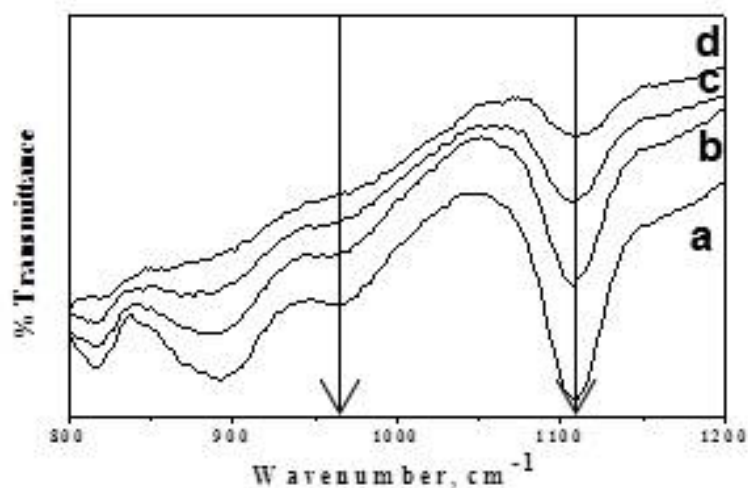


**Figure 4.9.** FTIR spectra of BCP films after (a) microphase separation, (b) reconstruction with ethanol for 20 minutes, (c) iron nitrate loading on the reconstructed film, and (d) UV/Ozone treatment for 3 hour.

The survey spectra (Figure 4.10a and c) of the samples after UV/Ozone treatment and further annealing/calcination indicates presence of the expected elements, Si, O, Fe and

a small C 1s (~285 eV) feature due to adventitious carbon. High resolution Fe 2p spectra were recorded to distinguish different phases of iron oxides. Fe 2p core level spectrum recorded on iron oxide nanodots prepared after UV/Ozone treatment (Figure 4.10b) consists of two broadened peaks associated with Fe 2p<sub>3/2</sub> at 710.8 eV and Fe 2p<sub>1/2</sub> at 724.8 eV due to the existence of both Fe<sup>+2</sup> and Fe<sup>+3</sup> ions. The curve fitted Fe 2p<sub>3/2</sub> and Fe 2p<sub>1/2</sub> binding energies are 709.6 and 722.8 eV (assigned to Fe<sup>+2</sup>) and 711.5 and 724.9 eV (assigned to Fe<sup>+3</sup>), respectively, matches literature values.<sup>50</sup>

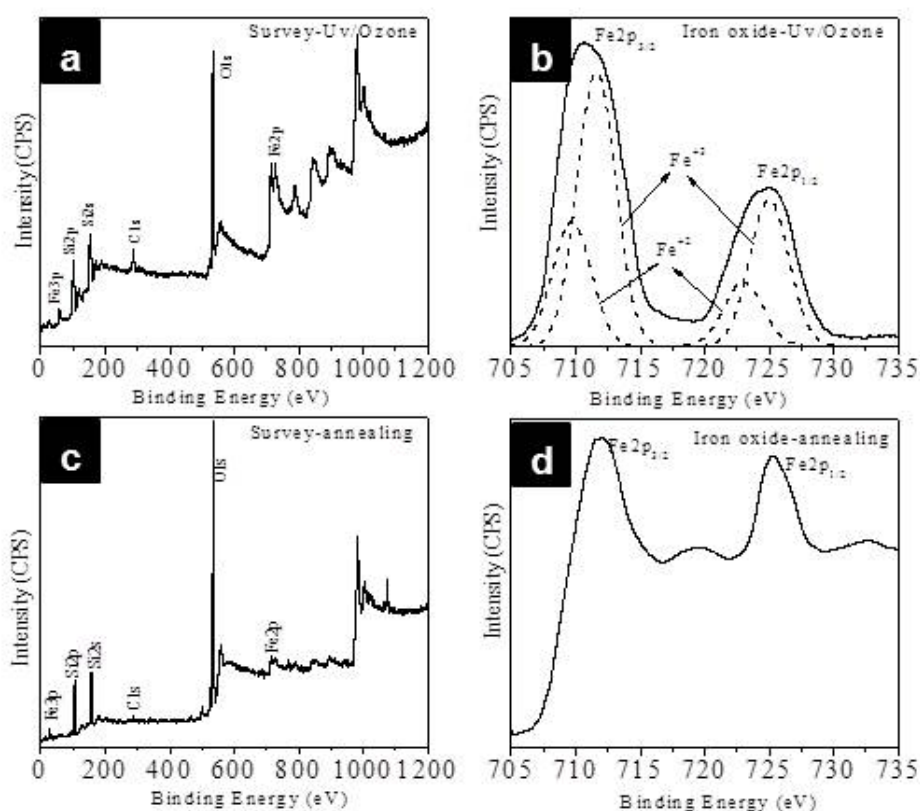


**Figure 4.10.** XPS survey (a, c) and high resolution Fe 2p core level (b, d) spectra of iron oxide nanodots on silicon substrates after UV/Ozone treatment (a, b) and calcination/annealing (c, d).

The concentration ratio of Fe<sup>+3</sup>/ Fe<sup>+2</sup> was calculated from the curve-fitted peak areas as about 2:1 as expected for Fe<sub>3</sub>O<sub>4</sub>. Fe 2p core level spectrum of iron oxide nanodots after

annealing/calcination (Figure 4.10d) consists of two sharp peaks at 711.5 and 725.1 eV associated with Fe  $2p_{3/2}$  and Fe  $2p_{1/2}$  accompanied by high binding energy satellite structures (+8 eV shift). These data are consistent with the existence of Fe<sup>+3</sup> (Fe<sub>2</sub>O<sub>3</sub>) ions only.<sup>51,52</sup> Thus, XPS analysis confirms the formation of phase pure iron oxides without any polymer residues.

#### 4.4.5. GISAXS of BCP Films at Different Stages

Further evidence of film morphology is provided by grazing incidence small angle X-ray scattering (GISAXS) data gathered as shown in Figure 4.11a-c. The data obtained was measured above the critical angle of the polymer but below the critical angle for silicon. With this incidence angle ( $\alpha = 0.20^\circ$ ) the reflected X-rays from the silicon interface enhance the scattering observed from the PS-*b*-P4VP films, specifically for the reconstructed and iron nitrate containing films owing to the large electron density difference. No diffraction features were observed for the initially microphase separated PS-*b*-P4VP structure on silicon oxide surface functionalized with an ethylene glycol layer (Figure 4.11a) most likely due to the low electron density between the two polymer blocks. However, following surface reconstruction first order diffraction spots were observed (Figure 4.11b). Furthermore, after loading of the reconstructed films with iron nitrate the intensity of the diffraction spots increased (Figure 4.11c), indicating that the metal ions are filling the void spaces in the film. As seen from Figure 4.11b and c the scattering along Qz indicates that the cylindrical microdomains are oriented perpendicular to the surface. Interestingly, the diffraction spots seen in Figure 4.11b are not as intense as one would expect most likely due to the fact that the pores do not traverse the entire film, as discussed earlier from TEM data (Figure 4.7c). It should also be noted

that the specular beam spot in Figure 4.11b has become more diffuse suggesting that the reconstructed film has become rougher.

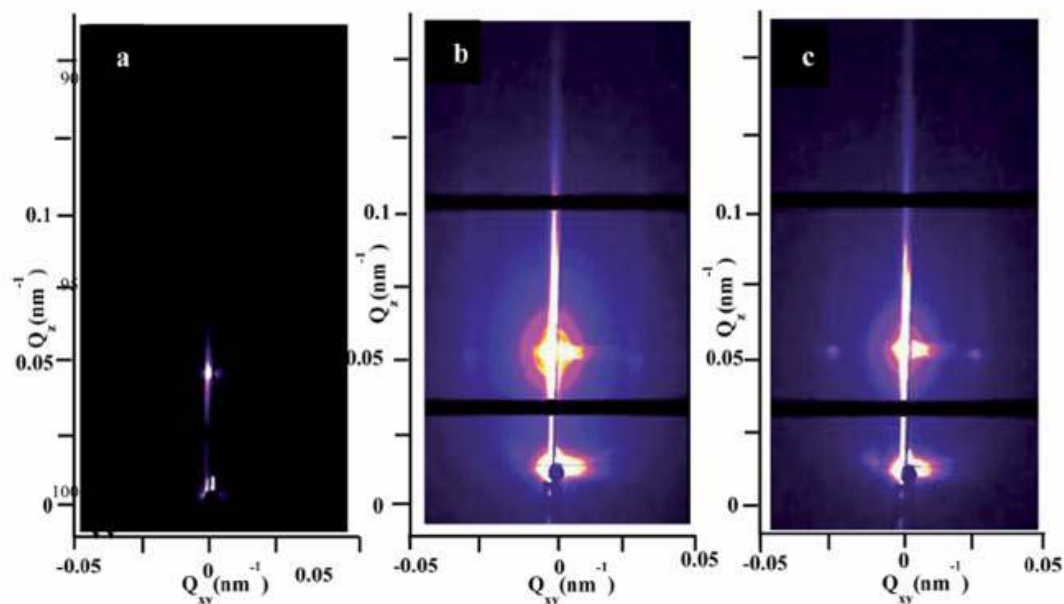


**Figure 4.11.** GISAXS patterns of the BCP film after (a) microphase separation, (b) reconstruction with ethanol for 20 minutes, and (c) iron nitrate loading on the reconstructed film.

It was also noticed that the d-spacings of these diffraction spots in the reconstructed and metal loaded films was not the same with the periodicity increasing from 24.6 nm to 29.7 nm. This is somewhat unexpected as the PS block is not solvated at all by the aqueous solution from which the metal ions are cast and therefore were not expected to be affected by the metal loading. In increasing the periodicity of the films the loading of the metal ions is causing a distortion of the PS matrix of the film, which presumably is accommodated by a stretching of the PS polymer chains. This distortion of the polymer matrix cannot however be simply accommodated across the film as a whole and we would therefore expect the formation of fault lines and defects in the film as a direct result of this expansion. X-ray reflectometry experiments were also attempted, but these did not yield any meaningful results (figure omitted for the sake of brevity).

#### 4.4.6. Fabrication of Silicon Nanopillars

Figure 4.12a-c shows the silicon nanopillars fabricated following pattern transfer using the FeOxide(s) nanodot array template. SEM images in Figure 4.12a-b confirm high surface coverage resulting and confirms that the FeOxide(s) template provided an ideal etch mask to develop these high aspect ratio silicon nanopillars. Additionally the high degree of order seen with the BCP thin film template is represented in the nanopillars structures in Figure 4.12b. This SEM image shows a high degree of order with silicon nanopillars diameter averaging 16 nm. Nanopillar structure height varies between 115 and 120 nm giving an aspect ratio of 1:6. This small difference in nanopillar height shows that the silicon etch used works satisfactorily even though the etch was performed for only 12 seconds. Again this point extends the significance of employing a metal oxide etch mask whereby high fidelity silicon nanostructures can be obtained in a relatively short period and by using a simple bottom up methodology. Further evidence of FeOxide(s) deposited on the silicon substrate is shown in Figure 4.12c. The high-resolution SEM image clearly shows the presence of FeOxide(s) nanodot on the top of the silicon nanopillar.

To verify the presence of Fe in the nanodots fabricated, EDX was performed in point mode to locate Fe on top of the nanopillar. It should be noted that when EDX is being carried out, it results in the deposition of a large amount of carbon on the sample, and since the

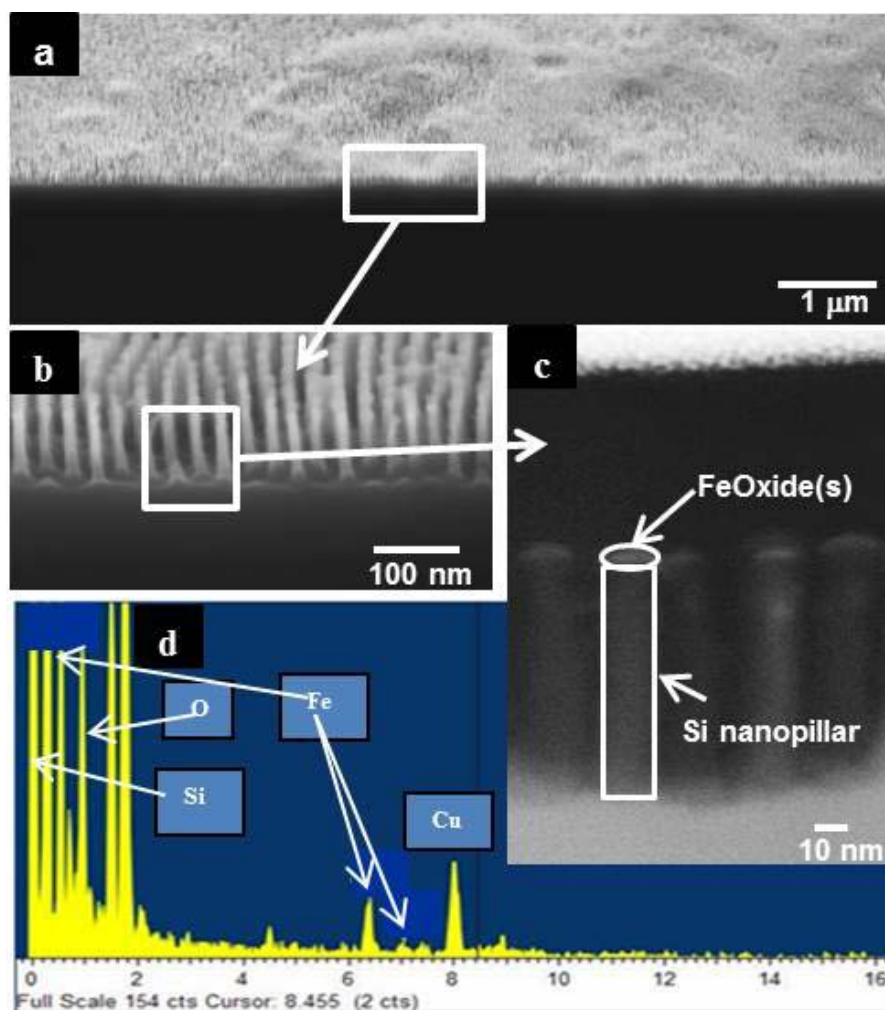


**Figure 4.12.** Fabrication of silicon nanopillars following pattern transfer process using FeOxide(s) as etch mask. Cross-section low-resolution SEM (a), high-resolution SEM images (70° tilted) (b, c) of silicon nanopillars. (d) EDX spectrum of (a).

feature of interest is small (~ 20 nm of FeOxide(s) on Si nanopillars) this then results in the rapid build-up of carbon on the sample surface which obscures the X-ray signals. For this particular reason, EDX is performed on a single point on the sample rather than obtaining a map of the elemental composition. From the EDX spectrum in Figure 4.12d, peaks are visible identifying that Fe is indeed present at the top of the silicon nanopillar structure. However these peaks are extremely small, representative of the low quantity of metal deposited on the silicon substrate, which accounts for the major peak. It should

be noted that the intense copper peak seen in the spectrum is due to the grid used during analysis.

#### 4.5. Conclusions

In conclusion, we have demonstrated a facile method for the enhancement of surface coverage and ordering through a molecular functionalization based around ethylene glycol which favorably interacted with PS-*b*-P4VP forming an ideal perpendicularly orientated template. This orientation along with surface reconstruction process allowed for the successful incorporation of a FeOxide(s) hard mask which enabled the fabrication of high aspect ratio silicon nanopillars. Additionally, further information was provided in this report with GISAXS and spectroscopic data aiding the understanding on film morphology following the reconstruction and iron nitrate deposition process. In summary, we have shown a simple approach using block copolymer lithography for the fabrication of silicon nanopillars with high degree of order and fidelity.

#### 4.6. References

- (1) Segalman, R. A. Patterning with block copolymer thin films. *Materials Science & Engineering R-Reports* **2005**, *48*, 191-226.
- (2) Park, C.; Yoon, J.; Thomas, E. L. Enabling nanotechnology with self assembled block copolymer patterns. *Polymer* **2003**, *44*, 6725-6760.
- (3) Tseng, Y.-C.; Darling, S. B. Block Copolymer Nanostructures for Technology. *Polymers* **2010**, *2*, 470-489.
- (4) Farrell, R. A.; Fitzgerald, T. G.; Borah, D.; Holmes, J. D.; Morris, M. A. Chemical Interactions and Their Role in the Microphase Separation of Block Copolymer Thin Films. *International Journal of Molecular Sciences* **2009**, *10*, 3671-3712.
- (5) Hamley, I. W. Nanostructure fabrication using block copolymers. *Nanotechnology* **2003**, *14*, R39-R54.
- (6) Kim, J. K.; Yang, S. Y.; Lee, Y.; Kim, Y. Functional nanomaterials based on block copolymer self-assembly. *Progress in Polymer Science* **2010**, *35*, 1325-1349.
- (7) Lodge, T. P. Block copolymers: Past successes and future challenges. *Macromolecular Chemistry and Physics* **2003**, *204*, 265-273.
- (8) Black, C. T. Polymer Self-Assembly as a Novel Extension to Optical Lithography. *ACS Nano* **2007**, *1*, 147-150.

- (9) Cho, H.; Choi, S.; Kim, J. Y.; Park, S. Fabrication of gold dot, ring, and corpuscle arrays from block copolymer templates via a simple modification of surface energy. *Nanoscale* **2011**, *3*, 5007-5012.
- (10) Xu, J.; Russell, T. P.; Ocko, B. M.; Checco, A. Block copolymer self-assembly in chemically patterned squares. *Soft Matter* **2011**, *7*, 3915-3919.
- (11) Albert, J. N. L.; Epps III, T. H. Self-assembly of block copolymer thin films. *Materials Today* **2010**, *13*, 24-33.
- (12) Ryu, D. Y.; Wang, J.-Y.; Lavery, K. A.; Drockenmuller, E.; Satija, S. K.; Hawker, C. J.; Russell, T. P. Surface Modification with Cross-Linked Random Copolymers: Minimum Effective Thickness. *Macromolecules* **2007**, *40*, 4296-4300.
- (13) Bang, J.; Bae, J.; Lowenhielm, P.; Spiessberger, C.; Given-Beck, S. A.; Russell, T. P.; Hawker, C. J. Facile routes to patterned surface neutralization layers for block copolymer lithography. *Advanced Materials* **2007**, *19*, 4552.
- (14) Ryu, D. Y.; Ham, S.; Kim, E.; Jeong, U.; Hawker, C. J.; Russell, T. P. Cylindrical Microdomain Orientation of PS-*b*-PMMA on the Balanced Interfacial Interactions: Composition Effect of Block Copolymers. *Macromolecules* **2009**, *42*, 4902-4906.
- (15) Kim, S. H.; Misner, M. J.; Russell, T. P. Controlling orientation and order in block copolymer thin films. *Advanced Materials* **2008**, *20*, 4851-4856.
- (16) Huang, W.-H.; Chen, P.-Y.; Tung, S.-H. Effects of Annealing Solvents on the Morphology of Block Copolymer-Based Supramolecular Thin Films. *Macromolecules* **2012**, *45*, 1562-1569.
- (17) Tung, S.-H.; Xu, T. Templated Assembly of Block Copolymer toward Nonequilibrium Nanostructures in Thin Films. *Macromolecules* **2009**, *42*, 5761-5765.
- (18) van Zoelen, W.; Polushkin, E.; ten Brinke, G. Hierarchical Terrace Formation in PS-*b*-P4VP(PDP) Supramolecular Thin Films. *Macromolecules* **2008**, *41*, 8807-8814.
- (19) Maki-Ontto, R.; de Moel, K.; de Odorico, W.; Ruokolainen, J.; Stamm, M.; ten Brinke, G.; Ikkala, O. "Hairy tubes": Mesoporous materials containing hollow self-organized cylinders with polymer brushes at the walls. *Advanced Materials* **2001**, *13*, 117-121.
- (20) Kuila, B. K.; Gowd, E. B.; Stamm, M. Supramolecular Assembly of Poly(styrene)-*b*-poly(4-vinylpyridine) and 1-Pyrenebutyric Acid in Thin Film and Their Use for Nanofabrication. *Macromolecules* **2010**, *43*, 7713-7721.
- (21) Borah, D.; Shaw, M. T.; Rasappa, S.; Farrell, R. A.; Mahony, C. O.; Faulkner, C. M.; Bosea, M.; Gleeson, P.; Holmes, J. D.; Morris, M. A. Plasma etch technologies for the development of ultra-small feature size transistor devices. *Journal of Physics D: Applied Physics* **2011**, *44*, 174012.
- (22) Borah, D.; Rasappa, S.; Senthamaraiannan, R.; Shaw, M. T.; Holmes, J. D.; Morris, M. A. The sensitivity of random polymer brush-lamellar polystyrene-*b*-polymethylmethacrylate block copolymer systems to process conditions. *Journal of Colloid and Interface Science* **2013**, *393*, 192-202.
- (23) Bhoje Gowd, E.; Nandan, B.; Vyas, M. K.; Bigall, N. C.; Eychmüller, A.; Schlörb, H.; Stamm, M. Highly ordered palladium nanodots and nanowires from switchable block copolymer thin films. *Nanotechnology* **2009**, *20*.
- (24) Yoo, H.; Park, S. The fabrication of highly ordered block copolymer micellar arrays: control of the separation distances of silicon oxide dots. *Nanotechnology* **2010**, *21*.
- (25) Xu, T.; Stevens, J.; Villa, J. A.; Goldbach, J. T.; Guarim, K. W.; Black, C. T.; Hawker, C. J.; Russell, T. R. Block copolymer surface reconstruction: A reversible route to nanoporous films. *Advanced Functional Materials* **2003**, *13*, 698-702.

- (26) Lu, J. Q. Nanocatalysts with tunable properties derived from polystyrene-*b*-poly(vinyl pyridine) block copolymer templates for achieving controllable carbon nanotube synthesis. *Journal of Physical Chemistry C* **2008**, *112*, 10344-10351.
- (27) Liu, Y.; Lor, C.; Fu, Q.; Pan, D.; Ding, L.; Liu, J.; Lu, J. Synthesis of Copper Nanocatalysts with Tunable Size Using Diblock Copolymer Solution Micelles. *The Journal of Physical Chemistry C* **2010**, *114*, 5767-5772.
- (28) Song, L. X.; Lam, Y. M.; Boothroyd, C.; Teo, P. W. One-step synthesis of titania nanoparticles from PS-P4VP diblock copolymer solution. *Nanotechnology* **2007**, *18*.
- (29) Si, H.-Y.; Chen, J.-S.; Chow, G.-M. A simple method to prepare highly ordered PS-*b*-P4VP block copolymer template. *Colloids and Surfaces A: Physicochemical and Engineering Aspects* **2011**, *373*, 82-87.
- (30) Black, C. T.; Ruiz, R.; Breyta, G.; Cheng, J. Y.; Colburn, M. E.; Guarini, K. W.; Kim, H.-C.; Zhang, Y. Polymer self assembly in semiconductor microelectronics. *IBM J. Res. Dev.* **2007**, *51*, 605-633.
- (31) Schachtschneider, J. H.; Snyder, R. G. Vibrational analysis of the *n*-paraffins—II: Normal co-ordinate calculations. *Spectrochimica Acta* **1963**, *19*, 117-168.
- (32) Lee, A. F.; Gawthrope, D. E.; Hart, N. J.; Wilson, K. A Fast XPS study of the surface chemistry of ethanol over Pt{1 1 1}. *Surface Science* **2004**, *548*, 200-208.
- (33) Bermudez, V. M.; Berry, A. D.; Kim, H.; Piqué, A. Functionalization of Indium Tin Oxide. *Langmuir* **2006**, *22*, 11113-11125.
- (34) Park, S.; Kim, B.; Wang, J. Y.; Russell, T. P. Fabrication of Highly Ordered Silicon Oxide Dots and Stripes from Block Copolymer Thin Films. *Advanced Materials* **2008**, *20*, 681-685.
- (35) Park, S.; Wang, J.-Y.; Kim, B.; Russell, T. P. From Nanorings to Nanodots by Patterning with Block Copolymers. *Nano Letters* **2008**, *8*, 1667-1672.
- (36) Park, S.; Wang, J.-Y.; Kim, B.; Xu, J.; Russell, T. P. A Simple Route to Highly Oriented and Ordered Nanoporous Block Copolymer Templates. *ACS Nano* **2008**, *2*, 766-772.
- (37) Shin, D. O.; Lee, D. H.; Moon, H. S.; Jeong, S. J.; Kim, J. Y.; Mun, J. H.; Cho, H.; Park, S.; Kim, S. O. Sub-Nanometer Level Size Tuning of a Monodisperse Nanoparticle Array Via Block Copolymer Lithography. *Advanced Functional Materials* **2011**, *21*, 250-254.
- (38) Park, S.; Kim, B.; Xu, J.; Hofmann, T.; Ocko, B. M.; Russell, T. P. Lateral Ordering of Cylindrical Microdomains Under Solvent Vapor. *Macromolecules* **2009**, *42*, 1278-1284.
- (39) Limary, R.; Green, P. F. Dewetting instabilities in thin block copolymer films: Nucleation and growth. *Langmuir* **1999**, *15*, 5617-5622.
- (40) Mokarian-Tabari, P.; Collins, T. W.; Holmes, J. D.; Morris, M. A. Cyclical "Flipping" of Morphology in Block Copolymer Thin Films. *ACS Nano* **2011**, *5*, 4617-4623.
- (41) Brandrup, J.; Immergut, E. H.; Grulke, E. A.; Abe, A.; Bloch, D. R.: *Polymer Handbook* (4th Edition). John Wiley & Sons.
- (42) Speight, J. A review of: "Physical Properties of Polymers Handbook" Mark, J.E. (Editor) American Institute of Physics Press, Woodbury, New York, 1996 *Fuel Science and Technology International* **1996**, *14*, 1461-1461.
- (43) Van Krevelen, D. W.: *Properties of polymers their correlation with chemical structure; their numerical estimation and prediction from additive group contributions Fourth, completely revised edition Preface To The Second Edition (1976)*; Elsevier Science Bv: Amsterdam, 2009.

- (44) Peng, J.; Kim, D. H.; Knoll, W.; Xuan, Y.; Li, B.; Han, Y. Morphologies in solvent-annealed thin films of symmetric diblock copolymer. *Journal of Chemical Physics* **2006**, *125*.
- (45) Park, S.; Wang, J.-Y.; Kim, B.; Chen, W.; Russell, T. P. Solvent-Induced Transition from Micelles in Solution to Cylindrical Microdomains in Diblock Copolymer Thin Films. *Macromolecules* **2007**, *40*, 9059-9063.
- (46) Ghoshal, T.; Shaw, M. T.; Bolger, C. T.; Holmes, J. D.; Morris, M. A. A general method for controlled nanopatterning of oxide dots: a microphase separated block copolymer platform. *Journal of Materials Chemistry* **2012**, *22*, 12083-12089.
- (47) Ghoshal, T.; Maity, T.; Godsell, J. F.; Roy, S.; Morris, M. A. Large Scale Monodisperse Hexagonal Arrays of Superparamagnetic Iron Oxides Nanodots: A Facile Block Copolymer Inclusion Method. *Advanced Materials* **2012**, *24*, 2390-2397.
- (48) Borah, D.; Rasappa, S.; Senthamaraiannan, R.; Kosmala, B.; Shaw, M. T.; Holmes, J. D.; Morris, M. A. Orientation and Alignment Control of Microphase-Separated PS-*b*-PDMS Substrate Patterns via Polymer Brush Chemistry. *ACS Applied Materials & Interfaces* **2012**, *5*, 88-97.
- (49) Magazu, S.; Migliardo, F.; Ramirez-Cuesta, A. J. Concentration dependence of vibrational properties of bioprotectant/water mixtures by inelastic neutron scattering. *Journal of the Royal Society Interface* **2007**, *4*, 167-173.
- (50) Ram, P.; Choudhary, R. J.; Chandra, L. S. S.; Lakshmi, N.; Phase, D. M. Electrical and magnetic transport properties of Fe<sub>3</sub>O<sub>4</sub> thin films on a GaAs(100) substrate. *Journal of Physics: Condensed Matter* **2007**, *19*, 486212.
- (51) Mills, P.; Sullivan, J. L. A study of the core level electrons in iron and its three oxides by means of X-ray photoelectron spectroscopy. *Journal of Physics D: Applied Physics* **1983**, *16*, 723.
- (52) Fujii, T.; de Groot, F. M. F.; Sawatzky, G. A.; Voogt, F. C.; Hibma, T.; Okada, K. *In-situ* XPS analysis of various iron oxide films grown by NO<sub>2</sub>-assisted molecular-beam epitaxy. *Physical Review B* **1999**, *59*, 3195-3202.

#### 4.7. Appendix – Chapter 4

### Self-Assembly of PS-*b*-P4VP Block Copolymer on Molecularly Functionalized Silicon Substrates: Fabrication of Inorganic Nanostructured Etchmask for Lithographic Use

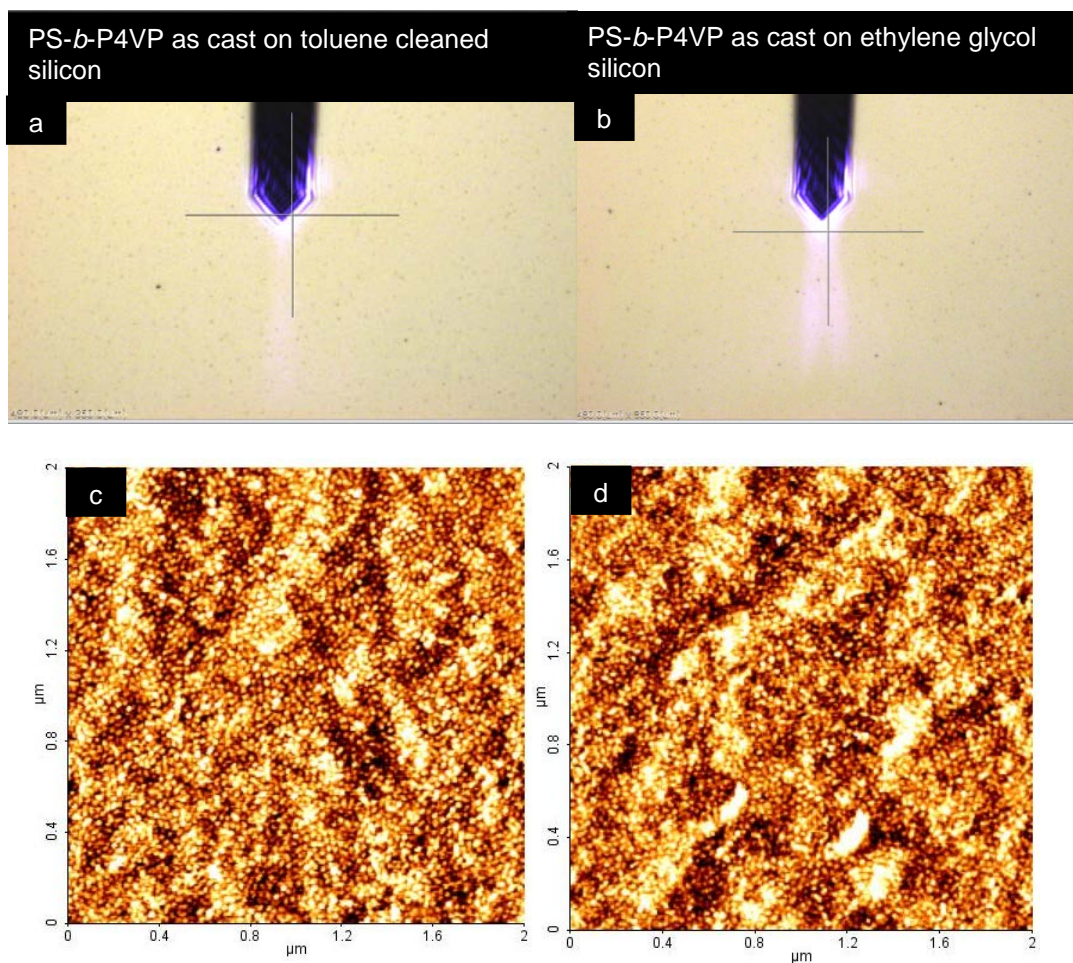


**Figure S4.7.1.** Optical images (480 x 360 micron) of (a) PS-*b*-P4VP as cast on toluene cleaned silicon and (b) PS-*b*-P4VP as cast on a silicon oxide surface functionalized with an ethylene glycol layer. (c) and (d) show the corresponding topographic AFM structures.

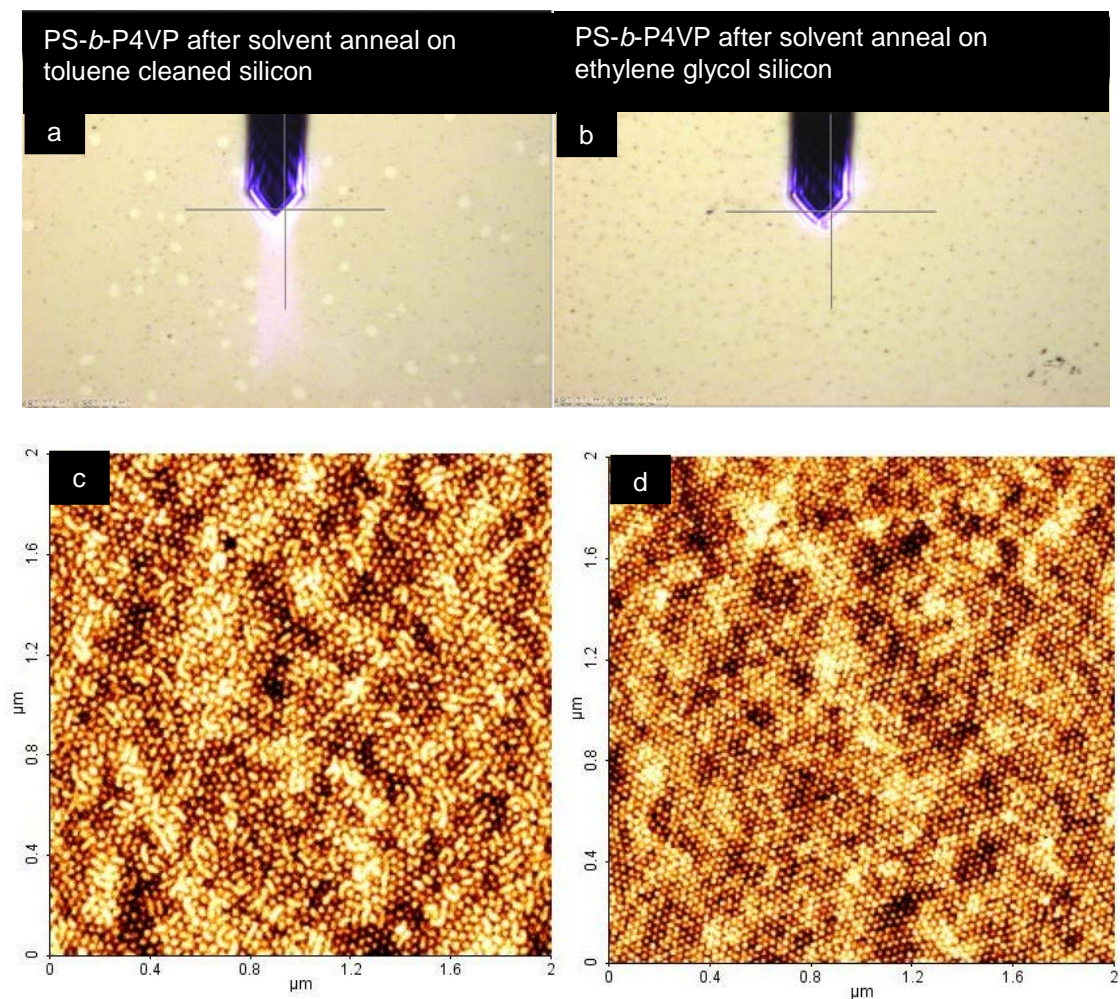


**Figure S4.7.2.** Optical images (480 x 360 micron) of (a) PS-*b*-P4VP after solvent anneal with THF at 50°C on toluene cleaned silicon and (b) PS-*b*-P4VP after solvent anneal with THF at 50°C on a silicon oxide surface functionalized with an ethylene glycol layer. (c) and (d) show the corresponding topographic AFM structures.

---

*Chapter 5*

---

**Aligned Silicon Nanofins via the Directed Self-Assembly of PS-*b*-P4VP Block Copolymer and Metal Oxide Enhanced Pattern Transfer**

## 5.1. Abstract

“Directing” block copolymer (BCP) patterns is a possible option for future semiconductor device patterning, but pattern transfer of BCP masks is somewhat hindered by the inherently low etch contrast between blocks. In this chapter, we demonstrate a “fab” friendly methodology for forming well-registered and aligned silicon (Si) nanofins following pattern transfer of robust metal oxide nanowire masks through the directed self-assembly (DSA) of BCPs. A cylindrical forming poly(styrene)-*block*-poly(4-vinyl-pyridine) (PS-*b*-P4VP) BCP was employed producing “fingerprint” line patterns over macroscopic areas following solvent vapor annealing treatment. The directed assembly of PS-*b*-P4VP line patterns was enabled by electron-beam lithographically defined hydrogen silsequioxane (HSQ) gratings. We developed metal oxide nanowire features using PS-*b*-P4VP structures which facilitated high quality pattern transfer to the underlying Si substrate. This chapter highlights the precision at which long range ordered  $\sim 10$  nm Si nanofin features with 32 nm pitch can be defined using a cylindrical BCP system for nanolithography application. The results show promise for future nanocircuitry fabrication to access sub-16 nm critical dimensions using cylindrical systems as surface interfaces are easier to tailor than lamellar systems. Additionally, the work helps to demonstrate the extension of these methods to a “high  $\chi$ ” BCP beyond the size limitations of the more well-studied PS-*b*-poly(methyl methacrylate) (PS-*b*-PMMA) system.

## 5.2. Introduction

Resolution enhancement techniques may be required to augment current lithography tools for fabricating fine patterns to achieve more densely packed electronic devices, *i.e.* Moore’s Law.<sup>1</sup> Physical limits will be reached that established photolithography is

unable to surpass and defining sub-wavelength dimensions/features has seen a plethora of alternative techniques explored.<sup>2</sup> Proposed alternative lithographic patterning techniques (*e.g.* extreme ultraviolet lithography or multi-source electron-beam lithography) are struggling to meet required industrial criteria because of the prohibitive costs involved, an inability to achieve density multiplication and the low throughput associated limiting their overall industrial implementation.<sup>3</sup> The use of conventional “top-down” lithography to guide “bottom up” self-assembling materials *i.e.*, directed self-assembly (DSA), is viewed as a possible compatible methodology.<sup>4</sup> DSA of BCPs has been highlighted to define intricate future electronic circuitry enabling higher speed and reduced energy consumption per device function.<sup>5,6</sup> The DSA of BCPs is achieved through chemoepitaxy and graphoepitaxy.<sup>7-14</sup> Chemoepitaxy utilizes lithographic methods to define a chemical pre-pattern to regulate polymer interactions and force strict pattern alignment and order. Likewise, graphoepitaxy uses top-down optical or electron-beam techniques to topographically pattern substrates forming trenches to guide the self-assembly of BCP materials.

These DSA methods are advanced for the PS-*b*-PMMA BCP system.<sup>7-10,14</sup> However, PS-*b*-PMMA BCP is limited in the feature size attainable by having a relatively small Flory-Huggins interaction parameter ( $\chi$ , measures the chemical dissimilarity of the BCP constituent blocks) of 0.04.<sup>15</sup> For sub-15 nm BCP defined pitch sizes, the product  $\chi N$  (where N is the degree of polymerization) needs to be tailored so that ordered microphase separation occurs at low BCP molecular weights. High  $\chi$  materials can also enable reduced line edge roughness since the interfacial width of the nanodomains are proportional to  $\chi^{0.5}$ .<sup>16</sup> A number of newly synthesized high  $\chi$  BCPs including N-maltoheptaosyl-3-acetamido-1-propyne-*block*-4-polytrimethylsilylmethacrylate (MH-*b*-

PTMSS),<sup>17</sup> PS-*b*-PTMSS,<sup>18</sup> PS-*block*-poly(methyltrimethylsilylmethacrylate) (PS-*b*-PTMSSM),<sup>18</sup> PTMSS-*block*-poly(D,L)lactide (PTMSS-*b*-PLA,  $\chi=0.4$ )<sup>19</sup>, and poly(cyclohexylethylene)-*block*-PMMA (PCHE-*b*-PMMA)<sup>20</sup> have been developed for ultra-small features sizes as well as enhanced block contrast for etch processing. These systems extend the work on PS-*block*-polydimethylsiloxane (PS-*b*-PDMS,  $\chi=0.26$ ) which combines both high  $\chi$  and the presence of a Si backbone that enhances etch contrast and facile pattern transfer when used as an on-chip etch mask.<sup>21,22</sup> Other notable commercially available high  $\chi$  BCP materials for etch mask applications include poly-2-vinylpyridine (P2VP)-*b*-PDMS ( $\chi \sim 1.06$ ),<sup>23</sup> PS-*b*-P2VP ( $\chi \sim 0.18$ )<sup>24</sup> and PS-*b*-PLA ( $\chi \sim 0.23$ ).<sup>25-27</sup> However to date, successful pattern transfer for high  $\chi$  BCPs (other than PS-*b*-PDMS)<sup>22,28</sup> has been limited. PS-*b*-PVP BCPs may be particularly attractive for nanolithography due to their high  $\chi$  and a reactive PVP group that can enable inclusion of etch contrast agents. For example, Buriak and coworkers have shown the formation of various metallic nanowires with PS-*b*-P2VP block copolymers.<sup>29,30</sup> Gu *et al.*<sup>24</sup> recently illustrated fine tuning of etch chemistry and pattern transfer methodologies using cryo inductively coupled plasma etching of PS-*b*-P2VP BCPs.

In this chapter, large scale coverage of highly oriented and aligned parallel cylinders via DSA and solvent vapor annealing (SVA) is demonstrated with a “high  $\chi$ ” PS-*b*-P4VP system. We have used topographical patterns of hydrogen silsequioxane (HSQ) created by electron beam lithography and an asymmetric PS-*b*-P4VP (24,000 g mol<sup>-1</sup> - 9,500 g mol<sup>-1</sup>) BCP self-assembly to fabricate aligned Si nanofins using etch enhanced pattern transfer. Orientation of BCP films was controlled through solvent vapor annealing (SVA) methodology forming in-plane cylinders (*i.e.* horizontal to the substrate surface, C<sub>II</sub>). PS-*b*-P4VP templates were developed through a surface reconstruction strategy and etch

contrast was enhanced via incorporation of metal oxide material either iron oxide ( $\text{Fe}_3\text{O}_4$ ) or aluminium oxide ( $\gamma\text{-Al}_2\text{O}_3$ ). The metal oxide inclusion enabled an effective pattern transfer producing uniform arrays of Si nanofins over macroscopic areas as characterized by scanning electron microscopy (SEM) and transmission electron microscopy (TEM). Whilst line-space features of PS-*b*-P4VP systems have been shown previously,<sup>31,32</sup> we further demonstrate the mask etch application potential of PS-*b*-P4VP by integrating DSA and metal oxide hardmask inclusion for high aspect ratio (1:4) Si pattern transfer. Critically, previous work only details orientation control (*i.e.* vertical or parallel to the surface plane). However, we show pattern alignment (to a surface direction) of the arrangements which is critical for application. This also means that we are essentially producing defect-free patterns over large areas. The methodology described herein resulted in highly parallel nanofin structures with translational alignment and registration of ~10 nm feature sizes within HSQ gratings.

### 5.3. Experimental

**Materials.** Planar substrates used were highly polished single-crystal silicon <100> wafers (p-type) with a native oxide layer of ~2 nm. Poly(styrene)-*block*-Poly(4-vinylpyridine) was purchased from Polymer Source, Inc., Canada, with a molecular weight of  $M_n = 33.5 \text{ kg mol}^{-1}$  ( $M_{n\text{PS}} = 24 \text{ kg mol}^{-1}$ ;  $M_{n\text{P4VP}} = 9.5 \text{ kg mol}^{-1}$ ,  $f_{\text{PS}} = 0.70$ ), a polydispersity ( $M_w/M_n$ ) of 1.15 (where,  $M_n$  and  $M_w$  are number average and weight average molecular weights) and was used without further purification.  $\text{Fe}_2(\text{NO}_3)_3 \cdot 9\text{H}_2\text{O}$  (Iron (III) nitrate nonahydrate),  $\text{Al}(\text{NO}_3)_3 \cdot 9\text{H}_2\text{O}$  (aluminium nitrate nonahydrate, ACS reagent,  $\geq 98\%$ ), acetone (ACS reagent,  $\geq 99.5\%$ ) chloroform (for HPLC,  $\geq 99.9\%$ , contains 0.5-1.0% ethanol as stabilizer), Tetrahydrofuran (inhibitor-free, CHROMASOLV Plus, for HPLC,  $\geq 99.9\%$ ), Toluene (CHROMASOLV, for HPLC,

99.9%), ethanol (dehydrated, 200 proof) were purchased from Sigma-Aldrich and used without further purification unless otherwise stated. De-ionized (DI) water was used wherever necessary.

**HSQ Substrate Preparation and Substrate Cleaning.** Ten × 10 mm bulk silicon ⟨100⟩ oriented substrates, nominal resistivity 0.001 Ω cm, were used for all DSA experiments. The substrates were first patterned using a HSQ EBL (Raith e-LiNE plus) process prior to deposition of the PS-*b*-P4VP block copolymer (BCP). The substrates were initially degreased via ultrasonication in acetone and iso-propanol (IPA) solutions (2 × 2 min), dried in flowing N<sub>2</sub> gas and baked for 2 minutes at 393 K in an ambient atmosphere to remove any residual IPA. The substrates were then spin coated (500 rpm, 5 seconds, 2000 rpm, 32 seconds) with a 2.4 wt % solution of HSQ (XR-1541 Dow Corning Corp.) in MIBK to produce a ~50 nm film of HSQ. The wafer was then baked at 393 K in an ambient atmosphere for 3 minutes prior to transfer to the EBL system for exposure. Arrays of 50 nm wide lines at pitches of (32n + 50) nm were exposed, where n is an integer and 0 < n < 8. HSQ pitches were measured at ~110, 145, 175, 205, 240, 270, and 300 nm. Following electron beam exposure the samples were developed in an aqueous solution of 0.25 M NaOH, 0.7 M NaCl for 15 seconds, followed by rinsing in flowing DI water for 60 seconds and 15 seconds rinse in IPA. The samples were then blown dry in flowing N<sub>2</sub> gas.

**Block Copolymer Film Preparation and Solvent Vapor Anneal.** 0.5 weight % solutions of PS-*b*-P4VP BCP were prepared in toluene/THF (80:20). The solutions were left stirring overnight to ensure complete dissolution. Prior to spin coating planar Si or HSQ substrates were sonicated for 20 minutes with acetone. Following this surface cleaning, the substrates were then further rinsed in acetone and blown dry with nitrogen. Spin coating of the PS-*b*-P4VP BCP solution was carried out at 3200 rpm for 30 seconds.

Solvent vapor annealing was carried out in the conventional manner with a small vial containing 8–10 ml of chloroform placed inside a glass jar (150 ml) with PS-*b*-P4VP sample for 30 minutes to 3 hours (room temperature ~ 290 K). Samples were removed from the glass jars after the desired anneal time and allowed to evaporate the trapped solvent at ambient conditions. The films did not exhibit any major swelling during annealing as the films were transparent throughout (same as spin cast). Surface reconstruction was carried out by placing the solvent annealed PS-*b*-P4VP sample in a glass jar with ethanol vapors for 20 minutes. After this vapor treatment, the sample was removed and left to dry at room temperature. This provided enough time for swelling of the P4VP domains to enable the reconstructed template to form for subsequent deposition of the metal nitrate solutions.

**Metal oxide nanowire pattern fabrication.**  $\text{Fe}_2(\text{NO}_3)_3 \cdot 9\text{H}_2\text{O}$  (iron nitrate hexahydrate) and  $\text{Al}(\text{NO}_3)_3 \cdot 9\text{H}_2\text{O}$  (aluminium nitrate nonahydrate, ACS reagent,  $\geq 98\%$ ) solutions of 0.4 wt % were prepared in ethanol and spin-coated on to the ethanol reconstructed samples for 30 seconds at 3200 rpm. UV/O<sub>3</sub> treatment was used to oxidize the precursor and remove polymer. Samples were UV/O<sub>3</sub> treated in a UV/ozone system (PSD Pro Series Digital UV Ozone System; Novascan Technologies, Inc., USA). The UV source is two low pressure mercury vapor grid lamps. Both lamps have an output current of 0.8–0.95 A and power of 65–100 W, as reported by the manufacturer, and have strong emissions at both wavelengths of UV radiation (184.9 nm and 253.7 nm). The system produces highly reactive ozone gas from oxygen that is present within the chamber.

**Pattern transfer recipes.** An STS, Advanced Oxide Etch (AOE) ICP etcher was used for etching to pattern transfer the iron oxide and aluminium oxide nanowires to the underlying Si substrate. The general plasma etch methodology for pattern transfer was as follows; the initial etch was to remove the native oxide and then Si etch time was

varied to form fins with different heights. The native oxide layer etch was carried out for 5 seconds using a combination of C<sub>4</sub>F<sub>8</sub>/H<sub>2</sub> gas mixture (21 sccm/30 sccm) using an ICP coil power of 800 W and a Reactive Ion Etching (RIE) power of 80 W. Following this, nanofin fabrication involved a controlled gas mixture of C<sub>4</sub>F<sub>8</sub>/SF<sub>6</sub> at flow rates of 90 sccm/30 sccm respectively and the ICP and RIE power were set to 600 W and 15 W respectively at a chamber pressure of 15 mTorr. Note that further details on the above etches can be found in previously reported work by Ghoshal *et al.*<sup>33,34</sup> Also as mentioned above, Fe<sub>3</sub>O<sub>4</sub> can be removed via wet etch procedures (oxalic acid), note that the  $\gamma$ -Al<sub>2</sub>O<sub>3</sub> hardmask used here can be removed using a mild base (NaOH) treatment.

**Characterization.** PS-*b*-P4VP BCP film thicknesses were measured with a spectroscopic ellipsometer “J.A. Woollam Ellipsometer” at a fixed angle of incidence of 70°, on at least three different places on the sample and was averaged as the film thickness. A two layer model (SiO<sub>2</sub> + BCP) for total BCP film was used to simulate experimental data. Atomic Force Microscopy (AFM) (Park systems, XE-100) was operated in AC (tapping) mode under ambient conditions using silicon microcantilever probe tips with a force constant of 42 N m<sup>-1</sup>. Topographic and phase images were recorded simultaneously. Scanning Electron Microscopy (SEM) images were obtained by a FEI Helios Nanolab 600i system at an accelerating voltage of 5 kV and at a working distance of 4 mm. For cross-section SEM images, the substrate was cleaved in half and positioned perpendicular to the incident beam of electrons. The stage was then tilted at an angle of 20°. Transmission Electron Microscopy (TEM) lamella specimen were prepared using the Helios NanoLab DB FIB and were analysed by JEOL 2100 high resolution transmission electron microscope operating at an accelerating voltage of 200 kV. Domain size, periodicity of HSQ trenches and feature sizes *etc.* were measured from SEM and TEM data using ImageJ software. X-ray Photoelectron Spectroscopy (XPS)

was performed on Vacuum Science Workshop CLASS100 high performance hemispherical analyser using Al K $\alpha$  ( $h\nu = 1486.6$  eV) X-ray at 200W power. Spectra were obtained at a take-off angle of 90°. Photoemission peak positions were corrected to C 1s at a binding energy of 284.8 eV.

#### 5.4. Results and Discussion

Figure 5.1 shows the overall process flow for the fabrication of Si nanofins following the DSA of PS-*b*-P4VP block copolymer in HSQ trenches. Large areas of translationally ordered, in plane (C<sub>11</sub>) P4VP were generated by confinement in the HSQ topography. Experimentally robust processes were established for developing P4VP C<sub>11</sub> patterns and their subsequent impregnation with Fe<sub>3</sub>O<sub>4</sub> and  $\gamma$ -Al<sub>2</sub>O<sub>3</sub> hardmask materials and eventual substrate pattern transfer. PS-*b*-P4VP thin films were spin coated onto HSQ topographically patterned substrates (such that HSQ feature spacing was 32n nm where n is an integer and 0 < n < 8). Full SEM characterization of these substrates is shown in Appendix – Chapter 5 Figure S5.7.1. SVA was carried out in an ambient atmosphere of chloroform and pattern transfer was then optimized for the DSA defined features. The graphoepitaxial alignment of PS-*b*-P4VP within the topographical HSQ substrates was carefully optimized using film thickness and SVA conditions.

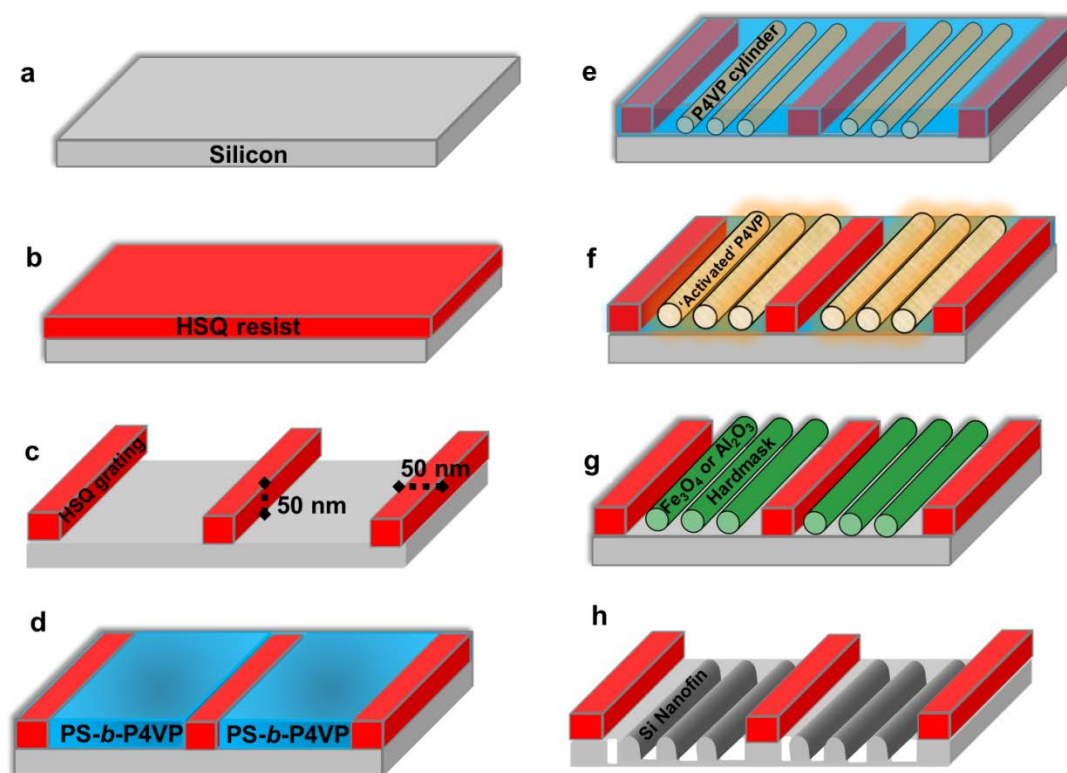


**Figure 5.1.** Overall process flow enabling Si nanofins via an enhanced metal oxide pattern transfer. (a) Si substrate (b) Uniform HSQ resist material spin coated (c) Electron beam lithography used to define 50 nm HSQ gratings at different pitches (see experimental) (d) PS-*b*-P4VP BCP spin coated (e) Solvent vapor annealing of BCP film in chloroform vapors at room temperature producing P4VP cylinders in plane (f) Film exposed to ethanol vapors to form ‘activated’ porous P4VP nanodomains (g) Iron or aluminium oxide formed via inclusion and UV/ozone treatment (h) Pattern transfer to underlying Si forming aligned Si nanofins.

0.5, 1 and 2 wt % PS-*b*-P4VP BCP solutions were spin coated onto Si substrates that had been ultrasonically cleaned. Characterization of 1 and 2 wt % films were initially examined after a 3 hour SVA period and data are presented in Figure S5.7.2~S5.7.9. The influence of different surface chemistries were also examined for the 0.5 wt % films (See Figure S5.7.10~S5.7.16). Films thicknesses were measured after SVA for 2 hours at 52.6 and 97.2 ( $\pm$  0.15) nm for 1 and 2 wt % films respectively. A color change associated with increased swelling<sup>35</sup> was observed for these films but not the thinner films as described below (Figure 5.2). Relief structures such as “islands” and “holes” were observed in these

thicker films and visible in both optical and atomic force microscopy (AFM). The thicker films proved unsuitable for nanolithography due to irregular thickness and also that they contained more than one layer of parallel cylinders. In comparison, an optical image (Figure S5.7.13b) of the 0.5 wt % film showed film thickness uniformity and the thickness of the film at 24.4 ( $\pm 0.15$ ) nm is consistent with a single layer of cylinders (as proven in TEM data presented below). Although 24.4 nm is below the ideal commensurability of the system (since the cylinder centre to centre spacing is 32 nm) it is suggested that under the chloroform solvent vapor that the thickness approaches an ideal value. Thus, the solvent annealing conditions of the 0.5 wt % films was examined in detail. Figure 5.2a~d show SEM characterization of the line pattern evolution for 0.5 wt % films with chloroform at room temperature ( $\sim 290$  K) from 30 minutes up to 3 hours (note films were selectively swelled using ethanol vapor to provide SEM contrast). The initial spin cast 0.5 wt % film (AFM image, Figure S5.13c) showed poorly ordered P4VP cylinders normal ( $C_{\perp}$ ) to the substrate. The top-down SEM images in Figure 5.2 show the film surface after 30 minutes to 3 hours. Well-developed line ( $C_{\parallel}$ ) patterns were observed with defects reducing as the anneal period was increased. The average domain feature size and cylinder periodicity ( $C_0$ ) for the films was 20 nm and 32 nm respectively for all samples. Self-assembled patterns were developed in HSQ trenches as shown in Figure S5.17. Patterns were stained using ruthenium tetroxide vapor to enhance contrast.

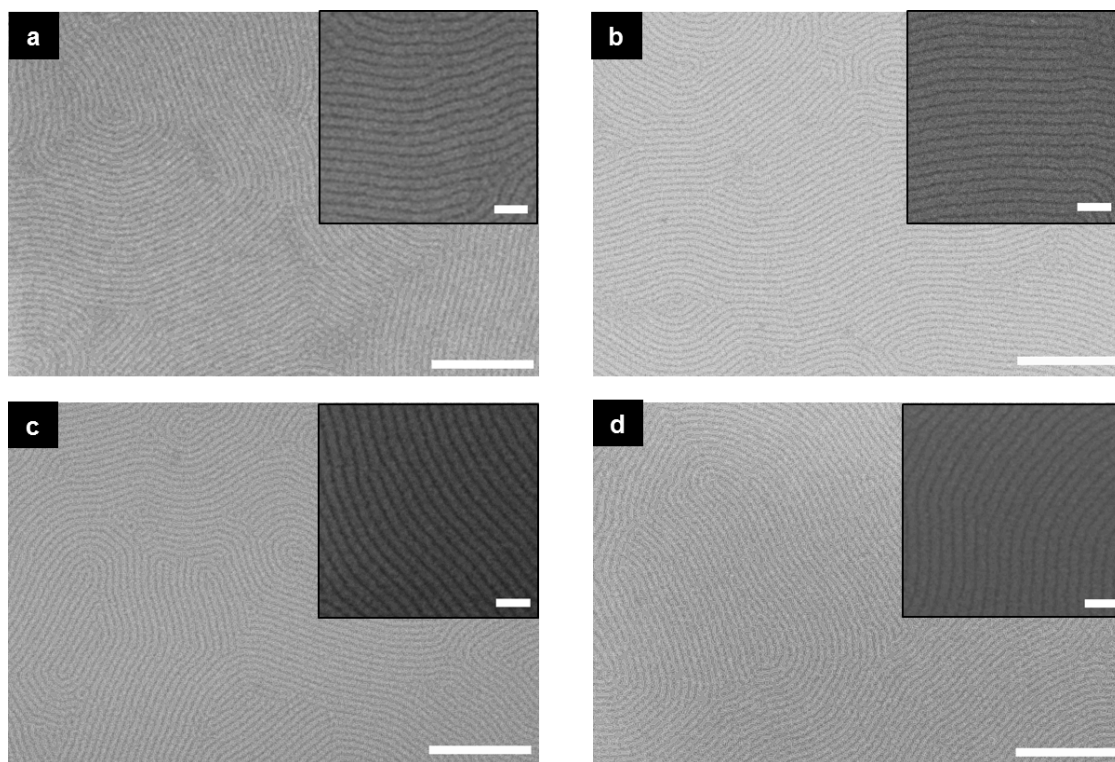


**Figure 5.2.** PS-*b*-P4VP BCP films were spin coated from a 0.5 wt % solution on to acetone degreased Si substrates. Top-down SEM images are shown in (a)-(d) after solvent vapor annealing with chloroform at room temperature ( $\sim 290$  K) of a 24 nm thick PS-*b*-P4VP BCP film for (a) 30 minutes, (b) 1 hour, (c) 2 hour and (d) 3 hours respectively. Note films were exposed to ethanol vapors following solvent vapor annealing to create porous structures. Scale bars are 500 nm, while inset scale bars are 100 nm.

*In-situ* ellipsometry suggests the swollen thickness does not reach the theoretically ideal thickness of 32 nm and after 2 hours SVA the measured thickness was 26.1 nm (see Figure S5.7.18a and b). It should be noted that we have observed that the ideal cylinder structure is compressed in thin films and this somewhat lower value might represent the true ideal thickness.<sup>36</sup> The relatively small increase in film thickness ( $\sim 15\%$ ) under SVA is probably due to the limited swelling of the BCP film during annealing as chloroform is a nonselective solvent for pure PS-*b*-P4VP.<sup>35</sup> Solubility parameters for chloroform, PS and P4VP are 19.0, 18.6 and  $\sim 23$  MPa<sup>1/2</sup> respectively.<sup>32,37</sup> The use of chloroform did result in formation of P4VP C<sub>||</sub> while PS selective annealing solvents (e.g. tetrahydrofuran or 1,4 dioxane) gave P4VP C<sub>⊥</sub> arrangements. It should be noted that the

SVA conditions and process window was optimized for this particular PS-*b*-P4VP system and cannot be considered universally applicable for all PS-*b*-P4VP BCP systems. Following SVA in chloroform we believe we have formed cylindrical morphological structures but we cannot definitively rule out other phases without through film analysis (GISAXS or cross-section TEM). However, we do believe that the lack of swelling with chloroform may ensure minimal change in the effective volume composition of the BCP film and thus the likely formation of cylinder structures. Substrates without any surface modification (acetone only cleaned Si or bare Si) gave the best ordered line patterns and thus this window was used for BCP deposition on planar and HSQ substrates. Acetone only cleaned substrates were used as degreasing the substrates provided a uniform film.

Surface reconstruction is a popular method for creating “nanoporous” structures after SVA for asymmetric PS-*b*-P4VP<sup>38,39</sup> and as shown in Figure 5.2, it is sufficient to generate SEM contrast. However, the ethanol reconstruction process needed to be carefully controlled and destruction of the film morphology was observed when the SVA films were immersed in ethanol (See Figure S5.7.19b and c) for extended periods. 10 minutes immersing times did produce porous structures (Figure S5.7.19a) of reasonable quality but at longer times significant distortion of the PS matrix occurs through swelling of the P4VP nanodomains. To create the nanoporous structure without distortion, we used a similar approach to Gowd *et al.*<sup>40</sup> where the film was exposed to ethanol vapor for 20 minutes. We believe that this allows more limited swelling of the P4VP and prevents degradation of the P4VP line patterns. As shown in previous work it is unlikely that this results in a fully developed pore system.<sup>41</sup> This differs from the ethanol treatment used for cylinder forming PS-*b*-PEO BCP systems where the pore system is well developed and suggests effective etching of the PEO.<sup>33,34</sup> The nature of these activation techniques

is under debate but it is clear that well-defined inclusion formed patterns are reliant on the optimization of the activation process. Figure 5.3a-d shows top-down SEM images of highly aligned porous features of PS-*b*-P4VP films in HSQ gratings with 160, 192, 224 and 265 nm channel width dimensions. The methodology developed for planar films can be extended to the HSQ topographical substrates as shown in Figure 5.3.

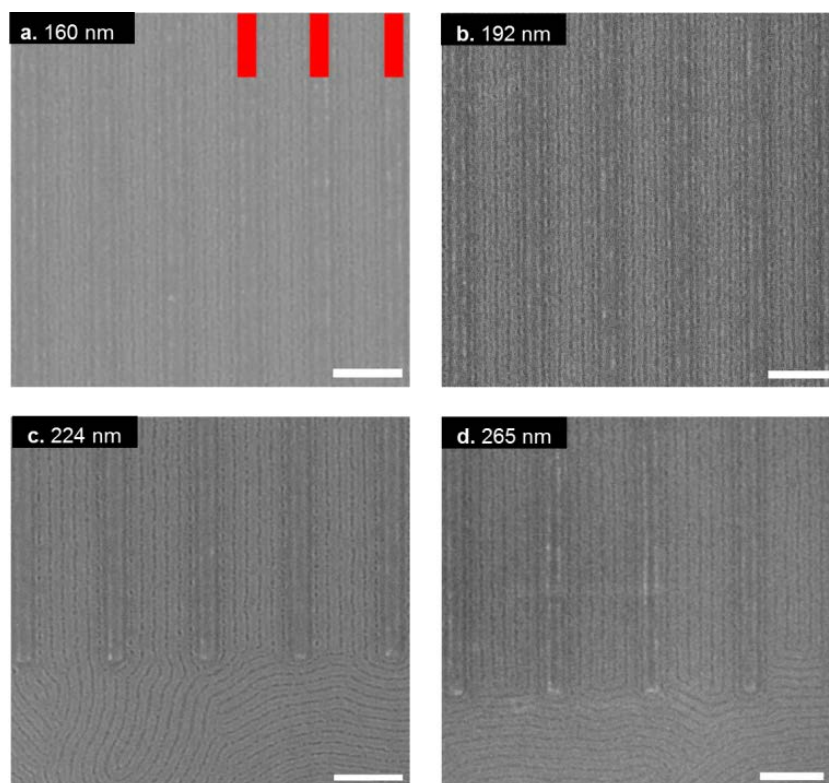
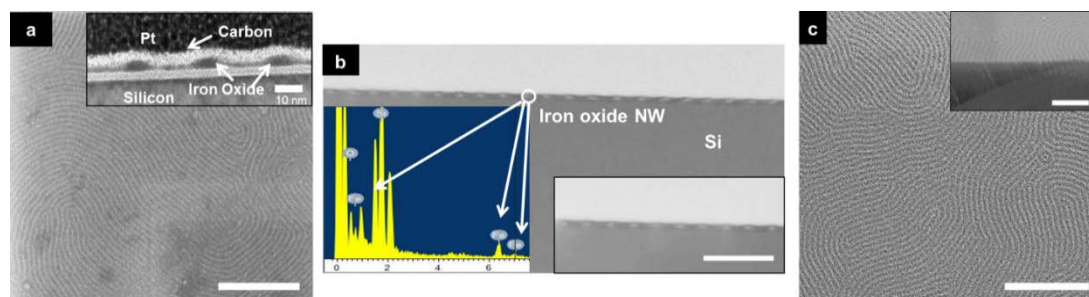


**Figure 5.3.** Top-down SEM images of graphoepitaxially aligned porous PS-*b*-P4VP templates in HSQ gratings following swelling of P4VP domains using ethanol vapor. (a) – (d) Show alignment of PS-*b*-P4VP features in 50 nm HSQ gratings (red bars in image a) at channel widths of (a) 160 nm, (b) 192 nm, (c) 224 nm and (d) 265 nm. (c) and (d) show areas where alignment has taken place from open areas in to the HSQ trench gratings. Scale bars are 200 nm.

Notably, the influence of the HSQ gratings is evident from Figure 5.3c and d as one can see the “fingerprint” pattern in the open area aligned in the HSQ guiding features over large areas.

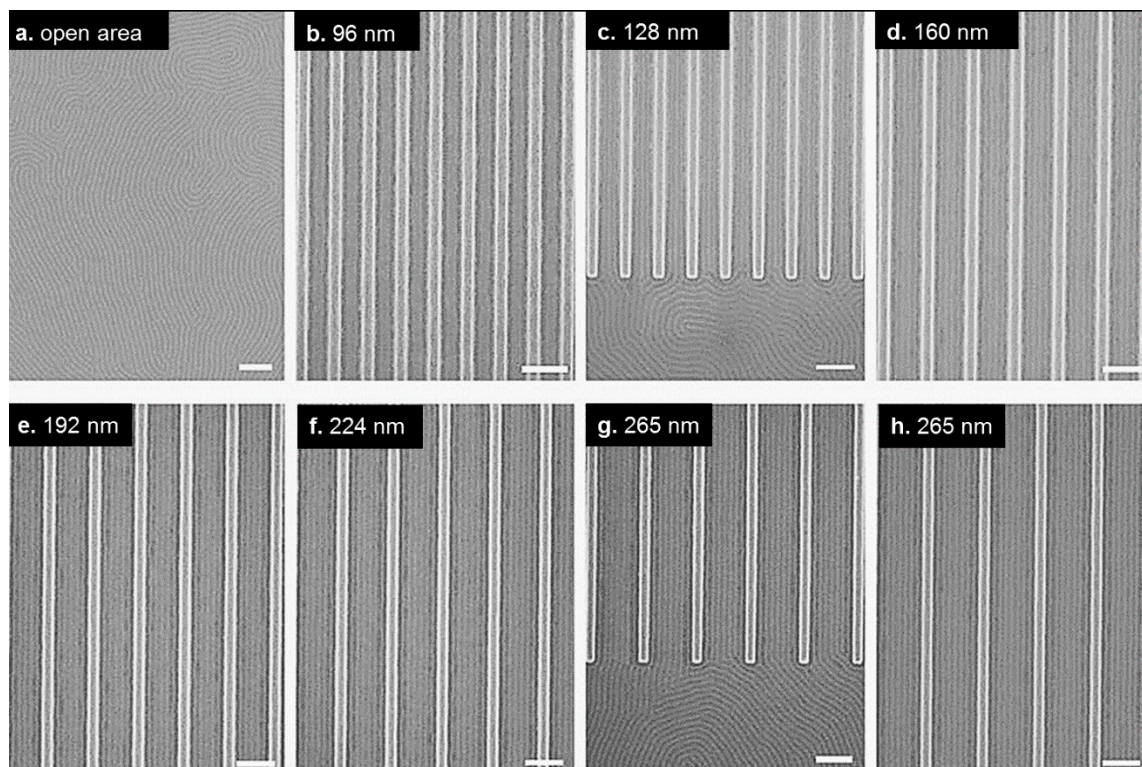
Following surface reconstruction, the “activated” PS-*b*-P4VP acts as a template for the development of metal oxide nanowires to form a hardmask for the pattern transfer process. Employing Fe<sub>3</sub>O<sub>4</sub> is an attractive and facile route to act as an etch mask during plasma etching due to the robust nature of the oxide material which allows the development of high fidelity nanostructures.<sup>38-40</sup> Improving etch contrast between polymer blocks is extremely important for pattern transfer and innovative methods have been explored. For example, Elam, Darling and co-workers have developed a process involving atomic layer deposition coined sequential infiltration synthesis (SIS) to enhance the etch contrast of as formed PS-*b*-PMMA BCP patterns with inorganic material.<sup>42,43</sup> Exotic BCPs containing an inorganic block have been reviewed lately showing potential for lithographic purposes.<sup>44</sup> Here we use simple metal nitrate salts to provide a robust inorganic moiety giving high etch contrast. The metal nitrate (iron or aluminium) solution was spin coated on the nanoporous polymer film structure and the surrounding polymer template was then removed via UV/O<sub>3</sub> treatment. Figure 5.4a displays large scale coverage of the Fe<sub>3</sub>O<sub>4</sub> nanowires and the TEM inset shows a slightly elliptical structure that may reflect the elliptical form of the cylinders noted before.<sup>36</sup> The inset also shows that what may be a small amount of Fe<sub>3</sub>O<sub>4</sub> material resides across the polymer substrate interface. This might result from a thin PVP wetting layer (as P4VP has a higher affinity to the hydrophilic native oxide layer)<sup>35</sup> in the self-assembled PS-*b*-P4VP structure. This was not problematic for pattern transfer and this suggests these darker areas may instead result from electron beam scattering events at the interface. Further characterization from the STEM images in Figure 5.4b show both low resolution and high resolution (inset) Fe<sub>3</sub>O<sub>4</sub> nanowires with high and regular uniformity. The EDX included in Figure 5.4b reveals the presence of iron in the expected regions<sup>41</sup> (but not in areas between wires suggesting that a scattering process is responsible for the apparent

thin film between wires) as well as Si (from the substrate) and oxygen (from the Si oxide layer and from the Fe<sub>3</sub>O<sub>4</sub>).



**Figure 5.4.** (a) Top-down SEM image of Fe<sub>3</sub>O<sub>4</sub> nanowire array after UV/O<sub>3</sub> treatment. Inset in (a) shows cross section TEM of Fe<sub>3</sub>O<sub>4</sub> nanowires/substrate interface. (b) EDX spectrum of Fe<sub>3</sub>O<sub>4</sub> nanowire array and HAADF image and inset show uniformity and regularity of Fe<sub>3</sub>O<sub>4</sub> nanowire array. (c) Top-down SEM image of  $\gamma$ -Al<sub>2</sub>O<sub>3</sub> nanowire arrays after UV/O<sub>3</sub> treatment. Inset in (c) shows cross-section SEM view of  $\gamma$ -Al<sub>2</sub>O<sub>3</sub> nanowires. Scale bars are 500 nm in (a) and (c) and represent 100 nm in (b).

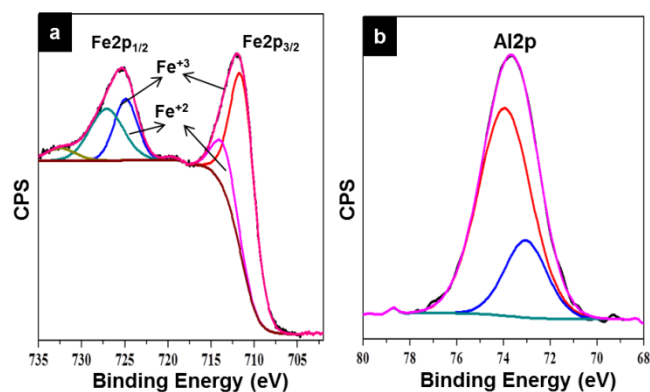
$\gamma$ -Al<sub>2</sub>O<sub>3</sub> inclusion was also carried out and the SEM image in Figure 5.4c show well-defined uniform nanowires.  $\gamma$ -Al<sub>2</sub>O<sub>3</sub> nanowires were produced in a similar manner to Fe<sub>3</sub>O<sub>4</sub> inclusion with an ethanolic metal precursor and the high uniformity is comparable to the Fe<sub>3</sub>O<sub>4</sub> nanowires described above. Figure 5.5a shows a large open area of HSQ topographical substrate with well-defined  $\gamma$ -Al<sub>2</sub>O<sub>3</sub> nanowires. Figure 5.5b-g displays the DSA of HSQ line gratings with aligned  $\gamma$ -Al<sub>2</sub>O<sub>3</sub> nanowire features over large areas with channel widths of 96 nm, 128 nm, 160 nm, 192 nm, 224 nm and 265 nm respectively. Distinct  $\gamma$ -Al<sub>2</sub>O<sub>3</sub> nanowires features are observed in all images with two  $\gamma$ -Al<sub>2</sub>O<sub>3</sub> nanowire features seen in the HSQ gratings with channel width of 96 nm and a total of seven  $\gamma$ -Al<sub>2</sub>O<sub>3</sub> nanowire features demonstrated in the 265 nm channel width. The  $\gamma$ -Al<sub>2</sub>O<sub>3</sub> nanowires mimic the nanoporous template used and possess centre to centre spacings (32 nm) comparable to the original PS-*b*-P4VP BCP film. Fe<sub>3</sub>O<sub>4</sub> inclusion in a 265 nm channel width HSQ grating is also shown over large areas in Figure S5.7.20.



**Figure 5.5.** (a) Shows top-down SEM image of  $\gamma$ -Al<sub>2</sub>O<sub>3</sub> nanowires in open area of HSQ substrate. (b)-(h) Top-down SEM images of aligned  $\gamma$ -Al<sub>2</sub>O<sub>3</sub> nanowires in 50 nm HSQ gratings with channel widths indicated in image. All scale bars are 200 nm.

X-ray photoelectron spectroscopy (XPS) was used to elucidate the chemical composition of the metal nanowire structures developed from metal nitrate ethanolic solutions. Figure 5.6a and b show the high resolution spectra of Fe 2*p* and Al 2*p* core level binding energies of Fe<sub>3</sub>O<sub>4</sub> and  $\gamma$ -Al<sub>2</sub>O<sub>3</sub> nanowires formed following UV/ozone treatment for 3 hours. The ozonation process allowed complete or near-complete removal (as determined by C1*s* signal reduction) of polymer material to form Fe<sub>3</sub>O<sub>4</sub> nanowires (as shown in Figure 5.4a and b) and  $\gamma$ -Al<sub>2</sub>O<sub>3</sub> nanowires (Figure 5.4c). The survey and high resolution O 1*s* spectra for the Fe<sub>3</sub>O<sub>4</sub> nanowires can be found in Figure S5.7.21. The metal 2*p* features were processed with the CasaXPS software using a Shirley background subtraction and curve-fitting with Voigt profiles. For the Fe 2*p* core level, peaks are found at 713.5 eV (Fe

2p<sub>3/2</sub>) and 724.9 eV (Fe 2p<sub>1/2</sub>) respectively. The values match previously reported literature values.<sup>34,41</sup> The 2p<sub>3/2</sub>:2p<sub>1/2</sub> ratio was the expected value of 2:1.



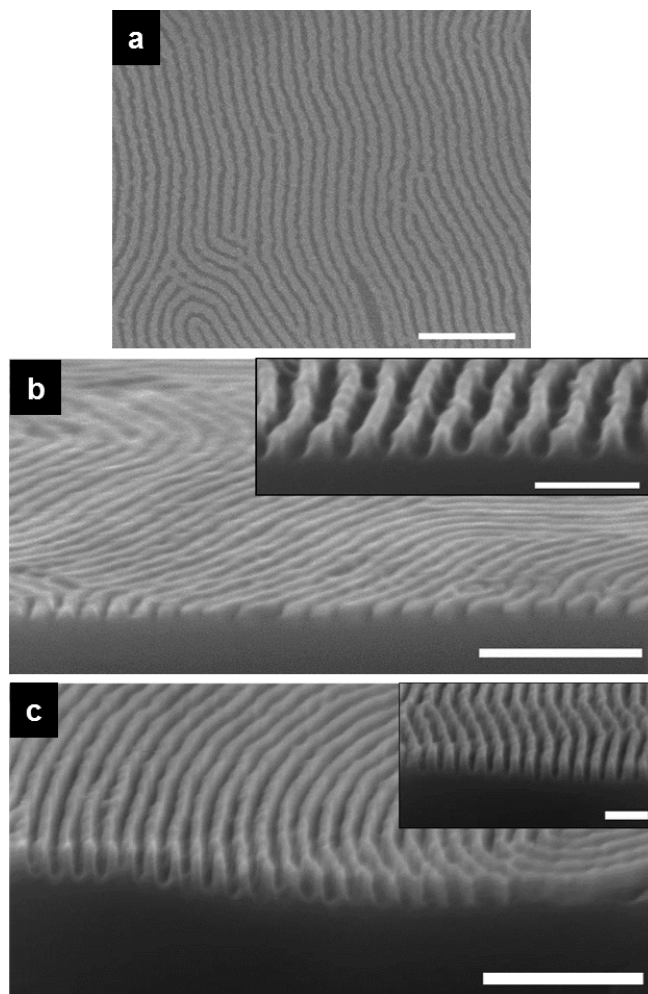
**Figure 5.6.** (a) High resolution XPS spectra of Fe 2p core level of iron oxide (Fe<sub>3</sub>O<sub>4</sub>) nanowires following UV/O<sub>3</sub> treatment. (b) High resolution XPS spectra of Al 2p core level of aluminium oxide nanowires ( $\gamma$ -Al<sub>2</sub>O<sub>3</sub>) following UV/O<sub>3</sub> treatment. Survey spectra and high resolution O 1s core level spectra are shown in Figure 5.7.21 and 5.7.22 for both samples.

Figure 5.6b displays XPS of the Al2p core level binding energy corresponding to the nanowire sample shown in Figure 5.4c. The Al 2p core level binding energy (Figure 5.6b) shows the characteristic peak for Al2p at 73.9 eV typical of  $\gamma$ -Al<sub>2</sub>O<sub>3</sub> and this was consistent with the O1s spectra (Figure S5.7.22).<sup>45</sup>

It has been speculated that the pattern transfer of an on-chip etch mask is second only to lithography in importance.<sup>46</sup> All etch processes are challenging<sup>24</sup> and it is vital that pattern transfer methods are highly selective<sup>46,47</sup> so that DSA of BCPs can move successfully from “lab to fab”. These Fe<sub>3</sub>O<sub>4</sub> and  $\gamma$ -Al<sub>2</sub>O<sub>3</sub> nanowires can act as efficient hardmasks for pattern transfer. C<sub>4</sub>F<sub>8</sub>/H<sub>2</sub> was employed to etch the native oxide layer thus exposing the underlying Si which was then subject to a Si etch (C<sub>4</sub>F<sub>8</sub>/SF<sub>6</sub>). The top-down SEM image in Figure 5.7a are of the Si nanofins following pattern transfer of the Fe<sub>3</sub>O<sub>4</sub> nanowires using a short Si oxide etch (5 seconds) and an ICP Si etch (1 minute 30

seconds). Note that the rough edges of the hardmask from the top-down SEM image in Figure 5.7a are due to the  $\text{Fe}_3\text{O}_4$  nanowire material that will inevitably be etched with extended plasma etching. However, the damage to the  $\text{Fe}_3\text{O}_4$  hardmask is not transferred to the underlying Si material (see Figure 5.7 b,c and Figure 5.8).

In contrast, the cross-section SEM in Figure 5.7b and the inset show the regularity of the Si structures where the Si was etched for 1 minute and 30 seconds. This provides evidence for the mechanical strength of the hardmask, and while some rough edges are visible from top-down SEM (Figure 5.7a) these did not affect the Si structure as seen from the TEM characterization below. As described elsewhere,<sup>40</sup>  $\text{Fe}_3\text{O}_4$  can be etched away/removed from the surface of the Si structures without damaging the existing Si. Figure 5.7c shows Si nanofins after 2 minutes Si etching. The profile seen in the cross-section SEM image and inset reveal an even greater depth and definition to the Si nanofins etched for 1 minute and 30 seconds in Figure 5.7b. TEM analysis was carried out on the Si nanofins fabricated from the  $\text{Fe}_3\text{O}_4$  nanowire hardmask template shown in Figure 5.7a and b.



**Figure 5.7.** (a) Top-down SEM of Si nanofins following plasma etching of  $\text{Fe}_3\text{O}_4$  nanowire hardmask for 1 minute and 30 seconds. (b) Cross-section SEM image of sample (a) while (c) shows cross-section SEM image of an  $\text{Fe}_3\text{O}_4$  nanowire hardmask plasma etched for 2 minutes. Insets in (b) and (c) show highly defined uniform nanofin arrays. Main scale bars are 250 nm while inset scale bars represent 100 nm.

The corresponding TEM characterization of the Si etched for 1 minute and 30 seconds are shown in Figure 5.8a-c and reveal the uniformity of the etch with dimensional control owing to the  $\text{Fe}_3\text{O}_4$  nanowire hardmask. The periodicity of the Si structure pattern ( $C_0 = 32$  nm) remains similar to the initial microphase separated, reconstructed template and  $\text{Fe}_3\text{O}_4$  nanowire patterns. The etched Si nanostructures possess features sizes of  $\sim 10$  nm and etch depths of  $\sim 40$  nm.

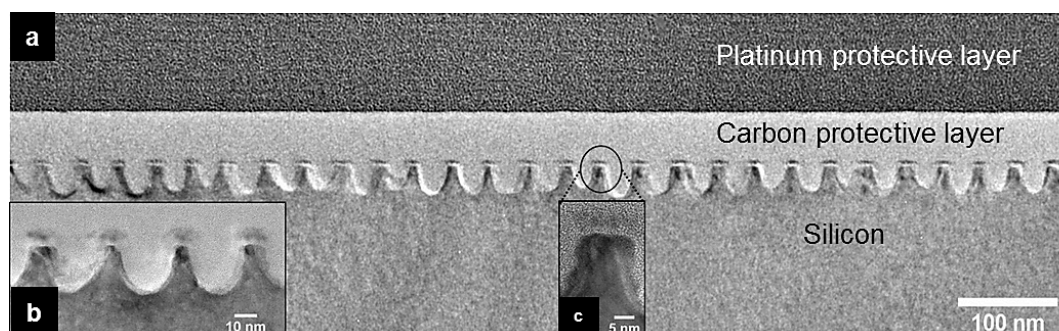


**Figure 5.8.** (a) Low resolution TEM image of Si nanofin array following plasma etching Si for 1 minute and 30 seconds using  $\text{Fe}_3\text{O}_4$  nanowire hardmask. (b) and (c) High resolution TEM images of Si nanofins with 10 nm feature size and 16 nm half-pitch as shown in (a).

Similarly, we examined the effectiveness of the  $\gamma\text{-Al}_2\text{O}_3$  hardmask material. The etching procedures were extended to the  $\gamma\text{-Al}_2\text{O}_3$  hardmask showing similar results. However, it should be noted that later etches were performed without the native oxide etch. The native oxide etch can sometimes result in significant damage to the  $\gamma\text{-Al}_2\text{O}_3$  hardmask and, thus, limits etch fidelity. Figure 5.9a displays the top-down SEM image of Si nanofin structures following etching of Si for 1 minute and 30 seconds using the  $\gamma\text{-Al}_2\text{O}_3$  hardmask. The top-down and cross-section SEM images in Figure 5.9a and b reveal a highly uniform etch with homogeneity across the Si surface. The use of a different metal oxide material shows the versatility of the metal-ethanolic precursor solution as it is simple, inexpensive, provides well-defined nanowires and acts as a robust hardmask for pattern transfer. Figure 5.9c shows the resulting profile from a 2 minute Si etch using the  $\gamma\text{-Al}_2\text{O}_3$  material. The cross-section view and inset in Figure 5.9c reveals a homogenous etching procedure with high reproducibility.

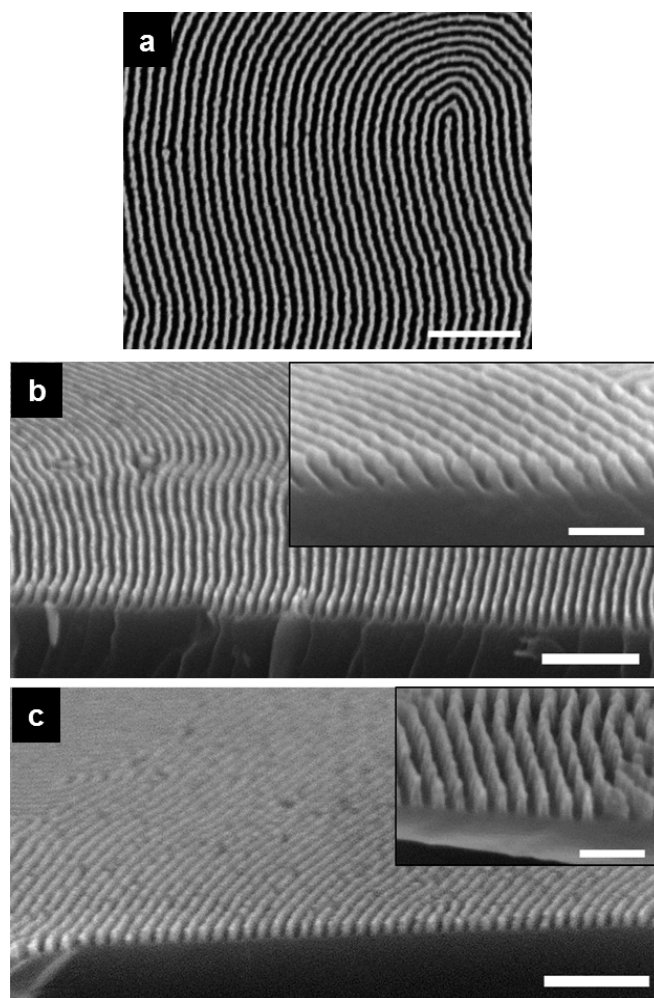


**Figure 5.9.** (a) Top-down SEM image of pattern transfer of  $\gamma$ -Al<sub>2</sub>O<sub>3</sub> hardmask nanowires on planar Si generating Si nanofins. (b) Cross-section SEM view of sample (a) after 1 minute and 30 seconds of Si etching. (c) Cross-section SEM view of Si nanofins over large area following 2 minutes of Si etching with  $\gamma$ -Al<sub>2</sub>O<sub>3</sub> as hardmask. Inset in (c) reveals the vertical profile and uniform nature of the nanofins. Main scale bars are 250 nm while inset scale bars represent 100 nm.

Finally we demonstrate the pattern transfer producing aligned Si nanofins generated from the  $\gamma$ -Al<sub>2</sub>O<sub>3</sub> nanowire hardmask using the HSQ gratings for DSA application. Figure 5.10a-c shows the top-down SEM images of Si nanofins following pattern transfer using Si etch (SF<sub>6</sub>/C<sub>4</sub>F<sub>8</sub>) for 1 minute and 30 seconds. Figure 5.10a displays an open area of the HSQ substrate where the alignment of one P4VP cylinder was directed. The nanofin shows good contrast in comparison to  $\gamma$ -Al<sub>2</sub>O<sub>3</sub> features shown earlier (Figure 5.5) due to

the Si etch. Distinct nanofins were also produced in the 160 nm and 265 nm trenches displaying 4 and 7 Si nanofins respectively as displayed in Figure 5.10b and c.

One can also see that the feature size of the nanofins aligned next to the HSQ sidewalls in the larger trench width (265 nm) is slightly smaller and we speculate that this may be due to swelling effects during SVA or the “activation” step. The issue does not affect the pattern transfer of the  $\gamma$ -Al<sub>2</sub>O<sub>3</sub> nanowires in the graphoepitaxy process however we suggest that by increasing the trench widths initially this problem may be overcome, and could lead to uniform nanofin formation by accounting for excess swelling of domains during SVA. A low resolution TEM image in Figure 5.10d shows the uniformity of the Si etch in the 160 nm channel width with the  $\gamma$ -Al<sub>2</sub>O<sub>3</sub> material acting as an effective etch stop. Feature sizes were measured at ~ 10 nm while the etch depth was ~ 40 nm i.e. an aspect ratio of 1:4. The high-resolution TEM images of Si nanofins are displayed in Figure 5.10e and f revealing the uniformity of the nanofin structure.

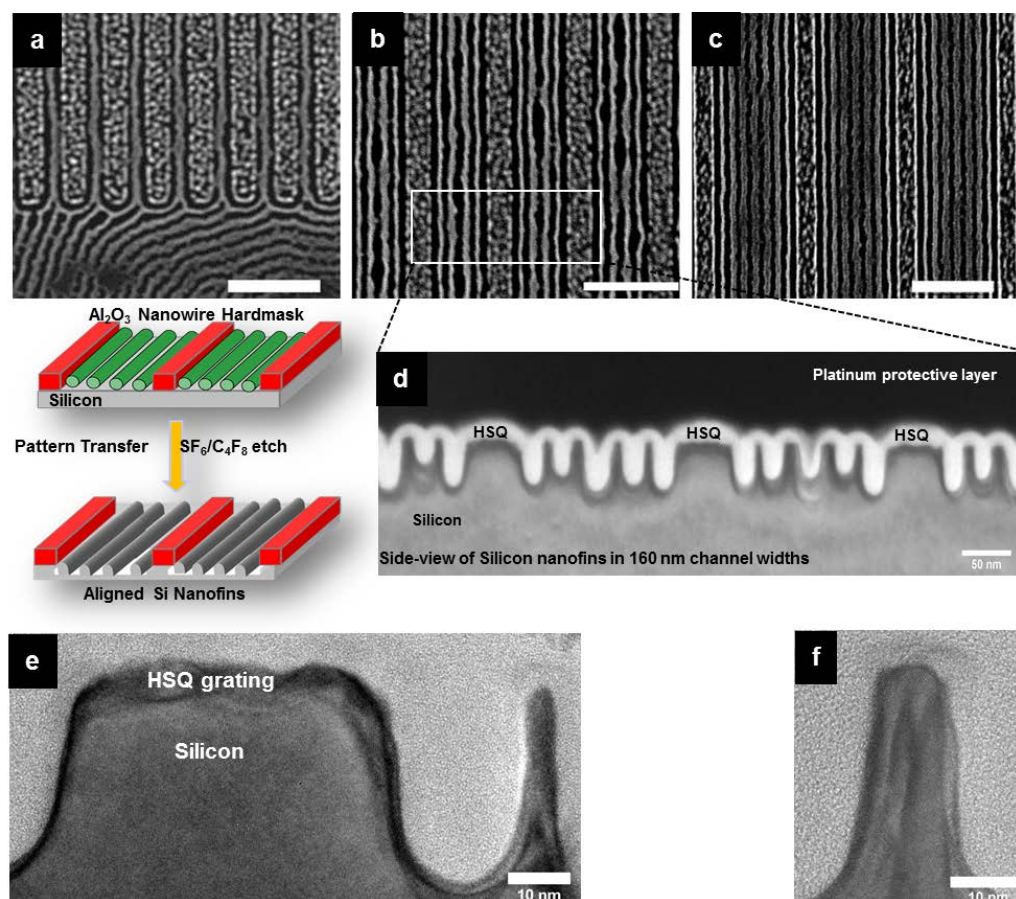


**Figure 5.10.** Top-down SEM images of pattern transferred Si nanofins in  $\sim 50$  nm HSQ gratings at channel widths of (a) 64 nm, (b) 160 nm and (c) 265 nm respectively. Schematic shows process for pattern transfer of aligned  $\gamma$ - $\text{Al}_2\text{O}_3$  nanowire hardmask. (d) Cross-section TEM of aligned Si nanofins in HSQ gratings possessing channel widths of 160 nm. (e,f) Show high resolution TEM images of Si nanofins fabricated from  $\gamma$ - $\text{Al}_2\text{O}_3$  nanowire hardmask. Scale bars are 250 nm unless indicated.

## 5.5. Conclusions

In this chapter, a straight forward, low cost and industrial compatible methodology for the fabrication of sub-wavelength semiconductor features has been demonstrated. SVA was shown to be an extremely effective route for controlling and optimizing cylindrical morphology in an asymmetric PS-*b*-P4VP BCP system. Furthermore, the ability to develop and control the orientation of the cylindrical morphology is promising for line space features for on-chip etch mask application. The tuning of the film thickness of the PS-*b*-P4VP is a significant process step for forming a monolayer of cylinders in thin film

for etch mask application. Creating an ultrathin mask is important for the subsequent pattern transfer to the device active layer that the mask patterns. The TEM characterization presented in this work shows the ability of PS-*b*-P4VP to form well oriented C<sub>11</sub> that enable metal oxide inclusion. Additionally, enhancing etch contrast over large areas via metal oxide inclusion technique was shown allowing a facile pattern transfer. The pattern transfer of the on-chip etch mask was shown to be extremely successful for both the Fe<sub>3</sub>O<sub>4</sub> and  $\gamma$ -Al<sub>2</sub>O<sub>3</sub> hardmask material on planar Si. Si nanofins were shown to be uniform from TEM characterization with feature sizes of sub-12 nm. DSA of the PS-*b*-P4VP line patterns via a graphoepitaxial approach was also demonstrated employing HSQ gratings. Metal oxide inclusion was carried out using “activated” PS-*b*-P4VP features guided by the HSQ gratings with high reproducibility comparable to the planar substrates. The pattern transfer of the metal oxide etch masks was shown to result in regularly aligned Si nanofins with ~ 10 nm feature size. The technique and approach used here has potential for industrial scale up owing to the simple and limited process steps required for the fabrication of highly dense Si nanostructures. Also the parallels with the semiconductor industry are clear as a top-down method was employed to fabricate the guiding trenches with a well-established negative tone electron-beam lithographic resist. The ability to fabricate Si structures with such high precision and placement accuracy are attractive aspects for key enabling future devices.

## 5.6. References

- (1) Stoykovich, M. P.; Nealey, P. F. Block copolymers and conventional lithography. *Materials Today* **2006**, 9, 20-29.
- (2) Pease, R. F.; Chou, S. Y. Lithography and other patterning techniques for future electronics. *Proceedings of the IEEE* **2008**, 96, 248-270.
- (3) ITRS. International Technology Roadmap for Semiconductors, “Lithography”, **2013**, <http://www.itrs.net/Links/2013ITRS/2013Chapters/2013Litho.pdf>, date accessed September 2014.

- (4) Hobbs, R. G.; Petkov, N.; Holmes, J. D. Semiconductor Nanowire Fabrication by Bottom-Up and Top-Down Paradigms. *Chemistry of Materials* **2012**, *24*, 1975-1991.
- (5) Poelma, J. E.; Hawker, C. J. Block copolymers: With a little help from above. *Nature Nanotechnology* **2010**, *5*, 243-244.
- (6) Morris, M. A. Directed self-assembly of block copolymers for nanocircuitry fabrication. *Microelectronic Engineering* **2015**, *132*, 207-217.
- (7) Kim, S. O.; Solak, H. H.; Stoykovich, M. P.; Ferrier, N. J.; de Pablo, J. J.; Nealey, P. F. Epitaxial self-assembly of block copolymers on lithographically defined nanopatterned substrates. *Nature* **2003**, *424*, 411-414.
- (8) Stoykovich, M. P.; Müller, M.; Kim, S. O.; Solak, H. H.; Edwards, E. W.; De Pablo, J. J.; Nealey, P. F. Materials Science: Directed assembly of block copolymer blends into nonregular device-oriented structures. *Science* **2005**, *308*, 1442-1446.
- (9) Ruiz, R.; Kang, H.; Detcheverry, F. A.; Dobisz, E.; Kercher, D. S.; Albrecht, T. R.; de Pablo, J. J.; Nealey, P. F. Density Multiplication and Improved Lithography by Directed Block Copolymer Assembly. *Science* **2008**, *321*, 936-939.
- (10) Borah, D.; Rasappa, S.; Senthamaraiannan, R.; Kosmala, B.; Shaw, M. T.; Holmes, J. D.; Morris, M. A. Orientation and Alignment Control of Microphase-Separated PS-*b*-PDMS Substrate Patterns via Polymer Brush Chemistry. *ACS Applied Materials & Interfaces* **2012**, *5*, 88-97.
- (11) Farrell, R. A.; Kinahan, N. T.; Hansel, S.; Stuen, K. O.; Petkov, N.; Shaw, M. T.; West, L. E.; Djara, V.; Dunne, R. J.; Varona, O. G.; Gleeson, P. G.; Jung, S. J.; Kim, H. Y.; Kolešnik, M. M.; Lutz, T.; Murray, C. P.; Holmes, J. D.; Nealey, P. F.; Duesberg, G. S.; Krstić, V.; Morris, M. A. Large-scale parallel arrays of silicon nanowires via block copolymer directed self-assembly. *Nanoscale* **2012**, *4*, 3228-3236.
- (12) Hobbs, R. G.; Farrell, R. A.; Bolger, C. T.; Kelly, R. A.; Morris, M. A.; Petkov, N.; Holmes, J. D. Selective Sidewall Wetting of Polymer Blocks in Hydrogen Silsesquioxane Directed Self-Assembly of PS-*b*-PDMS. *ACS Applied Materials & Interfaces* **2012**, *4*, 4637-4642.
- (13) Moon, H.-S.; Shin, D. O.; Kim, B. H.; Jin, H. M.; Lee, S.; Lee, M. G.; Kim, S. O. Large-area, highly oriented lamellar block copolymer nanopatterning directed by graphoepitaxially assembled cylinder nanopatterns. *Journal of Materials Chemistry* **2012**, *22*, 6307-6310.
- (14) Borah, D.; Rasappa, S.; Senthamaraiannan, R.; Holmes, J. D.; Morris, M. A. Tuning PDMS Brush Chemistry by UV-O<sub>3</sub> Exposure for PS-*b*-PDMS Microphase Separation and Directed Self-assembly. *Langmuir* **2013**, *29*, 8959-8968.
- (15) Jeong, S.-J.; Kim, J. Y.; Kim, B. H.; Moon, H.-S.; Kim, S. O. Directed self-assembly of block copolymers for next generation nanolithography. *Materials Today* **2013**, *16*, 468-476.
- (16) Semenov, A. N. Theory of block copolymer interfaces in the strong segregation limit. *Macromolecules* **1993**, *26*, 6617-6621.
- (17) Cushen, J. D.; Otsuka, I.; Bates, C. M.; Halila, S.; Fort, S.; Rochas, C.; Easley, J. A.; Rausch, E. L.; Thio, A.; Borsali, R.; Willson, C. G.; Ellison, C. J. Oligosaccharide/Silicon-Containing Block Copolymers with 5 nm Features for Lithographic Applications. *ACS Nano* **2012**, *6*, (4), 3424-3433.
- (18) Maher, M. J.; Bates, C. M.; Blachut, G.; Sirard, S.; Self, J. L.; Carlson, M. C.; Dean, L. M.; Cushen, J. D.; Durand, W. J.; Hayes, C. O.; Ellison, C. J.; Willson, C. G. Interfacial Design for Block Copolymer Thin Films. *Chemistry of Materials* **2014**, *26*, 1471-1479.

- (19) Cushen, J. D.; Bates, C. M.; Rausch, E. L.; Dean, L. M.; Zhou, S. X.; Willson, C. G.; Ellison, C. J. Thin Film Self-Assembly of Poly(trimethylsilylstyrene-*b*-*d,l*-lactide) with Sub-10 nm Domains. *Macromolecules* **2012**, *45*, 8722-8728.
- (20) Kennemur, J. G.; Yao, L.; Bates, F. S.; Hillmyer, M. A. Sub-5 nm Domains in Ordered Poly(cyclohexylethylene)-*block*-poly(methyl methacrylate) Block Polymers for Lithography. *Macromolecules* **2014**, *47*, 1411-1418.
- (21) Borah, D.; Ozmen, M.; Rasappa, S.; Shaw, M. T.; Holmes, J. D.; Morris, M. A. Molecularly Functionalized Silicon Substrates for Orientation Control of the Microphase Separation of PS-*b*-PMMA and PS-*b*-PDMS Block Copolymer Systems. *Langmuir* **2013**, *29*, 2809-2820.
- (22) Borah, D.; Rasappa, S.; Senthamarikannan, R.; Holmes, J. D.; Morris, M. A. Graphoepitaxial Directed Self-Assembly of Polystyrene-*Block*-Polydimethylsiloxane Block Copolymer on Substrates Functionalized with Hexamethyldisilazane to Fabricate Nanoscale Silicon Patterns. *Advanced Materials Interfaces* **2014**, *1*.
- (23) Son, J. G.; Chang, J.-B.; Berggren, K. K.; Ross, C. A. Assembly of Sub-10-nm Block Copolymer Patterns with Mixed Morphology and Period Using Electron Irradiation and Solvent Annealing. *Nano Letters* **2011**, *11*, 5079-5084.
- (24) Gu, X.; Liu, Z.; Gunkel, I.; Chourou, S. T.; Hong, S. W.; Olynick, D. L.; Russell, T. P. High Aspect Ratio Sub-15 nm Silicon Trenches From Block Copolymer Templates. *Advanced Materials* **2012**, *24*, 5688-5694.
- (25) Keen, I.; Yu, A.; Cheng, H.-H.; Jack, K. S.; Nicholson, T. M.; Whittaker, A. K.; Blakey, I. Control of the Orientation of Symmetric Poly(styrene)-*block*-poly(*d,l*-lactide) Block Copolymers Using Statistical Copolymers of Dissimilar Composition. *Langmuir* **2012**, *28*, 15876-15888.
- (26) Keen, I.; Cheng, H.-H.; Yu, A.; Jack, K. S.; Younkin, T. R.; Leeson, M. J.; Whittaker, A. K.; Blakey, I. Behavior of Lamellar Forming Block Copolymers under Nanoconfinement: Implications for Topography Directed Self-Assembly of Sub-10 nm Structures. *Macromolecules* **2013**, *47*, 276-283.
- (27) Mokarian-Tabari, P.; Cummins, C.; Rasappa, S.; Simao, C.; Sotomayor Torres, C. M.; Holmes, J. D.; Morris, M. A. Study of the Kinetics and Mechanism of Rapid Self-Assembly in Block Copolymer Thin Films during Solvo-Microwave Annealing. *Langmuir* **2014**, *30*, 10728-10739.
- (28) Rasappa, S.; Schulte, L.; Borah, D.; Morris, M. A.; Ndoni, S. Sub-15 nm Silicon Lines Fabrication via PS-*b*-PDMS Block Copolymer Lithography. *Journal of Nanomaterials* **2013**, *7*.
- (29) Chai, J.; Wang, D.; Fan, X.; Buriak, J. M. Assembly of aligned linear metallic patterns on silicon. *Nature Nanotechnology* **2007**, *2*, 500-506.
- (30) Chai, J.; Buriak, J. M. Using Cylindrical Domains of Block Copolymers To Self-Assemble and Align Metallic Nanowires. *ACS Nano* **2008**, *2*, 489-501.
- (31) Gowd, E. B.; Marcus, B.; Manfred, S. In Situ GISAXS Study on Solvent Vapour Induced Orientation Switching in PS-*b*-P4VP Block Copolymer Thin Films. *IOP Conference Series: Materials Science and Engineering* **2010**, *14*, 012015.
- (32) Gowd, E. B.; Koga, T.; Endoh, M. K.; Kumar, K.; Stamm, M. Pathways of cylindrical orientations in PS-*b*-P4VP diblock copolymer thin films upon solvent vapor annealing. *Soft Matter* **2014**, *10*, 7753-7761.
- (33) van Zoelen, W.; Asumaa, T.; Ruokolainen, J.; Ikkala, O.; ten Brinke, G. Phase Behavior of Solvent Vapor Annealed Thin Films of PS-*b*-P4VP(PDP) Supramolecules. *Macromolecules* **2008**, *41*, 3199-3208.

- (34) O'Driscoll, B. M. D.; Kelly, R. A.; Shaw, M.; Mokarian-Tabari, P.; Lontos, G.; Ntetsikas, K.; Avgeropoulos, A.; Petkov, N.; Morris, M. A. Achieving structural control with thin polystyrene-*b*-polydimethylsiloxane block copolymer films: The complex relationship of interface chemistry, annealing methodology and process conditions. *European Polymer Journal* **2013**, *49*, 3445-3454.
- (35) O'Driscoll, S.; Demirel, G.; Farrell, R. A.; Fitzgerald, T. G.; O'Mahony, C.; Holmes, J. D.; Morris, M. A. The morphology and structure of PS-*b*-P4VP block copolymer films by solvent annealing: effect of the solvent parameter. *Polymers for Advanced Technologies* **2011**, *22*, 915-923.
- (36) Sinturel, C.; Vayer, M.; Morris, M.; Hillmyer, M. A., Solvent Vapor Annealing of Block Polymer Thin Films. *Macromolecules* **2013**, *46* (14), 5399-5415.
- (37) Park, S.; Wang, J.-Y.; Kim, B.; Xu, J.; Russell, T. P. A Simple Route to Highly Oriented and Ordered Nanoporous Block Copolymer Templates. *ACS Nano* **2008**, *2*, 766-772.
- (38) Park, S.; Wang, J.-Y.; Kim, B.; Russell, T. P. From Nanorings to Nanodots by Patterning with Block Copolymers. *Nano Letters* **2008**, *8*, 1667-1672.
- (39) Bhoje Gowd, E.; Nandan, B.; Vyas, M. K.; Bigall, N. C.; Eychmüller, A.; Schlörb, H.; Stamm, M. Highly ordered palladium nanodots and nanowires from switchable block copolymer thin films. *Nanotechnology* **2009**, *20*.
- (40) Cummins, C.; Borah, D.; Rasappa, S.; Chaudhari, A.; Ghoshal, T.; O'Driscoll, B. M. D.; Carolan, P.; Petkov, N.; Holmes, J. D.; Morris, M. A. Self-assembly of polystyrene-*block*-poly(4-vinylpyridine) block copolymer on molecularly functionalized silicon substrates: fabrication of inorganic nanostructured etchmask for lithographic use. *Journal of Materials Chemistry C* **2013**, *1*, 7941-7951.
- (41) Ghoshal, T.; Maity, T.; Sentharamaikannan, R.; Shaw, M. T.; Carolan, P.; Holmes, J. D.; Roy, S.; Morris, M. A. Size and space controlled hexagonal arrays of superparamagnetic iron oxide nanodots: magnetic studies and application. *Scientific Reports* **2013**, *3*.
- (42) Ghoshal, T.; Sentharamaikannan, R.; Shaw, M. T.; Holmes, J. D.; Morris, M. A. Fabrication of ordered, large scale, horizontally-aligned Si nanowire arrays based on an in situ hard mask block copolymer approach. *Advanced Materials* **2014**, *26*, 1207-1216.
- (43) Peng, Q.; Tseng, Y.-C.; Darling, S. B.; Elam, J. W. Nanoscopic Patterned Materials with Tunable Dimensions via Atomic Layer Deposition on Block Copolymers. *Advanced Materials* **2010**, *22*, 5129-5133.
- (44) Peng, Q.; Tseng, Y.-C.; Darling, S. B.; Elam, J. W. A Route to Nanoscopic Materials via Sequential Infiltration Synthesis on Block Copolymer Templates. *ACS Nano* **2011**, *5*, 4600-4606.
- (45) Nunns, A.; Gwyther, J.; Manners, I. Inorganic block copolymer lithography. *Polymer* **2013**, *54*, 1269-1284.
- (46) Nie, L.; Meng, A.; Yu, J.; Jaroniec, M. Hierarchically Macro-Mesoporous Pt/ $\gamma$ -Al<sub>2</sub>O<sub>3</sub> composite microspheres for efficient formaldehyde oxidation at room temperature. *Scientific Reports* **2013**, *3*.
- (47) Gu, X.; Gunkel, I.; Russell, T. P. Pattern transfer using block copolymers. *Philosophical Transactions of the Royal Society A: Mathematical, Physical and Engineering Sciences* **2013**, *371*.
- (48) Borah, D.; Shaw, M. T.; Rasappa, S.; Farrell, R. A.; Mahony, C. O.; Faulkner, C. M.; Bosea, M.; Gleeson, P.; Holmes, J. D.; Morris, M. A. Plasma etch technologies for the development of ultra-small feature size transistor devices. *Journal of Physics D: Applied Physics* **2011**, *44*, 174012.

## 5.7. Appendix - Chapter 5

### Aligned Silicon Nanofins via the Directed Self-Assembly of PS-*b*-P4VP Block Copolymer and Metal Oxide Enhanced Pattern Transfer

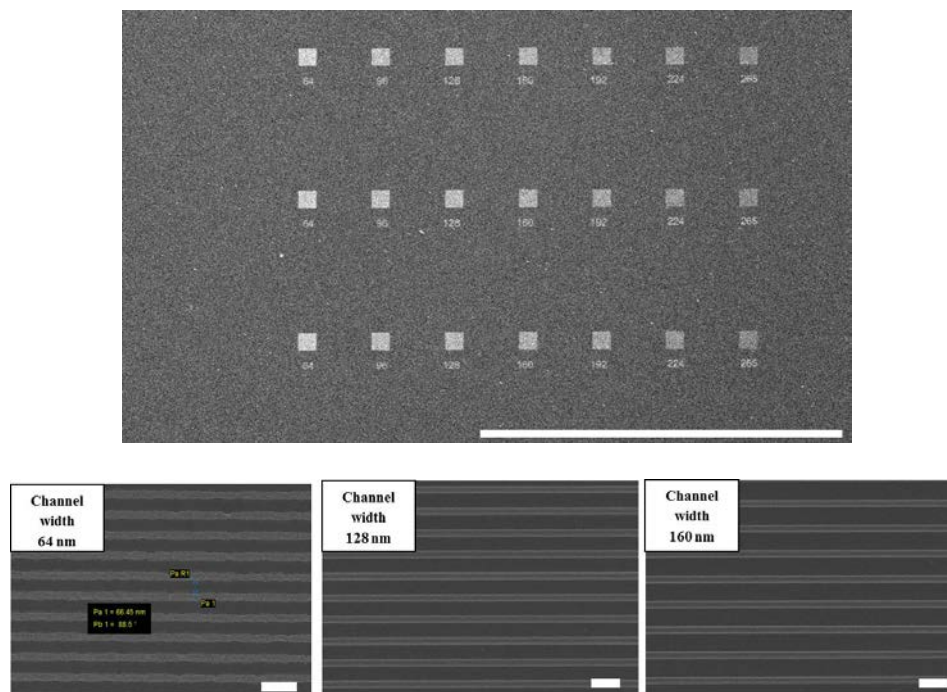


**Figure S5.7.1.** (a) and (b) (scale bars = 500  $\mu\text{m}$ ) show top-down SEM images of HSQ arrays following preparation as outlined in the experimental section in manuscript. High resolution top-down SEM images are shown in (c)-(e) (scale bars = 200 nm) of the HSQ trenches with channel widths of 64 nm, 128 nm and 160 nm respectively.

From our study of the thicker PS-*b*-P4VP films below (1 wt % and 2 wt %) it can be seen that P4VP C<sub>||</sub> (*i.e.* parallel cylinders) can also be developed during some periods (*e.g.* Figure S5.7.3). However, the quality of the features is extremely poor in comparison to the 0.5 wt % films. Notably, “relief” features associated with thicker films create non-uniform films increasing defect features.

It is evident that this PS-*b*-P4VP system forms C<sub>||</sub> due to the film thickness, balanced interfacial interactions and the solvent vapor anneal (SVA) conditions. With these contributing issues evaluated, 0.5 wt % PS-*b*-P4VP films were deposited on substrates

ultrasonically cleaned with organic solvent. Additionally, 0.5 wt % films SVA with chloroform for 2 – 4 hours were used that possessed long correlation lengths.

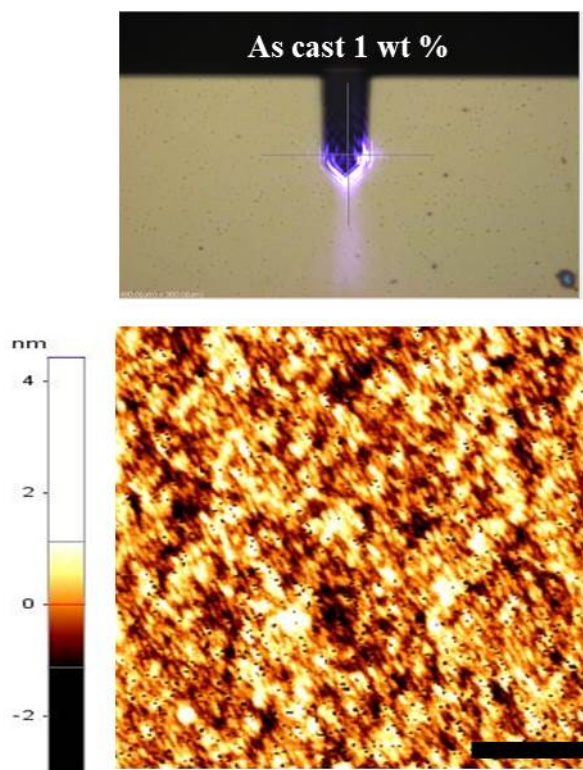


**Figure S5.7.2.** Optical image (~ 480 x 360 micron) (top) shows a uniform film following spin coating of 1 wt % PS-*b*-P4VP BCP thin film on an acetone cleaned silicon substrate. AFM topographic image (bottom, scale bar = 400 nm) reveals a poorly microphase separated structure. There appears to be some microphase separated features but these are not distinct.

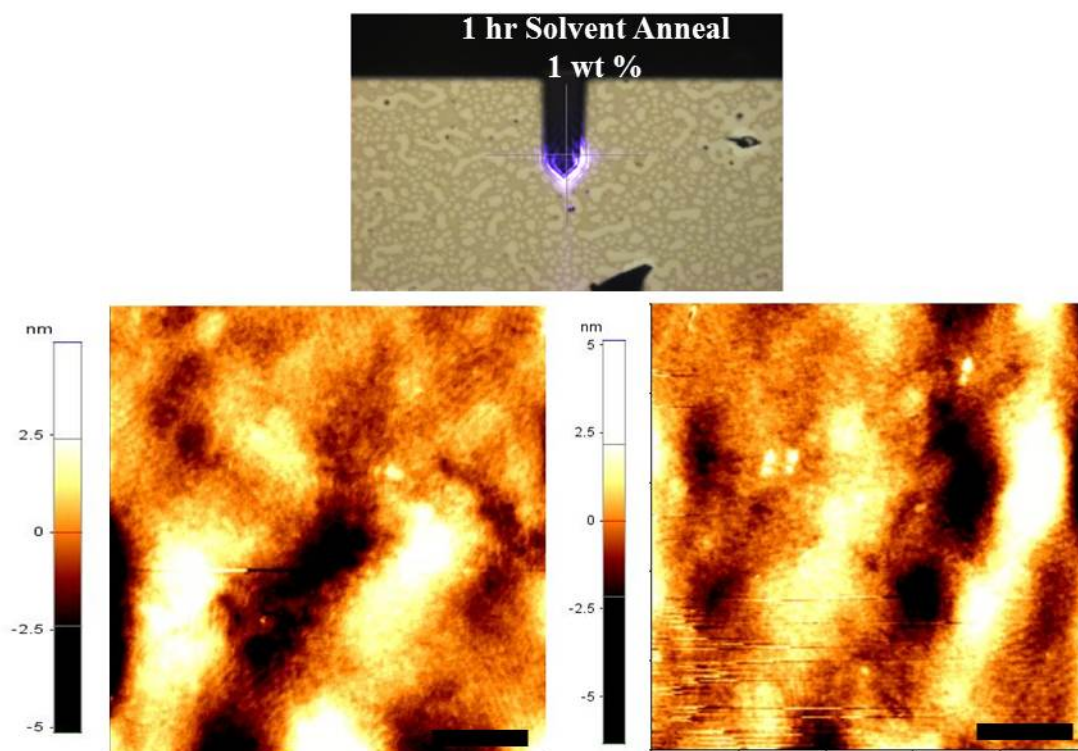


**Figure S5.7.3.** Optical image (top) ( $\sim 480 \times 360$  micron) show areas of 1 wt % PS-*b*-P4VP BCP film with dewetting present after 1 hour solvent vapor annealing with chloroform. The AFM topographic image (bottom left, scale bar = 400 nm) is from a bright area in the optical image. The image shows formation of P4VP C<sub>||</sub>, *i.e.* parallel to the substrate surface. Likewise the AFM topographic image (bottom right, scale bar = 400 nm) from the dark areas of the films shows P4VP C<sub>||</sub>. We do not observe C<sub>||</sub> across the whole film due to its non-uniformity. This is evident in both AFM images.

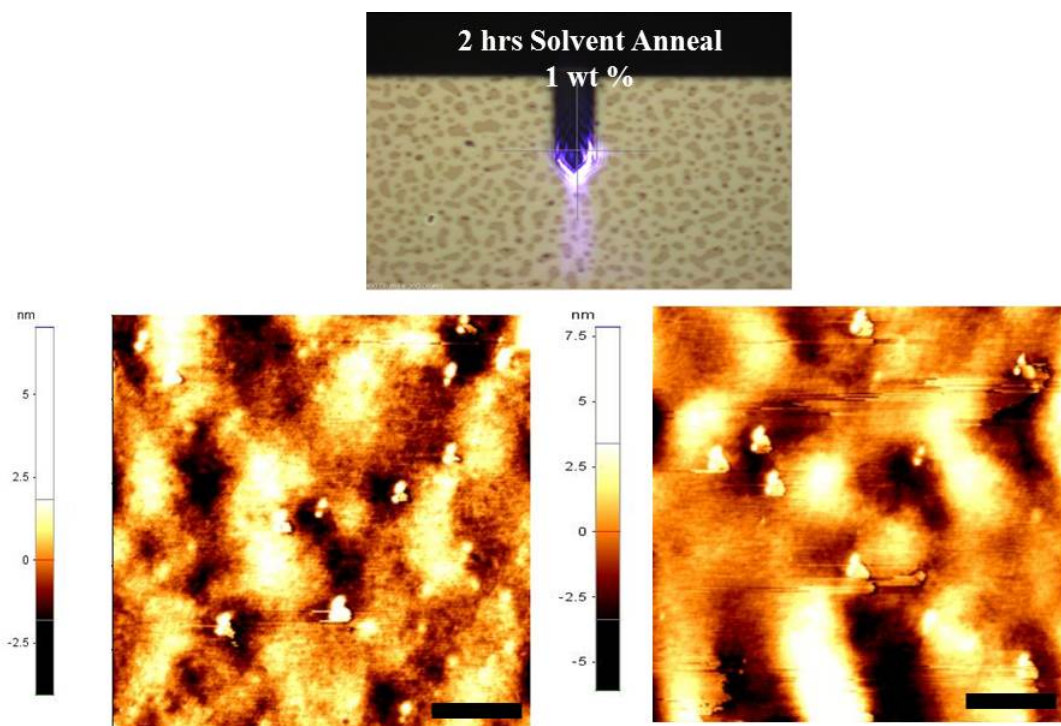


**Figure S5.7.4.** After 2 hours solvent vapor annealing the 1 wt % PS-*b*-P4VP BCP film, the optical image (top) (~ 480 x 360 micron) shows that the bright regions have grown from 1 hour solvent vapor annealing. The AFM topographic image (bottom left, scale bar = 400 nm) does not show any microphase separation. Likewise the AFM topographic image (bottom right, scale bar = 400 nm) does not show any hexagonal patterns. The height scale bars of both images show a non-uniform film surface with regions differing by at least 10 nm.

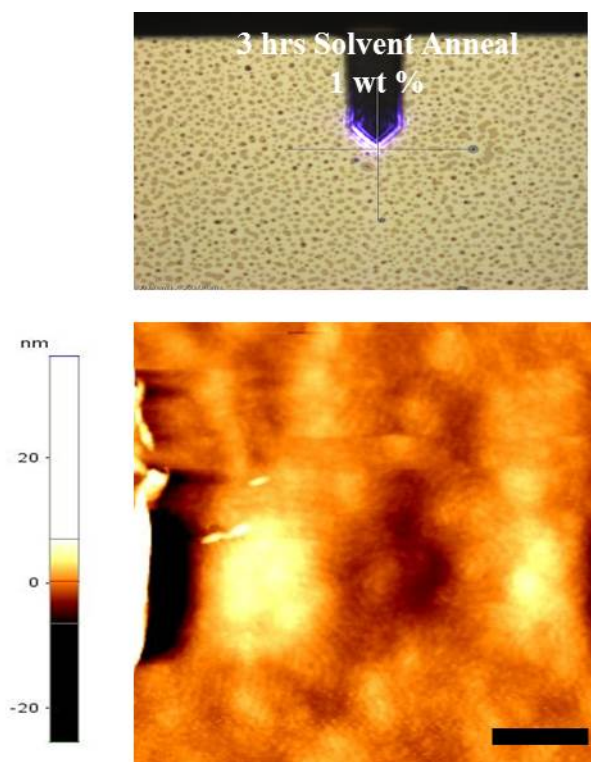


**Figure S5.7.5.** After 3 hours solvent vapor annealing the 1 wt % PS-*b*-P4VP BCP film, optical image (top) (~ 480 x 360 micron) reveals a greater coverage of the bright regions compared to the optical image in Figure S5.7.4. The AFM topographic image (bottom, scale bar = 400 nm) shows areas of microphase separated patterns (C<sub>II</sub>), however these areas are not distinct due to the non-uniform nature of the film. Areas of dewetting are also evident in the AFM image with greater than 20 nm depth (area indicated by arrows).

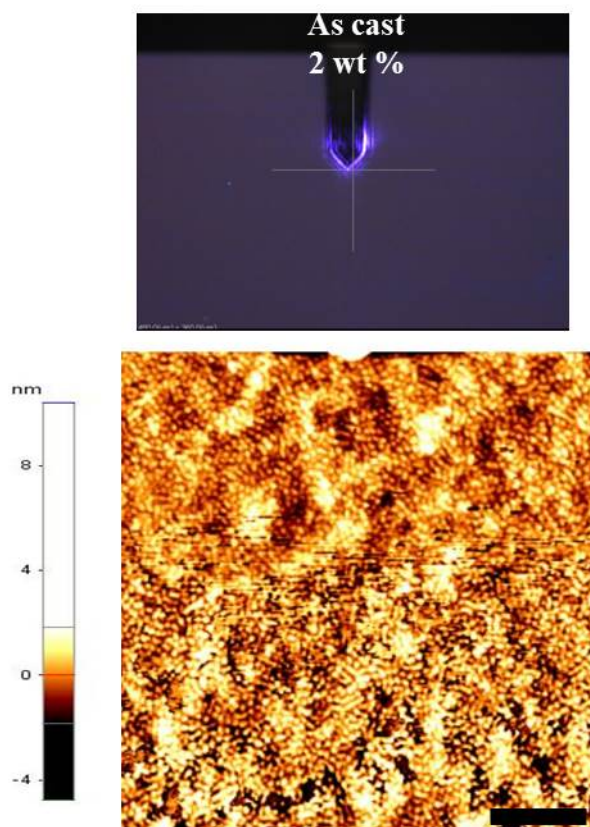


**Figure S5.7.6.** As cast optical image (top) ( $\sim 480 \times 360$  micron) of the PS-*b*-P4VP BCP film following spin coating from a 2 wt % PS-*b*-P4VP solution on an acetone cleaned silicon substrate. AFM topographic image (bottom, scale bar = 400 nm) shows microphase separated structures. The film shows cylinders normal to the substrate, however these have extremely poor order. These films have a distinct purple color.

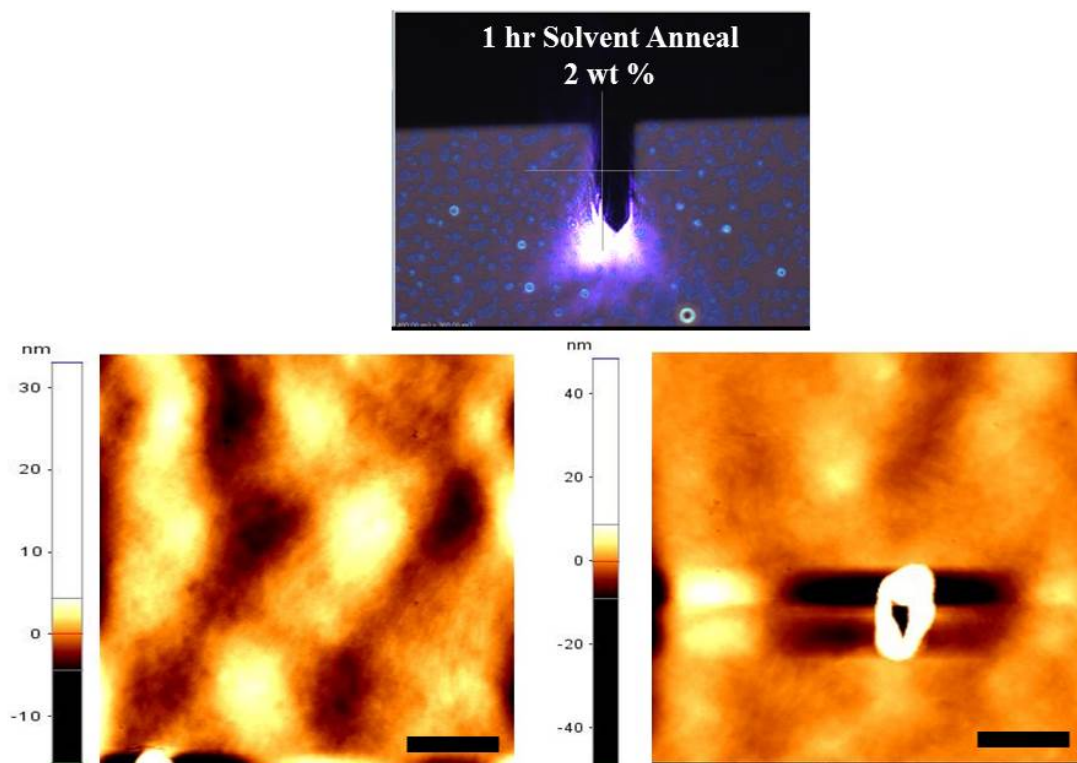


**Figure S5.7.7.** Optical image (top) ( $\sim 480 \times 360$  micron) reveals a non-uniform film following 1 hour of solvent vapor annealing with chloroform from a 2 wt % PS-*b*-P4VP BCP film. The AFM topographic image of the blue area of optical image (bottom left, scale bar = 400 nm) shows a featureless surface with height variation as seen from the height to the left of the image. Also the brown area (AFM image, bottom right, scale bar = 400 nm) reveals a similar topography. The feature in the centre of the image (indicated by arrow) shows a height difference of more than 40 nm.

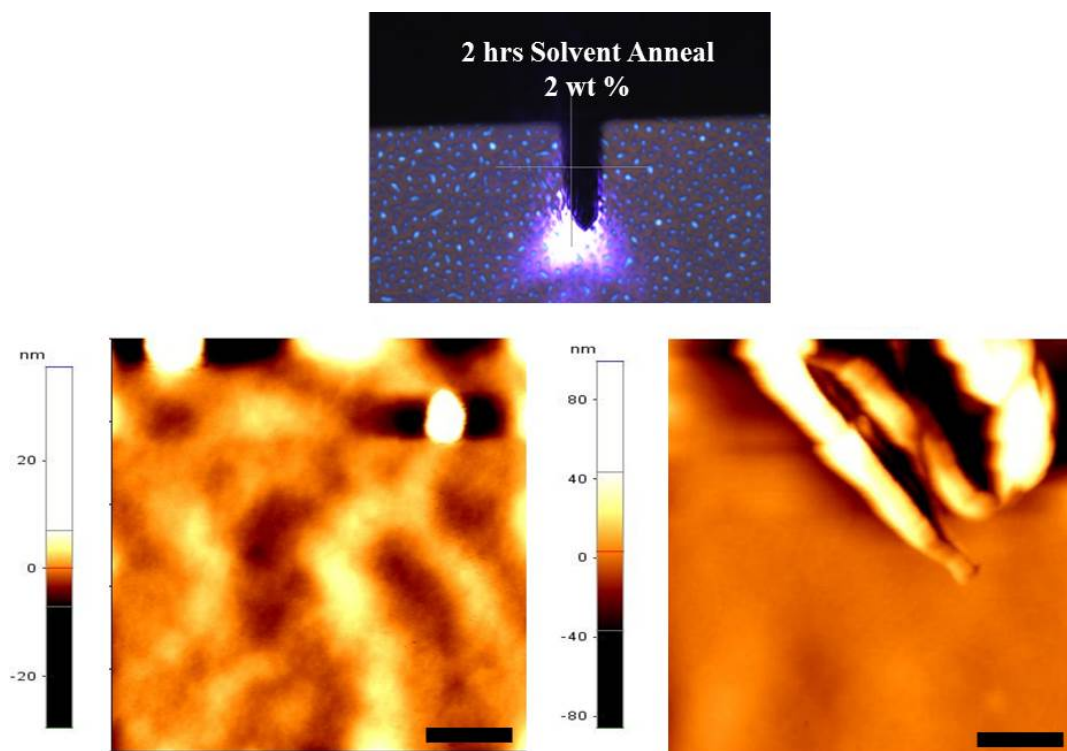


**Figure S5.7.8.** The optical image (top) ( $\sim 480 \times 360$  micron) shows film surface following 2 hours of solvent vapor annealing with chloroform from a 2 wt % PS-*b*-P4VP BCP film. Both AFM topographic images (scale bars = 400 nm) do not show any microphase separated areas. Blue areas (bottom left) and brown areas (bottom right) scanned show relief structures with greater than 50 nm depth in some areas. The film thickness not being an integer of the periodicity of the nanodomain results in such formations.

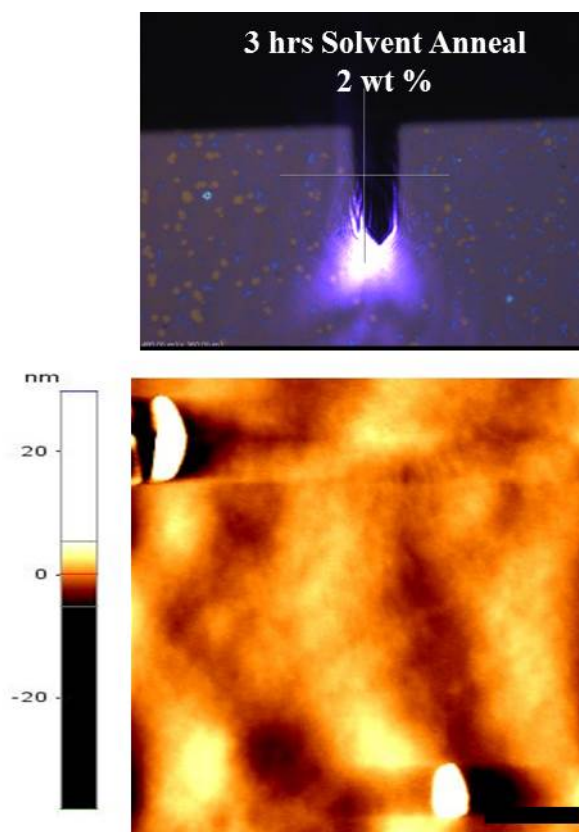


**Figure S5.7.9.** The AFM topographic image (bottom, scale bar = 400 nm) shows featureless areas following 3 hours of solvent vapor annealing with chloroform from a 2 wt % PS-*b*-P4VP BCP film. Microphase separation was absent from the film.

A screening procedure was also carried out with regard to different surface chemistries for the 0.5 wt % PS-*b*-P4VP films and only chloroform was used for SVA at ambient conditions. The contact angles were measured for all modified silicon substrate surfaces (see Figure S5.7.10). Surface chemistries analyzed included ultraviolet/ozone (UV/O<sub>3</sub>) cleaned, piranha cleaned, acetone cleaned, bare Si without any cleaning, PS-OH functionalized and PDMS-OH functionalized silicon. It was found that P4VP C<sub>⊥</sub> to the substrate were formed following spin coating on all surface chemistries studied except for PDMS-OH functionalized silicon surfaces (see Figure S5.7.16c). Although a piranha cleaned silicon surface showed P4VP C<sub>||</sub> after SVA (see Figure S5.7.12d), areas of dewetting are present suggesting that the silicon surface is too hydrophilic and thus the hydrophilic PVP block interaction with the surface causes instability in the thin film.

Likewise, the use of a hydrophobic (PDMS-OH functionalized) silicon surface did not exhibit any microphase separation for spin cast or solvent vapor annealed films (See Figure S5.7.16 c and d).

**Methods and materials for silicon substrate surface chemistry modifications:**

**UV/ozone:** Substrates were placed in UV/ozone system (PSD Pro Series Digital UV Ozone System; Novascan Technologies, Inc., USA) for a 30 minute treatment period.

**Piranha cleaned substrates:** Substrates were placed in a ‘piranha’ bath (sulfuric acid:hydrogen peroxide, 3:1) for 1 hour at 100°C. After piranha cleaning, substrates were cleaned and washed repeatedly with DI water. They were then blown dry under N<sub>2</sub> flow.

**Acetone:** As described in the manuscript, substrates were sonicated in acetone for 20 minutes and blown dry under N<sub>2</sub> flow.

**Bare Si:** Substrates were used as received and no cleaning or modification was employed.

**PS-OH functionalized Si:** Hydroxyl terminated polystyrene (PS-OH) was purchased from Polymer Source, Inc., Canada. The material’s total number average molecular weight  $M_n = 6 \text{ kg mol}^{-1}$  and has a polydispersity of 1.05 and was not further modified. 1 wt % solutions of PS-OH (6k) were made up in toluene and stirred for 1 hour until fully dissolved. ‘Piranha’ cleaned substrates were coated with the 1 wt % PS-OH (6k) solution at 3000 rpm and thermally annealed at 180°C for 6 hours. After annealing, the PS-OH modified films were then rinsed with toluene to remove any ungrafted PS-OH fragments.

**PDMS-OH functionalized Si:** Hydroxyl terminated polydimethylsiloxane (PDMS-OH) was purchased from Polymer Source, Inc., Canada. The material’s total number average molecular weight  $M_n = 5 \text{ kg mol}^{-1}$  and has a polydispersity of 1.07 and was not further modified. 1 wt % solutions of PDMS-OH (5k) were made up in toluene and stirred for 1

hour until fully dissolved. ‘Piranha’ cleaned substrates were coated with the 1 wt % PDMS-OH (6k) solution at 3000 rpm and thermally annealed at 180°C for 6 hours. After annealing, the PDMS-OH modified films were rinsed with toluene to remove any ungrafted PDMS-OH material.

All of the above modified surfaces were coated with a 0.5 wt % PS-*b*-P4VP BCP film and solvent vapor annealed with CHCl<sub>3</sub> vapor at room temperature (i.e., in the manner described in the manuscript).

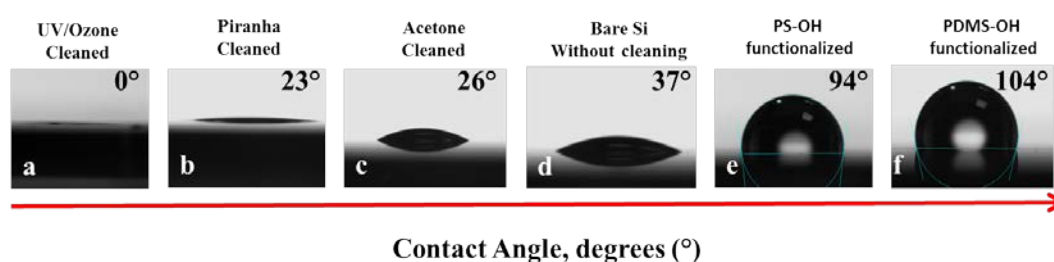


**Figure S5.7.10.** Contact angle (°) images of water droplets on (a) UV/ozone treated cleaned silicon (0°), (b) piranha cleaned silicon (23°), (c) acetone only cleaned silicon (26°), (d) bare silicon without cleaning (37°), (e) PS-OH functionalized silicon (94°) and (f) PDMS-OH functionalized silicon (104°).

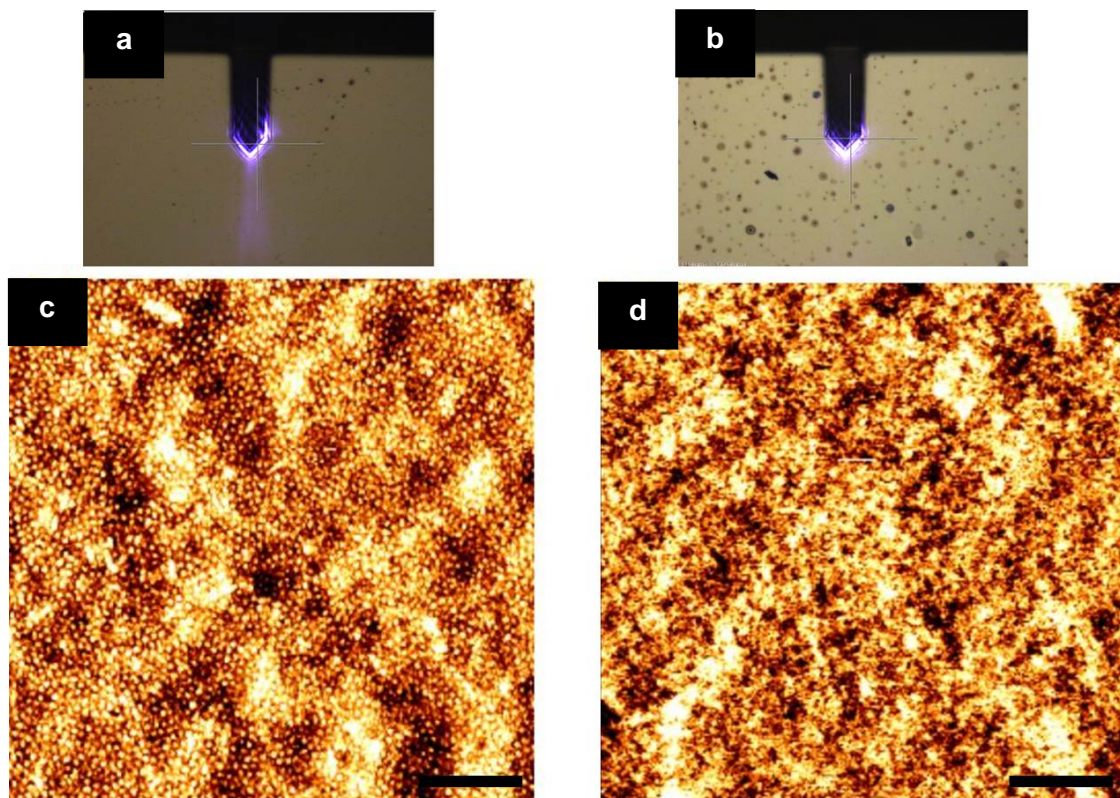


**Figure S5.7.11.** Optical images ( $\sim 480 \times 360$  micron) of (a) as cast 0.5 wt % PS-*b*-P4VP on UV/ozone cleaned silicon sample (contact angle,  $0^\circ$ ) and (b) following 2 hours of solvent vapor annealing with chloroform. Corresponding AFM topographic images (scale bar = 400 nm) are shown in (c) and (d). (c) AFM topographic image of as cast film showing poorly ordered P4VP  $C_{\perp}$  (normal) to the silicon substrate. (d) Following 2 hours solvent vapor annealing, the film is featureless.

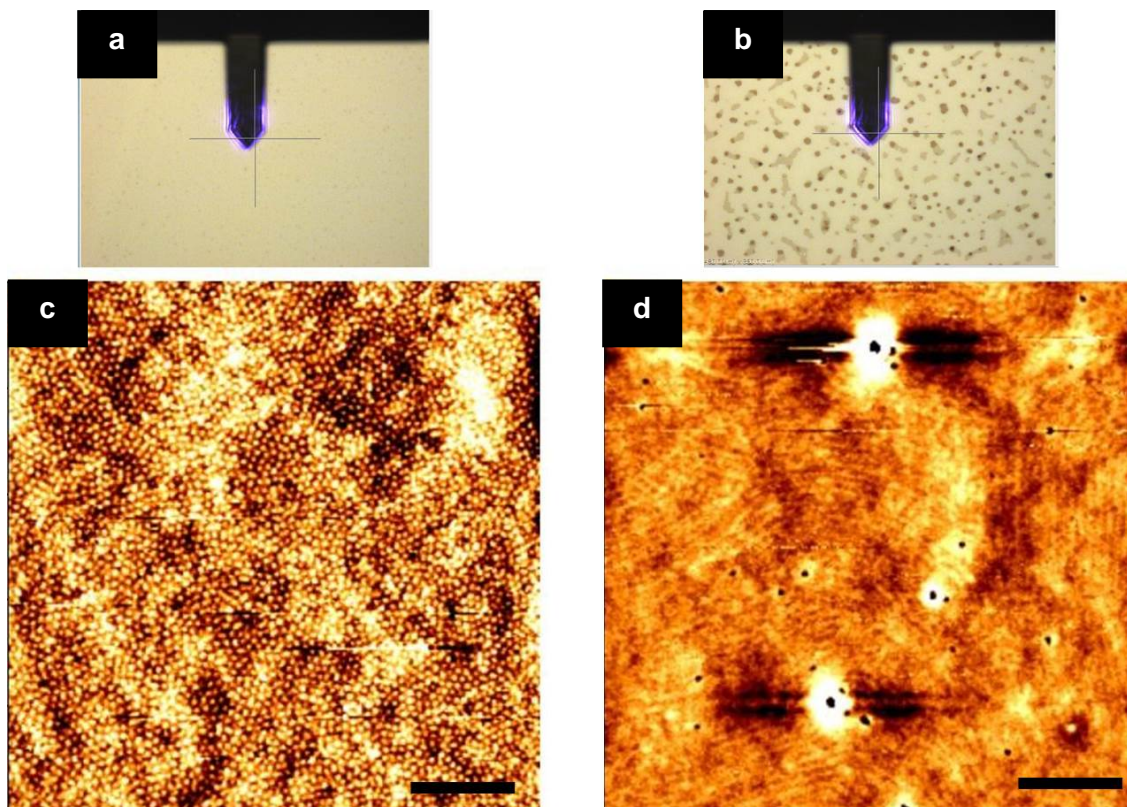


**Figure S5.7.12.** Optical images ( $\sim 480 \times 360$  micron) of (a) as cast 0.5 wt % PS-*b*-P4VP on piranha cleaned silicon sample (contact angle,  $23^\circ$ ) and (b) following 2 hours of solvent vapor annealing with chloroform. Corresponding AFM topographic images (scale bar = 400 nm) are shown in (c) and (d). (c) AFM topographic image of as cast film showing P4VP cylinders normal to the silicon substrate. (d) Following 2 hours solvent vapor annealing, the film shows P4VP cylinders lying in plane. Areas of dewetting can be seen in (d).

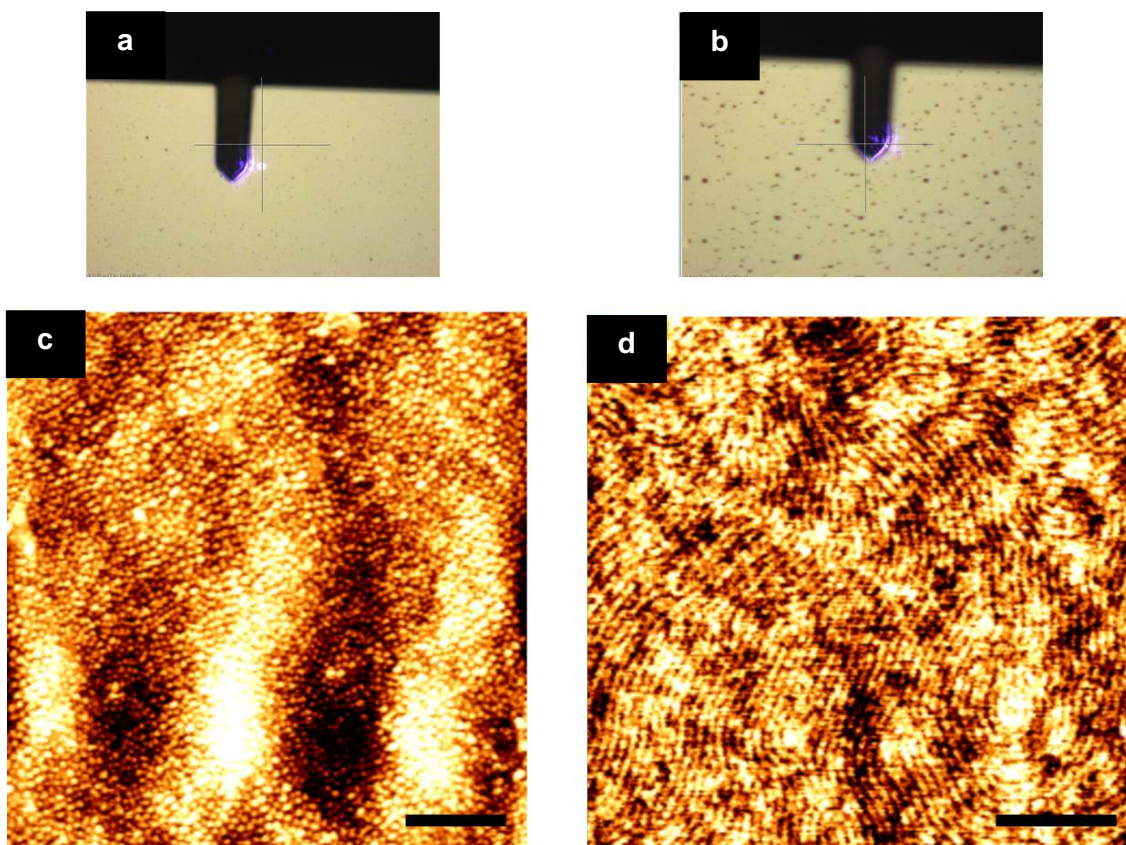


**Figure S5.7.13.** Optical images ( $\sim 480 \times 360$  micron) of (a) as cast 0.5 wt % PS-*b*-P4VP on acetone only cleaned silicon sample (contact angle,  $26^\circ$ ) and (b) following 2 hours of solvent vapor annealing with chloroform. Corresponding AFM topographic image (scale bar = 400 nm) of (a) is shown in (c). (c) AFM topographic image of as cast film showing P4VP cylinders normal to the silicon substrate. Corresponding AFM topographic image of (b) is shown in (d). A fully microphase separated pattern is observed with cylinder lying in plane. Reconstructed image in Figure 5.2 (c) in manuscript corresponds to Figure S5.7.13(d).

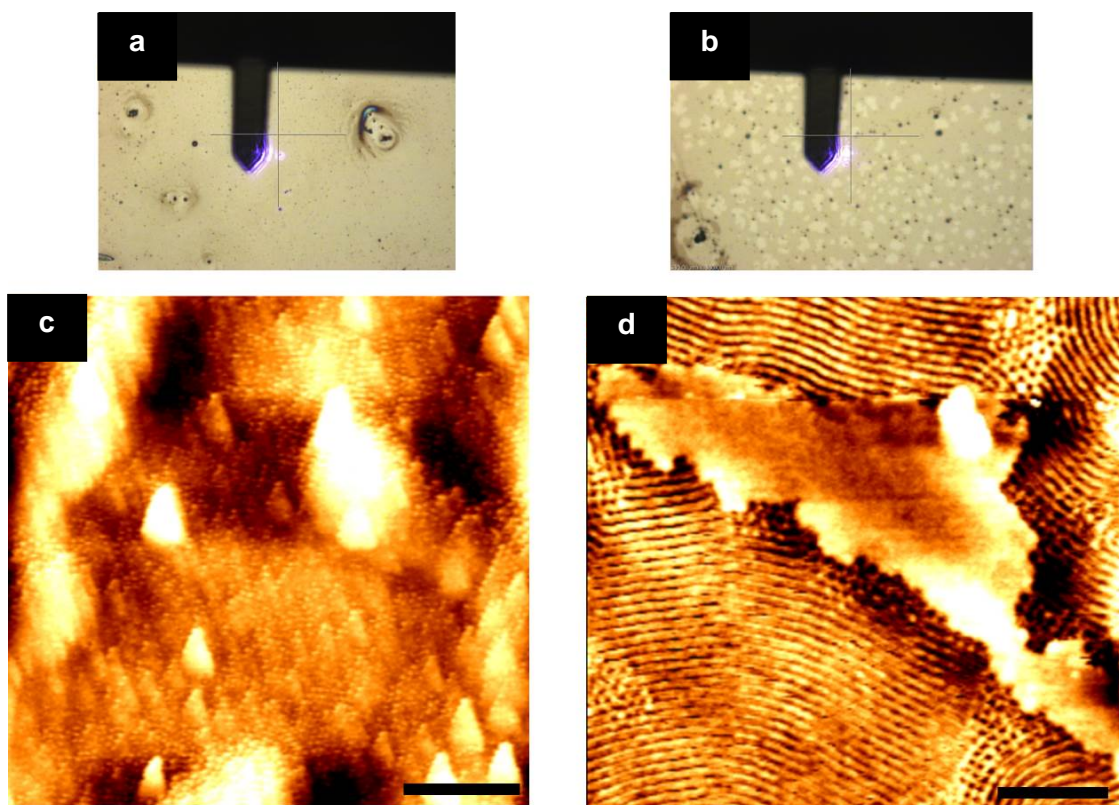


**Figure S5.7.14.** Optical images ( $\sim 480 \times 360$  micron) of (a) as cast 0.5 wt % PS-*b*-P4VP on bare silicon sample without cleaning (contact angle,  $37^\circ$ ) and (b) following 2 hours of solvent vapor annealing with chloroform. Corresponding AFM topographic images (scale bar = 400 nm) are shown in (c) and (d). (c) AFM topographic image of as cast film showing a poorly microphase separated pattern. (d) Following 2 hours solvent vapor annealing, the film shows well developed P4VP cylinders lying in plane. However a large defective area is seen in the AFM image. The non-uniform nature of the solvent vapor annealed film can be seen in the optical image in (b).

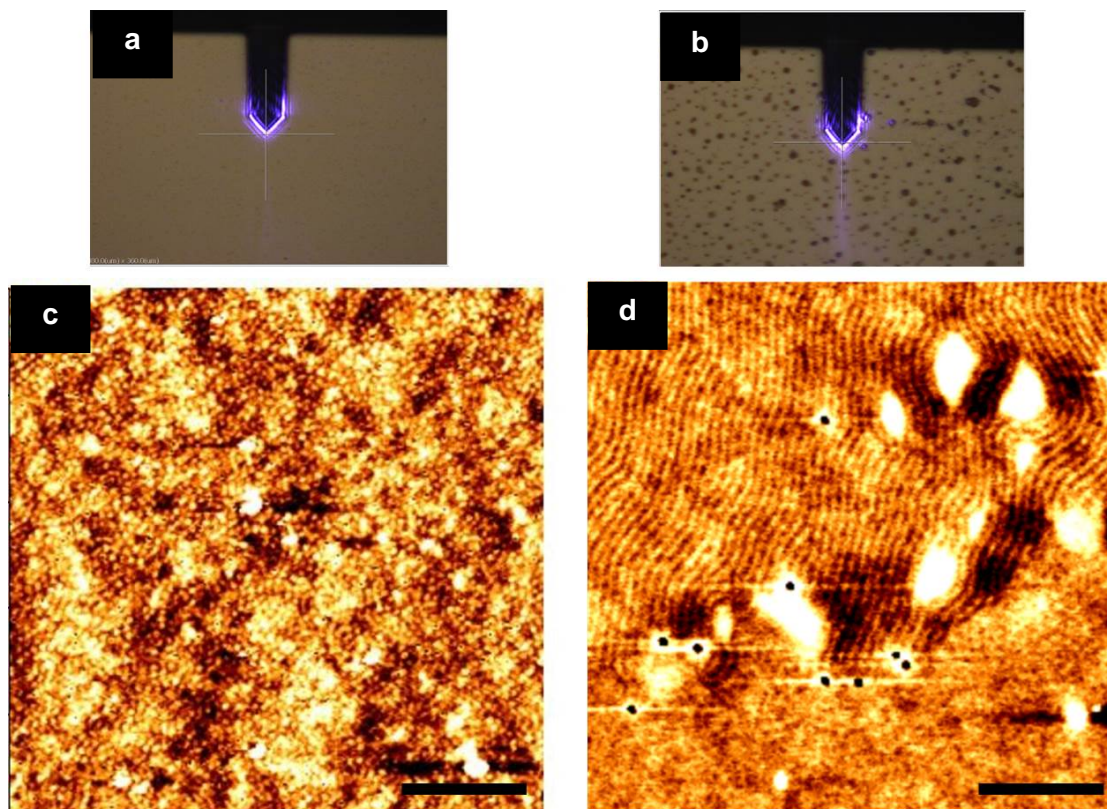


**Figure S5.7.15.** Optical images ( $\sim 480 \times 360$  micron) of (a) as cast 0.5 wt % PS-*b*-P4VP on PS-OH functionalized silicon substrate (contact angle,  $94^\circ$ ) and (b) following 2 hours of solvent vapor annealing with chloroform. Corresponding AFM topographic images (scale bar = 400 nm) are shown in (c) and (d). (c) AFM topographic image of as cast film showing P4VP cylinders normal to the silicon substrate. (d) Following 2 hours solvent vapor annealing, the film shows P4VP cylinders lying in plane. Dewetted areas as well as poorly microphase separated areas are also observed.

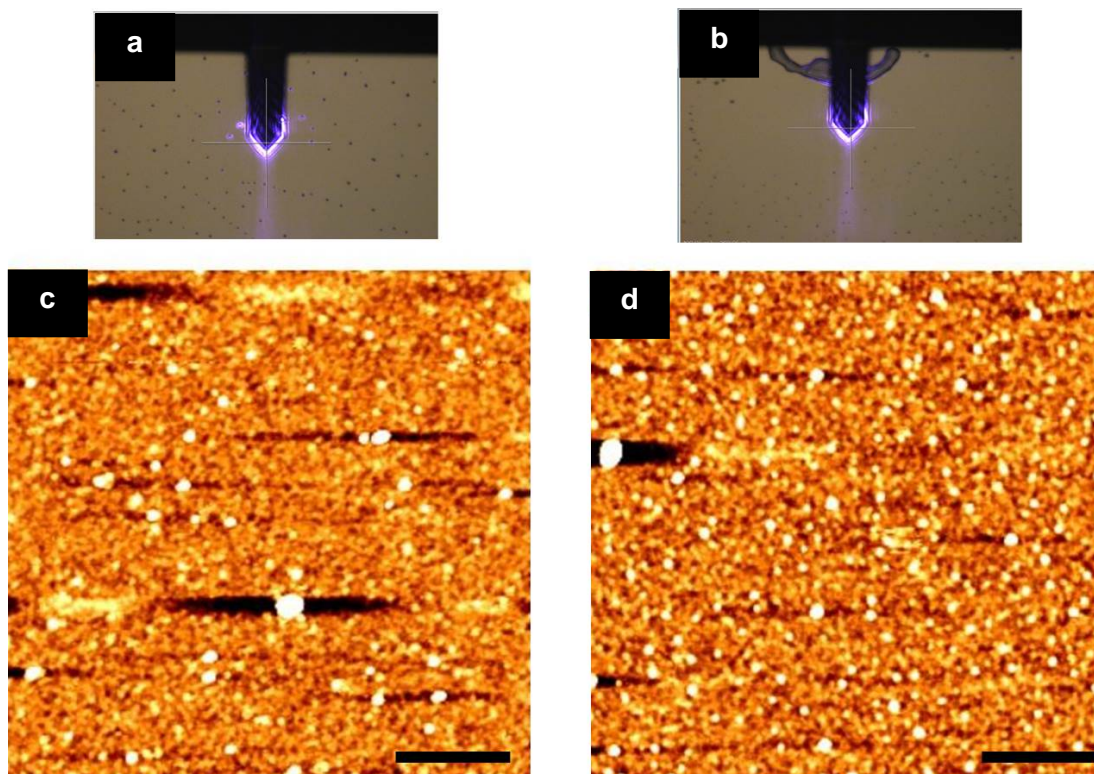


**Figure S5.7.16.** Optical images ( $\sim 480 \times 360$  micron) of (a) as cast 0.5 wt % PS-*b*-P4VP BCP on PDMS-OH functionalized silicon substrate (contact angle,  $104^\circ$ ) and (b) following 2 hours of solvent vapor annealing with chloroform. Corresponding AFM topographic images (scale bar = 400 nm) are shown in (c) and (d). Microphase separation was not observed in either sample, as seen from (c) as cast and (d) solvent vapor annealed.

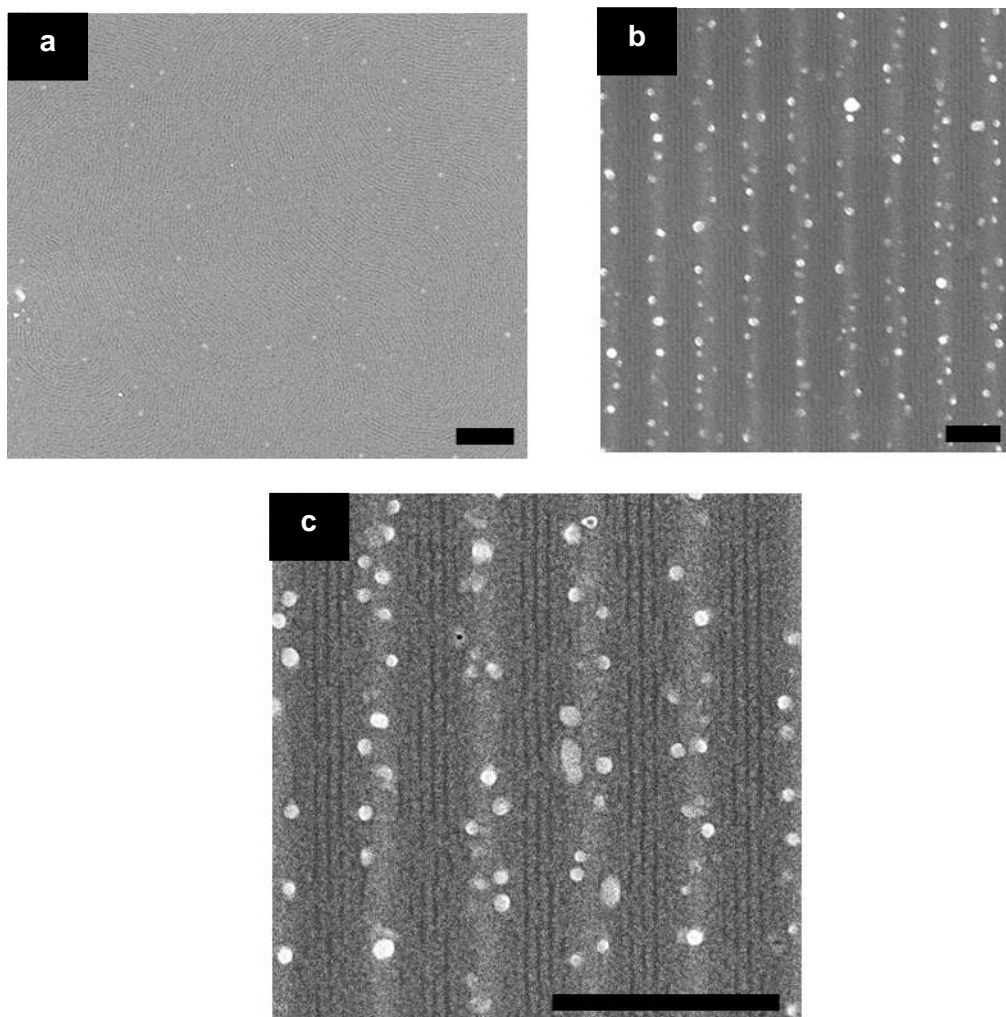


**Figure S5.7.17.** (a) Top-down SEM image of open area on HSQ patterned substrates showing P4VP cylinders lying in plane after self-assembly via solvent vapor annealing. (b) low resolution and (c) high resolution SEM images of P4VP cylinders lying in plane guided by 50 nm wide HSQ gratings at a channel width of 265 nm. Note that all images (a) – (c) were stained with ruthenium tetroxide for contrast purposes. All scale bars = 500 nm.

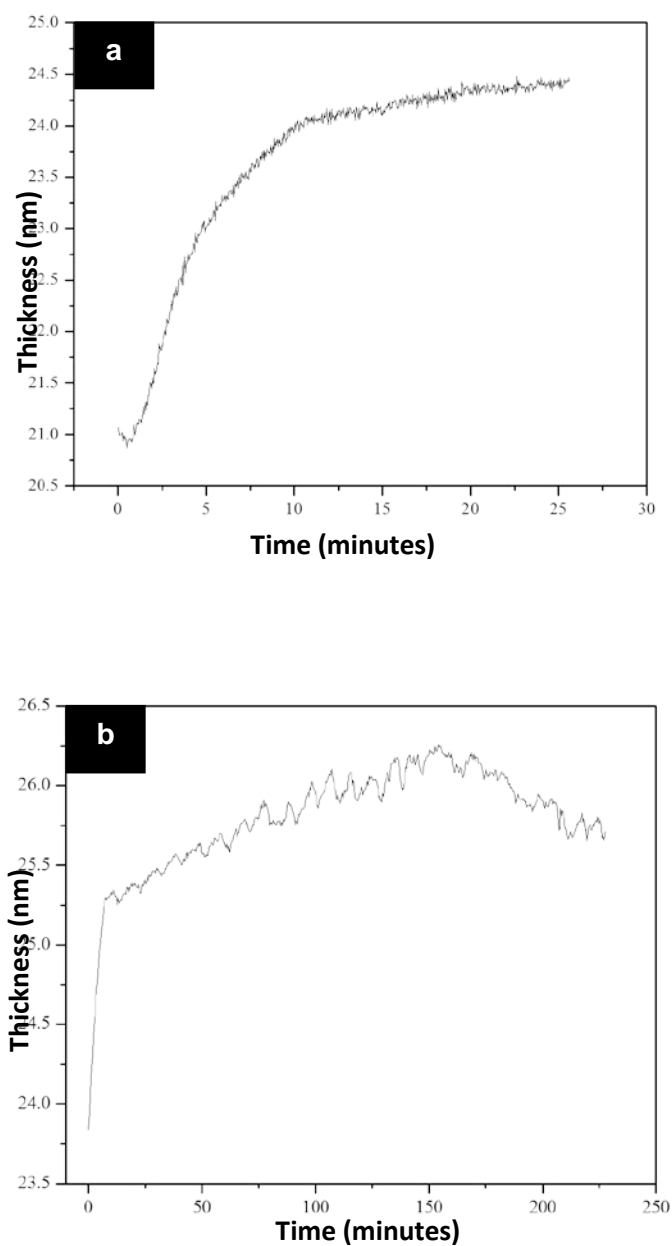


**Figure S5.7.18.** In-situ thickness measurement. Plot of thickness (nm) change versus time (minutes) of 0.5 wt % PS-*b*-P4VP BCP film spin coated on acetone only cleaned silicon followed by annealing with chloroform vapor for (a) 30 minutes and (b) 230 minutes. Both (a) and (b) indicate that the film does not rise more than 15% (~26.5 nm) from its initial thickness (~23nm).

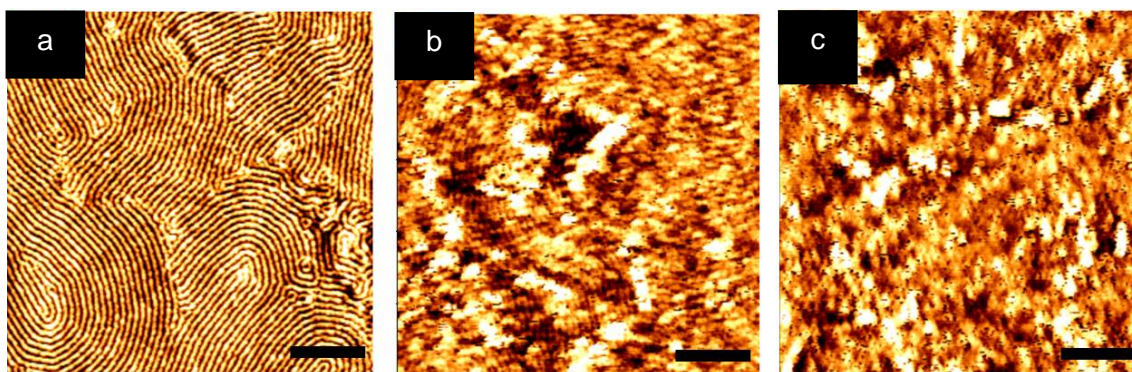


**Figure S5.7.19.** AFM topographic images (scale bars = 400 nm) of PS-*b*-P4VP BCP films following immersion in 10 ml ethanol for (a) 10 minutes, (b) 20 minutes and (c) 30 minutes. (b) and (c) show deformation of the original PS-*b*-P4VP BCP structure due to swelling of the P4VP nanodomains that distort the PS matrix.

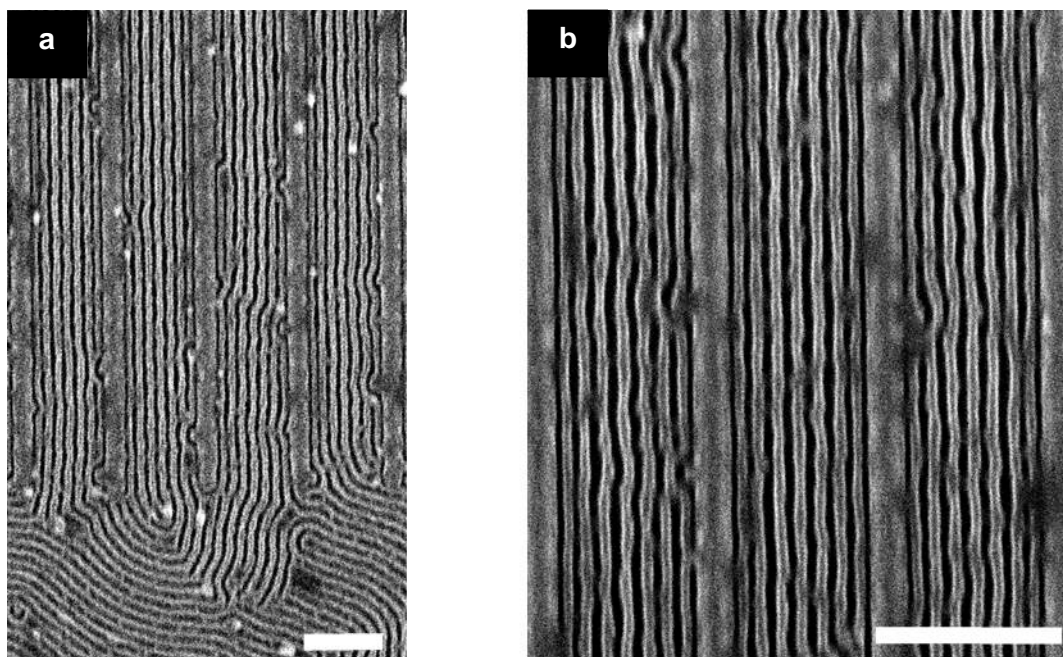


**Figure S5.7.20.** (a) and (b) show top-down SEM images of iron oxide nanowires where 50 nm wide HSQ prepatterns at a channel width of 265 nm that initially aligned PS-*b*-P4VP BCP material. Note that these samples were silicon etched for 5 seconds to improve contrast for SEM. Scale bars = 250 nm.

Figure S5.7.20a and b shows a top-down SEM image of the  $\text{Fe}_3\text{O}_4$  nanowires with long range order. The periodicity of the nanowires and domain size distributions are similar to the original PS-*b*-P4VP self-assembled BCP template. Figure S5.7.20a shows an open area of the substrate that exhibits the “fingerprint” like pattern evidenced on planar substrates. As the pattern enters the trenches alignment takes place guided by the HSQ sidewalls. The alignment and registration of the  $\text{Fe}_3\text{O}_4$  nanowires is shown for up to 2 microns in HSQ trenches with a channel width of 265 nm. A total of 7  $\text{Fe}_3\text{O}_4$  nanowire features can be seen in the SEM image. The high resolution SEM image in Figure S5.7.20b shows well-defined  $\text{Fe}_3\text{O}_4$  nanowire patterns from a 265 nm trench.

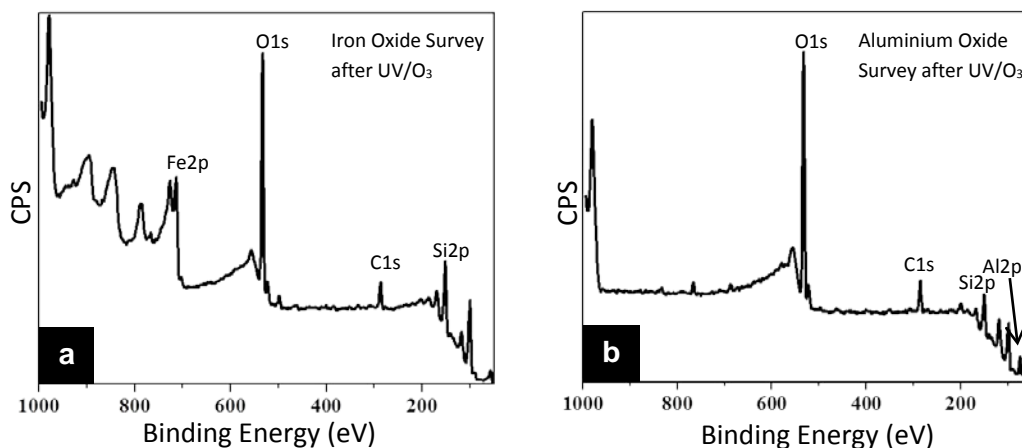


**Figure S5.7.21.** XPS survey spectrum of (a) Fe<sub>3</sub>O<sub>4</sub> nanowires and (b)  $\gamma$ -Al<sub>2</sub>O<sub>3</sub> nanowires formed via spin coating of metal nitrate-ethanolic solutions on porous PS-*b*-P4VP BCP followed by UV/O<sub>3</sub> for 3 hours.

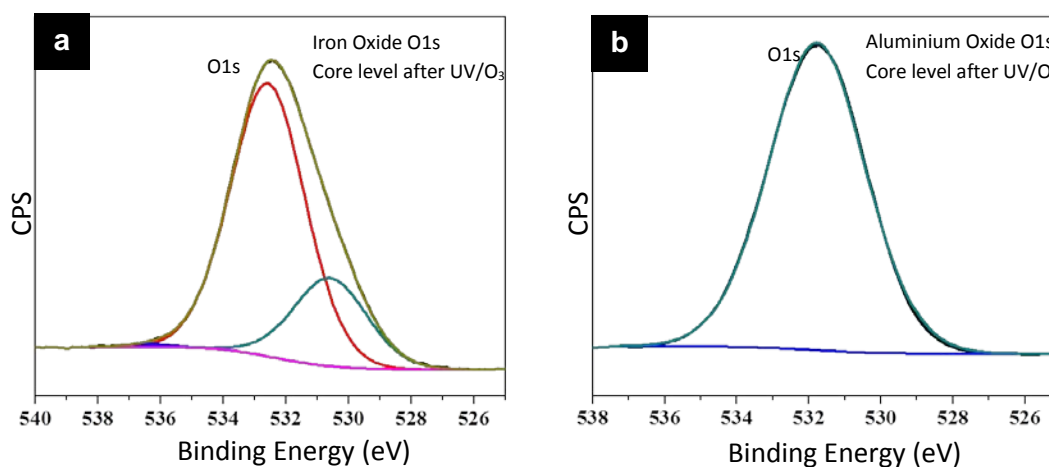


**Figure S5.7.22.** High resolution XPS spectra of O 1s region from (a) Fe<sub>3</sub>O<sub>4</sub> nanowires and (b)  $\gamma$ -Al<sub>2</sub>O<sub>3</sub> nanowires.

---

*Chapter 6*

---

**Solvent vapor annealing of block copolymers in confined topographies: commensurability considerations for nanolithography**

## 6.1. Abstract

The directed self-assembly (DSA) of block copolymer (BCP) materials in topographically patterned substrates (*i.e.* graphoepitaxy) is a potential methodology for the continued scaling of nanoelectronic device technologies. In this chapter, we detail an unusual feature size variation in BCP nanodomains under confinement with graphoepitaxially aligned cylinder-forming poly(styrene)-*block*-poly(4-vinylpyridine) (PS-*b*-P4VP) BCP. Graphoepitaxy of PS-*b*-P4VP BCP line patterns (C<sub>II</sub>) was accomplished via topography in hydrogen silsequioxane (HSQ) modified substrates and solvent vapor annealing (SVA). Interestingly, reduced domain sizes in features close to the HSQ guiding features were observed. The feature size reduction was evident after inclusion of alumina into the P4VP domains followed by pattern transfer to the silicon (Si) substrate. We suggest that this nanodomain size perturbation is due to solvent swelling effects during SVA. We propose that using a commensurability value close to the solvent vapor annealed periodicity will alleviate this issue leading to uniform nanofins.

## 6.2. Introduction

Microphase separation of di-block copolymers (di-BCPs) can form sub-20 nm arrays of spherical, cylindrical, gyroidal and lamellar geometries that have potential in electronic, environmental and energy applications.<sup>1-4</sup> In particular, BCP materials are of significant interest to chip manufacturers for use as on-chip etch masks for patterning future nanoelectronic circuitry.<sup>5,6</sup> In order to align (to a substrate direction) the randomly oriented domain structures that result from microphase separation and, thus, allow the formation of the periodic arrangements needed for development of advanced device technologies such as Fin-type field-effect transistors (FinFETs),<sup>7</sup> directed self-assembly

(DSA) is required. DSA is an absolute pre-requisite to attain the low defect density and overlay accuracy required for industrial integration.<sup>8</sup>

BCP self-assembly can be directed via pre-patterned chemical patterns (chemoepitaxy)<sup>9,10</sup> or using topographical patterns (graphoepitaxy).<sup>11,12</sup> Graphoepitaxy has been exploited in many BCP systems such as PS-*b*-PMMA (PS-*b*-polymethyl methacrylate),<sup>13,14</sup> PS-*b*-PDMS (PS-*b*-polydimethylsiloxane)<sup>15,16</sup> and PS-*b*-PVP.<sup>17,18</sup> DSA of BCP thin films through both thermal annealing<sup>19</sup> and solvent vapor annealing<sup>20</sup> (SVA) has been studied extensively and attention is being given to the selective removal of block components<sup>21,22</sup> or the inclusion of etch contrast agents to facilitate pattern transfer.<sup>23</sup>

Pattern transfer of BCP etch masks is probably the least studied aspect of published nanolithography work but is paramount for obtaining uniform integrated circuit elements.<sup>24,25</sup> This is particularly true for BCP materials with a high Flory-Huggins interaction parameter ( $\chi$ ) such as the PS-*b*-PVP systems ( $\chi = 0.18$  for PS-*b*-P2VP) since they can display low domain sizes.<sup>26,27</sup> This chapter describes an important observation for graphoepitaxially aligned line space features of PS-*b*-P4VP (24 kg mol<sup>-1</sup> – 9.5 kg mol<sup>-1</sup>) BCP system which suggests that SVA of graphoepitaxially aligned patterns may be more complex than often considered.

### 6.3. Experimental

**Solvents.** Acetone (ACS reagent,  $\geq 99.5\%$ ) chloroform (for HPLC,  $\geq 99.9\%$ , contains 0.5-1.0% ethanol as stabilizer), iso-propyl alcohol (LC-MS CHROMASOLV), ethanol (dehydrated, 200 proof), Tetrahydrofuran (inhibitor-free, CHROMASOLV Plus, for

HPLC,  $\geq 99.9\%$ ), Toluene (CHROMASOLV, for HPLC, 99.9%), were purchased from Sigma-Aldrich and used without further purification. De-ionized water was used wherever necessary.

### General Methods.

**Hydrogen silsequioxane (HSQ) substrate preparation.** Ten  $\times$  10 mm bulk Si (100) oriented substrates (nominal resistivity 0.001  $\Omega$  cm) were employed and were first patterned using a HSQ Electron Beam Lithography (Raith e-LiNE plus) process. The substrates were initially degreased via ultrasonication in acetone and iso-propanol (IPA) solutions ( $2 \times 2$  min), dried in flowing nitrogen gas and baked for 2 minutes at 393 K in an ambient atmosphere to remove any residual IPA. The substrates were then spin coated with a 2.4 wt % solution of HSQ (XR-1541 Dow Corning Corp.) in MIBK (methylisobutyl ketone) to produce a  $\sim 50$  nm film of HSQ. The wafer was subsequently baked at 393 K in an ambient atmosphere for 3 minutes prior to transfer to the EBL system for exposure. HSQ arrays of 50 nm wide lines at pitches of  $(32n + 50)$  nm were exposed, where  $n$  is an integer and  $0 < n < 8$ . Note that 32 was chosen as this is the repeating period of the PS-*b*-P4VP microdomains. Following electron beam exposure the samples were developed in an aqueous solution of 0.25 M NaOH, 0.7 M NaCl for 15 seconds, followed by rinsing in flowing DI water for 60 seconds and 15 seconds rinse in IPA. A process flow is shown in the appendix for HSQ fabrication. The samples were then blown dry in flowing nitrogen gas. HSQ gratings were fabricated at pitches of  $\sim 110$ , 145, 175, 205, 240, 270 and 300 nm (*i.e.*  $n = 2, 3, 4, 5, 6, 7$  and 8). The HSQ dimensions, PS-*b*-P4VP and alumina feature size, domain sizes *etc.* were measured through analysis of SEM and TEM images using ImageJ software. Note that the 265 nm ( $n = 8.28$ ) HSQ grating value was higher than the expected 256 nm ( $n = 8$ ) and this variation can be

attributed to a higher exposure dose. Larger HSQ channels were also fabricated at 285 nm and 350 nm as detailed below.

**PS-*b*-P4VP BCP thin film deposition, solvent vapor annealing and film “activation”.** Poly(styrene)-*block*-poly(4-vinylpyridine) was purchased from Polymer Source, Inc., Canada, with a molecular weight of  $M_n = 33.5 \text{ kg mol}^{-1}$  ( $M_{nPS} = 24 \text{ kg mol}^{-1}$ ;  $M_{nP4VP} = 9.5 \text{ kg mol}^{-1}$ ,  $f_{PS} = 0.70$ ), a polydispersity ( $M_w/M_n$ ) of 1.15 (where,  $M_n$  and  $M_w$  are number average and weight average molecular weights) and was used as received. Solutions of 0.5 weight % PS-*b*-P4VP BCP were prepared in toluene/THF (80:20). The solutions were left stirring for 12 hours to ensure complete dissolution. Prior to spin coating planar Si or HSQ substrates were sonicated for 20 minutes with acetone. The substrates were then rinsed in acetone and blown dry with nitrogen. Spin coating of the PS-*b*-P4VP solution was carried out at 3200 rpm for 30 seconds. Solvent vapor annealing was carried out in the conventional manner with a small vial containing 8–10 ml of chloroform placed inside a glass jar (150 ml) with PS-*b*-P4VP sample for ~ 2 hours (room temperature ~ 290 K). After removing samples and leaving excess solvent to evaporate, the solvent vapor annealed films (with a thickness of 25 nm) were further exposed to ethanol vapors for surface reconstruction. In order to create a nanoporous PS-*b*-P4VP film for metal-salt inclusion, films were exposed to ethanol vapors for “activation”. Conventional solvent vapor annealing was carried out by placing the self-assembled PS-*b*-P4VP film in a jar containing a vial with ~8 ml of ethanol solvent. Films were exposed to the ethanol vapors for 15-20 minutes. The films were then removed and left to dry/deswell at room temperature (~ 290 K). The resulting nanoporous line pattern was subsequently spin coated with the aluminium nitrate ethanol solution as described below.

**Metal oxide (alumina) nanowire fabrication.**  $\text{Al}(\text{NO}_3)_3 \cdot 9\text{H}_2\text{O}$  (aluminium nitrate nonahydrate, ACS reagent,  $\geq 98\%$ ) was employed as the metal nitrate salt precursor for inclusion to act as a hardmask (etchstop). Solutions of 0.4 weight %  $\text{Al}(\text{NO}_3)_3 \cdot 9\text{H}_2\text{O}$  were prepared in ethanol and spin-coated on to the ethanol reconstructed samples at 3200 rpm for 30 seconds. Ultraviolet/ozone (UV/ $\text{O}_3$ ) treatment was used to oxidize the precursor and remove polymer. Samples were UV/ $\text{O}_3$  treated in a UV/ozone system (PSD Pro Series Digital UV Ozone System; Novascan Technologies, Inc., USA).

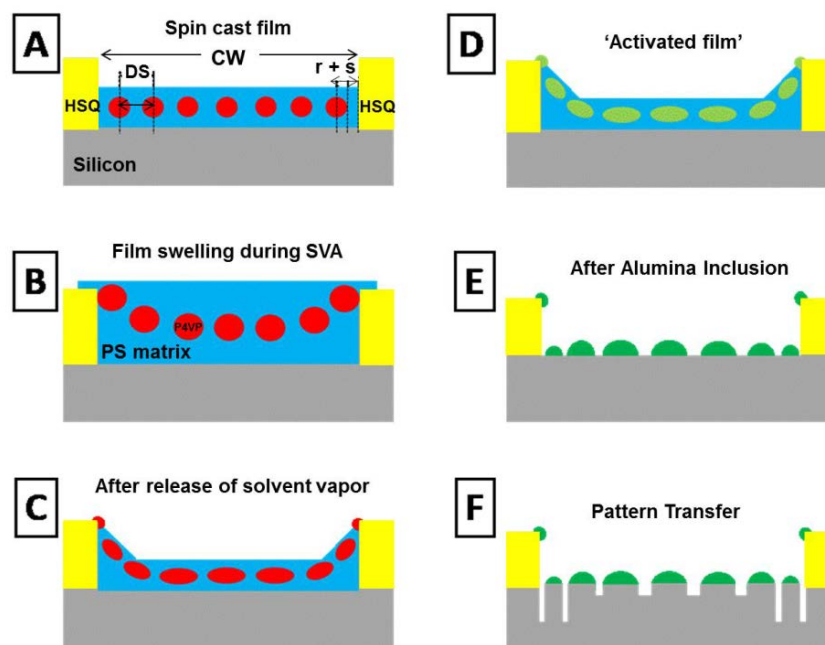
**Pattern Transfer Etch Procedure.** An STS, Advanced Oxide Etch (AOE) ICP etcher was used to pattern transfer alumina nanowires to the underlying Si substrate. Nanofin fabrication was carried out by using a controlled gas mixture of  $\text{C}_4\text{F}_8/\text{SF}_6$  at flow rates of 90 sccm/30 sccm and the ICP and RIE power were set to 600 W and 15 W respectively at a chamber pressure of 15 mTorr. Alumina nanowires were etched using  $\text{C}_4\text{F}_8/\text{SF}_6$  Si etch recipe. Nanofins shown in Figure 6.2.c,d, Figure 6.3. and Figure 6.4. result from a Si etch of 1 minute and 30 seconds. Nanofins shown in Figure 4 were fabricated after using the Si etch for 2 minutes. Note that most of the original HSQ material has been consumed during the etching process and is indicated in TEM images to show initial placement for the reader.

**Instrumentation and Characterization.** Block copolymer film thicknesses were measured with a spectroscopic ellipsometer “J.A. Woollam Ellipsometer” at a fixed angle of incidence of  $70^\circ$ , on at least three different places on the sample and was averaged as the film thickness. A two layer model ( $\text{SiO}_2 + \text{PS-}b\text{-P4VP}$ ) for total BCP film was used to simulate experimental data. Scanning Electron Microscopy (SEM) images were obtained by a FEI Helios Nanolab 600i system at an accelerating voltage of 5 kV and at a working distance of 4 mm. Transmission Electron Microscopy (TEM) lamella specimen were prepared using the Helios NanoLab DB FIB. FIB samples were

analysed by JEOL 2100 high resolution transmission electron microscope operating at an accelerating voltage of 200 kV.

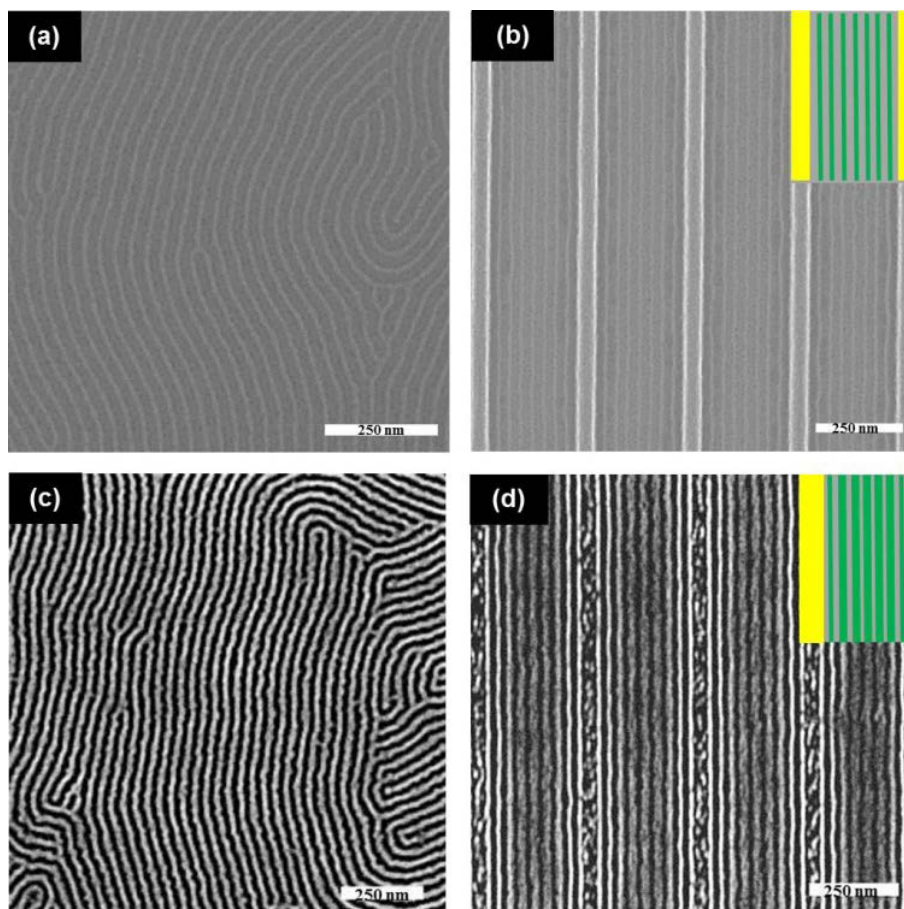
#### 6.4. Results and Discussion

Figure 6.1 outlines the process for fabricating Si nanofins directed in HSQ trenches. Self-assembly of PS-*b*-P4VP BCP thin films was induced via SVA in a chloroform atmosphere at room temperature ( $\sim 290$  K). P4VP cylinders were orientated parallel ( $C_{11}$ ) to the substrate, forming “fingerprint” patterns with a 32 nm periodicity. P4VP cylinder dimensions were measured at 20 nm. These patterns were guided and aligned in HSQ trenches of varying pitch (the nominal HSQ pitch was  $(32n + 50)$  nm where  $n$  is an integer and  $0 < n < 8$ ). An ethanol vapor treatment was employed to “activate” the PS-*b*-P4VP thin film creating a nanoporous structure.<sup>28,29</sup> This process introduces free volume to assist the salt inclusion process.<sup>30,31</sup> The selective inclusion of the salt into the P4VP block of the “activated” nanoporous films was achieved via spin coating of an ethanolic solution of aluminium nitrate. Following deposition of the metal-salt ethanolic precursor, UV/O<sub>3</sub> exposure was carried out for 3 hours leading to the formation of  $\gamma$ -Al<sub>2</sub>O<sub>3</sub> (alumina) nanowires at the substrate surface.



**Figure 6.1.** Outline of the swelling phenomenon occurring during solvent vapor annealing of PS-*b*-P4VP BCP graphoepitaxially aligned by HSQ gratings and fabrication of Si nanofins from side-view perspective. (a) Spin coated PS-*b*-P4VP BCP film, note that ordered equilibrium structures are shown for simplicity. CW = channel width, DS = domain spacing,  $r$  = cylinder radius and  $s$  = half cylinder edge to cylinder edge distance. BCP film shows majority PS (blue) matrix and minority P4VP cylinders (red). (b) Swelling of film and expansion when exposed to chloroform during solvent vapor annealing. (c) PS-*b*-P4VP Film after release of solvent vapor. (d) Exposure to ethanol vapor for 20 minutes during “activation” step to form a nanoporous structure, *i.e.* creating swollen P4VP domains (light green). (e) Fabrication of alumina (dark green) nanowires after spin coating of aluminium nitrate ethanol precursor on nanoporous PS-*b*-P4VP film followed by UV/O<sub>3</sub>. (f) Pattern transfer of alumina nanowire hardmask (etchstop) using dry etch procedure to underlying Si.

Figure 6.2a shows uniform alumina nanowires after metal-oxide inclusion on an open area of the patterned HSQ substrate. Figure 6.2.b displays a top-down SEM image of alumina nanowires graphoepitaxially aligned within  $\sim 50$  nm HSQ gratings with channel widths of  $\sim 265$  nm. Seven alumina nanowire features mimicking the original P4VP structure can be seen. Si nanofins resulting from pattern transfer of the alumina



**Figure 6.2.** Top-down SEM image of (a) large open area of alumina nanowires and (b) alignment of alumina nanowires within channel widths of  $\sim 265$  nm. Green bars represent the alumina nanowires while yellow bars represent the guiding HSQ gratings, see (Figure 6.1.E), (c) open area of Si nanofins following plasma etching of the alumina nanowires on the HSQ patterned Si substrate surface and (d) area of aligned Si nanofins within  $\sim 50$  nm HSQ gratings with channel widths of  $\sim 265$  nm. Note that green bars in (d) represent Si nanofins with alumina mask present on top, see Figure 6.1.F. It is evident that the nanofins closer to the sidewalls are smaller in diameter.

nanowire hardmask from an open area of the HSQ patterned substrate are shown in figure 6.2.c. Figure 6.2.d shows a top-down SEM image corresponding to Si nanofins fabricated from pattern transfer of DSA graphoepitaxy features. Etch recipes for pattern transfer are detailed in the experimental section. It is clear from Figure 6.2.d that the nanofins closest to the sidewall are considerably smaller in feature size than the five nanofins in the centre of the channel (feature sizes of 6 and 12 nm respectively).

The occurrence of this reduction in feature sizes was observed in several areas of HSQ arrays (10 x 10 micron each) and across varying HSQ periodicities (>100 nm). Figure 6.3 displays top-down SEM images of Si nanofins in 128 nm and 224 nm channel widths where sidewall nanofin feature size reduction is evident.

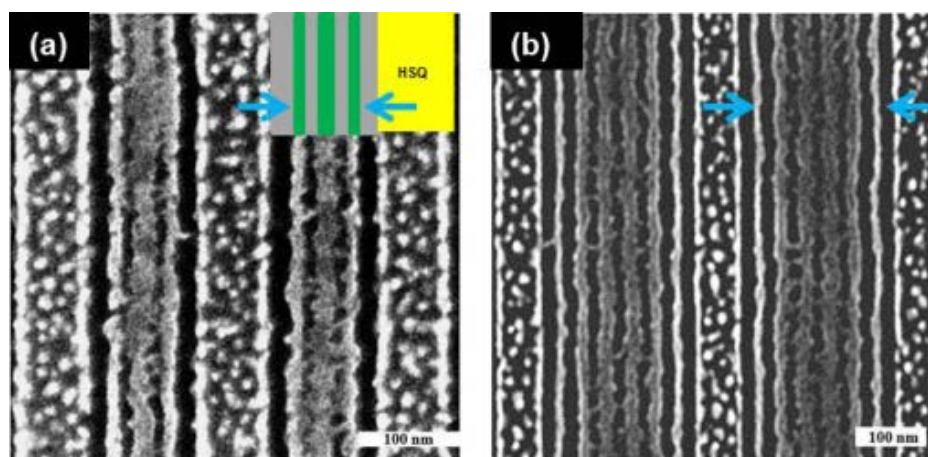


**Figure 6.3.** Top-down SEM image of (a) 3 Si nanofins within 128 nm HSQ gratings and (b) 6 Si nanofins within 224 nm HSQ gratings. Nanofins aligned next to the HSQ gratings show reduced feature sizes in comparison to the remaining Si nanofins. Green lines in (a) represent Si nanofins with alumina mask present on top. Arrows in (a) and (b) point to the reduced feature sizes of nanofins next to HSQ gratings.

As mentioned, this is in contrast to the uniform nanofins made on planar substrate areas, as there is no variation in feature size (figure 6.2.c). Also, there was no variation in feature size observed with Si etch time. Corresponding TEM data of the Si nanofins from the ~ 265 nm arrays (Figure 6.2.d) are displayed in Figure 6.4. following pattern transfer to the substrate and it is clear that the alumina nanowires closest to the HSQ sidewalls have produced deeper Si nanofins (up to ~ 15 nm) than the nanofins at the centre of the channel, which is consistent with enhanced etching in the more confined space.

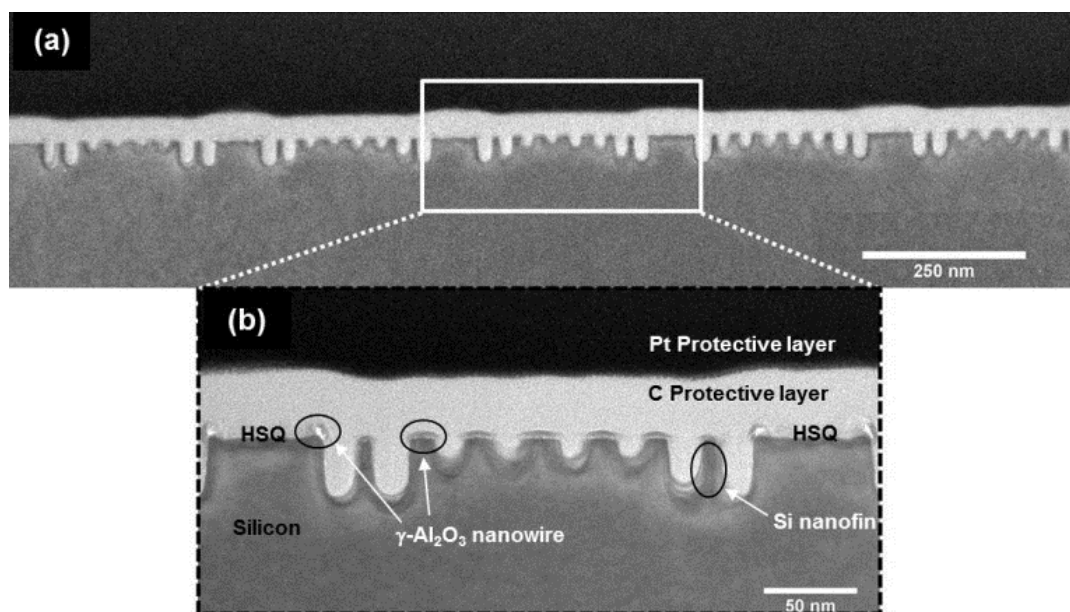


**Figure 6.4.** (a) Cross-section TEM image of large area of Si nanofins following pattern transfer of alumina nanowire hardmask in channel widths of  $\sim 265$  nm and 50 nm HSQ gratings. (b) High resolution TEM image of Si nanofins between HSQ gratings where the reduced Si nanofin feature size and increased etch depth at the HSQ sidewalls is evident.

To further show that this feature size variation was not a direct result of either the etch procedure or geometry related etch effects, we show data for pattern transfer of the BCP metal oxide enhanced structures formed in channels of  $\sim 285$  nm and  $\sim 350$  nm respectively (Figures 6.5.a and 6.5.b). These widths are too large for good DSA and a non-aligned arrangement is observed. An indicative TEM image is displayed in figure 4c of Si nanofins fabricated via pattern transfer (350 nm channels) in confinement of aligned patterns only.

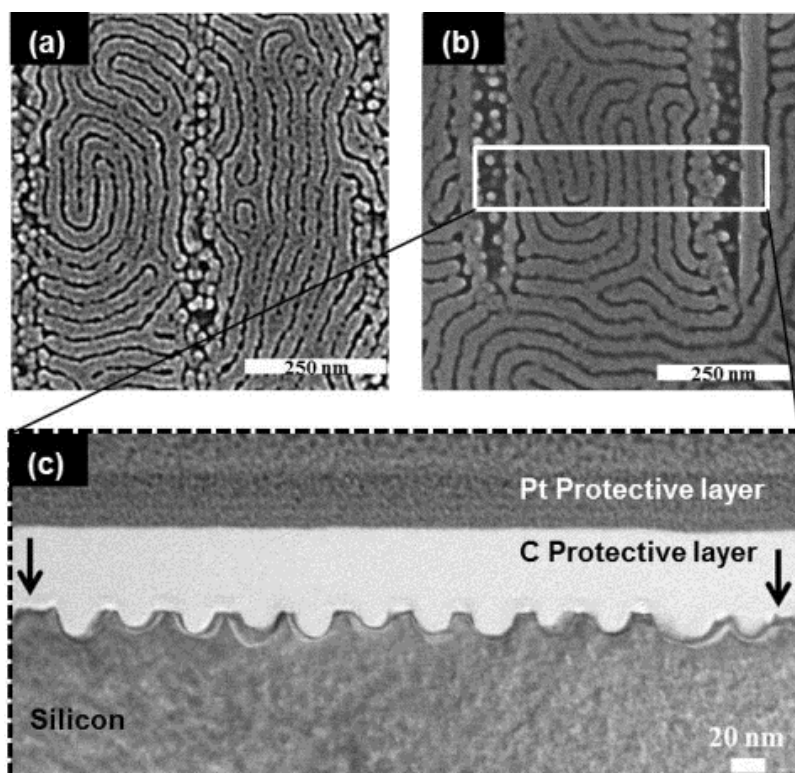


**Figure 6.5.** Top-down SEM images of Si nanofins in HSQ trenches of (a)  $\sim 285$  nm and (b)  $\sim 350$  nm respectively. (c) Cross-section TEM of Si nanofins fabricated from alumina nanowires acting as a hardmask in HSQ trenches. Arrows in (c) indicate where HSQ gratings were prior to etching.

To explain the observations we suggest that the solvent swelling that occurs during SVA is the cause of these complex structures. The dimensions of the channels were set according to the dimensions of the pattern seen on planar surfaces after solvent induced microphase separation. This is explained in Figure 6.1A and is set at number of domain spacings (DS) plus  $2(r+s)$  where  $r$  = cylinder radius and  $s$  = half cylinder edge to cylinder edge distance. Thus, the guiding channels employed were set at  $32n$  (where  $0 > n > 8$ ) nm. Whilst this approach is established for thermally annealed systems where polymer expansion is limited, in SVA there is a considerable expansion due to solvent swelling and this results in both film expansion and non-ideal feature spacing (Figure 6.1.B). The expansion might result in curvature at the side walls in the plane of the cylinders to allow optimum cylinder separation and also due to sidewall-polymer interfacial interactions.

We have shown previously that removal from the solvent atmosphere results in rapid film shrinkage and residual material at sidewalls as the solvent front moves rapidly through the film.<sup>32</sup> A direct result is a change in cylinder shape from a cylindrical to an elliptical cross-section.<sup>33,34</sup> The shape of the film in the channel results in a tilt of the cylinders close to the sidewall after the release of solvent following SVA (Figure 6.1.C). In certain instances, this might result in polymer being isolated at the top of the channel walls due to the additional binding at these edge sites. In Figure 6.1.D, ethanol is used to selectively swell the P4VP domains (see experimental for details) to create a nanoporous matrix assisting the metal-salt inclusion technique. In Figure 6.1.E the results of metal ion oxidation and polymer removal can be seen and in particular reduction of the alumina dimensions because of the smaller footprint (due to elliptical tilting and also partial volume reduction with material remaining at the edge of the mesa) of the P4VP derived feature. On pattern transfer (Figure 6.1.F), the narrow alumina features provide thinner Si features. Also because of the smaller dimensions, an enhanced etch rate (compared to the larger features) is observed due to gas confinement and aspect-ratio dependent etching (ARDE). It is quite apparent that the features are not only narrower but deeper into the substrate from TEM data (figure 6.4.). The enhanced etching of Si material near the HSQ gratings in figure 6.4 may be a direct result of the wider dimensions of the HSQ itself (with respect to the alumina nanowires). Furthermore, ARDE and other plasma issues are visible at the larger alumina features as these have produced a smaller aspect ratio in comparison to the sidewall alumina features. One can see that the proximity of the larger alumina mask features has resulted in a slower etch. The non-uniformity of the resultant Si etch that has led to an enhanced etching rate at the edges may be due to micro-trenching at the larger HSQ features and could be alleviated through process flows integrating passivation methods. Employing passivated Si etches

(e.g. pulsed-mode or mixed mode) can improve anisotropy of the Si etch<sup>35</sup> while protecting sidewall features.

## 6.5. Conclusions

The work presented in this chapter has significant importance in the application of BCP methods for producing ultra-fine features at substrates requiring the use of polymers that can only be annealed by solvent treatment. In nanolithography, methods must be developed that not only produce translational periodicity but also precisely and reproducibly create features of uniform dimensions. This work suggests feature size variation may be more challenging than expected. In order to alleviate the issues observed we believe trenches that are larger than the ideal commensurability (domain periodicity) of the BCP may be needed to allow for extra swelling. The additional “expansion” volume will be dependent on the degree of swelling which will be related to the solvent-polymer interactions, vapor pressure and temperature.

## 6.6. References

- (1) Farrell, R. A.; Petkov, N.; Morris, M. A.; Holmes, J. D. Self-assembled templates for the generation of arrays of 1-dimensional nanostructures: From molecules to devices. *Journal of Colloid and Interface Science* **2010**, *349*, 449-472.
- (2) Bang, J.; Jeong, U.; Ryu, D. Y.; Russell, T. P.; Hawker, C. Block copolymer nanolithography: Translation of molecular level control to nanoscale patterns. *Advanced Materials* **2009**, *21*, 4769-4792.
- (3) Hillmyer, M.: Nanoporous Materials from Block Copolymer Precursors. In *Block Copolymers II*; Abetz, V., Ed.; Advances in Polymer Science; Springer Berlin Heidelberg, **2005**; Vol. 190; pp 137-181.
- (4) Topham, P. D.; Parnell, A. J.; Hiorns, R. C. Block copolymer strategies for solar cell technology. *Journal of Polymer Science Part B: Polymer Physics* **2011**, *49*, 1131-1156.
- (5) Morris, M. A. Directed self-assembly of block copolymers for nanocircuitry fabrication. *Microelectronic Engineering* **2015**, *132*, 207-217.
- (6) Gay, G.; Baron, T.; Agraffeil, C.; Salhi, B.; Chevolleau, T.; Cunge, G.; Grampeix, H.; Tortai, J. H.; Martin, F.; Jalaguier, E.; Salvo, B. D. CMOS compatible strategy based on selective atomic layer deposition of a hard mask for transferring block copolymer lithography patterns. *Nanotechnology* **2010**, *21*, 435301.

- (7) Jeong, S.-J.; Kim, J. Y.; Kim, B. H.; Moon, H.-S.; Kim, S. O. Directed self-assembly of block copolymers for next generation nanolithography. *Materials Today* **2013**, *16*, 468-476.
- (8) Doerk, G. S.; Liu, C.-C.; Cheng, J. Y.; Rettner, C. T.; Pitera, J. W.; Krupp, L. E.; Topuria, T.; Arellano, N.; Sanders, D. P. Pattern Placement Accuracy in Block Copolymer Directed Self-Assembly Based on Chemical Epitaxy. *ACS Nano* **2012**, *7*, 276-285.
- (9) Stoykovich, M. P.; Kang, H.; Daoulas, K. C.; Liu, G.; Liu, C.-C.; de Pablo, J. J.; Müller, M.; Nealey, P. F. Directed Self-Assembly of Block Copolymers for Nanolithography: Fabrication of Isolated Features and Essential Integrated Circuit Geometries. *ACS Nano* **2007**, *1*, 168-175.
- (10) Delgadillo, P. A. R.; Gronheid, R.; Thode, C. J.; Wu, H.; Cao, Y.; Neisser, M.; Somervell, M.; Nafus, K.; Nealey, P. F. Implementation of a chemo-epitaxy flow for directed self-assembly on 300-mm wafer processing equipment. *Journal of Micro/Nanolithography, MEMS, and MOEMS* **2012**, *11*, 031302.
- (11) Hobbs, R. G.; Petkov, N.; Holmes, J. D. Semiconductor nanowire fabrication by bottom-up and top-down paradigms. *Chemistry of Materials* **2012**, *24*, 1975-1991.
- (12) Bitá, I.; Yang, J. K. W.; Jung, Y. S.; Ross, C. A.; Thomas, E. L.; Berggren, K. K. Graphoepitaxy of Self-Assembled Block Copolymers on Two-Dimensional Periodic Patterned Templates. *Science* **2008**, *321*, 939-943.
- (13) Tsai, H.; Pitera, J. W.; Miyazoe, H.; Bangsaruntip, S.; Engelmann, S. U.; Liu, C.-C.; Cheng, J. Y.; Bucchignano, J. J.; Klaus, D. P.; Joseph, E. A.; Sanders, D. P.; Colburn, M. E.; Guillorn, M. A. Two-Dimensional Pattern Formation Using Graphoepitaxy of PS-*b*-PMMA Block Copolymers for Advanced FinFET Device and Circuit Fabrication. *ACS Nano* **2014**, *8*, 5227-5232.
- (14) Borah, D.; Rassapa, S.; Shaw, M. T.; Hobbs, R. G.; Petkov, N.; Schmidt, M.; Holmes, J. D.; Morris, M. A. Directed self-assembly of PS-*b*-PMMA block copolymer using HSQ lines for translational alignment. *Journal of Materials Chemistry C* **2013**, *1*, 1192-1196.
- (15) Borah, D.; Rasappa, S.; Senthamaraiannan, R.; Holmes, J. D.; Morris, M. A. Graphoepitaxial Directed Self-Assembly of Polystyrene-Block-Polydimethylsiloxane Block Copolymer on Substrates Functionalized with Hexamethyldisilazane to Fabricate Nanoscale Silicon Patterns. *Advanced Materials Interfaces* **2014**, *1*.
- (16) Hobbs, R. G.; Farrell, R. A.; Bolger, C. T.; Kelly, R. A.; Morris, M. A.; Petkov, N.; Holmes, J. D. Selective Sidewall Wetting of Polymer Blocks in Hydrogen Silsesquioxane Directed Self-Assembly of PS-*b*-PDMS. *ACS Applied Materials & Interfaces* **2012**, *4*, 4637-4642.
- (17) Chai, J.; Wang, D.; Fan, X.; Buriak, J. M. Assembly of aligned linear metallic patterns on silicon. *Nature Nanotechnology* **2007**, *2*, 500-506.
- (18) Park, S.; Kim, B.; Yavuzcetin, O.; Tuominen, M. T.; Russell, T. P. Ordering of PS-*b*-P4VP on Patterned Silicon Surfaces. *ACS Nano* **2008**, *2*, 1363-1370.
- (19) Bates, C. M.; Maher, M. J.; Janes, D. W.; Ellison, C. J.; Willson, C. G. Block Copolymer Lithography. *Macromolecules* **2013**, *47*, 2-12.
- (20) Sinturel, C.; Vayer, M.; Morris, M.; Hillmyer, M. A. Solvent Vapor Annealing of Block Polymer Thin Films. *Macromolecules* **2013**, *46*, 5399-5415.
- (21) Cummins, C.; Mokarian-Tabari, P.; Holmes, J. D.; Morris, M. A. Selective etching of polylactic acid in poly(styrene)-*block*-poly(d,l)lactide diblock copolymer for nanoscale patterning. *Journal of Applied Polymer Science* **2014**, *131*.

- (22) Olayo-Valles, R.; Lund, M. S.; Leighton, C.; Hillmyer, M. A. Large area nanolithographic templates by selective etching of chemically stained block copolymer thin films. *Journal of Materials Chemistry* **2004**, *14*, 2729-2731.
- (23) Cummins, C.; Borah, D.; Rasappa, S.; Chaudhari, A.; Ghoshal, T.; O'Driscoll, B. M. D.; Carolan, P.; Petkov, N.; Holmes, J. D.; Morris, M. A. Self-assembly of polystyrene-*b*-poly(4-vinylpyridine) block copolymer on molecularly functionalized silicon substrates: fabrication of inorganic nanostructured etchmask for lithographic use. *Journal of Materials Chemistry C* **2013**, *1*, 7941-7951.
- (24) Gu, X.; Gunkel, I.; Russell, T. P. Pattern transfer using block copolymers. *Philosophical Transactions of the Royal Society A: Mathematical, Physical and Engineering Sciences* **2013**, 371.
- (25) Borah, D.; Shaw, M. T.; Rasappa, S.; Farrell, R. A.; Mahony, C. O.; Faulkner, C. M.; Bosea, M.; Gleeson, P.; Holmes, J. D.; Morris, M. A. Plasma etch technologies for the development of ultra-small feature size transistor devices. *Journal of Physics D: Applied Physics* **2011**, *44*, 174012.
- (26) Gu, X.; Liu, Z.; Gunkel, I.; Chourou, S. T.; Hong, S. W.; Olynick, D. L.; Russell, T. P. High Aspect Ratio Sub-15 nm Silicon Trenches From Block Copolymer Templates. *Advanced Materials* **2012**, *24*, 5688-5694.
- (27) Gu, X.; Dorsey, P.; Russell, T. P. High density and large area arrays of silicon oxide pillars with tunable domain size for mask etch applications. *Advanced Materials* **2012**, *24*, 5505-5511.
- (28) Bhoje Gowd, E.; Nandan, B.; Vyas, M. K.; Bigall, N. C.; Eychmüller, A.; Schlörb, H.; Stamm, M. Highly ordered palladium nanodots and nanowires from switchable block copolymer thin films. *Nanotechnology* **2009**, *20*.
- (29) Ghoshal, T.; Senthamaraikannan, R.; Shaw, M. T.; Holmes, J. D.; Morris, M. A. Fabrication of ordered, large scale, horizontally-aligned Si nanowire arrays based on an in situ hard mask block copolymer approach. *Advanced Materials* **2014**, *26*, 1207-1216.
- (30) Kim, S. H.; Misner, M. J.; Yang, L.; Gang, O.; Ocko, B. M.; Russell, T. P. Salt complexation in block copolymer thin films. *Macromolecules* **2006**, *39*, 8473-8479.
- (31) Ghoshal, T.; Shaw, M. T.; Bolger, C. T.; Holmes, J. D.; Morris, M. A. A general method for controlled nanopatterning of oxide dots: a microphase separated block copolymer platform. *Journal of Materials Chemistry* **2012**, *22*, 12083-12089.
- (32) Fitzgerald, T. G.; Farrell, R. A.; Petkov, N.; Bolger, C. T.; Shaw, M. T.; Charpin, J. P. F.; Gleeson, J. P.; Holmes, J. D.; Morris, M. A. Study on the Combined Effects of Solvent Evaporation and Polymer Flow upon Block Copolymer Self-Assembly and Alignment on Topographic Patterns. *Langmuir* **2009**, *25*, 13551-13560.
- (33) Borah, D.; Shaw, M. T.; Holmes, J. D.; Morris, M. A. Sub-10 nm Feature Size PS-*b*-PDMS Block Copolymer Structures Fabricated by a Microwave-Assisted Solvothermal Process. *ACS Applied Materials & Interfaces* **2013**, *5*, 2004-2012.
- (34) O'Driscoll, B. M. D.; Kelly, R. A.; Shaw, M.; Mokarian-Tabari, P.; Lontos, G.; Ntetsikas, K.; Avgeropoulos, A.; Petkov, N.; Morris, M. A. Achieving structural control with thin polystyrene-*b*-polydimethylsiloxane block copolymer films: The complex relationship of interface chemistry, annealing methodology and process conditions. *European Polymer Journal* **2013**, *49*, 3445-3454.
- (35) Henry, M. D. ICP Etching of Silicon for Micro and Nanoscale Devices. *PhD Thesis* **2010**, California Institute of Technology.

## 6.7. Appendix – Chapter 6

### Solvent vapor annealing of block copolymers in confined topographies: commensurability considerations for nanolithography

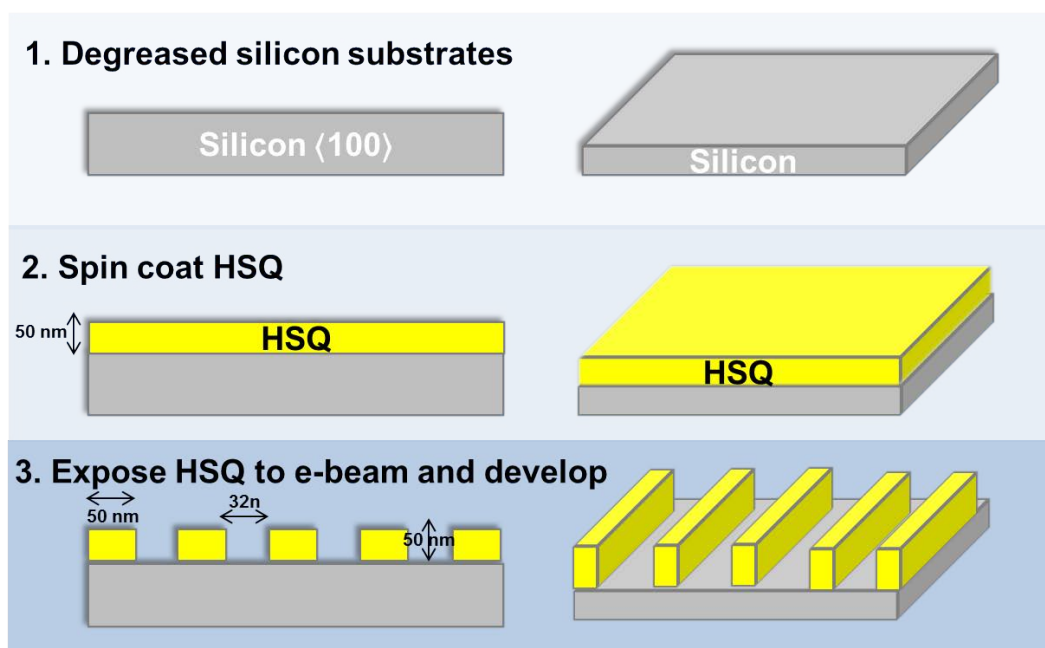


**Figure S6.7.1.** Preparation of HSQ patterned substrates via spin coating and electron beam lithography.

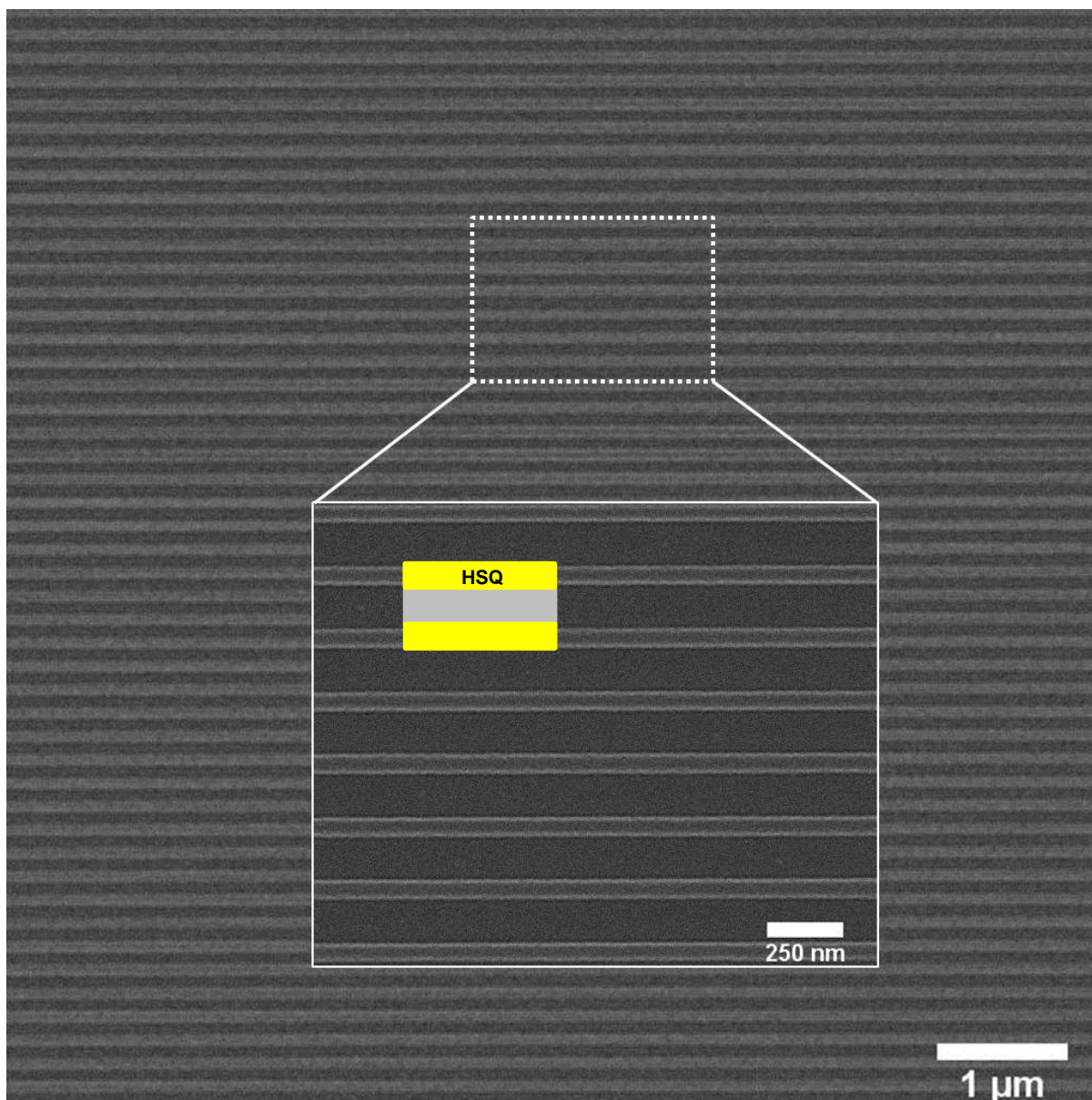


**Figure S6.7.2.** Top-down SEM image of large scale area of HSQ gratings with 128 nm channel widths. Inset shows high resolution SEM image of HSQ gratings after fabrication.

---

*Chapter 7*

---

**Parallel Arrays of Sub-10 nm Aligned Germanium Nanofins  
from an “*In-situ*” Metal Oxide Hardmask using Directed Self-  
Assembly of Block Copolymers**

## 7.1. Abstract

High-mobility materials and non-traditional device architectures are of key interest in the semiconductor industry because of the need to achieve higher computing speed and low power consumption. In this chapter, we present an integrated approach using directed self-assembly (DSA) of block copolymers (BCPs) to form aligned line-space features through graphoepitaxy on germanium on insulator (GeOI) substrates. Ge is an example of a high mobility material (III-V, II-VI) where the chemical activity of the surface and its composition sensitivity to etch processing offers considerable challenges in fabrication compared to silicon (Si). We believe the methods described here afford an opportunity to develop ultra-small dimension patterns from these important high-mobility materials. High quality metal oxide enhanced pattern transfer to Ge is demonstrated for the realization of nanofins with sub-10 nm feature size. Graphoepitaxial alignment of a poly(styrene)-*block*-poly(4-vinylpyridine) PS-*b*-P4VP BCP was achieved using pre-defined HSQ topography at a GeOI substrate. PS-*b*-P4VP was spin-coated onto the substrate and solvent vapor annealed to affect microphase separation. Subsequent impregnation of the aligned BCP templates with a salt precursor “*in-situ*” and simple processing was used to generate robust metal oxide nanowire (*e.g.* Fe<sub>3</sub>O<sub>4</sub>,  $\gamma$ -Al<sub>2</sub>O<sub>3</sub>, and HfO<sub>2</sub>) hardmask arrays. Optimized plasma based dry etching of the oxide modified substrate allowed the formation of high aspect ratio Ge nanofin features within the HSQ topographical structure. We believe the methodology developed has significant potential for high resolution device patterning of high mobility semiconductors. We envision that the aligned Ge nanofin arrays prepared here via graphoepitaxy might have application as a replacement channel material for complementary metal–oxide–semiconductor (CMOS) devices and integrated circuit (IC) technology. Furthermore, the low capital required to produce Ge nanostructures with DSA technology may be an attractive route

to address technological and economic challenges facing the nanoelectronic and semiconductor industry.

## 7.2. Introduction

With the inherent ability to form uniform periodically arranged nanoscale features, microphase separated BCPs have been under intense scrutiny as on-chip etch masks for patterning device relevant geometries (*e.g.* bends, junctions).<sup>1</sup> Microphase separation occurs due to the thermodynamic incompatibility between constituent blocks (A and B) of a di-BCP as represented by the dimensionless parameter,  $\chi$  (Flory-Huggins interaction parameter).<sup>2</sup> The degree of polymerization (N) is the number of monomers forming the polymer chain and offers control of the periodicity of the resulting BCP microdomains.<sup>3</sup> Likewise, tailoring the volume fraction ( $f$ ) of respective blocks allows different morphologies to be attained, namely lamellae, gyroidal, cylindrical and finally spherical as  $f_A$  reduces from 0.5. With the need to achieve low feature sizes and pitches for ever decreasing technology nodes, “high  $\chi$ ” materials are required to allow a relatively high segregation strength  $\chi \cdot N$  ( $> 10.5$ ) as this enables ordered equilibrium morphologies to form.<sup>4</sup> DSA methodologies (namely chemoepitaxy and graphoepitaxy) over the past decade have primarily been demonstrated on silicon substrates using “first generation material” PS-*b*-PMMA BCP systems.<sup>5,6</sup> Demonstrations on 300 mm wafer scale pilot processes have recently been reported.<sup>7-9</sup> Two concerning issues for PS-*b*-PMMA are the minimum feature size attainable due to its’ low  $\chi$  (0.04)<sup>10</sup> and limited etch contrast between the organic blocks reducing pattern transfer fidelity.

In this regard, “high  $\chi$ ” BCP materials such as PS-*b*-PDMS ( $\chi \sim 0.26$ ), PS-*b*-P<sub>x</sub>VPs ( $x = 2$  or 4, PS-*b*-P2VP  $\chi \sim 0.18$ ), and PS-*b*-PLA ( $\chi \sim 0.21$ ), are extremely attractive for reaching

ultra-small features and have dominated recent literature.<sup>11-15</sup> Moreover, methodologies to selectively infiltrate and subsequently enhance microdomain etch contrast in neat self-assembled BCPs is now an area of considerable interest. In particular, sequential infiltration synthesis (*i.e.* SIS) has been documented for achieving high-aspect (1:10) ratio silicon features from alumina infiltrated PS-*b*-PMMA.<sup>16,17</sup> Likewise, metal oxide inclusion has been reported to significantly enhance “activated” PS-*b*-PEO and PS-*b*-P4VP BCP systems for Si nanofeature fabrication.<sup>18-21</sup>

In order to extend the relentless dimensional scaling of semiconductor features (*i.e.* Moore’s Law) to the deep nanoscale regime (< 10 nm), employing DSA of BCP nanopatterns has emerged as a cost-effective route to controllably fabricate device-relevant features on a wafer scale level. In parallel to research on the efficacy and integration of patterning technologies (*e.g.* DSA, extreme ultraviolet, electron-beam lithography, nanoimprint lithography), non-Si based materials such as graphene,<sup>22-26</sup> Ge,<sup>27</sup> carbon nanotubes,<sup>28</sup> and III-V<sup>29</sup> have received significant attention for improved nanoelectronic device function mainly owing to their superior electrical properties. In particular, Ge has been suggested as a possible replacement material for MOSFETs to overcome future short channel effects which reduce device speed. Ge shares similar properties to its group IV neighbor Si, which makes a near term integration of a Si/Ge device possible or a complete replacement of Si channels viable in the future. Ge possesses a larger Bohr exciton radius (~ 24.3 nm) to Si (~ 4.9 nm)<sup>30</sup> consequently enhancing quantum effects, and Ge notably has higher electron and hole mobilities (3900 cm<sup>2</sup>/V.s, 1900 cm<sup>2</sup>/V.s) compared to Si (1500 cm<sup>2</sup>/V.s , 450 cm<sup>2</sup>/V.s)<sup>31</sup> thus potentially increasing electronic device speed. However, its’ brittleness, reactivity and unstable native oxides are serious areas of concern for device integration. If convenient process

methods could be developed for the fabrication of high-mobility Ge devices using a GeOI platform, this would represent significant progress towards next-generation IC technologies.<sup>32</sup> The work reported here is a synergistic approach combining DSA of a high  $\chi$  BCP material and an inclusion methodology to pattern transfer to GeOI substrates. To the best of our knowledge, there are no reports to date on the graphoepitaxial alignment of a high  $\chi$  BCP and pattern transfer on Ge surfaces (bulk or GeOI). We have reported the thermal evaporation of Ge on porous BCP templates,<sup>33</sup> however the present work achieves well-defined structures of importance for current Si transistor architectures based on Fin-FET designs.

### 7.3. Experimental

**Materials.** Poly(styrene)-*block*-Poly(4-vinylpyridine) (referred to as PS-*b*-P4VP BCP) was purchased from Polymer Source, Inc., Canada, with a molecular weight of  $M_n = 33.5 \text{ kg mol}^{-1}$  ( $M_{nPS} = 24 \text{ kg mol}^{-1}$ ;  $M_{nP4VP} = 9.5 \text{ kg mol}^{-1}$ ,  $f_{PS} = 0.70$ ), a polydispersity ( $M_w/M_n$ ) of 1.15 (where,  $M_n$  and  $M_w$  are number average and weight average molecular weights) and was used as received.  $\text{Fe}_2(\text{NO}_3)_3 \cdot 9\text{H}_2\text{O}$  (Iron (III) nitrate nonahydrate),  $\text{Al}(\text{NO}_3)_3 \cdot 9\text{H}_2\text{O}$  (aluminium nitrate nonahydrate, ACS reagent,  $\geq 98\%$ ),  $\text{HfCl}_4$  (hafnium(IV) chloride, 98%) chloroform (for HPLC,  $\geq 99.9\%$ , contains 0.5-1.0% ethanol as stabilizer), Tetrahydrofuran (inhibitor-free, CHROMASOLV Plus, for HPLC,  $\geq 99.9\%$ ), Toluene (CHROMASOLV, for HPLC, 99.9%), ethanol (dehydrated, 200 proof) were purchased from Sigma-Aldrich and used without further purification unless otherwise stated. De-ionized (DI) water was used wherever necessary.

**GeOI HSQ patterning.**

GeOI substrates were purchased from Soitech and consisted of a top layer of ~ 60 nm undoped Ge (100), a middle layer of SiO<sub>2</sub> measured at ~ 160 nm, and a bottom layer of Si. Ten × 10 mm GeOI substrates, were used for all DSA experiments. The substrates were patterned using a HSQ electron-beam lithography (Raith e-LiNE plus) process prior to deposition of the PS-*b*-P4VP BCP. The substrates were initially degreased via ultrasonication in acetone and iso-propanol (IPA) solutions (2 × 2 min), dried in flowing N<sub>2</sub> gas and baked for 2 minutes at 393 K in an ambient atmosphere to remove any residual IPA. Substrates were treated with 0.74 M citric acid solution for 6 minutes to remove surface GeO<sub>x</sub>, rinsed thoroughly with DI and blown dry under N<sub>2</sub>. The substrates were immediately spin coated (2000 rpm, 33 seconds) with a 2.4 wt % solution of HSQ (XR-1541 Dow Corning Corp.) in MIBK to produce a ~50 nm film of HSQ. The wafer was baked at 393 K in an ambient atmosphere for 3 minutes prior to transfer to the EBL system for exposure. Arrays of 50 nm wide lines at pitches of (32n + 50) nm were exposed, where n is an integer and 0 < n < 11. Note that 32 was chosen as this is close to the pitch of the PS-*b*-P4VP BCP employed. The basic electron dose employed was 800 μC/cm<sup>2</sup> and increased corresponding to larger trench sizes. Following electron beam exposure the samples were developed in an aqueous solution of 0.25 M NaOH, 0.7 M NaCl for 15 seconds, followed by rinsing in flowing DI water for 60 seconds and 15 seconds rinse in IPA. The samples were then blown dry in flowing N<sub>2</sub> gas. Note that channel widths of resulting prepatterns were measured at 192, 224, 265, 326, and 361 nm respectively.

**GeOI substrate treatment, block copolymer film preparation and solvent vapor annealing.** For removal of the GeO<sub>x</sub> layer, a recent approach was employed<sup>34</sup> as follows. GeOI substrates were treated using a 1M citric acid

solution. Samples were rinsed in DI water for 5 seconds and then immersed in the 1M citric acid solution for 1 minute. Substrates were removed and washed repeatedly in DI water, and blown dry with N<sub>2</sub> gas. The PS-*b*-P4VP solution was then immediately spin coated on the citric acid treated GeOI substrate at 3200 rpm. The PS-*b*-P4VP solutions were made at 0.5 weight % concentration, and were prepared in toluene/THF (80:20). Solvent vapor annealing (SVA) was carried out in the conventional manner with a small vial containing 8–10 ml of chloroform placed inside a glass jar (150 ml) with PS-*b*-P4VP sample from 30 minutes to 3 hours as reported previously by our group for SVA on silicon substrates. Samples were removed from the glass jars after the desired anneal time and allowed to evaporate the trapped solvent at ambient conditions. Note that the films did not exhibit any major swelling during SVA as the films were transparent throughout (same as spin cast). After solvent vapor annealing, the samples were “activated” via exposure to ethanol vapors at 50°C for 20 minutes to form a nanoporous matrix.

**Metal oxide nanowire hardmask fabrication.** Fe<sub>2</sub>(NO<sub>3</sub>)<sub>3</sub>·9H<sub>2</sub>O, Al(NO<sub>3</sub>)<sub>3</sub>·9H<sub>2</sub>O, and HfCl<sub>4</sub> solutions of 0.5 wt % were prepared in ethanol and spin-coated on to the ethanol “activated” samples for 30 seconds at 3200 rpm. UV/O<sub>3</sub> treatment was carried out for 3 hours to oxidize the precursor and remove polymer. Samples were UV/O<sub>3</sub> treated in a UV/ozone system (PSD Pro Series Digital UV Ozone System; Novascan Technologies, Inc., USA). The UV source is two low pressure mercury vapour grid lamps. Both lamps have an output current of 0.8–0.95 A and power of 65–100 W, as reported by the manufacturer, and have strong emissions at both wavelengths of UV radiation (184.9 nm and 253.7 nm).

The system produces highly reactive ozone gas from oxygen that is present within the chamber.

#### **Pattern transfer of metal oxide nanowire hardmask arrays to GeOI.**

An STS Multiplex ICP etcher was used for etching to pattern transfer the  $\text{Fe}_3\text{O}_4$ ,  $\gamma\text{-Al}_2\text{O}_3$ , and  $\text{HfO}_2$  nanowire mask to the underlying GeOI substrate.  $\text{CF}_4$  was used for etching Ge with the metal oxide nanowires as etchmasks. Samples were etched for 9 seconds in total with  $\text{CF}_4$  gas only using a flow rate of 40 sccm, pressure of 10mTorr, and ICP power of 400 W. RF power was set at 100 W. Note that the DC bias (and peak to peak voltage) on average for above runs was measured at  $\sim 355$  V for peak to peak voltage of 1125 V.

#### **7.4. Results and discussion**

Figure 7.1 displays the process flow used for the fabrication of the Ge nanofins detailed in this chapter. Native Ge oxide on GeOI surfaces was removed using a “green” approach of citric acid treatment based on previous work from these laboratories (Collins *et al.*<sup>34</sup>). The unstable native oxide of Ge is a major concern for its reintroduction to IC manufacture and the citric acid treatment is extremely effective for oxide removal and stabilization. The PS-*b*-P4VP BCP solution was spin-coated directly onto the passivated GeOI surface. Graphoepitaxially aligned self-assembled PS-*b*-P4VP line features were generated after solvent vapor annealing (SVA)<sup>35</sup> in a chloroform atmosphere. SVA of the 25 nm polymer thin film was carried out in an atmosphere of chloroform at room temperature for 2 hours to induce self-assembly. We have previously established a protocol for this cylinder forming PS-*b*-P4VP system with cylinder in-plane (C<sub>||</sub>) orientation achieved when employing non-selective solvent swelling conditions.<sup>21</sup>

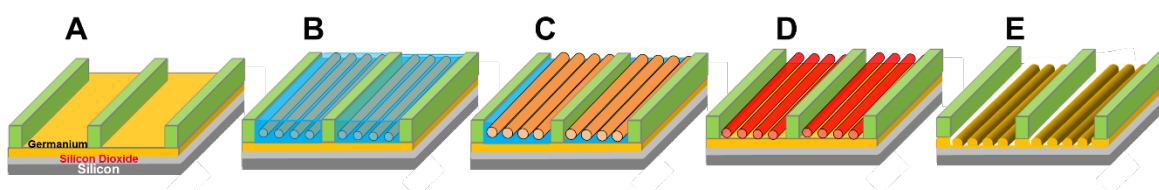


**Figure 7.1.** A. GeOI substrate after HSQ (green) prepattern development for graphoepitaxy. B. PS-*b*-P4VP film after solvent vapor annealing producing aligned P4VP cylinders parallel to substrate. C. Activated PS-*b*-P4VP film after ethanol vapor exposure. D. Metal oxide nanowire hardmask after spin coating metal-salt precursor and successful metal ion oxidation and polymer template removal via UV/O<sub>3</sub>. E. Aligned Ge nanofin fabrication following pattern transfer of hardmask.

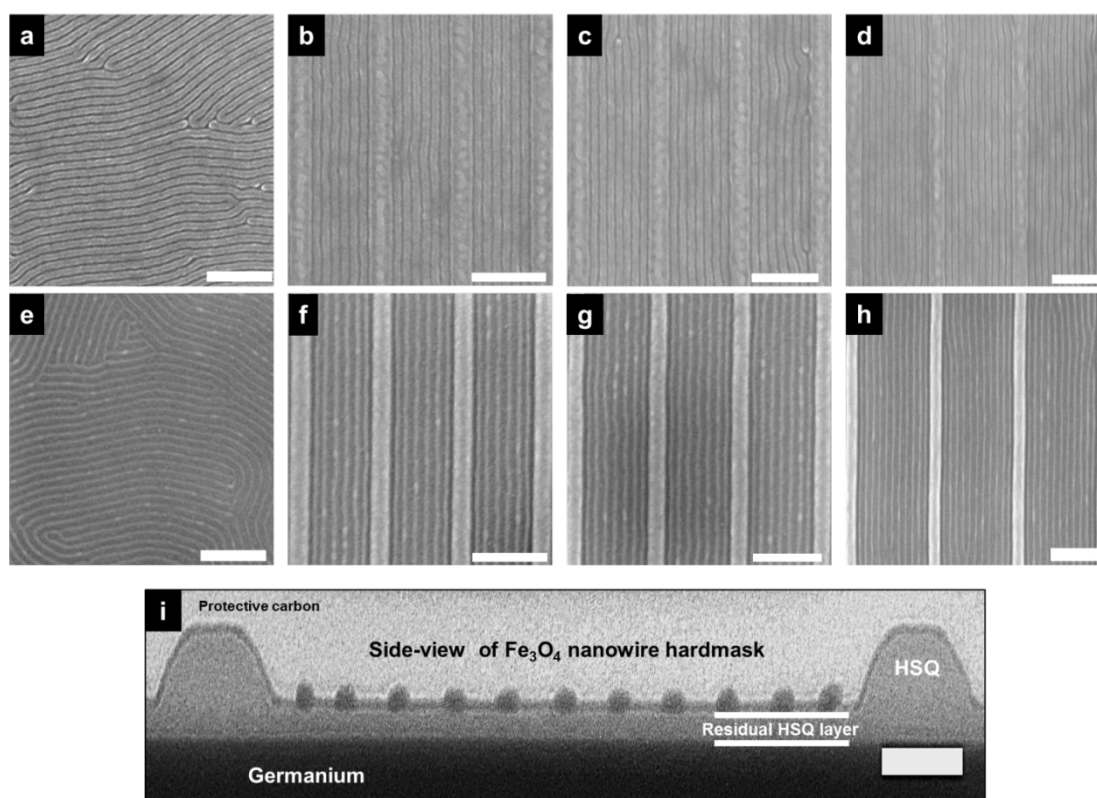
Exposure of the self-assembled PS-*b*-P4VP patterns to hot ethanol resulted in porous channels that could be impregnated with metal oxide material. “Activation” (*i.e.* surface reconstruction)<sup>36,37</sup> of P4VP domains through selective block swelling in ethanol vapors was carried out at 50°C, and SEM characterization was employed to analyze films. Figure 7.2a shows a top-down SEM image of open area of an “activated” PS-*b*-P4VP BCP film displaying line-space features with high uniformity. Pitch and P4VP microdomain dimensions of the fingerprint patterns were measured at 32.45 nm and 8.63 nm respectively (see Appendix Figure S7.7.1) following SVA. Whilst hot ethanol immersion methods have been demonstrated to great effect,<sup>19,38</sup> we have observed film destruction as discussed in previous work.<sup>21</sup> Thus we have used hot ethanol vapors to create a near complete porous film. Parallel arrays of DSA of the “activated” PS-*b*-P4VP line-space features is displayed with high uniformity in Figure 1b-d. The SEM images shows strict registration of the graphoepitaxially aligned “activated” PS-*b*-P4VP cylinder structures with the HSQ sidewall features. A total of 6, 7 and 11 P4VP C<sub>11</sub> features are visible within 224 nm, 265 nm, and 361 nm channel widths respectively.

Following the controlled development of porous templates, fabrication of metal oxide nanowires mimicking the original polymer pattern was achieved. As displayed in Figure

7.2e-h, Fe<sub>3</sub>O<sub>4</sub> nanowires on GeOI were enabled within HSQ prepatterns after spin coating of a low weight percentage iron nitrate ethanolic precursor onto the “activated” PS-*b*-P4VP template. An open area of Fe<sub>3</sub>O<sub>4</sub> nanowires on a GeOI substrate can be seen in the SEM image in Figure 7.2e. The high-resolution SEM image reveals nanowires that display a high level of regularity and uniformity. For pattern transfer lithography purposes, this is essential to avoid transferring any roughness or non-uniformity of the hardmask to the underlying substrate. The pitch and nanowire dimensions were comparable to the reconstructed films at 32.22 nm and 10.31 nm respectively. We elucidated the chemical composition of the iron nitrate precursor through XPS and Figure S7.7.2 shows confirmation of Fe<sub>3</sub>O<sub>4</sub> formation on GeOI. Figure 7.2f-h shows 6, 7, and 11 Fe<sub>3</sub>O<sub>4</sub> nanowires aligned within HSQ pre-patterns replicating the original “activated” PS-*b*-P4VP line-space features (Figure 7.2b-d). It can be seen that the precise nanowire feature positional accuracy and registration of Fe<sub>3</sub>O<sub>4</sub> material is consistent with aims to enhance current state-of-the-art IC patterning towards sub-10 nm features. The SEM images reveal that there is no P4VP wetting layer at the HSQ sidewalls allowing individually aligned nanowires to form. Substrate surface treatment or sidewall polymer brush modifications were not necessary to overcome interfacial effects. The neutrality of this cylinder forming PS-*b*-P4VP BCP system overcomes any previously outlined issues with selective wetting of polymer blocks at HSQ sidewalls such as PDMS containing BCPs in HSQ based prepatterns as described by Hobbs *et al.*<sup>39</sup> There is some indication of a Fe<sub>3</sub>O<sub>4</sub> wetting layer (~ 2 nm in thickness) after the inclusion step as displayed in the TEM image in Figure 7.2i.

There is possible evidence of hardened HSQ between Fe<sub>3</sub>O<sub>4</sub> nanowires and along surface of HSQ material. This extends across the channel base and the mesas (HSQ prepatterns).

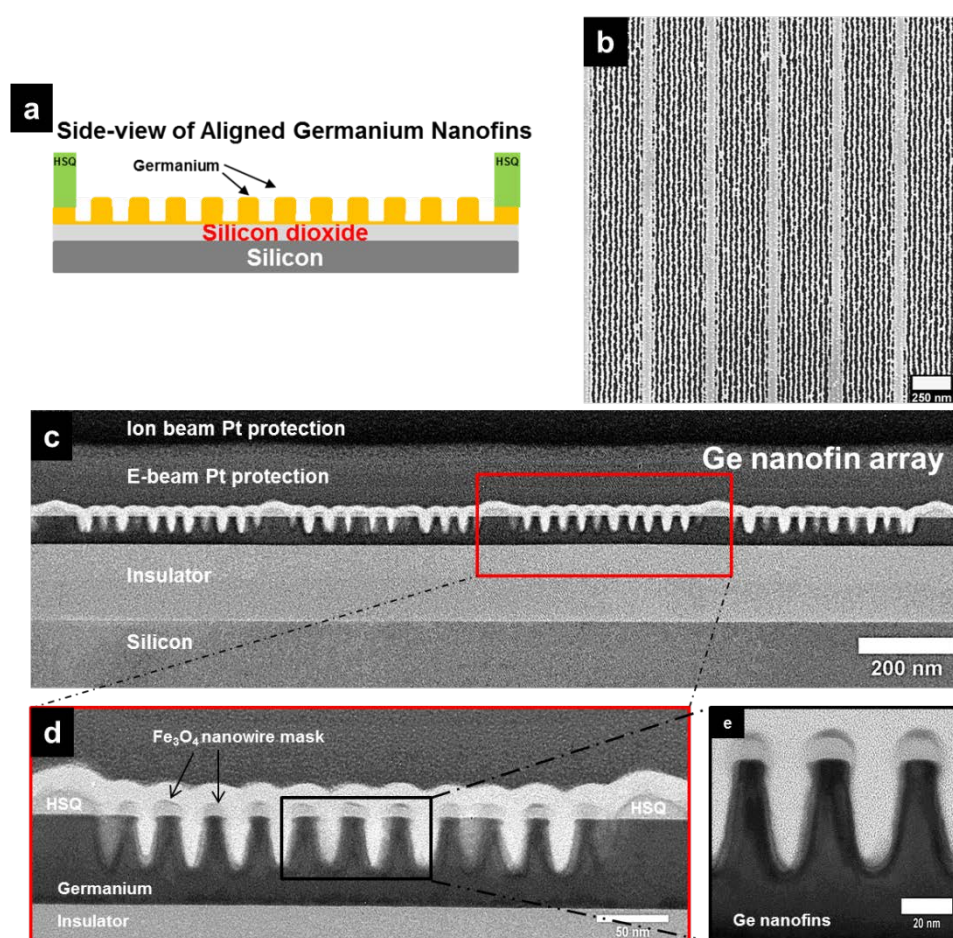
However, the nature of this layer remains uncertain. The possibility of forming such a regular wetting layer without forming cylinders would seem unlikely. There is also the possibility of surface scattering effects that can lead to these apparent layers. We also note the possibility of the UV/O<sub>3</sub> treatment forming dense silica from the HSQ. The origin of this layer is under strict investigation. However, whatever its cause, it is clear that the etch procedure can “punch” through the residual surface layer. We also believe there is a residual HSQ layer at the substrate interface as discussed below.



**Figure 7.2.** Top-down SEM images of (a) open area of porous “activated” PS-*b*-P4VP films. (b) – (d) display graphoepitaxial alignment of “activated” features in HSQ prepatterns of 224 nm, 265 nm and 361 nm channel widths respectively. SEM images in (e)-(h) show corresponding Fe<sub>3</sub>O<sub>4</sub> nanowire hardmask features after metal oxide inclusion in open areas and within HSQ prepatterns. All scale bars represent 250 nm. (i) Cross-section TEM image of Fe<sub>3</sub>O<sub>4</sub> nanowire hardmask features in HSQ prepattern of 361 nm channel widths [*i.e.* image (h)]. Scale bar is 50 nm. Note there is evidence of a residual HSQ layer (between white lines).

Note that the graphoepitaxial alignment of PS-*b*-P4VP and metal oxide inclusion was also carried out on bulk Ge substrates and large scale alignment were achieved with greater than 5 micron long features (see Figure S7.7.3).

Figure 7.3b displays a top-down image of parallel arrays of 11 Ge nanofins within HSQ prepatterns following pattern transfer. A highly selective etch was employed using carbon tetrafluoride (CF<sub>4</sub>) gas only.<sup>40</sup> The Ge nanofins displayed in the TEM image in



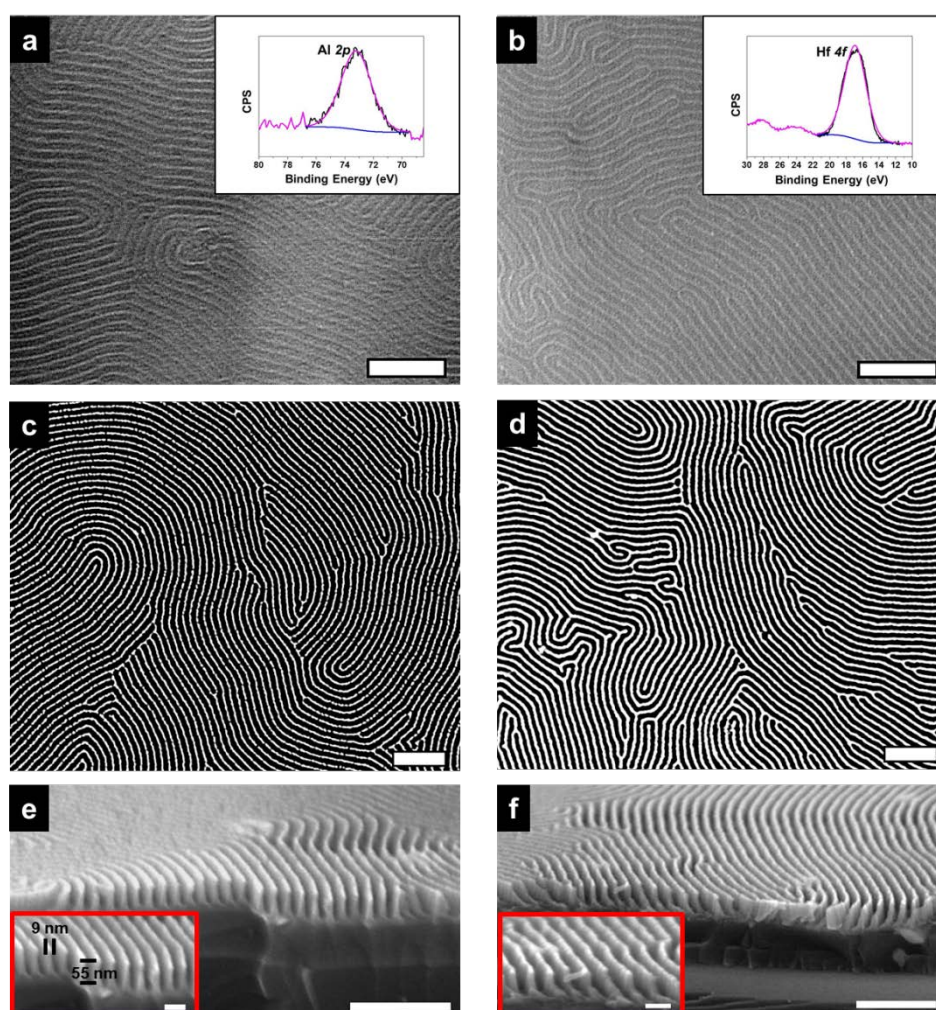
**Figure 7.3.** (a) Shows cross-section profile of aligned Ge nanofins following pattern transfer. (b) top-down SEM image of parallel arrays of pattern transferred Ge nanofins in channel widths of 361 nm. (c)-(e) Low resolution and high-resolution TEM images of graphoepitaxially aligned Ge nanofin structures corresponding to (b).

Figure 7.3c were fabricated after plasma etching of Ge for a total of 9 seconds. An initial shorter etch (3 seconds) revealed little removal of Ge material (see Figure S7.7.4).

However on continued etching with  $\text{CF}_4$ , aspect ratios of 1 : 3.5 were achieved within HSQ prepatterns as seen in the TEM data in Figure 7.3c, d and e. Feature sizes and etch depths were measured at  $\sim 9$  nm and  $\sim 31$  nm respectively. The high dimensional control of the etch process is clearly evident. Interestingly, attempted chlorine based etch processes did not result in any etching of Ge. We believe this may be due to the residual HSQ material as seen in the TEM image in Figure 7.2i at the substrate interface between nanowire hardmask features and the Ge layer. Therefore,  $\text{Cl}_2$  plasma is unable to successfully etch the residual HSQ layer and pattern transfer the nanowire template to the Ge layer. In contrast,  $\text{CF}_4$  is well known to consume HSQ material<sup>39</sup> and thus rapidly etches the HSQ material at the substrate surface and enables Ge etching to take place. Further surface studies are required to gain insight into the mechanism. Overall, the issue was circumvented through employing alternative plasma etch chemistries allowing the creation of Ge nanofins. Also, whilst we demonstrate Ge nanostructures of application for Fin-FET based devices, further etching or thinner Ge thicknesses would enable the fabrication of Ge nanowires for other technological application.

In order to show the efficacy and robustness of the methodology outlined above we have employed aluminum and hafnium precursors as hardmask materials to pattern high-aspect ratio (1:6) Ge features on planar GeOI substrates. Figure 7.4a and b display top-down SEM images of alumina ( $\gamma\text{-Al}_2\text{O}_3$ ) and hafnia ( $\text{HfO}_2$ ) nanowire arrays with large scale coverage on GeOI substrates. The  $\gamma\text{-Al}_2\text{O}_3$  and  $\text{HfO}_2$  nanowires were fabricated using ethanolic based precursors as the  $\text{Fe}_3\text{O}_4$  nanowire hardmask arrays discussed above. High resolution XPS of Al  $2p$  and Hf  $4f$  are shown in insets in Figure 7.4a and b respectively confirming the presence of  $\gamma\text{-Al}_2\text{O}_3$  and  $\text{HfO}_2$ . The survey and high-resolution oxygen spectrum of both samples are shown and discussed further in Figure

S7.7.5. The inclusion of semiconductor and high-k dielectric hardmask material in this simple reproducible process is advantageous for device processing considerations where industrial fabrication compatibility is essential. The spin-coating processes address scalability and throughput level that are paramount for high volume manufacturing (HVM) and very large scale integration (VLSI). Additionally, all steps for the fabrication of Ge nanofins were carried out at room temperature (290K). Ge etching using  $\text{CF}_4$  for 9 seconds was carried out for the pattern transfer of the  $\gamma\text{-Al}_2\text{O}_3$  and  $\text{HfO}_2$  hardmask



**Figure 7.4.** Top-down SEM images of  $\gamma\text{-Al}_2\text{O}_3$  nanowire (a) and  $\text{HfO}_2$  nanowire (b) arrays following metal-salt inclusion process. Insets in (a) and (b) show high resolution XPS scans for Al 2p and Hf 4f peaks. Top-down SEM of Ge nanofins following pattern transfer with (c)  $\gamma\text{-Al}_2\text{O}_3$  nanowire hardmask and (d)  $\text{HfO}_2$  nanowire hardmask. Corresponding cross-section SEM images in (e) and (f) reveal high uniformity of Ge nanofin structures. Main scale bars represent 250 nm whilst insets are 50 nm.

nanowires to the underlying GeOI. Well-defined Ge nanofins were produced as shown from top-down SEM images in Figure 7.4c ( $\gamma$ -Al<sub>2</sub>O<sub>3</sub>) and Figure 7.4d (HfO<sub>2</sub>) with good uniformity. Moreover, the cross-section SEM images displayed in Figure 7.4e and f reveal well-defined Ge nanofins from  $\gamma$ -Al<sub>2</sub>O<sub>3</sub> (Figure 7.4e) and HfO<sub>2</sub> (Figure 7.4f) nanowire hardmasks. Clear evidence is revealed in the images of vertical and lateral dimensional control owing to the robustness of the etch mask and high selectivity of the dry etching process. The vertical profile of the Ge nanofins is also evident in the inset of each cross-section SEM views. Feature sizes were measured at 9 nm while depths were measured at 55 nm, *i.e.* an aspect ratio of 1:6.

## 7.5. Conclusions

In summary, we have presented a robust process flow for the fabrication of well-defined high-aspect ratio sub-10 nm Ge nanofin feature sizes with vertical and lateral dimensional control. This chapter demonstrates the level of accuracy in which a high  $\chi$  material could be used to template passivated GeOI substrate surfaces. Distinct and isolated Fe<sub>3</sub>O<sub>4</sub>,  $\gamma$ -Al<sub>2</sub>O<sub>3</sub> and HfO<sub>2</sub> nanowire hardmask arrays were also shown at GeOI substrate surfaces and were found to perform as excellent hardmasks for pattern transfer with each exhibiting similar efficacy. Highly selective dry etch procedures were employed to pattern transfer the on-chip etch masks to the underlying GeOI substrate to generate Ge nanofins. More significantly, the self-assembly of PS-*b*-P4VP cylinders lying in-plane (C<sub>11</sub>), and selective P4VP infiltration with metal oxide material were all demonstrated with high reproducibility using a topographical DSA methodology. Graphoepitaxial HSQ prepatterns were fabricated using top-down electron-beam lithography to allow alignment and registration of cylinder forming PS-*b*-P4VP line-space features. Subsequent metal oxide nanowire fabrication and optimized etch time

and chemistry enabled high-aspect ratio Ge nanofins to be achieved in graphoepitaxy trenches. Overall, the work emphasizes the possibility to realize next-generation electronic devices based on GeOI material through DSA of BCP technology for HVM and VLSI device designs.

## 7.6. References

- (1) Stoykovich, M. P.; Kang, H.; Daoulas, K. C.; Liu, G.; Liu, C.-C.; de Pablo, J. J.; Müller, M.; Nealey, P. F. Directed Self-Assembly of Block Copolymers for Nanolithography: Fabrication of Isolated Features and Essential Integrated Circuit Geometries. *ACS Nano* **2007**, *1*, 168-175.
- (2) Mai, Y.; Eisenberg, A. Self-assembly of block copolymers. *Chemical Society Reviews* **2012**, *41*, 5969-5985.
- (3) Schacher, F. H.; Rugar, P. A.; Manners, I. Functional block copolymers: Nanostructured materials with emerging applications. *Angewandte Chemie - International Edition* **2012**, *51*, 7898-7921.
- (4) Koo, K.; Ahn, H.; Kim, S.-W.; Ryu, D. Y.; Russell, T. P. Directed self-assembly of block copolymers in the extreme: guiding microdomains from the small to the large. *Soft Matter* **2013**, *9*, 9059-9071.
- (5) Stoykovich, M. P.; Müller, M.; Kim, S. O.; Solak, H. H.; Edwards, E. W.; De Pablo, J. J.; Nealey, P. F. Materials Science: Directed assembly of block copolymer blends into nonregular device-oriented structures. *Science* **2005**, *308*, 1442-1446.
- (6) Farrell, R. A.; Kinahan, N. T.; Hansel, S.; Stuenkel, K. O.; Petkov, N.; Shaw, M. T.; West, L. E.; Djara, V.; Dunne, R. J.; Varona, O. G.; Gleeson, P. G.; Jung, S. J.; Kim, H. Y.; Kolešnik, M. M.; Lutz, T.; Murray, C. P.; Holmes, J. D.; Nealey, P. F.; Duesberg, G. S.; Krstić, V.; Morris, M. A. Large-scale parallel arrays of silicon nanowires via block copolymer directed self-assembly. *Nanoscale* **2012**, *4*, 3228-3236.
- (7) Delgadillo, P. A. R.; Gronheid, R.; Thode, C. J.; Wu, H.; Cao, Y.; Neisser, M.; Somervell, M.; Nafus, K.; Nealey, P. F. Implementation of a chemo-epitaxy flow for directed self-assembly on 300-mm wafer processing equipment. *Journal of Micro/Nanolithography, MEMS, MOEMS* **2012**, *11*, 031302.
- (8) Liu, C.-C.; Estrada-Raygoza, I. C.; Abdallah, J.; Holmes, S.; Yin, Y.; Schepis, A.; Cioria, M.; Hetzer, D.; Tsai, H.; Guillorn, M.; Tjio, M.; Cheng, J.; Somervell, M.; Colburn, M. Directed self-assembly process implementation in a 300mm pilot line environment, *Proc. SPIE* **2013**, 8680, 86801G.
- (9) Isabelle, S.; Raluca, T.; Ahmed, G.; Maxime, A.; Karine, J.; Gaëlle, C.-M.; Patricia Pimenta, B.; Xavier, C.; Jérôme, B.; Xavier, B.; Sylvain, M.; Christophe, N.; Gilles, C.; Sébastien, B.; Masaya, A.; Charles, P. Contact hole shrink by directed self-assembly: Process integration and stability monitored on 300 mm pilot line. *Japanese Journal of Applied Physics* **2014**, *53*, 06JC05.
- (10) Cheng, H.-H.; Keen, I.; Yu, A.; Chuang, Y.-M.; Blakey, I.; Jack, K. S.; Leeson, M. J.; Younkin, T. R.; Whittaker, A. K. EUVL compatible LER solutions using functional block copolymers, *Proc. SPIE* **2012**, 8323, 83231O.
- (11) Gotrik, K. W.; Ross, C. A. Solvothermal Annealing of Block Copolymer Thin Films. *Nano Letters* **2013**, *13*, 5117-5122.

- (12) Chai, J.; Buriak, J. M. Using Cylindrical Domains of Block Copolymers To Self-Assemble and Align Metallic Nanowires. *ACS Nano* **2008**, *2*, 489-501.
- (13) Gu, X.; Liu, Z.; Gunkel, I.; Chourou, S. T.; Hong, S. W.; Olynick, D. L.; Russell, T. P. High Aspect Ratio Sub-15 nm Silicon Trenches From Block Copolymer Templates. *Advanced Materials* **2012**, *24*, 5688-5694.
- (14) Mokarian-Tabari, P.; Cummins, C.; Rasappa, S.; Simao, C.; Sotomayor Torres, C. M.; Holmes, J. D.; Morris, M. A. Study of the Kinetics and Mechanism of Rapid Self-Assembly in Block Copolymer Thin Films during Solvo-Microwave Annealing. *Langmuir* **2014**, *30*, 10728-10739.
- (15) Keen, I.; Cheng, H.-H.; Yu, A.; Jack, K. S.; Younkin, T. R.; Leeson, M. J.; Whittaker, A. K.; Blakey, I. Behavior of Lamellar Forming Block Copolymers under Nanoconfinement: Implications for Topography Directed Self-Assembly of Sub-10 nm Structures. *Macromolecules* **2013**, *47*, 276-283.
- (16) Tseng, Y.-C.; Peng, Q.; Ocola, L. E.; Elam, J. W.; Darling, S. B. Enhanced Block Copolymer Lithography Using Sequential Infiltration Synthesis. *The Journal of Physical Chemistry C* **2011**, *115*, 17725-17729.
- (17) Johnston, D. E.; Lu, M.; Black, C. T. Plasma etch transfer of self-assembled polymer patterns. *Journal of Micro/Nanolithography, MEMS, and MOEMS* **2012**, *11*, 031306.
- (18) Ghoshal, T.; Senthamaraiannan, R.; Shaw, M. T.; Holmes, J. D.; Morris, M. A. "In situ" hard mask materials: a new methodology for creation of vertical silicon nanopillar and nanowire arrays. *Nanoscale* **2012**, *4*, 7743-7750.
- (19) Ghoshal, T.; Senthamaraiannan, R.; Shaw, M. T.; Holmes, J. D.; Morris, M. A. Fabrication of ordered, large scale, horizontally-aligned Si nanowire arrays based on an in situ hard mask block copolymer approach. *Advanced Materials* **2014**, *26*, 1207-1216.
- (20) Cummins, C.; Borah, D.; Rasappa, S.; Chaudhari, A.; Ghoshal, T.; O'Driscoll, B. M. D.; Carolan, P.; Petkov, N.; Holmes, J. D.; Morris, M. A. Self-assembly of polystyrene-block-poly(4-vinylpyridine) block copolymer on molecularly functionalized silicon substrates: fabrication of inorganic nanostructured etchmask for lithographic use. *Journal of Materials Chemistry C* **2013**, *1*, 7941-7951.
- (21) Cummins, C.; Gangnaik, A.; Kelly, R. A.; Borah, D.; O'Connell, J.; Petkov, N.; Georgiev, Y. M.; Holmes, J. D.; Morris, M. A. Aligned silicon nanofins via the directed self-assembly of PS-*b*-P4VP block copolymer and metal oxide enhanced pattern transfer. *Nanoscale* **2015**, *7*, 6712-6721.
- (22) Schwierz, F. Graphene transistors. *Nat Nano* **2010**, *5*, 487-496.
- (23) Liang, X.; Wi, S. Transport Characteristics of Multichannel Transistors Made from Densely Aligned Sub-10 nm Half-Pitch Graphene Nanoribbons. *ACS Nano* **2012**, *6*, 9700-9710.
- (24) Liu, G.; Wu, Y.; Lin, Y.-M.; Farmer, D. B.; Ott, J. A.; Bruley, J.; Grill, A.; Avouris, P.; Pfeiffer, D.; Balandin, A. A.; Dimitrakopoulos, C. Epitaxial Graphene Nanoribbon Array Fabrication Using BCP-Assisted Nanolithography. *ACS Nano* **2012**, *6*, 6786-6792.
- (25) Son, J. G.; Son, M.; Moon, K.-J.; Lee, B. H.; Myoung, J.-M.; Strano, M. S.; Ham, M.-H.; Ross, C. A. Sub-10 nm Graphene Nanoribbon Array Field-Effect Transistors Fabricated by Block Copolymer Lithography. *Advanced Materials* **2013**, *25*, 4723-4728.
- (26) Seokhan, P.; Je Moon, Y.; Uday Narayan, M.; Hyoung-Seok, M.; Hyeong Min, J.; Sang Ouk, K. Device-oriented graphene nanopatterning by mussel-inspired directed block copolymer self-assembly. *Nanotechnology* **2014**, *25*, 014008.
- (27) O'Regan, C.; Biswas, S.; Petkov, N.; Holmes, J. D. Recent advances in the growth of germanium nanowires: synthesis, growth dynamics and morphology control. *Journal of Materials Chemistry C* **2014**, *2*, 14-33.

- (28) Baughman, R. H.; Zakhidov, A. A.; de Heer, W. A. Carbon Nanotubes-the Route Toward Applications. *Science* **2002**, *297*, 787-792.
- (29) Monemar, B. III-V nitrides - important future electronic materials. *Journal of Materials Science-Materials in Electronics* **1999**, *10*, 227-254.
- (30) Gu, G.; Burghard, M.; Kim, G. T.; Düsberg, G. S.; Chiu, P. W.; Krstic, V.; Roth, S.; Han, W. Q. Growth and electrical transport of germanium nanowires. *Journal of Applied Physics* **2001**, *90*, 5747-5751.
- (31) Drinek, V.; Fajgar, R.; Klementova, M.; Subrt, J.: Deposition of Germanium Nanowires from Digermane Precursor: Influence of the Substrate Pretreatment. In *Eurocvd 17 / Cvd 17*; Swihart, M. T., Barreca, D., Adomaitis, R. A., Worhoff, K., Eds.; ECS Transactions **8**, **2009**; Vol. 25; pp 1015-1022.
- (32) Akatsu, T.; Deguet, C.; Sanchez, L.; Allibert, F.; Rouchon, D.; Signamarcheix, T.; Richtarch, C.; Boussagol, A.; Loup, V.; Mazen, F.; Hartmann, J.-M.; Campidelli, Y.; Clavelier, L.; Letertre, F.; Kernevez, N.; Mazure, C. Germanium-on-insulator (GeOI) substrates—A novel engineered substrate for future high performance devices. *Materials Science in Semiconductor Processing* **2006**, *9*, 444-448.
- (33) Rasappa, S.; Borah, D.; Senthamaraiannan, R.; Faulkner, C. C.; Wang, J. J.; Holmes, J. D.; Morris, M. A. Fabrication of Germanium Nanowire Arrays by Block Copolymer Lithography. *Science of Advanced Materials* **2013**, *5*, 782-787.
- (34) Collins, G.; Aureau, D.; Holmes, J. D.; Etcheberry, A.; O’Dwyer, C. Germanium Oxide Removal by Citric Acid and Thiol Passivation from Citric Acid-Terminated Ge(100). *Langmuir* **2014**, *30*, 14123-14127.
- (35) Sinturel, C.; Vayer, M.; Morris, M.; Hillmyer, M. A. Solvent Vapor Annealing of Block Polymer Thin Films. *Macromolecules* **2013**, *46*, 5399-5415.
- (36) Park, S.; Kim, B.; Wang, J. Y.; Russell, T. P. Fabrication of Highly Ordered Silicon Oxide Dots and Stripes from Block Copolymer Thin Films. *Advanced Materials* **2008**, *20*, 681-685.
- (37) Park, S.; Wang, J.-Y.; Kim, B.; Xu, J.; Russell, T. P. A Simple Route to Highly Oriented and Ordered Nanoporous Block Copolymer Templates. *ACS Nano* **2008**, *2*, 766-772.
- (38) Yin, J.; Yao, X.; Liou, J.-Y.; Sun, W.; Sun, Y.-S.; Wang, Y. Membranes with Highly Ordered Straight Nanopores by Selective Swelling of Fast Perpendicularly Aligned Block Copolymers. *ACS Nano* **2013**, *7*, 9961-9974.
- (39) Hobbs, R. G.; Farrell, R. A.; Bolger, C. T.; Kelly, R. A.; Morris, M. A.; Petkov, N.; Holmes, J. D. Selective Sidewall Wetting of Polymer Blocks in Hydrogen Silsesquioxane Directed Self-Assembly of PS-*b*-PDMS. *ACS Applied Materials & Interfaces* **2012**, *4*, 4637-4642.
- (40) Shim, K.-H.; Yang, H. Y.; Kil, Y.-H.; Yang, H. D.; Yang, J.-H.; Hong, W.-K.; Kang, S.; Jeong, T. S.; Kim, T. S. Nanoscale dry etching of germanium by using inductively coupled CF<sub>4</sub> plasma. *Electronic Materials Letters* **2012**, *8*, 423-428.

## 7.7. Appendix – Chapter 7

### Parallel Arrays of Sub-10 nm Aligned Germanium Nanofins from an “*In-situ*” Metal Oxide Hardmask using Directed Self-Assembly of Block Copolymers

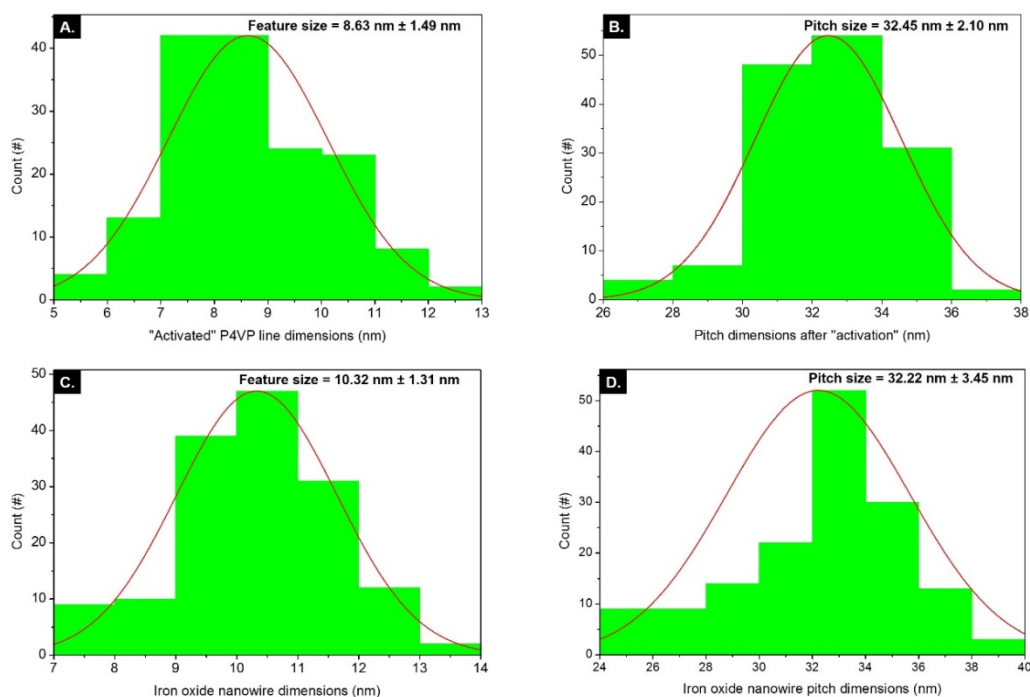


**Figure S7.7.1.** Graphs showing (a) P4VP microdomain feature size following “activation”, (b) P4VP pitch dimensions following “activation”, (c) feature size of iron oxide nanowires following iron oxide inclusion step, and (d) pitch of iron oxide nanowires following iron oxide inclusion process. Note that 150-170 features were measured from respective SEM images using ImageJ software for processing and calculation.

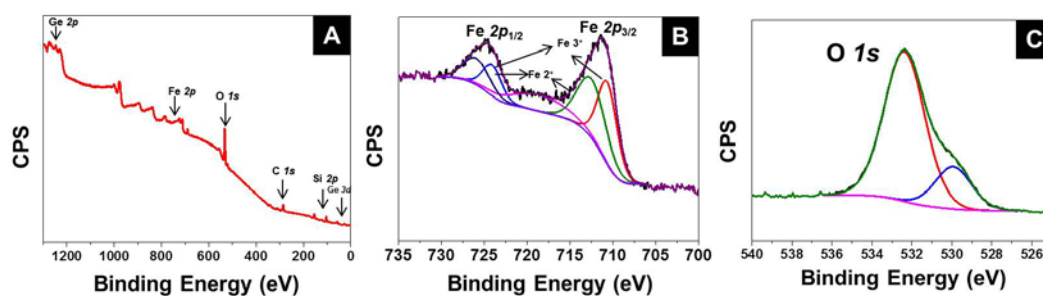


**Figure S7.7.2.** XPS data of iron oxide nanowires following metal ion oxidation and polymer removal through UV/O<sub>3</sub> treatment. (a) Survey spectrum of Fe<sub>3</sub>O<sub>4</sub> nanowires on GeOI substrate with HSQ prepatterns. Peaks identified include Ge 2*p*, Fe 2*p*, O 1*s*, C 1*s*, Si 2*p*, and Ge 3*d*. Expected peaks were observed at binding energies of ~1220-1215 eV for Ge 2*p*<sub>3/2</sub> and ~29 eV for Ge 3*d* due to the top layer of Ge of the GeOI substrate. We believe the C 1*s* peak and Si 2*p* are present due to residual polymer and residual HSQ material at the GeOI surface. Furthermore, high-resolution Fe 2*p* core level energy spectrum displayed in Figure S7.7.2b shows both Fe 2*p*<sub>3/2</sub> and Fe 2*p*<sub>1/2</sub> peaks at 710 eV and 724 eV respectively. These are in good agreement with previous literature.<sup>1</sup> The 2*p*<sub>3/2</sub> : 2*p*<sub>1/2</sub> ratio was calculated to be 2 : 1. Note that the 2*p* features were processed with the CasaXPS software using a Shirley background subtraction and curve-fitting to Voigt profiles. High resolution O 1*s* core level energy spectrum at 532 eV is shown in (c).

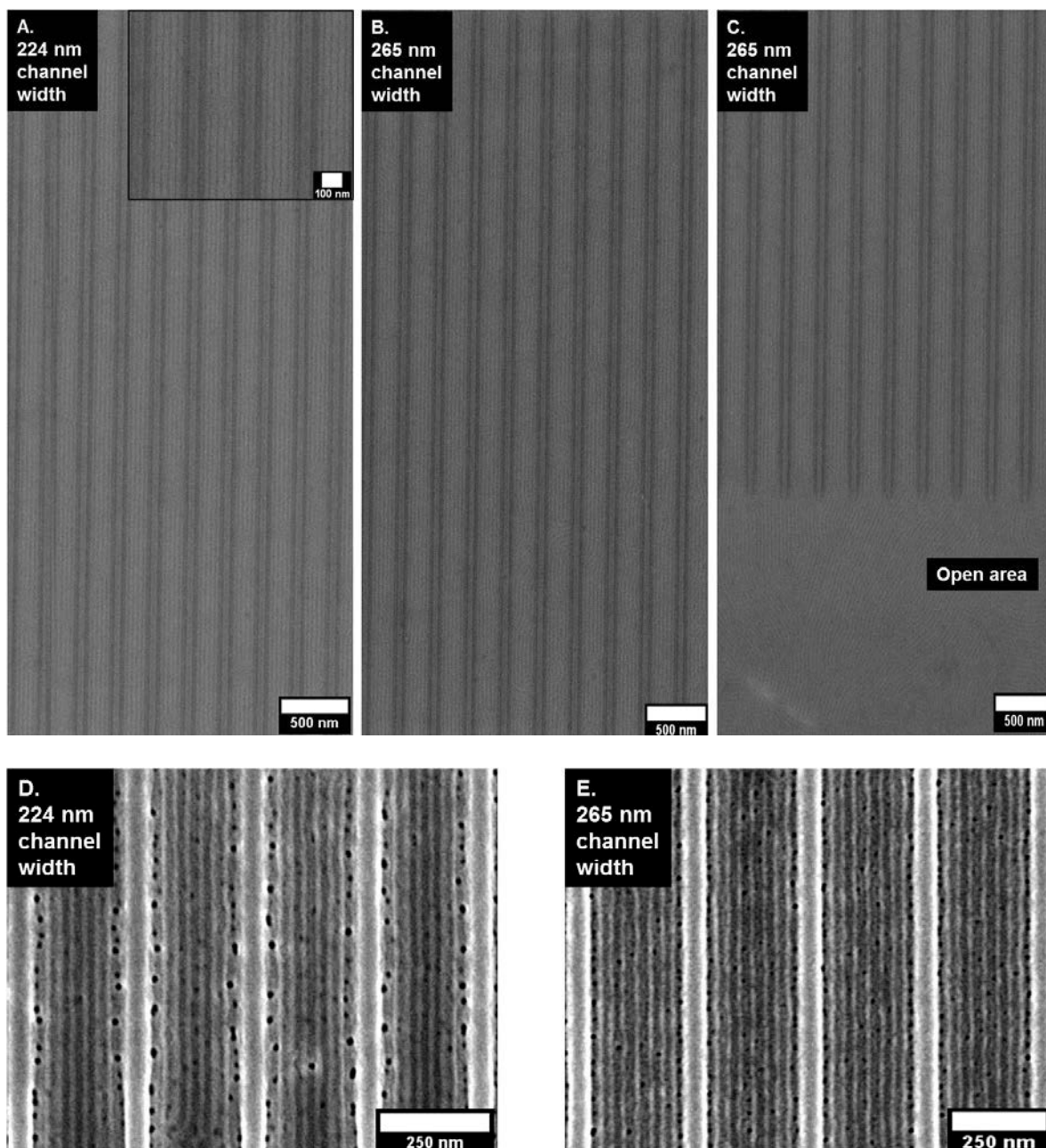


**Figure S7.7.3.** Top-down SEM images of large scale graphoepitaxial alignment of “activated” PS-*b*-P4VP templates following ethanol exposure on Ge in HSQ prepatterns of 224 nm channel width (a), and 265 nm channel widths (b) and (c). Note in (c) open unpatterned areas are evident with characteristic “fingerprint” patterns of cylinder lying parallel to substrate surface. (d) Top-down SEM image of arrays of 6 Fe<sub>3</sub>O<sub>4</sub> nanowires within HSQ prepatterns of 224 nm channel width after metal oxide inclusion process. (e) Top-down SEM image of arrays of 7 Fe<sub>3</sub>O<sub>4</sub> nanowires within HSQ prepatterns of 265 nm channel width after metal oxide inclusion process.

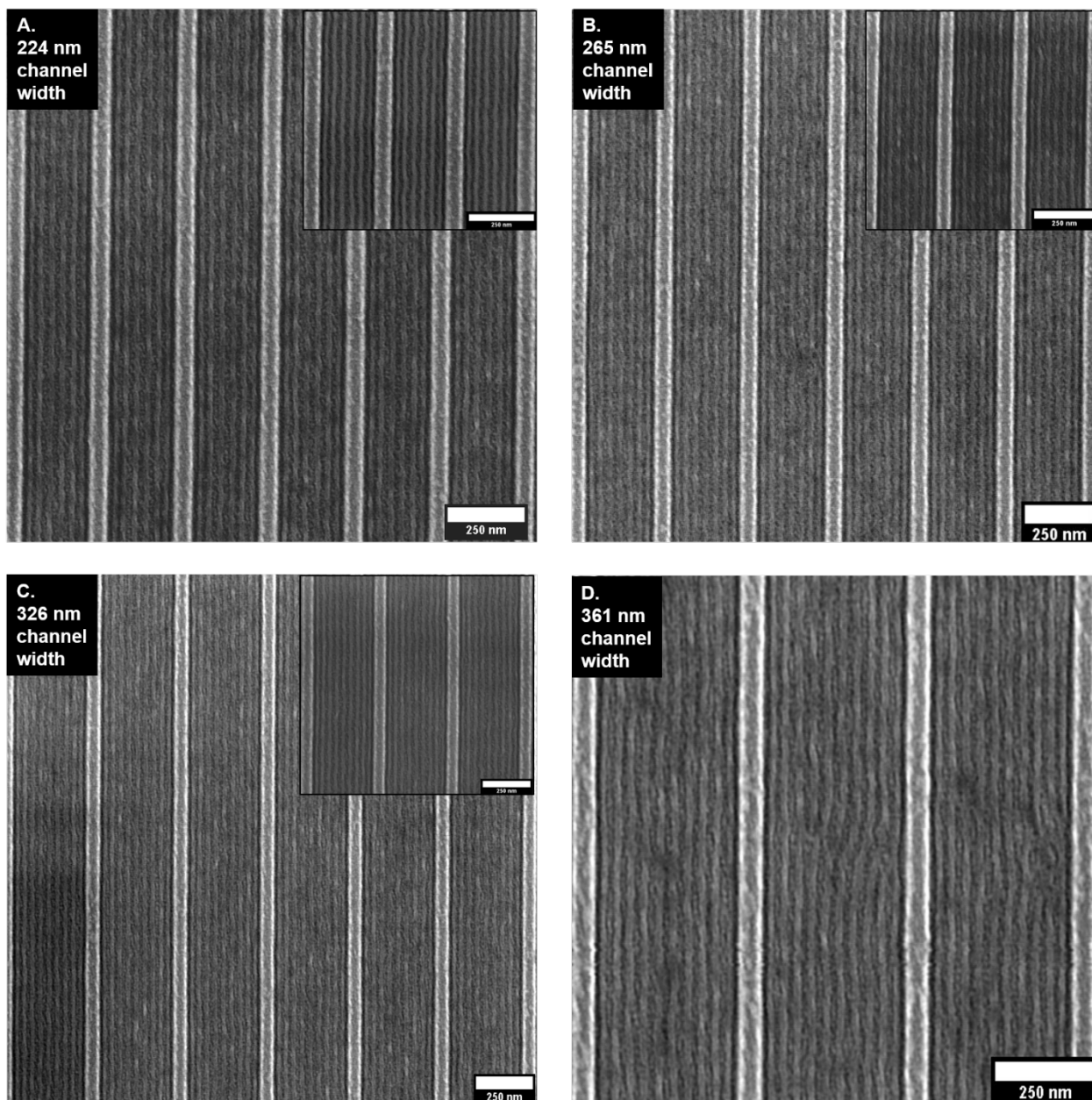


**Figure S7.7.4.** Top-down SEM images of DSA  $\text{Fe}_3\text{O}_4$  nanowire hardmasks in different channel widths after 3 seconds  $\text{CF}_4$  etching for pattern transfer. Channel widths for each are 224 nm (a), 265 nm (b), 326 nm (c), and 361 nm (d) respectively. One observes the contrast of the hardmask relative to the Ge material after plasma treatment. The contrast is slightly enhanced in comparison to unetched samples as displayed in Figure 7.2e-h in main chapter.

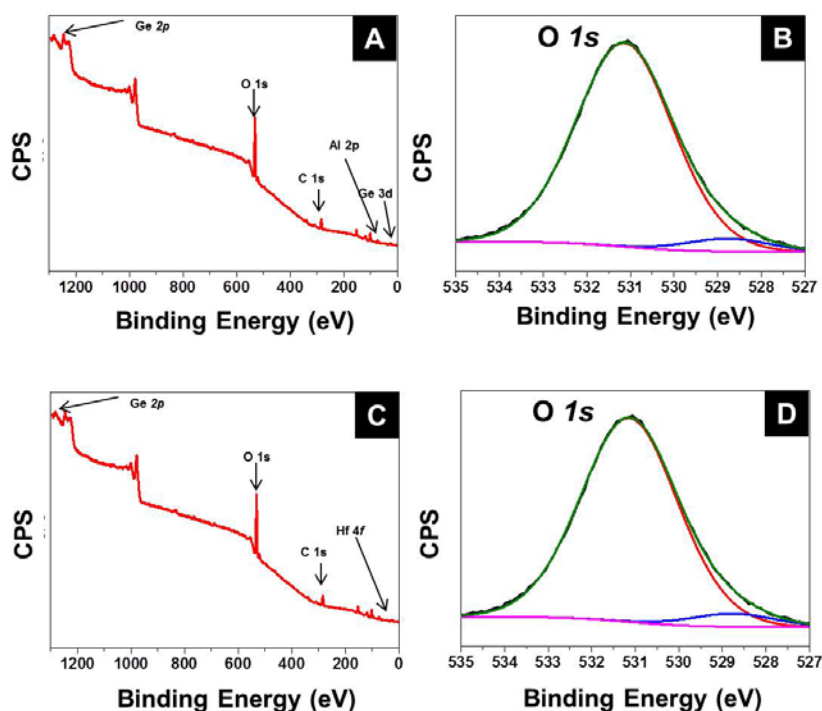


**Figure S7.7.5.** XPS spectra of (a) survey of  $\gamma$ - $\text{Al}_2\text{O}_3$  nanowires on planar GeOI following effective metal oxide inclusion and UV/ $\text{O}_3$  exposure for 3 hours showing expected peaks. (b) High resolution O  $1s$  of  $\gamma$ - $\text{Al}_2\text{O}_3$  with peak at 531 eV. High-resolution level energy spectrum of the Al  $2p$  peak at 73 eV is shown in inset in chapter 7 Figure 7.4a. XPS survey spectra and high-resolution level energy spectrum of oxygen for  $\text{HfO}_2$  nanowire sample on planar GeOI are shown in Figure S7.7.5 (c) and (d). High-resolution level energy spectrum of the Hf  $4f$  peak at 17 eV is shown in inset in chapter 7 Figure 7.4.b. The XPS of Al  $2p$  and Hf  $4f$  and corresponding high-resolution O  $1s$  values agree well with literature reports for both  $\gamma$ - $\text{Al}_2\text{O}_3$  and  $\text{HfO}_2$  material.<sup>2,3</sup>

## 7.8. References

- (1) Yamashita, T.; Hayes, P. Analysis of XPS spectra of  $\text{Fe}^{2+}$  and  $\text{Fe}^{3+}$  ions in oxide materials. *Applied Surface Science* **2008**, *254*, 2441-2449.
- (2) Yun, S. J.; Kang, J. S.; Paek, M. C.; Nam, K. S. Large-area atomic layer deposition and characterization of  $\text{Al}_2\text{O}_3$  film grown using  $\text{AlCl}_3$  and  $\text{H}_2\text{O}$ . *Journal of the Korean Physical Society* **1998**, *33*, S170-S174.
- (3) Kim, M. S.; Ko, Y. D.; Yun, M. S.; Hong, J. H.; Jeong, M. C.; Myoung, J. M.; Yun, I. G. Characterization and process effects of  $\text{HfO}_2$  thin films grown by metal-organic molecular beam epitaxy. *Materials Science and Engineering B-Solid State Materials for Advanced Technology* **2005**, *123*, 20-30.

---

*Chapter 8*

---

**Conclusions and Future Work**

## 8.1. Conclusions and Future Work

Next-generation electronic devices are expected to comprise an unprecedented level of sophistication. Whilst high speed and low power consumption are prerequisites, multi-functionality and increased connectivity will be anticipated by consumer's *i.e.* Internet of Things (IoT). Semiconductor and nanoelectronic industries have continually achieved increased growth and density of silicon device components every ~ 18 months. However, dimensional scaling of integrated circuit features at sub-10 nm may be problematic due to the physical limits of optical lithography and performance issues associated with silicon (leakage, voltage variability and signal delay) and thus new materials and processes are required to augment the lithographic process. This thesis aimed to demonstrate on-chip etch masks to fabricate high fidelity and high density silicon and germanium nanostructures using BCP lithography practices to provide viable routes for next-generation electronic technologies. The advantages of BCP patterning are clear and well-known including; 1) low cost, 2) high areal density with high throughput and 3) ability to access sub-20 nm features. Limitations and challenges in the DSA of BCPs field that this PhD work focused on included; 1) extending etch methodologies using a PS-*b*-PLA BCP, 2) enabling high etch contrast using "in-situ" metal oxide hardmasks with PS-*b*-P4VP BCP, and 3) integrating these processes with DSA technology.

Chapter 1 introduced the fundamental areas of BCP materials and employed methods in the past and more recently for inorganic incorporation with "neat" BCPs. The incorporation methods detailed were in relation to their use as on-chip etch masks for advanced lithography purposes. Additionally, functional uses for devices and non-electronic uses were also mentioned. Whilst efforts for advanced lithography patterning will continue, the area of BCP patterning for inorganic inclusion and resulting pattern

transferred geometries are now being used for diverse functions as smart surfaces, in biomedical devices and for energy conservation. This is an area that will continue to grow and much future work will focus on these uses with possibilities for commercialization.

Chapter 2 outlined simple wet etch processes for removing the PLA block from PS-*b*-PLA lamellar patterns. The processes developed can be easily adopted by university research laboratories or small scale processes where dry etching tools are not available/accessible. The presence of a wetting layer or weak PS interactions requires careful substrate modification to retain the BCP film and avoid detachment. Another notable issue identified was pattern collapse in the PS-*b*-PLA system that was due to the thickness of the film. High aspect ratio of resist or on-chip etch masks will limit overall pattern transfer fidelity. The dry etch process described in chapter 2 for the removal of PLA from PS-*b*-PLA forming line space features was highly selective with great promise for lithographic patterning process to sub-20 nm features.

Chapter 3 focused on the self-assembly of PS-*b*-PLA BCP line patterns using conventional solvent vapor annealing to form ultra-thin lithography relevant etch masks. Chapter 3 described short processing periods (< 1 hour) to form thin BCP films on silicon that are ideal for pattern transfer purposes. The through film uniformity was characterized via GISAXS measurements. Wet etch processes for PLA etching were also shown with high selectivity. DSA was utilized for guiding self-assembly of PS-*b*-PLA features. Future work must be carried out to optimize the DSA process to meet acceptable levels of pattern registration and control of alignment direction.

Chapter 4 highlighted a simple and short processing route using a molecular functionalization process to enhance and increase PS-*b*-P4VP BCP ordering and coverage. The route described avoided time consuming and costly polymer brush surface modifications. Moreover, the BCP templates were utilized for demonstrating the efficacy of a metal oxide inclusion procedure. Iron oxide nanodots were generated at the substrate surface after simple spin coating and following ICP etching, Si nanopillars were generated. The process surpasses “soft mask” templates as high aspect ratio (1:6) Si features were fabricated after pattern transfer.

Chapter 5 detailed the self-assembly and alignment of PS-*b*-P4VP line features using HSQ prepatterns over large areas. Metal oxide inclusion was utilized for the generation of aligned 16 nm half-pitch silicon nanofins. The ability to position and orientate PS-*b*-P4VP features and successfully enhance contrast using metal oxides integrated with graphoepitaxy is important for DSA to address device relevant geometries. Additionally, the alternative pattern transfer strategy was accomplished using various metal oxide materials showing the versatility of the process to enhance contrast leading to high fidelity (>1:4) silicon nanofins. Future work must focus on reproducing similar fidelity nanofins using smaller pitch patterns. The etching process at smaller dimensions will be considerably more complex in the sub-10 nm range as plasma based etches at the deep nanoscale regime are not well understood.

Chapter 6 is closely related to the process described in chapter 5 and highlights an issue observed following metal oxide inclusion and upon pattern transfer of nanodomain variation along guiding sidewalls. Graphoepitaxy was used to guide PS-*b*-P4VP line features and feature size reduction was observed at sidewalls following solvent vapor

annealing. Excess swelling during solvent vapor annealing causing volume expansion was postulated to be the cause of the feature perturbation observed. Using wider trenches to compensate for the added volume expansion and thus larger BCP periodicity during solvent vapor annealing and monitoring of solvent-polymer parameters were put forward as means to avoid domain variations. Further study is needed to address this phenomenon and as suggested, trench widths should be adjusted to match the solvent vapor annealed periodicity and not the dried state periodicity. Additionally, investigation of solvents with different selectivity values that form line patterns of PS-*b*-P4VP may lead to less swelling/volume expansion and thus avoid deformation or feature size reduction. Moreover, “*in-situ*” swelling studies would be insightful to precisely calculate the solvent vapor annealed BCP periodicity and thus identify an optimum window for channel widths. Jung and co-workers<sup>1</sup> recently described employing warm solvent vapor annealing to reduce cylinder line edge roughness and cylinder deformation in a PS-*b*-PDMS BCP system.

Chapter 7 presented an integrated approach to achieve high aspect ratio sub-10 nm aligned germanium nanofins using metal oxide enhanced PS-*b*-P4VP line features. Germanium is of much interest in the scientific community as a high mobility material to advance next generation electronic devices.<sup>2</sup> As described in chapter 5 and chapter 6, HSQ prepatterns initially employed to guide PS-*b*-P4VP features during solvent vapor annealing. Germanium-on-insulator (GeOI) substrates were used for demonstration and after metal oxide inclusion and pattern transfer resulted in high fidelity Ge nanofins. GeOI is potentially a very promising substrate for industrial integration as Ge nanostructures can be fabricated on a substrate possessing similar properties to silicon. BCP patterning has been shown using other high mobility materials such as graphene<sup>3,4</sup>

however this chapter demonstrated pattern transfer of a BCP mask on germanium for the first time. Future work regarding the applicability of patterning smaller features must be carried out to assess the viability of DSA BCP patterning on GeOI.

Whilst this thesis has documented sub-20 nm half-pitches and sub-10 nm pattern transferred features, many challenges exist and will emerge as BCP patterning and DSA methodologies aim to achieve sub-10 nm pattern transferred pitches. With this goal, new materials and innovative processes will be needed to achieve further fin scaling. Since BCP microphase separation is difficult to achieve with lower  $\chi N$  values, “exotic” BCP materials or new additives to BCPs will be needed that can retain a  $\chi N$  value in the ordered phase. This may be possible using sugar<sup>5</sup> based BCPs as was reported lately to effectively raise a BCPs  $\chi N$  value at low molecular weight or using salt addition<sup>6</sup> to effect a BCPs  $\chi$  value.

Additionally, the study of scaling BCPs for etch-mask application will encompass metrology methods for assessing global coverage and defects of polymer patterns. Moreover, high-resolution imaging, including helium ion microscopy<sup>7</sup> and 3-D electron tomography<sup>8,9</sup> of patterns will be required as the resolution of current techniques may not be able to characterize patterns effectively in the sub-10 nm regime.

## 8.2. References

- (1) Kim, J. M.; Kim, Y.; Park, W. I.; Hur, Y. H.; Jeong, J. W.; Sim, D. M.; Baek, K. M.; Lee, J. H.; Kim, M.-J.; Jung, Y. S. Eliminating the Trade-Off between the Throughput and Pattern Quality of Sub-15 nm Directed Self-Assembly via Warm Solvent Annealing. *Advanced Functional Materials* **2015**, *25*, 306-315.
- (2) O'Regan, C.; Biswas, S.; Petkov, N.; Holmes, J. D. Recent advances in the growth of germanium nanowires: synthesis, growth dynamics and morphology control. *Journal of Materials Chemistry C* **2014**, *2*, 14-33.
- (3) Liu, G.; Wu, Y.; Lin, Y.-M.; Farmer, D. B.; Ott, J. A.; Bruley, J.; Grill, A.; Avouris, P.; Pfeiffer, D.; Balandin, A. A.; Dimitrakopoulos, C. Epitaxial Graphene Nanoribbon Array Fabrication Using BCP-Assisted Nanolithography. *ACS Nano* **2012**, *6*, 6786-6792.

- (4) Son, J. G.; Son, M.; Moon, K.-J.; Lee, B. H.; Myoung, J.-M.; Strano, M. S.; Ham, M.-H.; Ross, C. A. Sub-10 nm Graphene Nanoribbon Array Field-Effect Transistors Fabricated by Block Copolymer Lithography. *Advanced Materials* **2013**, *25*, 4723-4728.
- (5) Otsuka, I.; Tallegas, S.; Sakai, Y.; Rochas, C.; Halila, S.; Fort, S.; Bsiesy, A.; Baron, T.; Borsali, R. Control of 10 nm scale cylinder orientation in self-organized sugar-based block copolymer thin films. *Nanoscale* **2013**, *5*, 2637-2641.
- (6) Kim, S. H.; Misner, M. J.; Yang, L.; Gang, O.; Ocko, B. M.; Russell, T. P. Salt complexation in block copolymer thin films. *Macromolecules* **2006**, *39*, 8473-8479.
- (7) Borah, D.; Ghoshal, T.; Shaw, M. T.; Chaudhari, A.; Petkov, N.; Bell, A. P.; Holmes, J. D.; Morris, M. A. The Morphology of Ordered Block Copolymer Patterns as Probed by High Resolution Imaging. *Nanomaterials and Nanotechnology* **2014**, *4*.
- (8) Gotrik, K. W.; Lam, T.; Hannon, A. F.; Bai, W.; Ding, Y.; Winterstein, J.; Alexander-Katz, A.; Liddle, J. A.; Ross, C. A. 3D TEM Tomography of Templated Bilayer Films of Block Copolymers. *Advanced Functional Materials* **2014**, *24*, 7689-7697.
- (9) Segal-Peretz, T.; Winterstein, J.; Doxastakis, M.; Ramírez-Hernández, A.; Biswas, M.; Ren, J.; Suh, H. S.; Darling, S. B.; Liddle, J. A.; Elam, J. W.; de Pablo, J. J.; Zaluzec, N. J.; Nealey, P. F. Characterizing the Three-Dimensional Structure of Block Copolymers via Sequential Infiltration Synthesis and Scanning Transmission Electron Tomography. *ACS Nano* **2015**, *9*, 5333-5347.